Contribution of atomic force microscopy to local mechanical characterization of polymer materials

Benjamin Megevand

N°d'ordre NNT : 2018LYSEI023

THESE de DOCTORAT DE L'UNIVERSITE DE LYON
opérée au sein de
l'Institut National des Sciences Appliquées de Lyon

Ecole Doctorale N° ED34
Matériaux de Lyon

Spécialité de doctorat : Matériaux

Soutenue publiquement le 29/03/2018, par :
Benjamin MEGEVAND

Contribution of atomic force microscopy to local mechanical characterization of polymer materials

---

Devant le jury composé de :

LECLERE, Philippe	Directeur de Recherche (Université de Mons)	Rapporteur
CARRIERE, Pascal	Maître de Conférences HDR (Université de Toulon)	Rapporteur
LAHOUD DIGNAT, Nadine	Maître de Conférences (Université Toulouse III)	Examinatrice
CHAPEL, Jean-Paul	Directeur de Recherche (CRPP Bordeaux)	Examinateur
FEBVRE, Mickael	Ingénieur d'application (Bruker Nano, Inc.)	Invité
DUCHET-RUMEAU, Jannick	Professeure des Universités (INSA-Lyon)	Directrice de thèse
PRUVOST, Sébastien	Maître de Conférences HDR (INSA-Lyon)	Co-directeur de thèse

Département FEDORA – INSA Lyon - Ecoles Doctorales – Quinquennal 2016-2020

SIGLE	ÉCOLE DOCTORALE	NOM ET COORDONNEES DU RESPONSABLE
CHIMIE	**CHIMIE DE LYON** **http://www.edchimie-lyon.fr** Sec. : Renée EL MELHEM Bât. Blaise PASCAL, 3e étage **secretariat@edchimie-lyon.fr** INSA : R. GOURDON	M. Stéphane DANIELE Institut de recherches sur la catalyse et l'environnement de Lyon IRCELYON-UMR 5256 Équipe CDFA 2 Avenue Albert EINSTEIN 69 626 Villeurbanne CEDEX **directeur@edchimie-lyon.fr**
E.E.A.	**ÉLECTRONIQUE, ÉLECTROTECHNIQUE, AUTOMATIQUE** **http://edeea.ec-lyon.fr** Sec. : M.C. HAVGOUDOUKIAN **ecole-doctorale.eea@ec-lyon.fr**	M. Gérard SCORLETTI École Centrale de Lyon 36 Avenue Guy DE COLLONGUE 69 134 Écully Tél : 04.72.18.60.97 Fax 04.78.43.37.17 **gerard.scorletti@ec-lyon.fr**
E2M2	**ÉVOLUTION, ÉCOSYSTÈME, MICROBIOLOGIE, MODÉLISATION** **http://e2m2.universite-lyon.fr** Sec. : Sylvie ROBERJOT Bât. Atrium, UCB Lyon 1 Tél : 04.72.44.83.62 INSA : H. CHARLES **secretariat.e2m2@univ-lyon1.fr**	M. Fabrice CORDEY CNRS UMR 5276 Lab. de géologie de Lyon Université Claude Bernard Lyon 1 Bât. Géode 2 Rue Raphaël DUBOIS 69 622 Villeurbanne CEDEX Tél : 06.07.53.89.13 **cordey@univ-lyon1.fr**
EDISS	**INTERDISCIPLINAIRE SCIENCES-SANTÉ** **http://www.ediss-lyon.fr** Sec. : Sylvie ROBERJOT Bât. Atrium, UCB Lyon 1 Tél : 04.72.44.83.62 INSA : M. LAGARDE **secretariat.ediss@univ-lyon1.fr**	Mme Emmanuelle CANET-SOULAS INSERM U1060, CarMeN lab, Univ. Lyon 1 Bâtiment IMBL 11 Avenue Jean CAPELLE INSA de Lyon 69 621 Villeurbanne Tél : 04.72.68.49.09 Fax : 04.72.68.49.16 **emmanuelle.canet@univ-lyon1.fr**
INFOMATHS	**INFORMATIQUE ET MATHÉMATIQUES** **http://edinfomaths.universite-lyon.fr** Sec. : Renée EL MELHEM Bât. Blaise PASCAL, 3e étage Tél : 04.72.43.80.46 Fax : 04.72.43.16.87 **infomaths@univ-lyon1.fr**	M. Luca ZAMBONI Bât. Braconnier 43 Boulevard du 11 novembre 1918 69 622 Villeurbanne CEDEX Tél : 04.26.23.45.52 **zamboni@maths.univ-lyon1.fr**
Matériaux	**MATÉRIAUX DE LYON** **http://ed34.universite-lyon.fr** Sec. : Marion COMBE Tél : 04.72.43.71.70 Fax : 04.72.43.87.12 Bât. Direction **ed.materiaux@insa-lyon.fr**	M. Jean-Yves BUFFIÈRE INSA de Lyon MATEIS - Bât. Saint-Exupéry 7 Avenue Jean CAPELLE 69 621 Villeurbanne CEDEX Tél : 04.72.43.71.70 Fax : 04.72.43.85.28 **jean-yves.buffiere@insa-lyon.fr**
MEGA	**MÉCANIQUE, ÉNERGÉTIQUE, GÉNIE CIVIL, ACOUSTIQUE** **http://edmega.universite-lyon.fr** Sec. : Marion COMBE Tél : 04.72.43.71.70 Fax : 04.72.43.87.12 Bât. Direction **mega@insa-lyon.fr**	M. Philippe BOISSE INSA de Lyon Laboratoire LAMCOS Bâtiment Jacquard 25 bis Avenue Jean CAPELLE 69 621 Villeurbanne CEDEX Tél : 04.72.43.71.70 Fax : 04.72.43.72.37 **philippe.boisse@insa-lyon.fr**
ScSo	**ScSo*** **http://ed483.univ-lyon2.fr** Sec. : Viviane POLSINELLI Brigitte DUBOIS INSA : J.Y. TOUSSAINT Tél : 04.78.69.72.76 **viviane.polsinelli@univ-lyon2.fr**	M. Christian MONTES Université Lyon 2 86 Rue Pasteur 69 365 Lyon CEDEX 07 **christian.montes@univ-lyon2.fr**

*ScSo : Histoire, Géographie, Aménagement, Urbanisme, Archéologie, Science politique, Sociologie, Anthropologie

À pépé

Remerciements

Le présent manuscript cristallise plus de trois ans de travail minutieux de planification, d'apprentissage, de manipulation, d'analyse, de communication, de rédaction, d'arrachage méthodique de cheveux et de réflexion acharnée sur le sens de la vie. J'en ressors pourtant vivant, en bonne santé et même épanoui. J'ai beaucoup appris durant ces années, et ce bien au-delà des seules caractérisations nano-mécaniques, grâce aux personnes qui m'ont entouré et dont je vais tenter, de manière la plus exhaustive possible, de faire mention ci-dessous.

Tout oubli, aussi impardonnable soit-il, doit m'être immédiatement signalé afin d'être pris en compte dans les plus brefs délais. Une version corrigée du présent manuscript sera envoyée à la personne lésée.

Je tiens premièrement à remercier sincèrement Jannick et Sébastien, mes directeurs de thèse, pour m'avoir encouragé, accompagné et conseillé pendant ces quelques 40 mois. J'en tire une expérience encore plus enrichissante que je ne l'imaginais, tant scientifiquement qu'humainement.

Je remercie vivement Philippe Leclère et Pascal Carrière de me faire l'honneur d'avoir accepté de rapporter cette thèse, ainsi que Nadine Lahoud et Jean-Paul Chapel pour l'intérêt porté à ce travail.

Merci à l'équipe de Bruker nano France, pour les nombreuses discussions enrichissantes et leur accueil à chaque fois que j'en ai eu besoin.

Merci à Sébastien Livi, à Jean-François Gérard, pour leurs conseils précieux. Je tiens aussi à remercier Pierre Alcouffe et Ruben Vera pour les manips additionnelles et les discussions enrichissantes.

Je veux réserver ici une place d'honneur pour l'ensemble du laboratoire IMP, ceux du passé et du présent, des permanents aux plus ponctuels, avec une mention spéciale à mes consœurs et confrères doctorants, grâce à qui la vie au labo fut bien plus agréable (à défaut parfois d'être respirable, pour cause d'effluves de chambre froide). Aux anciens et aux nouveaux de mon bureau, Héloïse, Jane et son art de décaler les sons, Camou, José, Fourmi, Mamandine, Gomar, Thibor, VMatthieu, Raïssa, pour tous les beaux moments, pour les sommets (de tous types) gravis ainsi que pour les bas-fonds (de type intellectuel) atteints. À tous les autres avec qui j'ai pu tisser des amitiés que je souhaite durables (je sens l'oubli fatal venir), Gaby, Soso, Spigo, JC, Quentin, Nour, Jclnt, Bouchax, Marie, Tibère, Toto, et surtout à ceux que j'ai oubliés (j'ai trouvé la parade).

Merci à l'AFM du labo, aussi, finalement. Sans rancune, on a fini par faire de belles choses ensemble. Je passerai te voir à l'occasion. Je te souhaite un bel avenir, et j'espère te laisser en de bonnes mains. Je présente mes plus plates excuses envers toutes les pointes que j'ai maltraitées.

Je tiens aussi à remercier du fond du cœur mon entourage personnel, qui fut garant (avec succès, je présume) de ma santé mentale (ou pas) pendant ces trois années et quelques, et sans qui je n'aurais pas eu une infime fraction du courage nécessaire à la conduite de ce travail. Merci en particulier à Celia et Axel, pour les relectures et surtout pour tout le reste, LH et les sessions BU salutaires, Joel, mon colloc de toujours, tous mes voisins géniaux — en particulier Marianne, Luc, Lucas et Alice qui ont bien pris soin de moi dans les phases terminales, à mon médecin traitant Jacques, aux anciens du 77 et associés, à la mafia latina, et à tous les potes de tout poil partout dans le monde. Merci au Badhinjan Trio, à IZR, à Mari Pegá, au Grand Ensemble, aux Amerinsas, à Pirca et tous ceux avec qui j'ai pu jouer. Merci à Dhafer. Merci à Aytaç. Merci à mon vélo d'avoir tenu bon.

J'ai envie d'en dire tellement plus, mais par un souci d'économies de papier et de sentimentalisme, je vais terminer en dédiant cette thèse à ma famille, Maman, Mamie, ma frangine, Papa et tous les autres.

List of Abbreviations and Symbols

$\Delta_c H$	crystallization enthalpy
$\Delta_m H$	melting enthalpy
ϵ	mechanical strain
$\bar{\varepsilon_r}$	complex relative dielectric permittivity
ε_r'	real part of relative dielectric permittivity
ε_r"	imaginary part of relative dielectric permittivity (loss)
θ	Bragg's diffraction angle; tip angle in chapter 2
λ	Maugis-Dugdale parameter
ν	Poisson's ratio
ξ_0	interatomic equilibrium distance
ρ	volumetric mass density
σ	mechanical stress
τ	relaxation time
χ_c	crystallinity
AFM	atomic force microscopy/atomic force microscope
CNWs	cellulose nanowhiskers
DMA	Dynamic mechanical analysis
DMT	Derjaguin-Muller-Toporov (contact mechanics model)
DSC	Differential Scanning Calorimetry
E	Young's modulus
E_{DMT}	DMT modulus
E_A	activation energy
HOPG	highly oriented pyrolytic graphite
ILs	ionic liquids
il-Cl	trihexyltetradecyl phosphonium chloride
il-TMP	trihexyltetradecyl phosphonium bis-2,4,4-(trimethylpentyl)phosphinate
JKR	Johnson, Kendall and Roberts (contact mechanics model)
K	Scherrer shape factor
k_B	Boltzmann constant
k_{tip}	spring constant of a cantilever
MA	maleic acid
MAF	mobile amorphous fraction
MWNT	multiwall carbon nanotubes
PA	polyamide
PAA	poly(acrylic acid)
PBA	polybutylene adipate
PBAT	poly(butylene adipate-*co*-terephtalate)
PBT	polybutylene terephtalate
PCL	polycaprolactone
PDMS	polydimethylsiloxane
PE	polyethylene
PEG	polyethylene glycol
PEI	polyethyleneimine
PLA	poly(lactic acid)
POSS	polyhedral oligometric silsesquioxane

PS	polystyrene
PU	polyurethane
PVA	poly(vinyl alcohol)
PVC	poly(vinyl chloride)
PVME	poly(vinyl methyl ether)
P(VDF-CTFE)	poly(vinylidene fluoride-*co*-chlorotrifluoroethylene)
QNM	(PeakForce-) Quantitative NanoMechanics^{TM} (Bruker AFM mode)
RAF	rigid amorphous fraction
R_{tip}	tip radius
SEM	scanning electron microscopy
SPM	scanning probe microscopy
T_α	α transition temperature
T_g	glass transition temperature
T_m	melting temperature
$tan(\delta)$	loss factor (dielectric or dynamic mechanical analysis)
TEM	transmission electron microscopy
TUNA	(PeakForce-) TUNneling AFM^{TM} (Bruker AFM mode)
UV	ultraviolet
w	Bradley's adhesion work
WAXS	wide-angle X-ray scattering
XRD	X-ray diffraction
Z	vertical axis

Abstract

This thesis work aims to show how nanomechanical characterizations in AFM can provide a better understanding of structure-properties relationships in polymers. In this context, the technique itself and the associated theoretical basis are first analyzed to implement a robust methodology in order to perform reproducible, quantitative measurements.

Two main studies are carried out around a common topic: the understanding of the interactions between biopolymers and ionic liquids (ILs). First, the compatibilization of PBAT/PLA blends by two different ILs (namely il-Cl and il-TMP) is studied. Adhesion and local modulus mappings evidence the resulting microstructures, and highlight that the compatibilization mainly results from a modification of the PBAT/PLA interface, becoming a cohesive interphase. This is due to specific interaction with the cations and the anions of each IL, which are preferentially located at those interphases.

The second study is more specifically about the understanding of the modification of semicrystalline PBAT by the addition of small amounts of the same ionic liquids. While il-TMP forms dissipative nodules dispersed into the matrix with a cohesive interphase between both, il-Cl, miscible into the amorphous phase of PBAT, amplifies the chain mobility in the bulky MAF (*i.e.* Mobile Amorphous Fraction) and hinders it in the confined RAF (*i.e.* Rigid Amorphous Fraction), leading to interesting macroscopical properties modifications.

More than showing some interesting capabilities of ILs as additives in polymers, those results also show an outstanding potential of AFM nanomechanical mappings for the in-deep understanding of structure-properties relationships in materials.

Résumé

Ce travail de thèse a pour but de montrer comment des caractérisations nanomécaniques en AFM peuvent apporter une meilleure compréhension des relations structure-propriétés dans les polymères. Dans ce contexte, la technique elle-même et sa base théorique sont d'abord analysées pour mettre en œuvre une méthodologie robuste afin d'effectuer des mesures reproductibles.

Deux études principales sont menées sur un thème commun : la compréhension des interactions entre les biopolymères et les liquides ioniques (ILs). Tout d'abord, la compatibilisation des mélanges PBAT/PLA par deux ILs différents (à savoir il-Cl et il-TMP) est étudiée. Les images AFM d'adhésion et de module local mettent en évidence les différentes microstructures, et soulignent que la compatibilisation résulte principalement d'une modification de l'interface PBAT/PLA, devenant une interphase cohésive. Ceci est dû à une interaction spécifique avec les cations et les anions de chaque liquide ionique, qui se situent préférentiellement au niveau de ces interphases.

La deuxième étude porte plus précisément sur la modification du PBAT semi-cristallin par de petites quantités des mêmes liquides ioniques. Alors que il-TMP forme des nodules dissipatifs dispersés dans la matrice et une interphase cohésive avec celle-ci, il-Cl, miscible dans la phase amorphe du PBAT, augmente la mobilité de la chaîne dans la MAF (*i.e.* fraction amorphe mobile) et l'entrave dans la RAF confinée(*i.e.* fraction amorphe rigide), conduisant à des modifications intéressantes des propriétés macroscopiques.

En plus de montrer certaines capacités intéressantes des ILs comme additifs dans les polymères, ces résultats dévoilent également un potentiel exceptionnel des caractérisations nanomécaniques en AFM pour la compréhension en profondeur des relations structure-propriétés dans les matériaux.

Contents

Résumé Étendu

Contents

Cette thèse de doctorat a été conduite au sein du laboratoire Ingénierie des Matériaux Polymères (IMP—UMR CNRS 5223) de L'INSA-Lyon, de 2014 à 2017 sous la co-direction de Sébastien Pruvost (Maître de Conférences à l'INSA-Lyon) et de Jannick DUCHET-RUMEAU (Professeure des Universités à l'INSA–Lyon). Ces travaux ont été financés par le Ministère de l'Enseignement Supérieur et de la Recherche (MESR).

0.1 Introduction et objectifs

Comprendre le lien entre la formulation, la structure et les propriétés d'un matériau constitue un aspect fondamental de la science des polymères, en particulier lorsqu'il s'agit de mélanges, de composites ou de formulations originales. Cela permet de concevoir des matériaux fonctionnels en anticipant leurs propriétés, et ainsi d'adapter les procédés de mise en oeuvre et les choix de formulation au résultat souhaité. Cela implique cependant la maîtrise de nombreux paramètres, à différentes échelles, caractérisables individuellement mais difficiles à mettre en relation entre eux.

La Microscopie à Force Atomique (AFM) permet, comme peu de techniques de caractérisations, de mesurer des propriétés locales de matériaux en les cartographiant, donc non seulement de mesurer des propriétés locales, mais aussi d'observer leur distribution sur une surface, avec une excellente résolution spatiale (latérale et en hauteur). La pointe de la sonde de l'AFM, ayant un rayon de courbure de quelques nanomètres, balaie la surface et peut en chaque point acquérir des informations.

L'unicité de cette technique réside ainsi dans le fait que les propriétés caractérisées sont des propriétés *locales*, c'est-à-dire qu'elles ne reflètent que le point de la surface auquel elles ont été mesurées (et éventuellement son proche voisinage), et non l'ensemble du matériau. Cela permet de mettre en regard structure et propriétés, en observant l'organisation spatiale de ces dernières.

Le mode PeakForce QNM (Bruker, États-Unis) permet au microscope à force atomique de cartographier les propriétés mécaniques locales des matériaux : module élastique, force d'adhésion (par rapport au retrait de la pointe), déformation et énergie de dissipation. Ses particularités sont notamment qu'il s'appuie sur des calibrations permettant d'atteindre une reproductibilité de mesure sans précédent, et sur un contrôle de la force d'appui de la pointe, lui conférant une excellente sensibilité.

Cette technique encore nouvelle est ainsi très prometteuse dans l'étude des systèmes polymères : on peut ainsi visualiser le comportement mécanique individuel des différentes phases d'un système (pour les polymères semicristallins, mélanges ou encore des composites), en même temps que leur organisation spatiale. Il est aussi possible d'explorer les interfaces, jouant un rôle prépondérant dans les propriétés d'un système multiphasé. Le but de ces travaux est ainsi de corréler ces observations avec le comportement mécanique macroscopique des matériaux étudiés, afin d'en approfondir la compréhension.

Il a été choisi d'axer ces caractérisations autour de deux thèmes : d'une part, les liquides ioniques, sels dont la température de fusion est inférieure à 100°C (mais souvent inférieure à la température ambiante), possèdant des propriétés uniques (pression de vapeur saturante très faible, bonne stabilité en température, non-inflammabilité...). Ajoutés en tant qu'additifs dans les systèmes polymères, ils ont récemment montré des résultats prometteurs en tant que com-

patibilisants pour mélanges, modificateurs de structure, ou encore plastifiants. Les mécanismes dont ils sont à l'origine étant encore peu décrits, leur étude semble intéressante.

D'autre part, les biopolymères (polymères biosourcés et/ou biodégradables) seront étudiés, dans la logique actuelle de leur développement en vue d'un affranchissement grandissant des ressources pétrolières. La microscopie à force atomique sera mise à contribution pour tenter d'approfondir ce qui explique, dans leur structure à l'échelle nanoscopique, le comportement mécanique de systèmes biopolymères, modifiés ou non par des liquides ioniques.

0.2 Mécanique en microscopie à force atomique

Il est tout d'abord utile de rappeler que le microscope à force atomique fonctionne grâce à une sonde constituée d'un levier, que l'on appellera *cantilever* par la suite, au bout duquel se situe une pointe orientée vers le bas, destinée à l'interaction avec l'échantillon. Le terme *pointe* peut aussi désigner la sonde dans sa totalité.

Bien que d'autres existent, le mode *Peak Force QNM* est aujourd'hui le principal outil de mesures mécaniques en microscopie à force atomique. Ce travail de thèse s'axe ainsi principalement sur ce mode et ses apports.

0.2.1 Principe général du mode PeakForce QNM

La technologie du Peak Force Tapping, apparue à la fin des années 2000, permet d'ouvrir la microscopie à force atomique à la possibilité d'effectuer simultanément des cartographies de propriétés locales.

Le principe reste le même que pour le mode Tapping, largement utilisé en AFM : la pointe en oscillation verticale vient au contact de l'échantillon à chaque cycle. Cependant, la manière de la piloter est différente :

- Le paramètre principal de contrôle n'est pas l'**amplitude** d'oscillation du cantilever frappant une surface, mais la force maximale imposée à la surface par la pointe à chaque contact. La force d'appui est connue et contrôlée grâce à la déflection du cantilever et sa constante de raideur, préalablement mesurée avec précision lors d'une étape de calibration.

- Le cantilever, excité en mode Tapping à une fréquence proche de sa résonnance, oscille **hors résonnance** en Peak Force Tapping, à une fréquence plus basse (quelques kHz). Cela facilite grandement l'acquisition et le contrôle de la force appliquée par la pointe.

Avec ce contrôle, à chaque contact pointe-échantillon, donc à chaque pixel de l'image, l'évolution de la force d'interaction est enregistrée et mise en relation avec la position de la pointe. Les courbes de force obtenues à chaque pixel d'une image sont analysées directement pendant l'acquisition pour produire des images de **forces d'adhésion**, de **modules d'Young**, d'**énergie de dissipation** et de **déformation** en même temps qu'une cartographie classique de la topographie. La Figure 1 montre une courbe de force typique sur laquelle on a accès aux mesures de propriétés locales.

- La **déformation** correspond à la distance parcourue par la pointe jusqu'au pic après avoir passé ce qui a été défini comme le contact. Il s'agit généralement du point où la force se met à augmenter significativement.

- La **force d'adhésion** est la force négative maximale au début du retrait de la pointe.

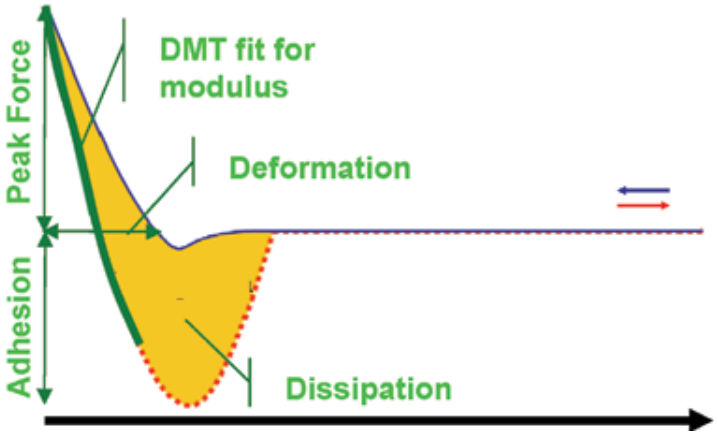

Figure 1 – Courbe de force traitée et propriétés mécaniques locales. L'axe des abscisses représente la distance pointe-échantillon. Cette image est issue du document *Application Note #128* (Bruker, États-Unis).

- L'**énergie de dissipation** est l'aire entre les courbes d'approche et de retrait, en jaune sur la figure 1.
- Le **module** correspond à la pente de la courbe de retrait (haut de la portion verte sur la figure 1). Selon le modèle de contact choisi, le module calculé peut prendre en compte plusieurs paramètres (voir section 0.2.2).

0.2.2 Mécanique du contact

Le module d'élasticité ne dépend pas uniquement des données accessibles avec l'AFM (force et position de la pointe); la *géométrie du contact* pointe-échantillon doit aussi être connue.

La mécanique du contact a permis le développement de plusieurs théories pouvant s'appliquer à la mesure de module local par une pointe AFM. Les modèles diffèrent principalement entre eux par leur prise en compte des forces d'adhésion et par la géométrie de pointe considérée. Ils permettent ainsi de décrire plusieurs types de comportements mécaniques donc de matériaux.

Les principaux modèles utilisés en AFM sont les suivants :

Modèle de Hertz : L'extrémité de la pointe en contact avec l'échantillon est considérée sphérique, et les phénomènes d'adhésion sont négligés. Ce modèle fonde la mécanique du contact et est peu utilisé en pratique, mais a servi de base au développement des autres modèles.

Modèle DMT (Derjaguin-Muller-Toporov) : Il s'agit du modèle de Hertz auquel un terme adhésif a été ajouté. Il s'agit du modèle le plus utilisé en AFM, adapté pour les petites déformations (2—5 nm).

Modèle JKR (Johnson-Kendall-Roberts) : La géométrie du contact est toujours de type sphère-plan. Ce modèle peut être vu comme une variante du modèle DMT, au niveau de la prise en compte de l'adhésion (et plus particulièrement du comportement adhésif du matériau constituant l'échantillon). Il est notamment particulièrement adapté aux élastomères.

Modèle Sneddon : La géométrie du contact est de type cône-plan. Ce modèle est utilisé lorsque les déformations induites par la pointe sont grandes, soit plus de 30 nm.

Des théories transitoires expliquent aujourd'hui qu'il est rare (en particulier pour les matériaux polymères) qu'un modèle corresponde exactement au comportement réel du matériau. Ces modèles, en outre, ne sauraient décrire exactement la réalité, l'extrémité d'une pointe AFM n'étant jamais parfaitement sphérique ou conique.

Le modèle DMT, largement connu et implémenté directement dans les logiciels d'acquisition d'images AFM, est utilisé le plus conformément possible à ses conditions d'application. La Figure 2 schématise le contact pointe-échantillon tel qu'il est prévu par le modèle DMT, qui lie le module élastique local E aux paramètres du contact selon l'équation 1. F est la force d'appui de la pointe, contrôlée par le microscope, F_{adh} la force d'adhésion, R est le rayon de courbure de la pointe et d la distance d'indentation.

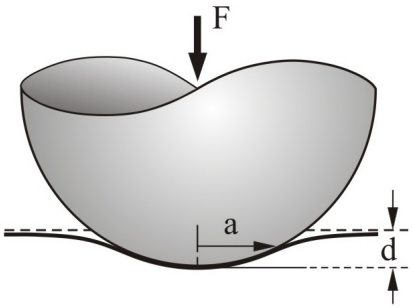

Figure 2 – Schéma du contact pointe-échantillon prévu par les modèles de Hertz et DMT. F est la force d'appui de la pointe, contrôlée par le microscope, a est l'aire de contact et d la distance d'indentation.

$$F = \frac{4}{3} E \sqrt{R d^3} + F_{adh} \tag{1}$$

Chaque résultat est issu d'observations sur plusieurs images, si possible issues de sessions différentes, afin de garantir sa robustesse. Un protocole de calibration, décrit ci-dessous, a été mis au point pour obtenir des mesures reproductibles et quantitatives.

0.2.3 Méthodologie pour des mesures quantitatives en AFM

Les mesures en mode QNM peuvent offrir des contrastes de propriétés intéressants, mais ne sont ni quantitativement représentatives, ni même reproductibles sans une étape de calibration préalable, consistant en l'évaluation précise de certaines conditions variables selon la session, liées notamment à la pointe et à son cantilever.

Les étapes sont les suivantes :

Sensibilité à la déflection : La relation entre la position verticale du piézo (connue) et celle de la pointe est notamment déterminée par la déflection du cantilever, mesurée par la photodiode via le laser qui s'y réfléchit. Une première étape de calibration consiste donc en la mesure de la déflection sur une surface dure (typiquement du saphir), où la pointe ne s'enfonce pas et où la déflection est maximale. La déflection sera donc plus faible sur un matériau où la pointe s'enfonce, et la déformation exercée pourra ainsi être calculée.

Synchronisation temporelle de la courbe de force : Simultanément à l'étape précédente, l'oscillation du cantilever doit être correctement synchronisée avec les courbes de forces. Le scan de la surface rigide permet d'ajuster facilement ces courbes, l'approche et le retrait étant quasiment superposables.

Constante de raideur du cantilever : Afin d'évaluer la force transmise à la pointe par le piézo, il est nécessaire d'évaluer précisément la constante de raideur du cantilever utilisé, qui peut dévier de sa valeur nominale indiquée par le constructeur. Plusieurs méthodes existent, mais les plus utilisées (méthodes *Sader* et *Thermal Tune*) s'appuie sur une modélisation du cantilever comme un oscillateur harmonique, et la constante de raideur est calculée en enregistrant ses mouvements thermiques dans le domaine fréquentiel.

Rayon de courbure de la pointe : Enfin, pour appliquer un modèle de contact sphère-plan (en particulier DMT, voir équation 1), le rayon de courbure équivalent de l'extrêmité de la pointe doit être évalué. Deux approches sont possibles, la première consistant en la mesure directe de ce rayon en analysant des images sur des objets plus pointus que la pointe (l'image obtenue reflète ainsi la forme de la pointe). L'autre approche consiste à évaluer ce rayon avec l'imagerie en module local d'une surface de module élastique connu, en ajustant le rayon de pointe jusqu'à ce que le module mesuré corresponde à celui de l'échantillon. Cette dernière approche est utilisée car plus pertinente : bien que le rayon de courbure calculé soit virtuel, l'approche compense les approximations telles que la modélisation de l'extrémité de la pointe comme objet sphérique. Les propriétés mécaniques calculées sont ainsi plus quantitatives et reproductibles.

Afin de garantir la viabilité de ces calibrations, il est ensuite nécessaire de veiller, lors des sessions d'acquisition d'images, à ne pas endommager ou modifier l'état de la pointe par rapport à l'état dans lequel la calibration a été effectuée.

0.3 Principaux résultats expérimentaux

Comme mentionné plus haut, les présents travaux portent sur les apports de l'AFM dans la compréhension des liens structure-propriétés des polymères, à travers le cas particuliers des interactions entre biopolymères et liquides ioniques.

Deux études principales ont été menées. La première porte sur l'utilisation de deux différents liquides ioniques comme compatibilisants pour le mélange biodégradable PBAT[1]/PLA[2]. La seconde porte plus spécifiquement sur les interactions des mêmes liquides ioniques avec la seule matrice PBAT. Le tableau 2 montre les structures chimiques de toutes les éspèces utilisées. L'abbréviation **il-Cl** désigne le chlorure de trihexyl-tetradécyl-phosphonium, et **il-TMP** désigne le sel de trihexyl-tetradécyl-phosphonium avec anion bis-2,4,4-(triméthylpentyl)phosphinate.

0.3.1 Compatibilisation PBAT/PLA avec des liquides ioniques

Une première étude porte sur la compréhension des mécanismes expliquant la compatibilisation du PBAT et du PLA par l'addition de liquides ioniques. Des mélanges PBAT/PLA de ratio massique 80/20 ont été préparés avec une extrudeuse bi-vis, avec ajout ou non d'1% en masse de l'un des deux liquides ioniques. Les trois mélanges obtenus (sans liquide ionique, avec il-Cl et avec il-TMP) ont été injectés dans des éprouvettes de traction, dans lesquelles les échantillons AFM ont été obtenus par cryofracture.

Les différences de propriétés mécaniques des trois mélanges (voir Figure 3) témoigne d'une compatibilisation réussie, car le module d'Young et l'allongement à la rupture augmentent avec l'ajout de liquides ioniques. De plus, le mécanisme de compatibilisation est vraisemblablement

[1] Poly(bultylène adipate-*co*-terephtalate)
[2] Poly(acide lactique)

Table 2 – Structures chimiques et désignation des principales éspèces étudiées.

Désignation	Structure chimique
Polymères :	
PBAT	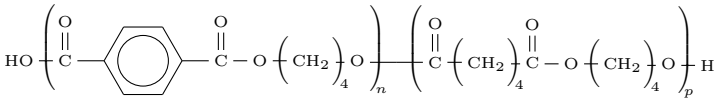
PLA	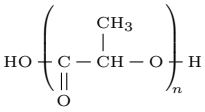
Liquides ioniques :	
il-Cl	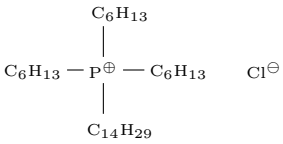
il-TMP	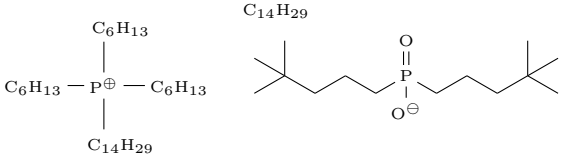

différent pour chaque liquide ionique, car les propriétés n'augmentent pas de la même manière. Ces observations ont constitué le point de départ de l'étude, qui a ainsi pour but de les expliquer via des caractérisations mécaniques à l'échelle nanométrique.

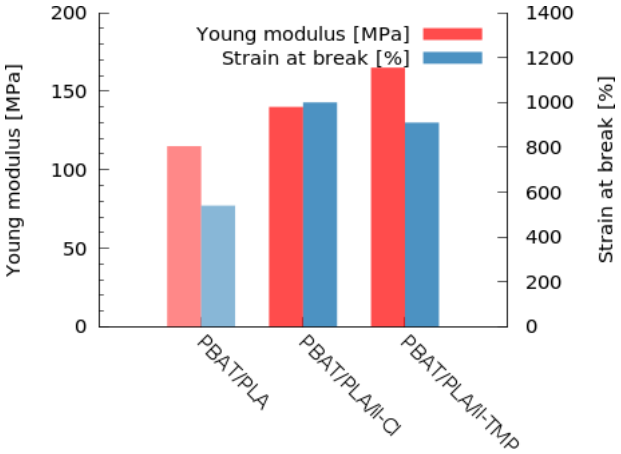

Figure 3 – Module d'Young et allongement à la rupture, obtenus par des tests de traction, pour les trois mélanges considérés.

Observation de la morphologie

En premier lieu, la morphologie des trois mélanges a été observée en AFM, afin d'identifier des différences de structuration induites par les liquides ioniques. Le PLA ayant un module d'Young *macroscopique* (3,5 GPa selon le fournisseur) de deux ordres de grandeur plus élevé que celui du PBAT (env. 40 MPa), il est facile d'identifier les phases qu'ils constituent respectivement au moyen d'images de module DMT, dont des exemples sont présentés Figure 4. Les modules élevés, en orange et blanc sur l'échelle de couleur, correspondent ainsi aux inclusions de PLA,

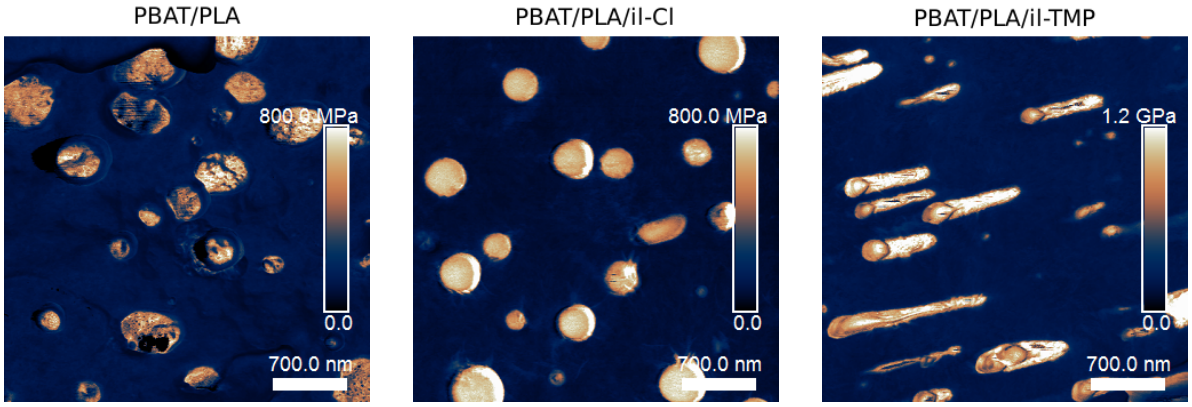

Figure 4 – Images AFM en module DMT ($3.5 \times 3.5\ \mu m$) de la microstructure du PBAT/PLA (gauche), du PBAT/PLA/il-Cl (centre) et du PBAT/PLA/il-TMP (droite).

tandis que les zones bleu foncé correspondent aux faibles modules donc à la matrice PBAT.

D'une structure nodulaire irrégulière pour la phase PLA dans le mélange de polymères sans additif, une structure plus fine, plus homogène et mieux dispersée est atteinte avec l'ajout de 1% en masse de il-Cl. Grâce à des cryofractures effectuées dans plusieurs directions de la barre centrale des éprouvettes de traction injectées, il a été déterminé que, pour le mélange contenant il-TMP, la phase PLA s'organise sous forme de fibrilles dans la direction de l'injection. L'image AFM de droite sur la figure 4 correspond ainsi à une surface parallèle à cette direction.

Ces changements d'organisation contribuent à expliquer l'amélioration des propriétés mécaniques des mélanges.

Localisation d'une phase cristalline

Lors des tests préalables en calorimétrie différentielle à balayage (DSC), des pics de fusion sont apparus pour le mélange PBAT/PLA/il-TMP (voir Figure 5). Ces pics correspondent à des formes cristallines du PLA.

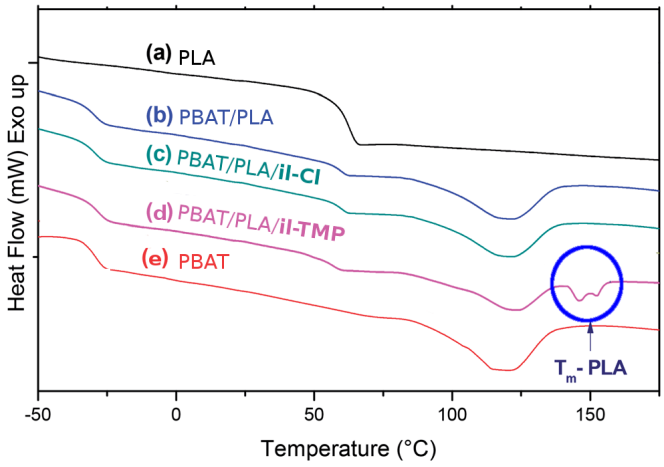

Figure 5 – Thermogrammes DSC de (a) PLA, (b) PBAT/PLA, (c) PBAT/PLA/IL-Cl, (d) PBAT/PLA/IL-TMP et (e) PBAT (Rampe: $10\,°C.min^{-1}$). Un phénomène de fusion, entouré en bleu, traduit l'apparition d'une phase cristalline dans le mélange PBAT/PLA/il-TMP, et la température d'environ 150°C le fait correspondre à la phase PLA.

Combiné à une structure en fibrilles, ce phénomène peut contribuer à l'explication de l'augmentation du module d'Young du mélange induite par l'ajour de il-TMP. Des profils transversaux aux fibrilles ont été tracés sur des images AFM de module DMT (Figure 6).

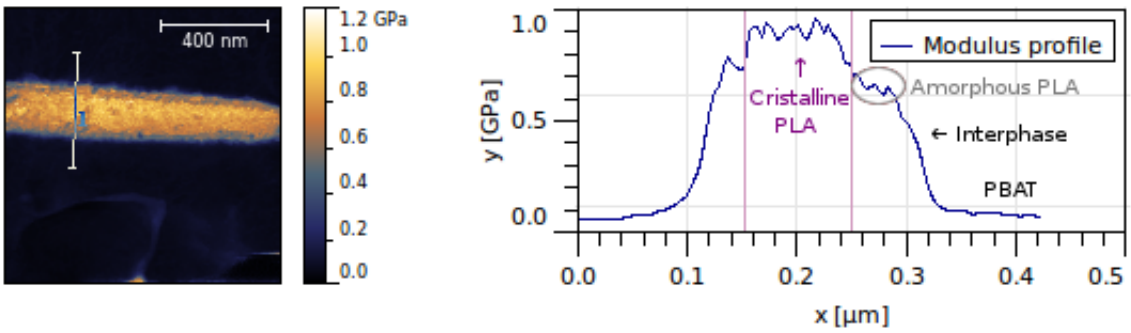

Figure 6 – Image AFM en module DMT (1×1 μm) du mélange PBAT/PLA/il-TMP, et profil de module transversal à la fibrille de PLA. La phase cristalline est mise en évidence au centre de la fibrille.

On distingue ainsi quatre parties selon leur module :

- La matrice PBAT à l'extérieur de la fibrille, de module stable (environ 100 MPa);
- Une zone interfaciale, où le module augmente;
- Une zone où le module du PLA est établi, formant une couche externe de la fibrille;
- Une zone centrale où le module augmente encore par rapport à la couche externe. Par déduction, il s'agit vraisemblablement de la phase cristalline, entourée par la couche externe de PLA amorphe.

Ces observations ont ainsi permis de localiser une phase cristalline dans les fibrilles, contribuant certainement à leur robustesse et expliquant le haut module d'Young mesuré sur le mélange PBAT/PLA/il-TMP.

Module d'élasticité des phases individuelles

En filtrant les modules sur les images AFM, il est possible d'isoler les phases PBAT et PLA du mélange, afin d'étudier individuellement l'effet de l'ajout de liquides ioniques sur chacune d'entre elles. Les modules DMT moyens de chaque phase pour chaque mélange ont été calculés, en utilisant au moins 6 images par mélange. Les résultats sont présentés en Figure 7.

Une tendance claire se dégage : d'une part, pour la matrice PBAT, il-Cl engendre une baisse de module d'au moins 20% tandis que il-TMP semble avoir peu d'effet. D'autre part, la phase PLA subit une claire baisse de module en présence de liquides ioniques.

Cela va totalement à l'encontre des résultats mécaniques macroscopiques en test de traction, qui montrent une augmentation du module en présence de liquide ionique, dans les deux cas. Ce n'est donc pas l'effet du liquide ionique à l'intérieur des phases PBAT et PLA qui est responsable de l'augmentation globale du module macroscopique. Il reste ainsi à explorer le rôle des interfaces entre les deux phases pour comprendre ces résultats.

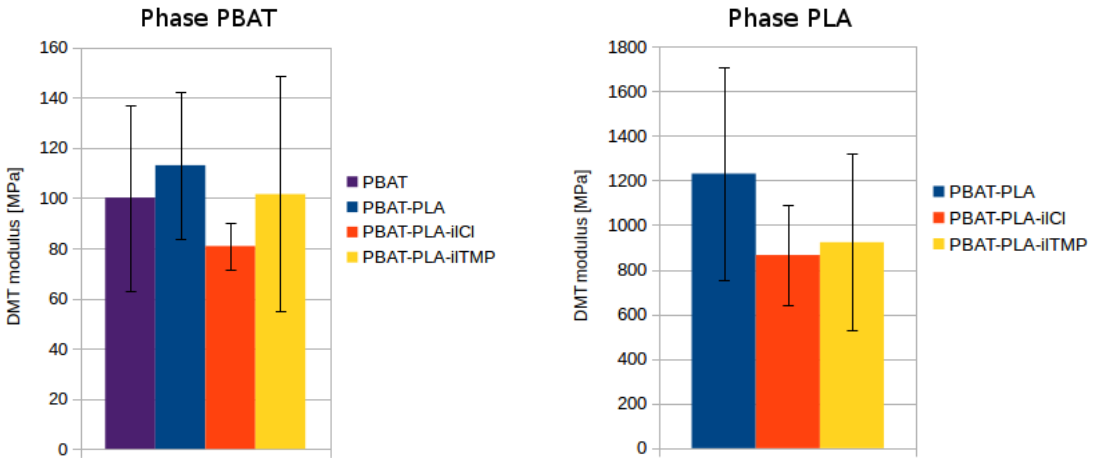

Figure 7 – Modules DMT moyens des phases individuelles obtenus par AFM, dans chaque mélange : PBAT (gauche) et PLA (droite).

Interfaces PBAT/PLA et localisation des liquides ioniques

La zone interfaciale est définie ici en module DMT : il s'agit de la zone de transition où le module varie entre ceux, stables, du PBAT et du PLA. Cette zone a été définie sur plus d'une vingtaine d'interfaces pour chaque mélange, en utilisant des profils de module comme sur la Figure 8.

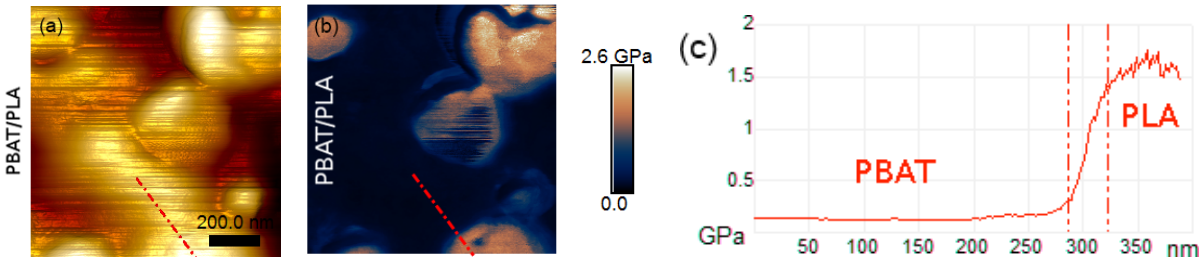

Figure 8 – Analyse de profil d'interphase nodule-matrice pour le mélange PBAT/PLA : (a) image de topographie; (b) image de module DMT; (c) profil de module acquis selon la ligne rouge sur les images, avec la zone transitoire (interphase) définie entre les deux lignes verticales en pointillés.

L'épaisseur de la zone interfaciale a été mesurée dans chaque cas, donnant les moyennes présentées en Figure 9. La dimension de cette zone augmente ainsi de 50% avec l'ajout de il-TMP, et de plus de 100% avec 1% en masse de il-Cl. On peut ainsi parler d'une interphase cohérente induite par l'ajout de liquides ioniques. L'hypothèse retenue est celle d'une miscibilité locale des deux polymères, dont les chaines respectives sont ainsi mises en présence les unes des autres, et ont ainsi une meilleure capacité d'interactions, aidées par les ions.

Afin de confirmer cette hypothèse, le liquide ionique doit se situer préférentiellement au niveau de cette interphase. Pour le vérifier, les mêmes profils utilisés précédemment ont été transférés sur les images correspondantes de force d'adhésion, présentées en Figure 10. Dans chaque mélange, la force d'adhésion pointe-échantillon reste relativement stable pour chaque phase. Les seuls facteurs pouvant la faire augmenter sont :

- Des artefacts liés à de fortes variations topographiques sur l'échantillon : lorsque la pointe rencontre de telles zones, sa surface de contact avec l'échantillon peut être substantiellement modifiée par rapport à celle prévue par sa calibration, faussant la force d'adhésion mesurée.

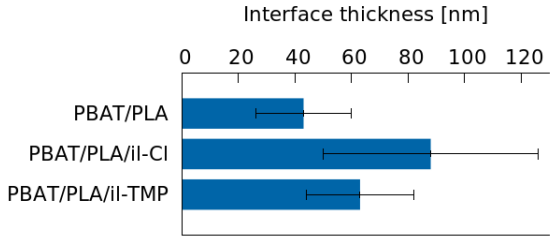

Figure 9 – Épaisseur moyenne de l'interphase PBAT/PLA pour chaque mélange.

- Dans ce cas, un soin particulier ayant été apporté à ne pas mesurer de profils sur des zones de fortes variations topographiques, les pics d'adhésion ne peuvent traduire que la présence d'une espèce étrangère aux deux polymères, donc les liquides ioniques, aucune autre espèce n'ayant été introduite dans les formulations.

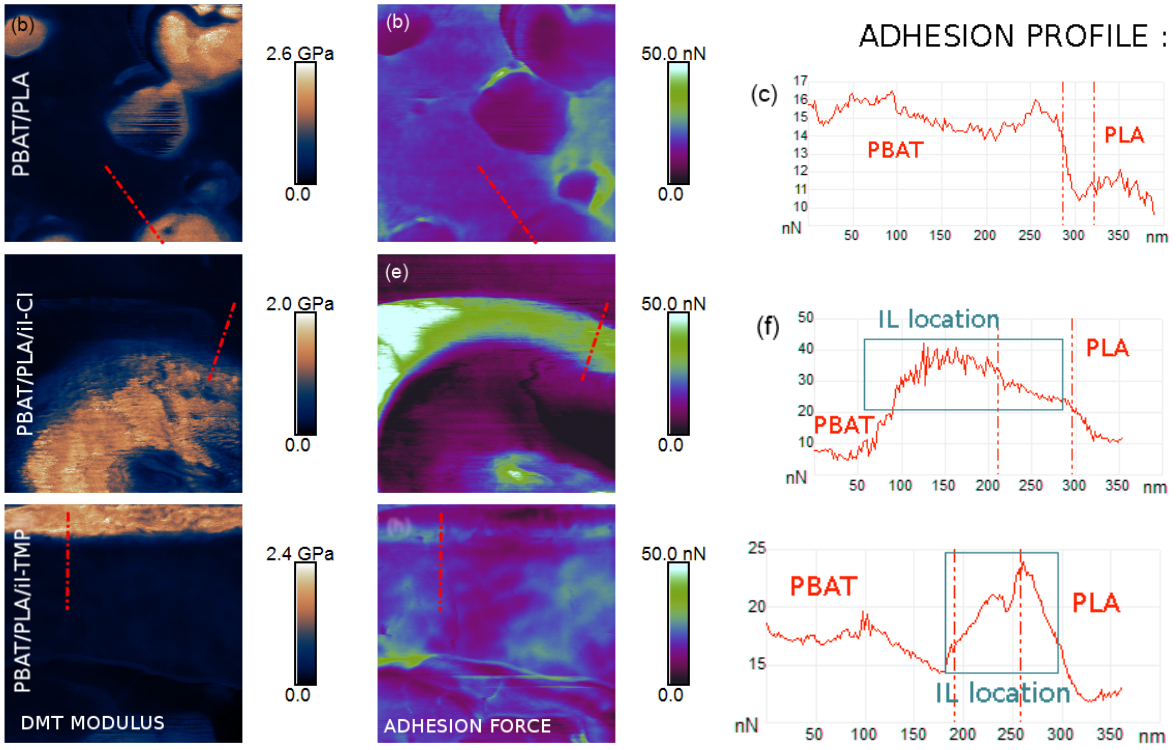

Figure 10 – Analyses de profils de force d'adhésion à l'interphase nodule-matrice pour les 3 mélanges : (gauche) images de module DMT montrant les phases en présence; (centre) images de force d'adhésion; (droite) profils de force d'adhésion acquis selon la ligne rouge sur les images, avec l'interphase définie en module DMT entre les deux lignes verticales en pointillés. Des pics d'adhésion non caractéristiques des polymères sont encadrés en bleu et témoignent de la présence du liquide ionique en forte concentration.

Des pics significatifs d'adhésion ont été observés au niveau des interphases dans les mélanges contenant les liquides ioniques, alors qu'une simple marche transitoire de force d'adhésion entre celle correspondant au PBAT et celle correspondant au PLA est obtenue pour la mélange PBAT/PLA (Voir haut de la Figure 10). Cela confirme l'hypothèse d'une présence préférentielle

des liquides ioniques au niveau des interphases.

Tandis que il-Cl semble concentré sur une zone plus large, préférentiellement du côté de la matrice PBAT, il-TMP semble majoritairement situé sur une zone plus réduite, plus proche du PLA, dont la concentration en dipôles (groupements esters) est plus élevée. En se basant sur ces observations et sur les structures des composants, il est possible de formuler les hypothèses d'interaction suivantes, illustrées Figure 11 :

- Présent dans les deux liquides ioniques, le cation phosphonium peut interagir avec des dipôles des polymères (essentiellement des groupementss esters) mais aussi avec des morceaux de chaînes alkyles via ses chaines pendantes, notamment avec les segments adipates et butylène du PBAT.
- L'anion chlorure de il-Cl joue un faible rôle. Il équilibre la charge du cation.
- L'anion phosphinate semble avoir peu d'affinités avec le PBAT, d'où les pics d'adhésion côté PLA en Figure 10. Il est ainsi amené à interagir avec cette phase, formant une double couche anions-cations à l'interphase, agissant comme un tensio-actif. Cela expliquerait la formation de fibrilles à l'injection.

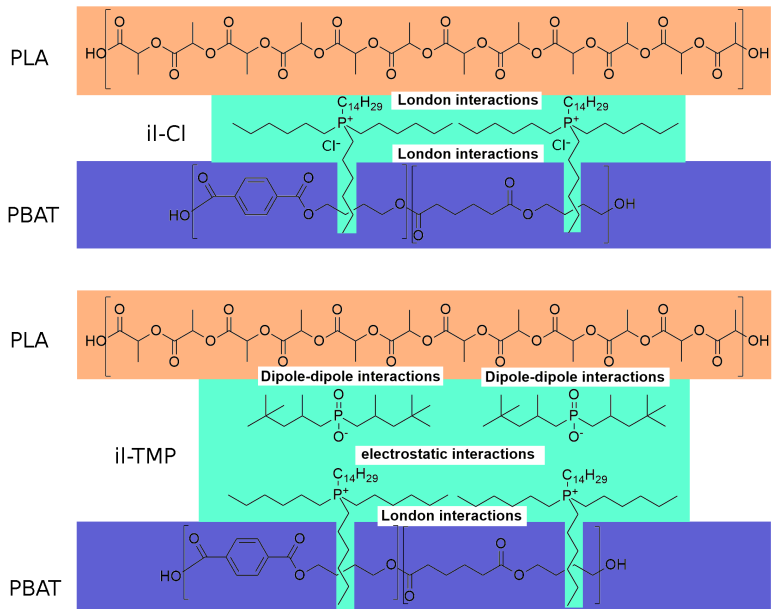

Figure 11 – Représentation schématique des interactions entre PBAT et PLA avec l'addition d'il-Cl (haut) et il-TMP (bas).

La figure 12 propose ainsi un schéma simplifié de la structure des trois types d'interfaces observés: d'une interface franche, présentant peu d'interaction donc peu de transfert de contrainte dans le cas du mélange brut :

- On passe avec l'ajout d'1% de il-Cl à une interphase diffuse, induite par la miscibilisation locale des deux polymères. Le transfert de contrainte est bien plus efficace, d'où l'augmentation des propriétés mécaniques. Les interphases ne sont plus des points d'où peuvent naître les défauts lors de la déformation macroscopique du mélange, et l'allongement à la rupture augmente significativement.

- Avec l'ajout d'1% en masse de il-TMP, une interphase moins épaisse se forme, mais le liquide ionique y forme une double couche tensio-active, ne favorisant pas la dispersion de nodules de PLA mais plutôt la formation de fibrilles dans le sens de l'injection.

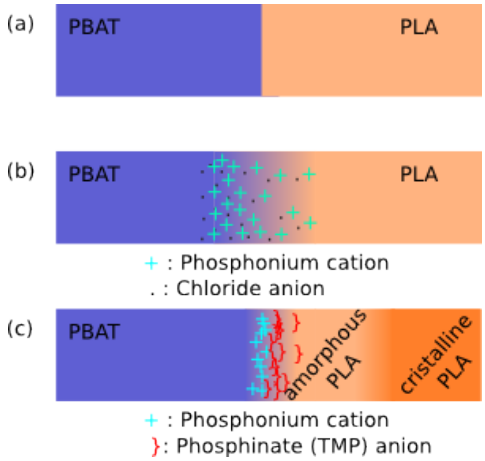

Figure 12 – Schéma des structurations interfaciales pour (a) PBAT/PLA, (b) PBAT/PLA/il-Cl et (c) PBAT/PLA/il-TMP.

Cette étude a ainsi permis d'établir une méthodologie pour obtenir un modèle des interfaces (ou interphases) dans les mélanges considérés, expliquant l'évolution des propriétés mécaniques en fonction de l'ajout de liquides ioniques, en utilisant des cartographies de propriétés mécaniques par AFM.

0.3.2 Interactions PBAT/liquides ioniques

Une seconde étude porte sur l'effet des mêmes liquides ioniques sur la structuration et les propriétés du PBAT seul. Trois systèmes sont donc étudiés, le premier constitué de PBAT pur et les deux autres de PBAT dans lequel ont été respectivement ajoutés 2% en masse de il-Cl et de il-TMP. L'impact d'une si faible quantité d'additifs sur les propriétés mécaniques de la matrice est notoire, comme l'illustre la figure 13. Dans le cas du système PBAT/il-TMP, l'allongement à la rupture augmente de 33% par rapport à la matrice seule, sans effet notable sur le module d'Young. Le liquide ionique il-Cl induit quant à lui une augmentation de près de 60% de l'allongement à la rupture, avec une légère baisse de module élastique.

Afin d'expliquer ces résultats, une étude approfondie de l'action des liquides ioniques est menée, utilisant en particulier les cartographies de propriétés nanomécaniques en AFM ainsi que la spectroscopie diélectrique.

Morphologie et propriétés thermiques et mécaniques

Dans un premier temps, des caractérisations classiques ont été effectuées afin de vérifier d'une part les données présentes dans la littérature, et de chercher des caractéristiques discriminantes entre les mélanges d'autre part. La densité des échantillons a été mesurée à $1,217\ g.cm^{-3}$ dans les trois cas, donc une piste impliquant des variations globales de volume libre induites par les liquides ioniques est écartée.

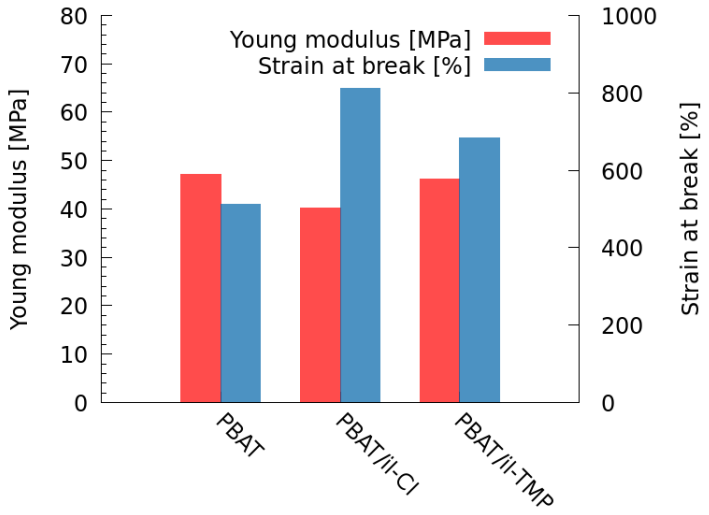

Figure 13 – Module d'Young et allongement à la rupture, obtenus par des tests de traction, pour les trois systèmes considérés.

Morphologies La figure 14 montre des images de module DMT de surfaces préparées en cryomicrotomie (à -130°C) des trois systèmes étudiés.

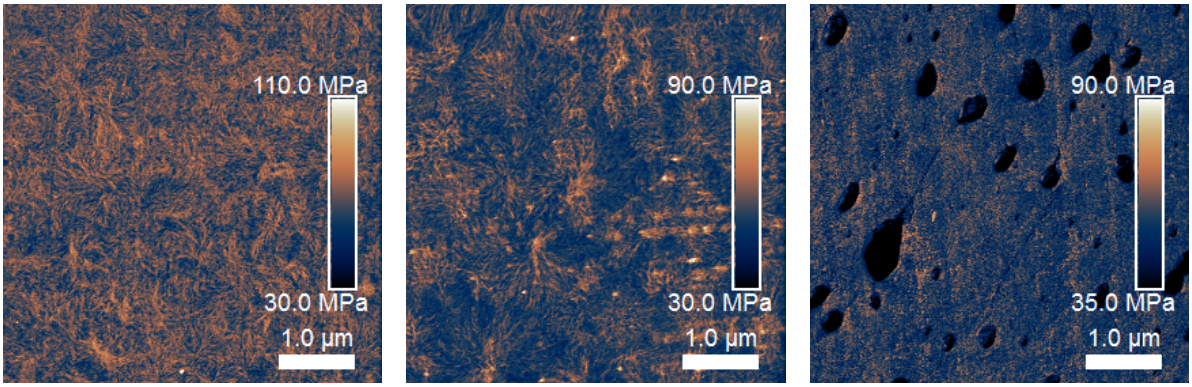

Figure 14 – Images AFM en module DMT ($3.5 \times 3.5\ \mu m$) de la microstructure du PBAT (gauche), du PBAT/il-Cl (centre) et du PBAT/il-TMP (droite).

Les images sont assez similaires, sauf pour le système PBAT/il-TMP qui présente des zones de très faible module (en noir sur la figure). Cela correspond, en accord avec d'autres études, à la structuration en nodules du liquide ionique il-TMP qui est immiscible dans le PBAT.

Structure cristalline La structure cristalline semble aussi apparaître sur les images de module DMT, et est semblable pour les trois mélanges : une fine structure lamellaire est identifiable, s'organisant en sphérolithes de diamètre 1 à 2 μm environ. Cette structure cristalline a été identifiée par diffraction des rayons X (XRD) comme étant uniquement celle du polybutylène téréphtalate (PBT), l'un des deux segments du copolymère. La grande majorité des unités polybutylène adipate (PBA) se trouve donc dans la phase amorphe. De plus, la cristallinité de tous les mélanges a été évaluée à 14±1% par calorimétrie différentielle à balayage (DSC), sans différence significative induite par les liquides ioniques.

Table 3 – Températures de transition observées en DMA et en DSC.

Système :	T_α (DMA) [°C]	T_g (DSC) [°C]
PBAT	-30.5	-35.1
PBAT/il-Cl	-32.4	-35.0
PBAT/il-TMP	-30.8	-36.0

Relaxations thermomécaniques L'analyse mécanique dynamique (DMA) en torsion des trois mélanges donne les résultats présentés en figure 15.

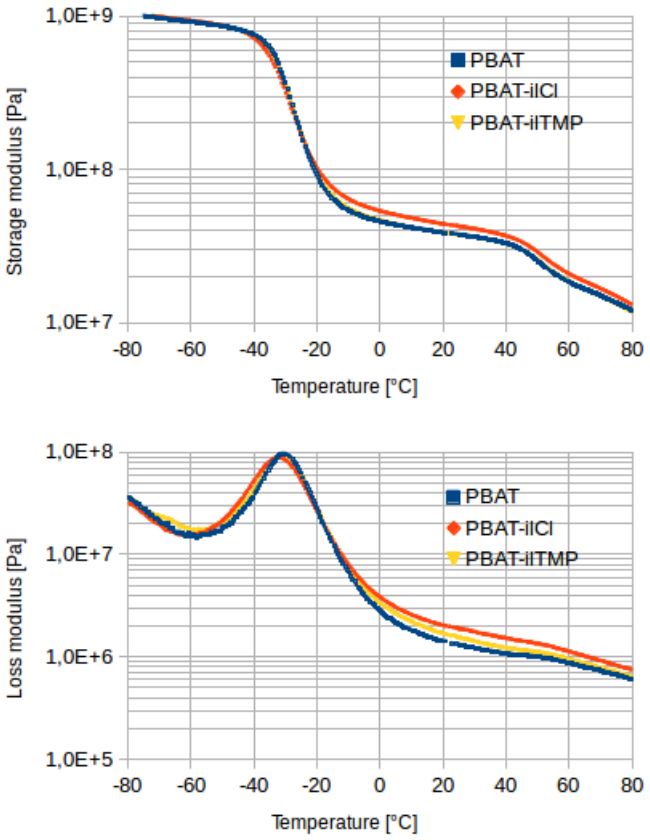

Figure 15 – Variation du module de conservation (haut) et du module de perte (bas) du PBAT et des mélanges PBAT/ILs avec la température, en torsion à 1 Hz.

Les températures de transition vitreuse (obtenues en DSC) et α (obtenues en DMA), correspondant au même phénomène, sont regroupées en table 3.

Si les données semblent pas ou peu discriminantes selon les mélanges, les courbes d'évolution des modules de conservation et de perte traduisent une seconde transition autour de 50°C. Cela traduit une relaxation α', liée à des phénomènes d'interfaces. Étant présente dans les trois cas, l'interface en question est certainement celle entre les phases cristalline et amorphe. Des études suggèrent que cette zone caractéristique constitue une seconde phase amorphe, moins mobile car constituées de chaînes ancrées dans la phase cristalline et/ou confinées entre ses lamelles.

Excepté la structuration en nodules de il-TMP, peu d'informations discriminantes, c'est-à-dire capables de donner des pistes pour l'explication des différences de propriétés mécaniques entre

chaque système, ont été obtenues avec les méthodes de caractérisations classiques. Cependant certaines informations, dont la présence d'une phase amorphe intermédiaire rigide, méritent une exploration plus poussée pour comprendre les différences entre les trois systèmes.

Etude des mécanismes d'interactions

Spectroscopie diélectrique Afin de caractériser plus précisément les relaxations susmentionnées, les échantillons ont été caractérisés en spectroscopie diélectrique de 10^6 à 10^{-2} Hz, sur une plage de température allant de -70 à 60°C. Les deux phénomènes de relaxation α et α' ont été isolés, ainsi que le phénomène de conduction (principalement ionique) apparaissant à basse fréquence ou à haute température.

Pour plusieurs température et pour chaque mélange, un fit de type Havriliak-Negami a été appliqué sur les spectres obtenus montrant les différentes relaxations, permettant le calcul des énergies d'activation associées à chacun de ces phénomènes, données en table 4. Seule celle associée à la relaxation α du PBAT/il-TMP n'a pas pu être calculée, en raison de difficultés au niveau du fit causées par la superposition de la conduction et de la relaxation. L'ensemble des résultats indiquent cependant qu'elle ne devrait pas varier significativement par rapport à l'énergie d'activation de la transition α des deux autres mélanges.

Table 4 – Énergies d'activation (E_A) de chaque phénomène observé en spectroscopie diélectrique. Toutes les valeurs sont données en $kJ.mol^{-1}$

Énergie d'activation de :	**Relaxation α**	**Relaxation α'**	**Conduction**
PBAT	232.6	72.4	69.4
PBAT/il-Cl	239.0	82.8	80.7
PBAT/il-TMP	-	72.4	67.0

L'augmentation de l'énergie d'activation liée à la relaxation α' dans le mélange PBAT/il-Cl indique clairement un effet du liquide ionique sur la RAF (rigid amorphous phase en anglais, soit la phase amorphe confinée mentionnée plus haut). Le liquide ionique semble entraver la relaxation. Il en est de même pour la conduction : si elle est généralement bien plus importante pour le mélange PBAT/il-Cl en raison d'une meilleure miscibilité avec le PBAT et de la taille de ses porteurs de charge (par comparaison avec il-TMP), son activation requiert une énergie plus importante.

Il-TMP, au contraire, semble avoir très peu d'effet sur la matrice PBAT, ce qui confirme une immiscibilité, donc une présence uniquement au niveau des nodules.

Caractérisations nanomécaniques Plusieurs phénomènes sont mis en évidence par les mesures quantitatives de propriétés mécaniques à l'échelle nanométrique. La Figure 16 montre des distributions typiques du module DMT obtenues sur des images des trois mélanges.

Il est nécessaire de rappeler que les propriétés mécaniques à cette échelle, pour un copolymère semi-cristallin, ont peu de raisons de correspondre quantitativement à leurs équivalents macroscopiques, ce dernier prenant en compte des phénomènes supplémentaires à des échelles intermédiaires, liés notamment à la mise en oeuvre du matériau.

L'épaulement à bas module du système PBAT/il-TMP représente simplement les nodules de liquide ionique, et le fait qu'il ne soit pas un autre pic détaché du principal laisse croire à la présence d'une interphase. La Figure 17 confirme cette idée : la transition observée en module, encadrée par les lignes pointillées bleues, correspond sur le profil de topographie à la matrice (car avant le trou formé par le nodule).

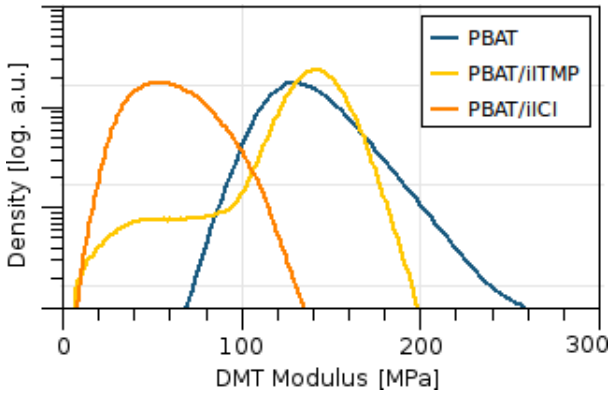

Figure 16 – Distributions représentatives du module DMT sur les images AFM pour chaque système. L'axe vertical représente la densité de probabilité associéeà chaque valeur de module cartographiée.

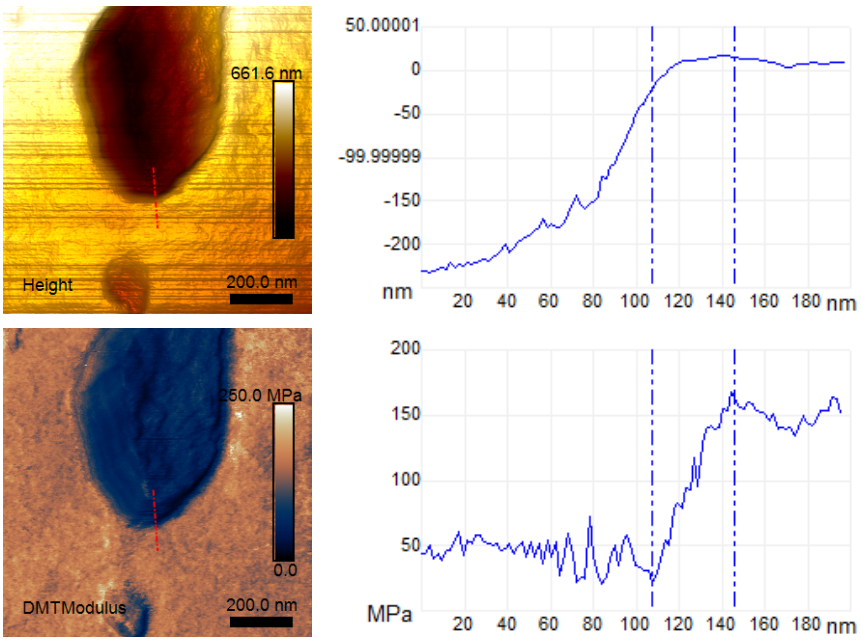

Figure 17 – Images AFM de 1×1 μm^2 de la topographie (haut) et du module DMT (bas) d'une surface PBAT/il-TMP avec les profils correspondants, acquis selon la ligne rouge.

On peut interpréter ceci comme une zone d'environ 40 nm d'épaisseur où la densité de chaînes polymères baisse progressivement, interagissant avec les cations phosphonium. Cette zone joue certainement un rôle important dans l'augmentation de l'allongement à la rupture induit par l'ajout de il-TMP. Les nodules étant par ailleurs très dissipatifs, ils sont enclins à entraver la propagation de défauts sous contrainte.

La Figure 16 indique aussi que le système PBAT/il-Cl subit une réduction de module élastique bien plus importante à cette échelle qu'à l'échelle macroscopique. Il-Cl semble ainsi augmenter grandement la mobilité des chaînes, tout en apportant un effet compensatoire qui, à l'échelle macroscopique, se traduit en une réduction moins importante du module, et un effet faible voire nul sur les propriétés thermiques : il ne s'agit donc pas d'un plastifiant.

Pour aller plus loin dans la compréhension du rôle de il-Cl, la localisation du liquide ionique est nécessaire. La figure 18 montre des images de module DMT et de force d'adhésion pour les

systèmes PBAT et PBAT/il-Cl. Des sphérolithes clairement identifiables ont été marquées en rouge dans les deux cas. Ces zones sont constituées de la phase cristalline et de la phase amorphe confinée (RAF), tandis que les zones entre ces sphérolithes sont constituées de phase amorphe aux chaines plus libres (MAF), ainsi que de RAF.

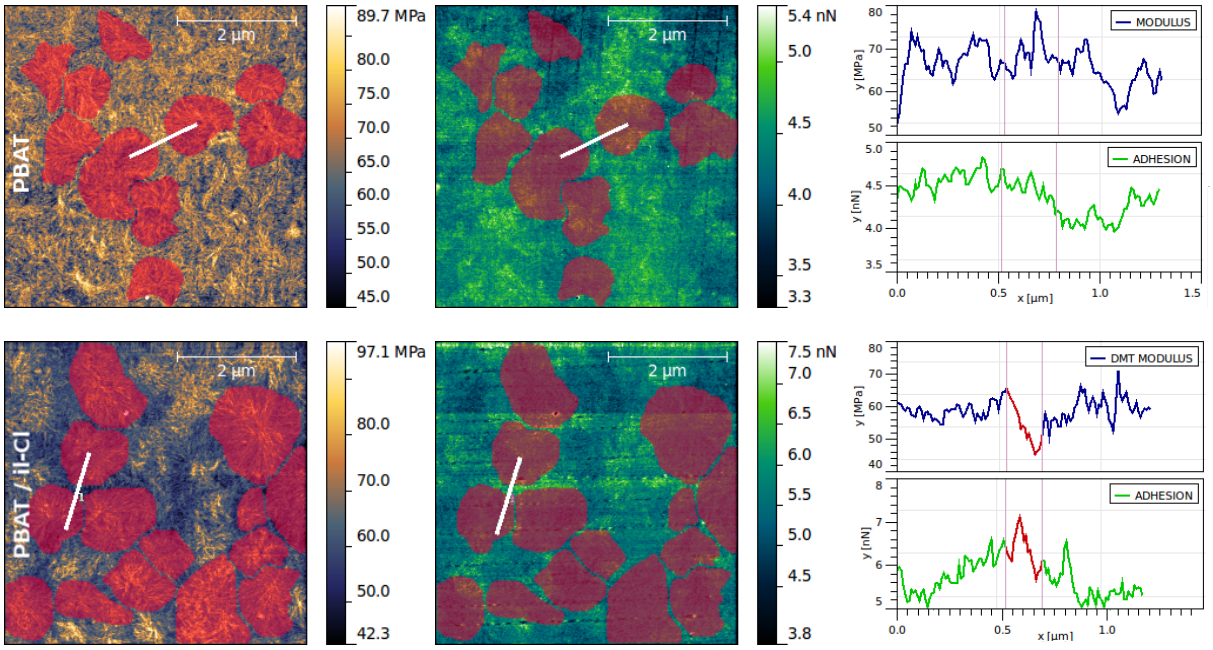

Figure 18 – Images AFM (5×5 μm^2) de module DMT (gauche) et de force d'adhésion (centre) avec les profils correspondants (droite) pour le PBAT (haut) et le PBAT/il-Cl (bas). Les profils sont acquis suivant les lignes blanches sur les images, et les lignes verticales violettes sur les profils correspondent aux espaces entre les zones marquées en rouge. Certaines des sphérolithes les mieux identifiables sont marquées en rouge sur les images.

Dans le cas du PBAT, peu de différences sont observées, en particulier en adhésion, entre l'extérieur et l'intérieur des sphérolithes, tandis qu'avec il-Cl, les zones entre les sphérolithes présentent non seulement une baisse de module DMT mais aussi un pic d'adhésion, signature de la présence du liquide ionique.

Il-Cl se situe ainsi préférentiellement dans les phases amorphes. D'une part, la mobilité des chaines dans les zones purement amorphes est grandement augmentée, et d'autre part, sa présence dans les zones interfaciales et confinées, proche des lamelles de la phase cristalline, joue un rôle inverse et gêne les phénomènes à ce niveau : la relaxation (α') de cette zone requiert alors plus d'énergie, ainsi que la libération des porteurs de charge. Cette dualité dans l'effet du liquide ionique explique un effet plus réduit sur les propriétés mécaniques à l'échelle macroscopique, ainsi qu'un effet nul ou extrêmement réduit sur les propriétés thermiques.

Effet des liquides ioniques Un modèle complet des interactions PBAT/liquides ioniques a ainsi pu être établi. Si des liquides ioniques ont déjà pu être utilisés comme plastifiants, les deux utilisés ici permettent des effets différents, promettant de vastes possibilités dans leur utilisation comme additifs :

- **il-Cl** permet d'obtenir l'effet d'un plastifiant sur les propriétés mécaniques (baisse du module, augmentation de l'allongement à la rupture), mais sans effet sur les propriétés

thermiques (donc pas de baisse de la température de transition vitreuse). Cet effet est conditionné par la structure du PBAT, copolymère semi-cristallin, qui présente une phase amorphe rigide (RAF) et une phase amorphe plus mobile (MAF).

- **il-TMP** se structure en nodules dissipatifs permettant de conserver les propriétés de la matrice PBAT, augmentant seulement son allongement à la rupture en rendant difficile la propagation des défauts.

0.4 Conclusions

Le recours à des caractérisations mécaniques à l'échelle nanométrique par AFM a montré son efficacité pour comprendre le lien entre formulation et propriétés dans les systèmes polymères. Cette étude basée sur les interations entre liquides ioniques et biopolymères en montre deux exemples approfondis, l'un à travers l'étude des mécanismes de compatibilisation entre PBAT et PLA et l'autre avec la caractérisation des interactions et structurations de deux liquides ioniques dans le PBAT. Les bases théoriques de la mécanique du contact à cette échelle sont préalablement discutées, délimitant le cadre expérimental et analytique de l'étude.

La versatilité de la technique a été démontrée, de l'identification de phases à la localisation de liquides ioniques par cartographie de force d'adhésion, pour finalement proposer des modèles complets explicant la structuration des matériaux induite par les liquides ioniques. De manière plus générale, une méthodologie a été mise au point pour la caractérisation de tels systèmes, permettant des mesures AFM quantitatives et reproductibles.

Ce travail pourra servir de base méthodologique à l'étude *in situ* des micro-phases et des interfaces dans les matériaux multiphasés (notamment les composites), proposant comme nouvel angle d'attaque l'étude des propriétés locales et de leur évolution aux interfaces. Ce type de caractérisations peut jouer un rôle, par exemple, dans l'établissement et la validation de modèles prédisant le comportement des interfaces en fonction de la composition, des traitements et des paramètres de mise en oeuvre des matériaux multiphasés.

General introduction

Understanding the connection between the formulation, structure and properties of a material is a fundamental aspect of polymer science, especially when it comes to mixtures, composites or original formulations. This makes it possible to design functional materials by anticipating their properties, and thus to adapt the methods of implementation and the formulation choices to the desired result. However, this implies the control of many parameters, at different scales, individually characterizable but difficult to link to each other.

Atomic Force Microscopy (AFM) allows, as few characterization techniques, to measure local properties of materials by mapping them, thus also to observe their distribution on a surface, with an excellent resolution. The tip of the AFM probe, having a radius of curvature of a few nanometers, scans the surface to acquire information in each point.

The uniqueness of this technique thus lies in the fact that the characterized properties are *local* properties, so they only reflect the point of the surface at which they are measured (and possibly its close neighborhood), and not the entire material. This allows to link structure and properties, observing the spatial organization of the latter.

PeakForce QNM mode (Bruker, USA) allows the AFM to map the local mechanical properties of materials: elastic modulus, adhesion force (relative to the tip withdraw), deformation, and dissipation energy. Its particularities include that it relies on calibrations to achieve unprecedented reproducibility of measurements, image resolution, and a control of the force applied by the tip, giving it an excellent sensitivity.

This novel technique is thus very promising in the study of polymer systems : the individual mechanical behavior of the different phases of a system can be visualized (for semicrystalline polymers, blends or composites), as well as their spatial organization. It is also possible to explore the interfaces, which play a preponderant role in the properties of a multiphased system. The purpose of this work is thus to correlate these observations with the macroscopic behavior of the materials studied, in order to understand better the mechanisms that underlie this behavior, and thus to be able to predict and tailor them better when designing polymer systems.

It was chosen to focus these characterizations around two topics : on the one hand, ionic liquids, salts with a melting point that is lower than 100°C (often even lower than the ambient temperature), exhibiting unique properties (very low saturation vapor pressure, good temperature stability, non-flammability...). Added as additives in polymer systems, they have recently shown promising results as compatibilizers for blends, structural modifiers, or plasticizers. Their interesting behavior when added with polymers still being little described, their study in this work seems relevant.

On the other hand, biopolymers (biobased and/or biodegradable polymers) are also studied in this work, in the current logic of their development as an alternative for oil–based plastic. Atomic force microscopy will be used to investigate what explains, in their structure at the nanoscopic scale, the mechanical behavior of biopolymer systems, modified or not by ionic liquids.

Chapter 1

Literature review

Contents

1.1 Introduction

Atomic force microscopy, a scanning probe technique developed by Binnig *et al.* [1] in 1986, opened a broad range of new possibilities in surface analysis, giving the access to a nanometric resolution imaging with almost any kind of materials. This is made possible by the interaction of an extremely sharp tip with the sample surface. That implies atomic scale forces, such as Van der Walls forces, electrostatic forces, or steric repulsions.

The tip scans the surface, using this sample-tip interaction to record data and gather them into map-like images. The original use of the atomic force microscope, which is still currently its most common purpose, is to observe the topography of a sample.

In fact, there are several ways to use this technique, and many kinds of data can be deduced, reflecting different properties of surfaces. This is why different *modes* were successively developped, which are distinct ways of using the technology, giving access to different properties or being adapted for different materials. Information about the structure and the electrical, mechanical or even magnetical properties are now accessible at the nanoscopic scale (conventionally called *nanoscale*).

Atomic force microscopy is thus a unique tool for nano-mechanical characterization of materials. Cartography of local properties, such as the local Young's Modulus is made possible. Those informations and their macroscopic equivalents may not have the same meaning, but the mechanical behavior of a material is necessarily conditioned by its structure and the interactions at a local scale. Understanding such interactions can open interesting fields in the study of the links between structure and properties of materials.

The goal of this chapter is to cover the scientific achievements of mechanical measurements with atomic force microscopy. In a first part, the general principle will be presented, with an introduction to AFM mechanical modes and their evolution through the last decades.

A second part will be dedicated to a general state of the art on this characterization technique, with the diversity of informations it can give, in many scientific fields and particularly in polymer science.

1.2 Mechanical measurements using Atomic Force Microscopy

The atomic force microscope belongs to the family of the Scanning Probe Microscopes (SPM). This means that the key component is a probe, constituted by a cantilever and a tip on its end to interact with the sample. To reach a good resolution, the tip is often extremely sharp, *i.e.* with a radius of curvature of a few nanometers. Scanning Electron Microscopy (SEM) images of some AFM probes are shown in Figure 1.1.

Although others exist, the Peak Force QNM^{TM} mode is today the main tool for mechanical measurements in atomic force microscopy. This thesis is thus principally based on this new mode and its operation. Tapping mode (TM) also deserves a quick overview : this is the currently most used mode and a parallel is interesting to establish.

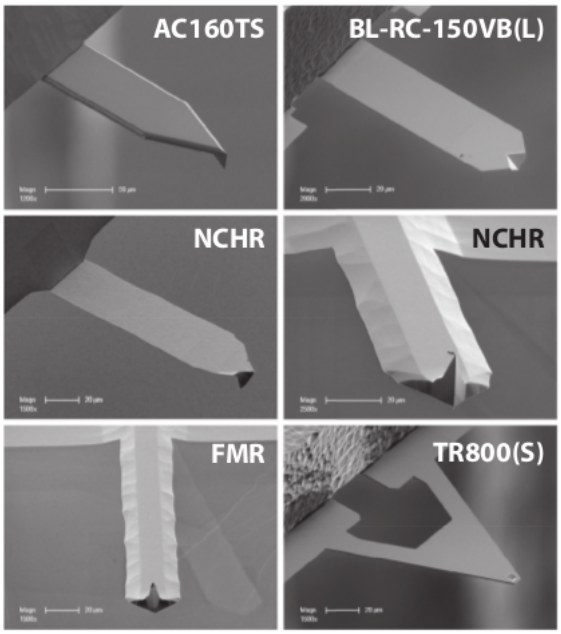

Figure 1.1 – SEM micrographs showing various AFM probes, with rectangular or triangular cantilevers [2].

1.2.1 Intermittent contact AFM: Tapping Mode (TM)

Presentation

History The first applications of atomic force microscopy were in Contact Mode. Still existing but less broadly used today, this mode is characterized by a constant contact of the tip on the sample. The resulting repulsive force bends the cantilever on which the tip is fastened and thus deflects the laser pointing its extremity. That deflection is measured by a photodiode and is kept constant by the feedback system of the microscope, allowing to follow and to record the topography of the sample.

Although it appears to be promising in the imaging of materials, with mechanical information [3], this mode suffers some limitations, particularly a risk to damage the sample surface (or to wear the tip) and an important dependance on humidity conditions and electrostatic forces. These flaws are crippling for the study of certain kinds of samples, especially soft materials.

In the early 1990s, the Tapping mode (amplitude modulation) emerged [4] and bypassed some limitations of the Contact Mode, making it viable for imaging more sensitive materials.

The tip here is in quasi-vertical oscillation and thus in intermittent contact with the surface, in order to avoid the lateral forces which can damage it and to minimize the influence of possible pollution or a liquid film.

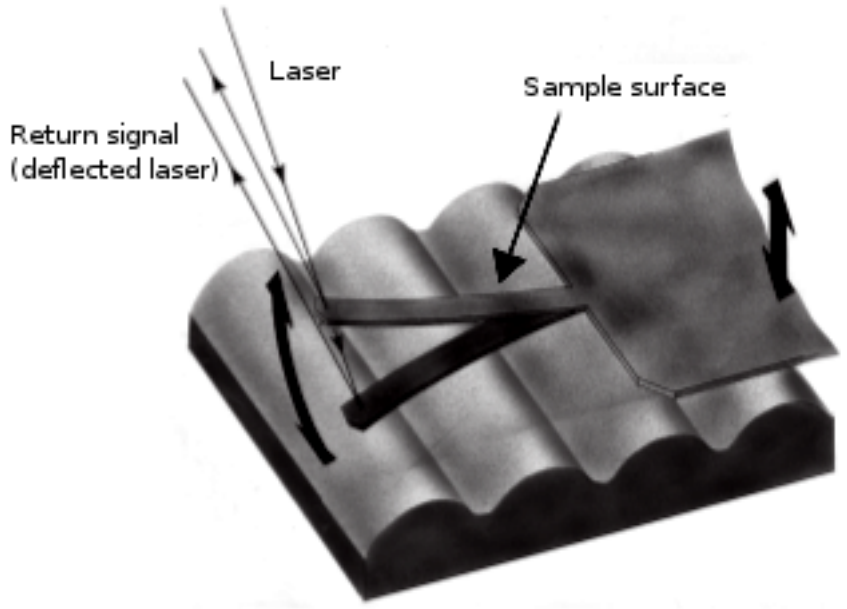

Figure 1.2 – Representation of a probe scanning a surface using Tapping mode. The laser is reflected on the upper part of the end of the cantilever. Source: AFM Multimode 8 User's Manual [5].

Operation (Figure 1.2) The cantilever is excited close to its resonant frequency by a piezoelectric element. A laser is reflected on its extremity (above the tip) allowing to transmit its movements to a photodiode. When the cantilever oscilates freely, the movements of the tip and that of the piezo correspond and are in phase.

On the contrary, on contact with a sample, at each vibration cycle, the tip hits the surface, limiting and modifying the *oscillation amplitude*. By setting a value for the amplitude reduction, it is possible to keep it constant via the feedback loop by constantly adjusting the vertical position of the piezo and thus to follow the topography of the sample. One of the main parameters is the *Amplitude Setpoint*, the fixed value for the reduced oscillation amplitude when the tip is engaged on the sample.

Measurements Three simultaneously acquired data channels, giving three images of the surface, are obtained during Tapping Mode imaging :

Topography: Directly obtained when recording the vertical position of the piezo (without the oscillating part).

Amplitude error: The real oscillation amplitude of the probe may change slightly from the Amplitude Setpoint when important topographic variations occur on the sample (to readjust the amplitude so the setpoint, the feedback loop must first quantify the error). This error is recorded during the acquisition. This data has no physical meaning, but it reflects

the topography in a contrasted way and provides an additional visual tool, sometimes useful for the interpretation.

Phase: Some properties of a material (principally the viscoelastic properties) induce a certain phase shift of the probe with its excitation by the piezo (input signal). This phase shift is visible by the output signal recorded on the photodiode. Various parameters contribute to it, it is therefore very difficult to interpret it precisely. However, when several materials constitute a surface, each induces a different phase shift and the contrast is visible on the phase image. This qualitative data can thus give information about the mechanical and/or chemical contrast on the surface.

Mechanical informations using phase contrast

In Tapping Mode, the phase shift difference between the piezoelectric modulation of the sample and the response of the cantilever (deflected laser signal on the photodiode) is a qualitative information, mainly linked to the mechanical response of a zone of the sample [6]. If two zones exhibit different stiffnesses on the same image, the measured phase shift will also be different: it is the *phase contrast*.

Magonov and Heaton [7] documented in 1998 the possibilities offered by the Tapping Mode, thanks to the recording of the phase contrast, to get qualitative informations on the organization of mechanical properties on a sub-micrometric scale. It is observed that *soft* and *hard tapping* (in the former case the tip just come softly in contact with the surface, while in the latter it hits the sample harder) are complementary techniques: *soft tapping*, being absolutely non-destructive, allows a precise topography recording and the *hard tapping* shows a clear phase contrast. It become thus possible to observe semi-crystalline organizations in polymers (Figure 1.3), latex microstructures or copolymers.

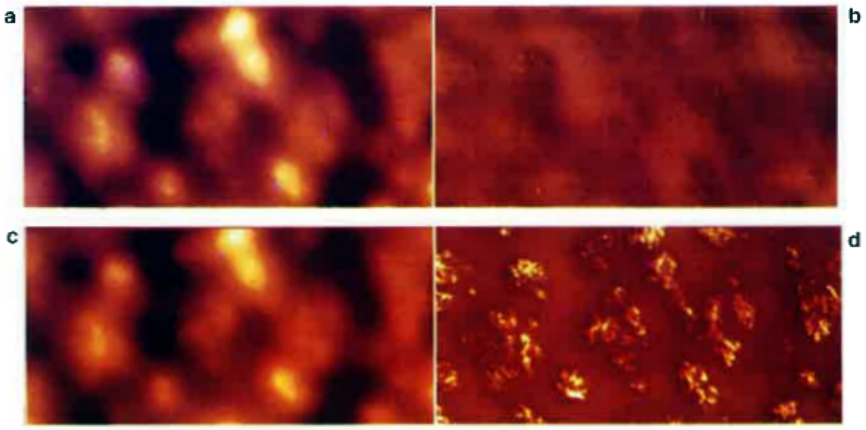

Figure 1.3 – AFM height (right) and phase (left) of a low densiy polyethylene ($15 \times 7,5\ \mu m$). Top: *soft tapping*; bottom: *hard tapping*. The *hard tapping* phase image highlights the stiffer crystalline zones [7].

Kajiyama *et al.* [8] use the Tapping mode out of the resonnance frequency of the cantilever to map viscoelastic properties, estimating that the measured phase corresponds to the loss factor ($tan\ \delta$) at a given frequency. This approach was also used by Wang *et al.* [9] to study nanometrical heterogeneities in amorphous polystyrene.

However, quantitative interpretations of the mechanical data obtained in tapping mode must

be taken with great caution. If the phase contrast is clearly linked to a contrast of properties on the studied surface, phenomena that are not only linked to a pure mechanical contrast can interfere and distort the results : chemical affinity with the tip, adhesion, electrostatic charges... This remains however a simple method to observe qualitatively different regions of a sample.

A similar approach, using frequency shifts induced by the contact (the piezo is modulated in frequency instead of amplitude), seems to give more informations, but remains a contrast qualitative method [10].

1.2.2 First AFM modes for mechanical measurements

The fact that the imaging technology used in AFM is based on a direct contact between the tip and the sample quickly made it possible to integrate measurements of mechanical properties. The use of the AFM for this purpose dates back to the 1990s, first with the qualitative *Tapping mode* but then with efforts towards quantitative measurements. A brief history is proposed here, in order to highlight the evolution of the technique and its advances, before arriving at the current tools — in particular the QNM mode.

Force Modulation mode (FM)

The *Force Modulation* mode, also emerging in the early 90s, is entirely dedicated to observing mechanical contrasts [11]. In this case, the tip is always in contact with the sample, which is subjected to a vertical sinusoidal oscillation of a few nanometers of amplitude. There is therefore a harmonic stress applied to the sample at the contact point under the tip. The signal transmitted to the photodiode then depends on the deflection of the cantilever, which depends directly on the damping of the oscillation by the surface. Thus, the amplitude of the recovered signal reflects the stiffness of the scanned zone (Illustration Figure 1.4).

This technique appears to be very promising, in particular for the field of polymers [12], in which the observation of local mechanical heterogeneities is a major challenge.

Attempts to make this method quantitative quickly appeared, in particular with Radmacher *et al.* [13]. The team introduced the calibration of the deflection sensitivity on a silicon wafer, using the nominal characteristics of the cantilever (stiffness) and the tip (radius), and the JKR contact model [14], to study the contrasts of viscoelastic properties of soft materials (polymer films, structured fatty acids).

However, at this stage there are still many approximations and difficulties in dissociating all the components of the tip-sample interaction [12]. The need to use cantilevers suited to each type of sample appears. Many difficulties and artifacts are described, such as a frequent slipping effect of the tip on the surface—mistakenly recorded as an indentation [15][1]. Given the permanent contact between the surface and the tip, difficulties in contact mode (dangerous for the tip and/or the surface) are also to be deplored. The *Force Modulation* mode at least sets the basis of mechanical studies with atomic force microscopy, and opens the path towards quantitative studies.

AFM Nano-indentation

The next step towards quantitative mechanical studies with atomic force microscopes came up with the recording and the complete analysis of force curves [16, 17, 18] (see Figure 1.11).

[1] One suggested solution to this particular problem is then to measure a lateral force rather than normal, but it is a complex method that does not bypass other difficulties

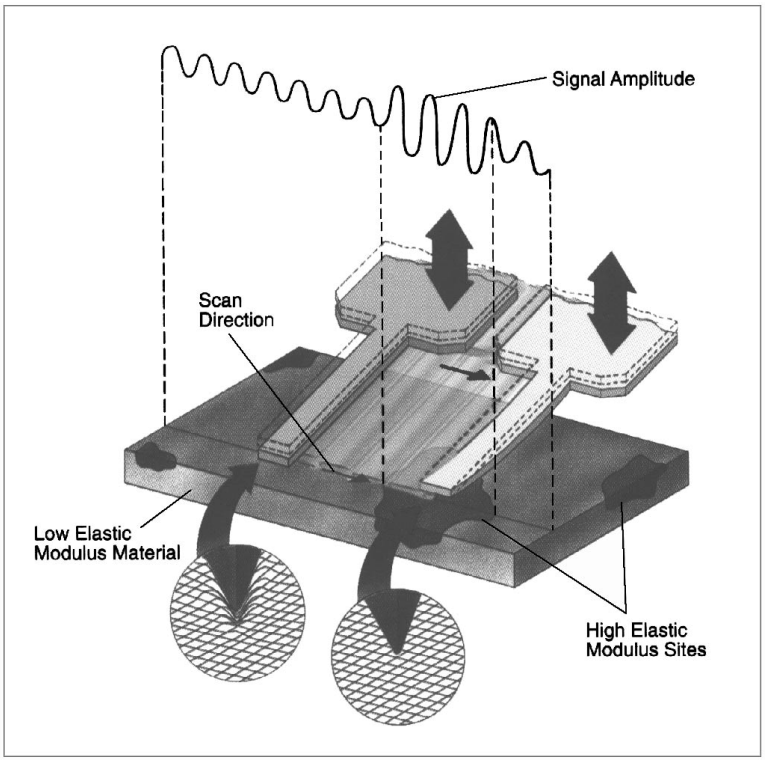

Figure 1.4 – Representation of the scan of a sample with low modulus. When the tip encounters a zone of higher modulus (in black), the amplitude signal increases [12].

The AFM was used like a nano-indenter. Each measurement is thus punctual, and the image recording (for topography and additional data) is made separately if necessary, in tapping mode for instance, until the developement of proper mechanical AFM modes such as Force-Volume, allowing to obtain simultaneously topography and force curves, on each scanned point.

Quantification of mechanical properties such as elasticity modulus with an AFM tip is made possible by the use of contact models (see chapter 2), thus by the precise knowledge of each tip's geometry and each cantilever's spring constant. Alternative *relative* methods emerge [19], allowing to use reference sample (with known properties) to bypass the difficulties and the approximations of the modelling.

Using the Atomic Force Microscope as a nano-indenter has been popular in polymer science [20]. It is a quite easy and robust way to study the mechanical properties of materials such as biological composites [21] or polymer thin films [22]. By combining a tensile testing machine and an AFM, Opdahl and Somorjai [23] used AFM nano-indentation and topography mapping in parallel to highlight the evolution of the surface stiffness modulus and roughness of polyethylene samples through macroscopical deformation. They were able to show that a superficial stiffening happens in the elastic domain, and then the modulus decreases in the plastic domain, as the polymer chains align themselves with each other.

AFM nano-indentation has also been used in the study of composites interfaces. Linear profiles can be acquired, point by point, acquiring force curves across a fiber-matrix interphase (as shown in Figure 1.5), and the evolution of the modulus can be acquired. Using this method, Mäder and Gao [24, 25] highlighted the influence of the fiber sizing on the interface modulus, directly linked to the fiber-matrix adhesion and thus to the composite resistance.

More recently, Chen *et al.* [26] used an AFM as a nano-indenter to evaluate the stiffness of

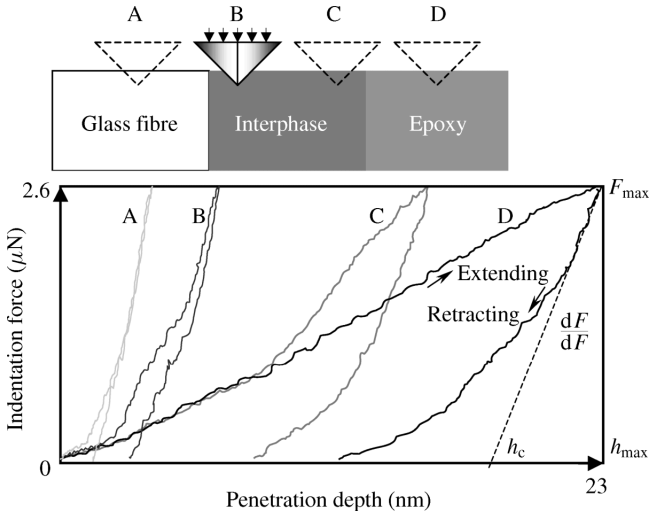

Figure 1.5 – Indentation force–penetration depth curves corresponding to the indentation of different locations across a sized glass fiber/epoxy resin interface. [24].

200 nm polystyrene/silica core-shell particles. Interestingly, they were able to show that the silica shell alone has a higher modulus than the one of the core-shell particle with a PS core. The modulus also rises when the thickness of the shell increases. For the calculation part, a Hertzian contact model (see chapter 2) was applied and the tips were characterized using scanning electronic microscopy (SEM).

It is also worth mentioning an original AFM microhardness measurement method, used by Zhang *et al.* [27] to investigate the mechanical behavior of PS–grafted silica nanparticles agglomerates in a polypropylene matrix. The so modified nanoparticles play a limited role as direct hardening fillers, but act as crosslinking sites in the matrix. A specific contact model, established according to the shape of the tip's indents, was used.

The use of the AFM as a nano-indenter has been one of the milestones in the path towards quantitative nano-mechanical mappings, with the introduction of force curves. That technique, however, does not use the imaging capability of the microscope, and the single-indentation approach makes its operation long and hardly precise: to aim at the right spot to indent can be difficult. However, it is still used when mapping is not necessary: for instance, methods emerged to recognize, depending on nanomechanical properties, normal and pathological tissues such as pulmonary artery [28].

Force Volume mode (FV) and Force mode

The combination of the indentation method using force curves and the imaging capability of the AFM was first implemented in Force mode or Force-Volume mode [29, 30]. The word "volume" refers to the control, not only on the X-Y piezo movements (as traditionally in mapping modes), but also on the Z piezo, allowing the acquisition of the force curves.

As in AFM nano-indentation, the quantification of mechanical properties is made possible by the use of contact models (see chapter 2) and thus by the precise knowledge of each tip's geometry and each cantilever's spring constant. Alternative *relative* methods emerge [19], allowing to use reference sample (with known properties) to bypass the difficulties and the approximations of the modelling.

Nitta *et al.* [31] made such measurements on agar gels. Figure 1.6 shows the kind of im-

age obtained with this mode, and Figure 1.7 shows a corresponding distribution of the moduli obtained on various concentrations of agar gels.

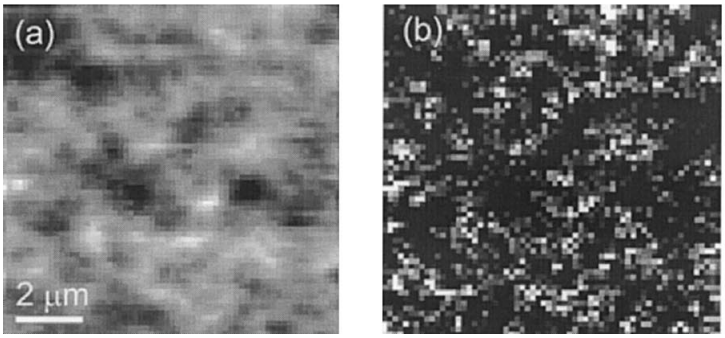

Figure 1.6 – AFM Force mode images of an agar gel [31] (a) topography and (b) modulus. No scale is given, but modulus histograms are given in Figure 1.7.

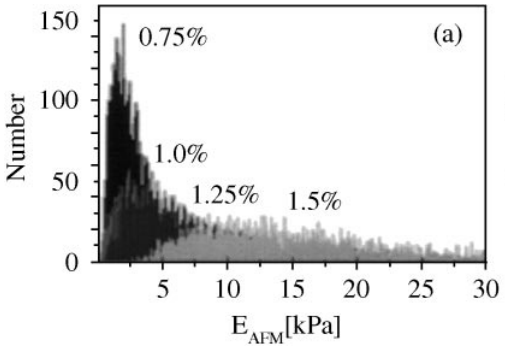

Figure 1.7 – Modulus histograms obtained by Nitta *et al.* [31] for different agar concentrations.

However, authors often express doubts on the reliability of the measurements, or its applicability in specific cases, such as thin films [32]. As it will be discussed in the next chapter, there is an importance of contact models used to fit the modulus on the force curves, but also an importance of other factors such as the choice of the tip. Nevertheless, in the right conditions, it is the first reliable quantitative mechanical mapping technique. The main remaining technical drawback is the acquisition time, which can be up to several hours for a poor resolution image.

Other contemporary mechanical mapping techniques

The present work is principally about AFM using Peak Force technology, described in Section 1.2.3. However, a quick review of other mechanical mapping modes that are used nowadays can be useful.

Harmonic modes such as HarmoniX, developped by Bruker (formerly Veeco), appeared in the 2000s, and are based on Tapping Mode, but using the higher harmonics of the signal to measure mechanical properties [33]. This has been useful on biological samples [34], and new mechanical properties, such as adhesion force, are accessible. Studies compared, as current quantitative mechanical mapping modes, HarmoniX and QNM (both from Bruker) and concluded that QNM is more appropriate in polymer science to reach quantitative measurements [35]. Anyway, both modes can be complementary as they use different approaches to reach the same result [36].

Contact Resonance is a contact mode with a high-frequency modulation applied between the tip and the sample [37]. This approach was first developed in the 1990s by the Yamanaka [38] and Rabe [39] groups, and is still regarded today [40, 41]. The tip is drived by a low amplitude vertical and high frequency modulation while scanning the sample, and the response, modulated by the viscoelastic properties of the sample, is recorded via the feedback loop. The properties are extracted from the recorded resonance peak and its harmonics. Typically, the frequency shifts are linked to elastic informations and the quality factors to the viscous, dissipative properties. This method is extremely promising, but there are still some doubts on its reliability on specific material, such as elastomers [42].

Anyway, all the modes cited above, and including Peak Force QNM mode (further detailed), are specifically relevant in certain conditions, depending on the samples and on the aim of the measurements. Figure 1.8 shows a map of the relevance of some mechanical mode, depending on the modulus of the sample and the working frequency.

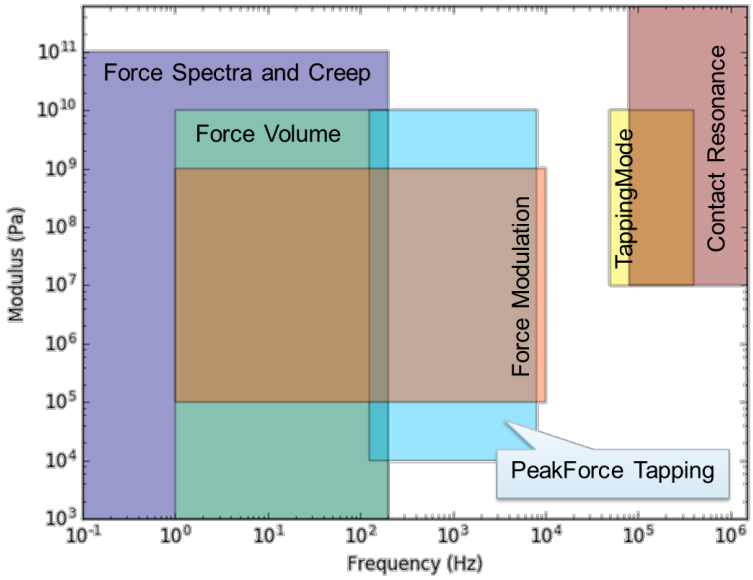

Figure 1.8 – Domains of relevance of different mechanical mapping modes, according to the Young's modulus of the sample, and of the working frequency (typically the oscillation of the cantilever). Source: Bruker.

1.2.3 Peak Force: towards quantitative measurements

Peak Force Tapping

The Tapping mode was a considerable advance in atomic force microscopy and a step towards nano-mechanical characterization with its phase contrast, although purely qualitative. Nevertheless, the control of the tip-to-sample contact remains insufficient: certain samples, in particular biological samples, remain too sensitive. The quantitative modes cited above also have particular drawbacks, in particular a low acquisition speed and/or a poor resolution.

The Peak Force Tapping technology, developped in the late 2000s, allows to open the atomic force microscopy to those materials, and above all permits the simultaneous mapping of local properties.

The basis remains the same as for Tapping Mode : the vertically oscillating tip hits the sample at each cycle. However, it is driven differently :

- The main control parameter is not anymore the *oscillating amplitude* of the cantilever, but the maximum force, or *peak force*, applied by the tip on the sample surface at each contact. This force is known and monitored precisely with the feedback loop of the microscope.
- In Tapping mode the cantilever is excited at a frequency close to its resonnance. In Peak Force Tapping mode, it oscillates at a much lower frequency, typically few kHz. That facilitates the acquisition and the control of the applied force.

With that control, at each tip-sample contact, thus for each pixel on the acquired image, the evolution of the interaction force is recorded. The curve in Figure 1.9 is the typical "heartbeat" curve obtained for one contact, showing the successive phenomena: approach (A), attractive forces (B), contact and peak force (C), adhesion (D) and withdraw (E). By recording the position of the piezo (Z position) along with the time, a force curve like the one showed in Figure 1.10 can be obtained. These curves contain useful information on the mechanical properties of each contact point.

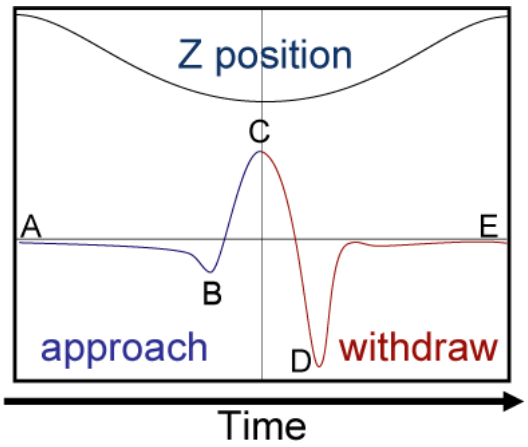

Figure 1.9 – Typical evolution of the recorded tip-sample interaction force during a contact. Source: Peak Force QNM User Guide [43].

Quantitative NanoMechanics (QNM)

PeakForce Quantitative NanoMechanics mode (PF-QNM or simply QNM) is based on the Peak Force Tapping technology and is currently the main mode for the mapping of local mechanical properties. The force curves obtained at each pixel of a scan are directly analyzed during the acquisition to obtain mappings for **adhesion force**, **local modulus** (see contact models on chapter 2), **dissipation energy**[2] and **deformation**, along with the traditional topography (height) image.

With, as an additional information, the deflection of the laser of the feedback loop on the cantilever, it is possible to deduce the tip position from the piezo Z position. The tip-sample distance is thus accessible. Figure 1.11 shows a typical force curve on which the local mechanical properties can be evaluated.

[2]The works of Gómez and Garcia [44] can help to understand the dissipation process in AFM

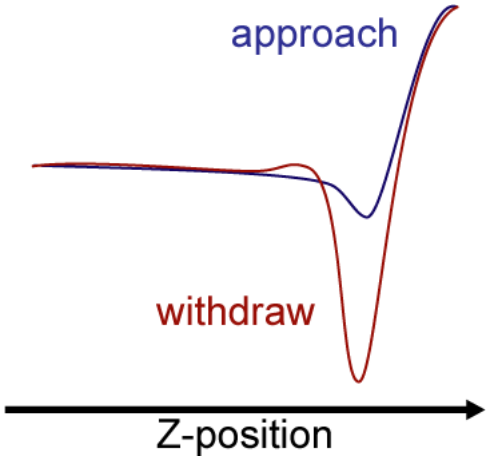

Figure 1.10 – Typical force curve : approach (blue) and withdraw (red) versus piezo Z (vertical) position. Source: Peak Force QNM User Guide [43].

- **Deformation** corresponds to the distance made by the tip from the point defined as the contact to the point corresponding to the peak force. The contact point is usually defined by the user as there is no precise definition of the contact at this scale. It is commonly understood on the approach curve as the point, after the generally slight attractive force zone, where the slope leading to the peak force begins to reach a positive value.
- The **adhesion force** is the height of the negative force peak in the withdraw curve.
- The **dissipation energy** is the area between the approach and the withdraw curves, in yellow in Figure 1.11.
- The **modulus** is evaluated from the slope in the beginning of the withdraw curve, just after the peak force (bold green line in Figure 1.11). Depending on the chosen contact model, the calculated modulus can take into account several external parameters, often related to the shape of the tip (see chapter 2).

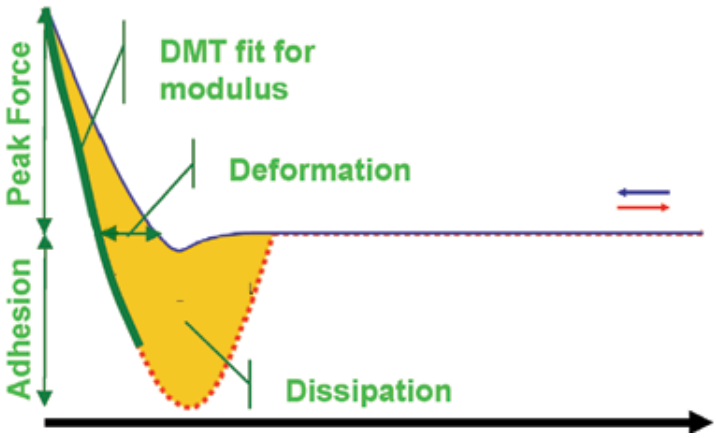

Figure 1.11 – Processed force curve with specific parts corresponding to local mechanical properties. The x axis represents the tip-sample distance. Source: Bruker, reference [45].

The PeakForce approach, combined with a wide variety of tips allowed to quantitatively map the local mechanical properties of materials from hard cement [46] to sensitive cells (see sections 1.3.1 and 1.3.2).

1.3 State of the art on AFM nanomechanical studies

This work aims to propose methodologies to reveal links between structure and properties of polymer-based materials using nanomechanical measurements by AFM. Peak Force QNM mode, described above, was chosen to constitute the skeleton of the work presented in the next chapters. It seems useful to start here with a bibliographic review on the studies performed with this mode, to identify what are the situations in which it is used, and what kind of conclusions can be taken from those nanomechanical measurements.

1.3.1 Non quantitative studies: PeakForce Tapping to contrast or to preserve sensitive materials

An important calibration process, which can be specific to the studied materials, is necessary to perform quantitative measurements with PeakForce Tapping. But this technology already provides some advantages without complete calibration, which will be reviewed here.

A non destructive scanning method for sensitive materials

The two main historical AFM modes, Contact and Tapping, still remained insufficiently sensitive for the non-destructive imaging of topography and mechanical contrasts (phase or lateral forces) of very soft materials.

Tapping Mode was already an improvement of Contact Mode, but the fact that the oscillation is controlled in amplitude (or frequency in some cases [10]) does not allow a precise control of the pushing force of the tip onto the sample. Some materials being sensitive to forces lower than a nanonewton (nN), a precise control of the tip-sample interaction is needed for the microscope. Some calibration steps are still needed to measure accurately this force: the spring constant of the cantilever (many authors use nominal values) and its deflection sensitivity (see Chapter 2).

This is a typical situation in the imaging of biological samples and soft polymers such as hydrogels. Ciejka *et al.* [47] used PeakForce Tapping to obtain high resolution topographic images of genepin-chitosan hydrogel microspheres. As such objects are designed to adsorb coronaviruses, the AFM images allowed to observe those elements on sphere surfaces under certain conditions, which would have been destructive or too coarse with another imaging method.

A similar method was used by Škvarla for the precise evaluation, using height (topography) AFM images, of the radius of silica gel-like spherical colloid particles [48]. An extremely low force in the 10—100 pN range was sucessfully applied to preserve the particles.

This is also useful for nano-structrurated materials, such as Kelly and Albert's "nano-roses" obtained from the crystallisation of poly(ε-caprolactone) in blends containing styrene-isoprene block copolymers [49] (see Figure 1.12), or the poly(glycidyl ether) brushes developed by Heinen *et al.*, scanned in liquid with a 1 nN applied force [50].

This shows an interesting feature of PeakForce Tapping, even using the traditional height channel only. This low–force scanning capability is also often combined with mechanical properties quantification, as reviewed in the following sections.

Beside the capability of imaging sensitive materials, AFM mapping with a low and controlled force also allows an outstanding resolution: Korokolov *et al.* evidenced the assembly of adsorbed

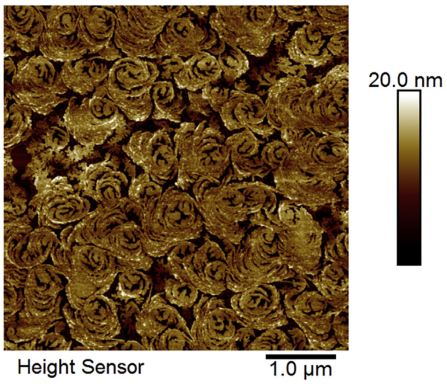

Figure 1.12 – "nano-roses" morphology imaged by AFM using PeakForce Tapping [49].

trimesic acid on HOPG[3] with olecular resolution using PeakForce Tapping [51], as shown in Figure 1.13.

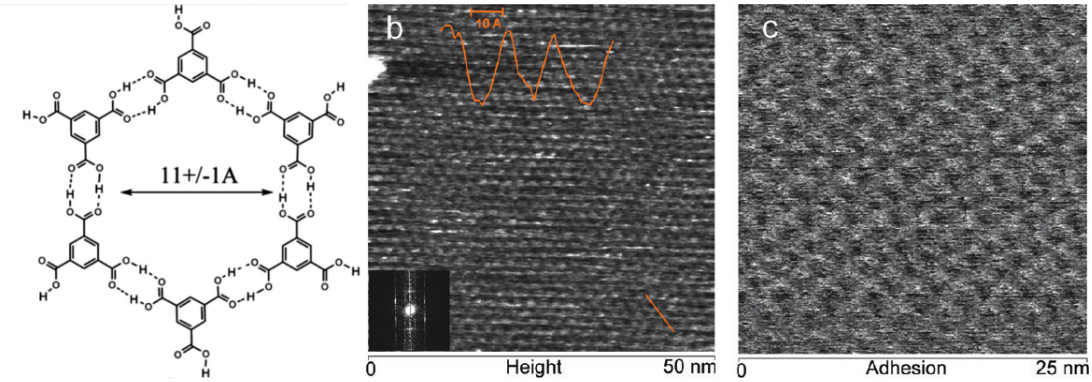

Figure 1.13 – Theoretical structure of the assembly of trimesic acid on HOPG (left), high resolution ($50 \times 50\ nm^2$) topographic mapping (b, center) and $25 \times 25\ nm^2$ adhesion mapping (c, right) showing the structure of adsorbed trimesic acid [51].

Contrast and identification with Peak Force Tapping

Using the different channels of PeakForce QNM mode, even without calibration, useful qualitative information can be obtained. The main difference with phase contrast in tapping mode, except being able to control the interaction force as mentioned above, is that the nature of contrasting information is identified: knowing if the contrast reveals differences in adhesion, stiffness or deformation can bring the interpretations one step forward. Furthermore, even in arbitrary units, the direction of any property variation is also revealed: instead of measuring just a phase difference between two zones, it can be measured, for instance, that one zone is more adhesive than another.

This has been widely used to identify dispersed phases or particles in polymer blends and composites. Grigorescu *et al.* used the deformation channel in PeakForce QNM to identify graphite (giving a lower deformation in AFM mappings) in SEBS[4] based composites [52], as

[3] Highy Oriented Pyrolytic graphite
[4] polystyrene-b-(ethylene-co-butylene)-b-polystyrene

shown in Figure 1.14. Kfoury *et al.* also used deformation mappings to differentiate the microstructures induced by a reactive and by a physical blend of PLA and poly(ethylene glycol) methyl ether acrylate [53]. The modulus channel, giving information on the relative stiffness of different components, is the most common use for contrast and identification purposes on nanocomposites [54, 55] and blends [56], allowing, from the analysis of their morphology, to explain macroscopic behaviors such as hydrolytic degradation [57].

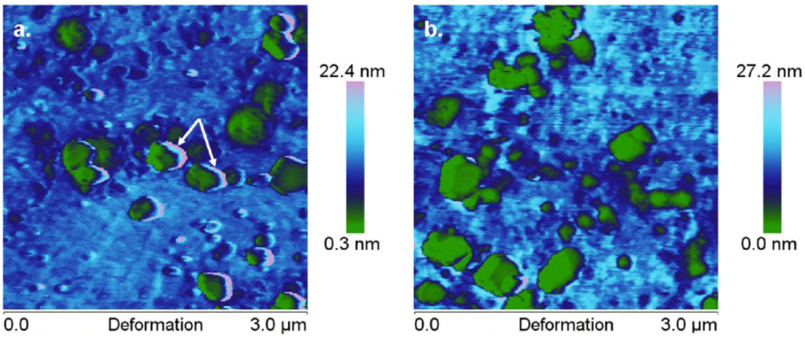

Figure 1.14 – AFM nanomechanical deformation maps of SEBS/graphite nanocomposites. The green parts, corresponding to lower deformation, indicate graphite particles [52].

Modulus and adhesion contrasts It is worth noting that even without calibration, this method using the modulus channel allows to evaluate the relative stiffness of different surfaces, which can be useful to compare surface treatments [58]. A great care should however be taken if no calibration is performed: each sample has to be scanned in the exact same conditions (applied force, deformation, and tip shape) so that it is possible to compare them.

Adhesion force qualitative mappings can also provide useful contrasting informations, especially in heterogeneous materials: the nano-structure of phase-separating copolymers [59, 60], blends [61, 62] or nanocomposites [63, 64] can easily be revealed. Choi *et al.* use the three mentionned channels (adhesion, DMT modulus and deformation) along with topography to image star copolymer micelles on graphene oxide flakes with an optimal resolution, as shown in Figure 1.15 [65]. Anderson [60] also used modulus and adhesion contrasts to analyse the structure of copolymer films.

Sokolova *et al.* [66], imaging imprints of zirconium oxide nanostars on a polyheteroarylene matrix, reached interesting conclusions on the packing density of polymer chains near the particles using qualitative modulus maps, and on the density of polar groups in the imprint using qualitative adhesion maps. Chu and collaborators used DMT modulus and adhesion contrasts to distinguish between the folding and stacking of reduced graphene oxide nanosheets [67].

The nanometric resolution of PeakForce QNM allowed Woods *et al.* to quantify the self-reorientation of graphene flakes on boron nitride crystals [68]. Profiles and Fourier transformations of modulus images of the graphene patterns were used, allowing to detect angle variations of less than 2°.

Qualitative AFM studies using adhesion, modulus and deformation mapings is also used to observe the morphologies of membranes [69, 70, 71]. Heisgen *et al.* used it to recognize zones affected by swelling, caused by a water flow associated with an ionic current [70]. The nanomechanical study is coupled here with an electrical AFM study using PeakForce TUNA mode, applying a potential difference between the conductive tip and the sample basis, and mapping the electric current flow along with mechanical properties. The water flow associated

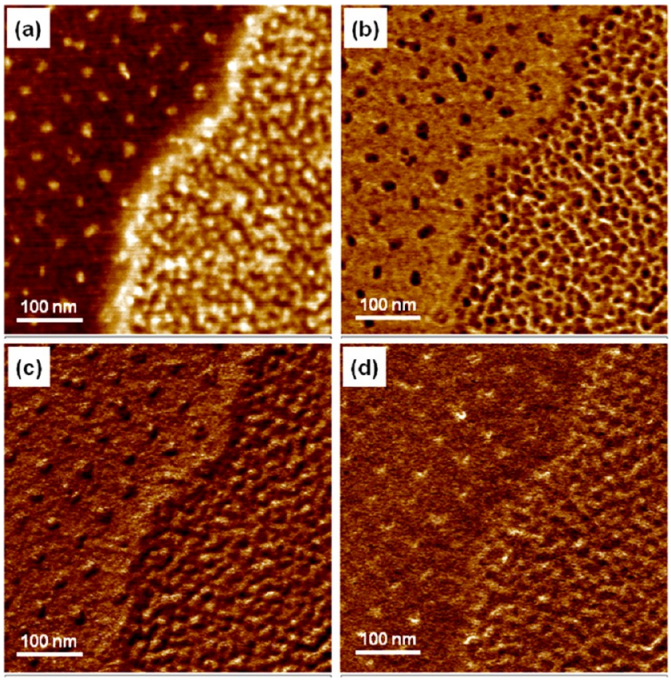

Figure 1.15 – High-resolution images of (a) topography, (b) adhesion, (c) apparent modulus, and (d) deformation showing different self-assembly of copolymer micelles on graphene oxide (on the left of each image) and on silicon oxide (on the right). Z-scale: 4 nm (topography) [65].

with the ionic current caused a buildup of water pressure and subsequent swelling.

CFM A high-end possibility offered by qualitative PeakForce Tapping is its use in CFM (Chemical Force Microscopy [72]). Initially used with forces curves in modes such as Force Volume (descripted above), it uses chemically modified tips to map adhesion with specific chemical groups, allowing conclusions on the chemical nature of scanned surfaces. As it allows easy and fast adhesion force mappings, PeakForce Tapping gives the advantage of this mode, applied to CFM. An illustration is given Figure 1.16, taken from Alsteens *et al.* [73]. In this study, various materials, including dimethylmethylsilane/silica composites (see Figure 1.17), yeast cells (*Saccharomyces cerevisiae*) and pathogen fungus spores (*Aspergillus Fumigatus*) were scanned, revealing spatial distributions and organization of chemical functions showing good or bad affinity with the ones grafted on the tip. PeakForce tapping also permits, in this case, to scan living cells without damaging, applying extremely low forces (0.75nN). The results are remarkable with methyl-functionalized tips (as represented in Figure 1.16). Alcohol (—OH) functionalized tips, however, seem to give poor results, as also reported by Colson *et al.* [74] who obtained better contrasts with standard silicon tips on hydrophilic glass, functionalized (methyl and alcohol) silicon and a wood/wax sample. Anyway with certain chemical functions and under the right conditions, tip modification combined with PeakForce Tapping offers a specific method to map chemical affinities using principally qualitative adhesion force.

The PeakForce Tapping technology gives thus easy methods to contrast phases and components in heterogeneous materials and biological samples. The force control allows unprecedented resolution and non-destructive scanning of sensitive samples. However, the force curves–based technology can be pushed one step forward, using calibration to quantify the nanoscale properties described in section 1.2.3. The following sections aim to review the different meanings

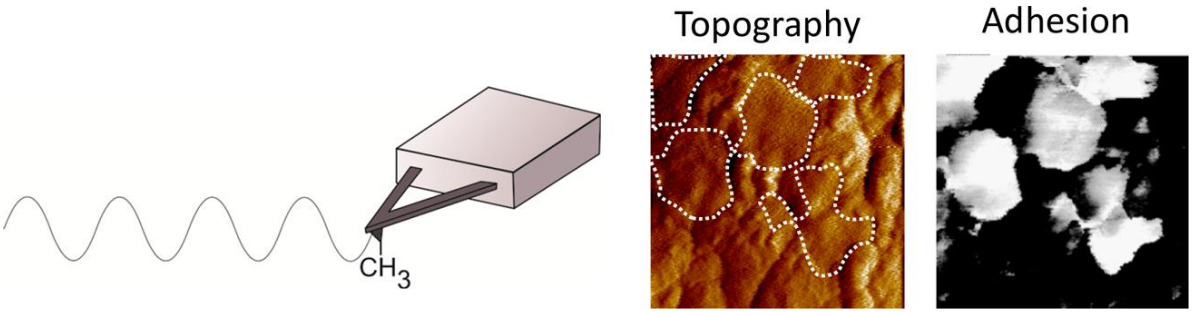

Figure 1.16 – Illustration of the principle of CFM: chemically modified tips allowing to map adhesion with specific chemical groups [73].

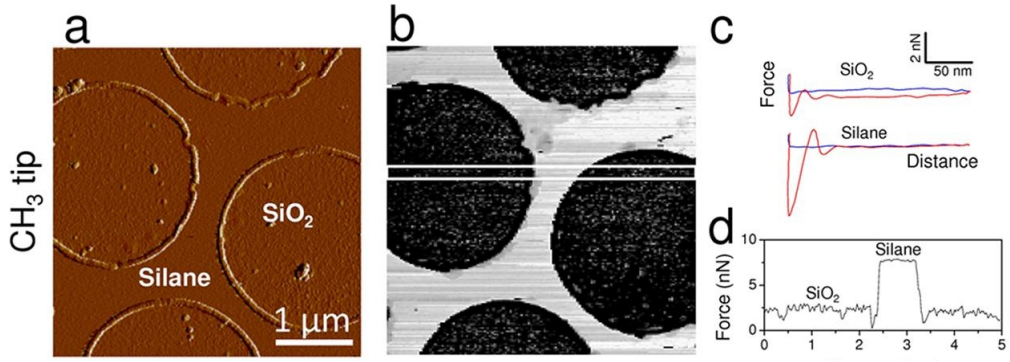

Figure 1.17 – Images of the error signal (a, reflecting the topography), adhesion force (b), representative force curves (c) and adhesion profile (d) recorded with a hydrophobic (CH_3) functionalized tip on dimethylmethylsilane—SiO_2 micropatterns [73].

interpretations taken from those new properties, as their meaning is still relatively unknown at this scale.

1.3.2 Cells, soft tissues and proteins: Nanomechanics in biology

AFM nanomechanical mappings using PeakForce Tapping are of great interest in the biological field, on the one hand because of the sensitivity of many samples, including living cells [73], requiring extremely low and controlled forces. On the other hand, given the variety of nanostructurated biological materials, understanding their mechanical behavior is a critical challenge in many applications including medicine and genetics.

Amyloid fibrils are insoluble filiform protein aggregates, implied in many diseases such as neurodegenerative disorders. The growth, assembly and mechanical properties (modulus) of such fibrils were observed and described by Lara *et al.* [75] under varying conditions, distinguishing between different types of fibrils depending on their modulus. Yang *et al.* investigated a light-driven treatment to inhibit or modify the formation of amyloid aggregates implied in Type-II diabetes mellitus [76]. While regular AFM topography confirmed the inhibitory effect of photo-activated porphyrin on the formation of amyloid aggregates, the modulus mappings showed an increased stiffness of the fibrils under treatment, interpreted as stronger interactions between porphyrin and amyloid peptides than between peptides in the aggregates.

AFM provides thus a unique tool to investigate the mechanical behavior of amyloid fibrils,

but retrospectively their studies as a model nanostructured biomaterial led to some interesting conclusions on how to use and interpret quantitative nanomechanical results. Adamcik *et al.* used AFM QNM measurements and an indirect method to image (see Figure 1.18) and calculate the modulus of β-lactoglobulin amyloid fibrils [77, 78]. The complex indirect method, based on topological statistical analysis of fibrils' structural conformations and size deduced from topographic images, only allowed to evaluate an upper estimation of the modulus of the fibrils, calculated to be 4.98 GPa. The value obtained by direct imaging by PeakForce QNM measurements being 3.7 GPa, which is 26% lower than the upper estimation, was considered acceptable by the authors, validating the QNM measurement method.

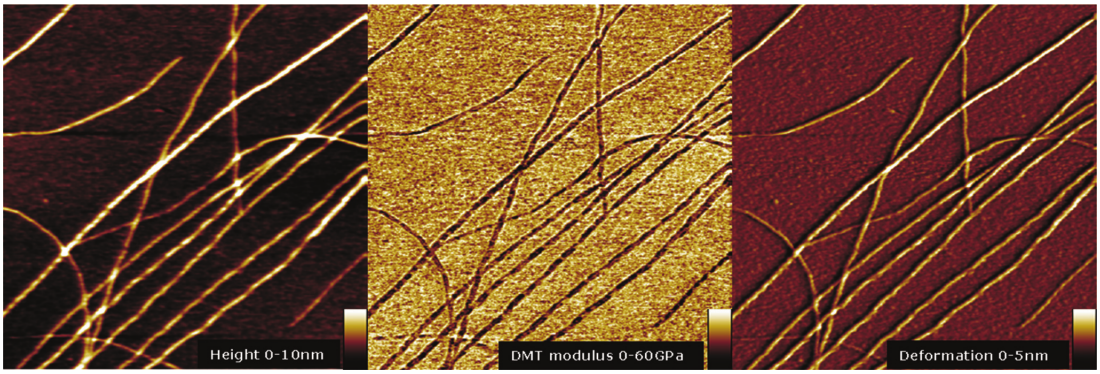

Figure 1.18 – 1.3×1.3 μm^2 topography (left), DMT modulus (center) and deformation (right) AFM PeakForce QNM images of β-lactoglobulin amyloid fibrils deposited on a mica substrate [77].

The straightforwardness of such measurements still imply to take a great care of the calibration and imaging conditions. The ideal method is not necessarily known and documented, as it is specific to each sample. Some authors used thus parallel methods to confirm their results, helping the scientific community on how to reach true quantitative results by detailing their methodologies. Different AFM–based methods were also compared by Sweers *et al.* [79] to measure the elasticity modulus of α-synuclein amyloid fibrils that are associated with Parkinson's disease. Moduli were evaluated using AFM nanoindentation (detailed in Section 1.2.2), HarmoniX mode (described in Section 1.2.2) and PeakForce QNM in air and in a buffer solution (liquid). As they reached a good agreement between results (all method giving a modulus in the 1.0—1.3 GPa range), they made some observations on the right conditions to obtain good results using PeakForce QNM on amyloid fibrils, and in general:

- It is important to adapt the probe to the material: the cantilever stiffness has to be of the same order of magnitude as the sample
- The peak force has to be low enough to prevent fibrils from breaking. Also, the modulus can be affected by the hard substrate and overestimated if the applied force is too high.
- On the edge of the fibrils, it is often observed that the measured properties are aberrant: it is attributed to the changing contact area between the tip and the fibril in this zone, as this contact area is taken into account in the calculation of some properties (see Chapter 2)
- Again on the contact area, fibrils have to be considered as cylinders in the contact models (see Chapter 2) to reach true quantitative values for the moduli. A correction factor is applied.

Other biological materials PeakForce QNM helped to better understand the relation between structure and properties for many other biological materials. It allowed to measure mechanical properties for objects that are too small to be characterized *in situ* by any other mean, such as antibodies [80], leading to a better understanding of their mechanical behavior (see Figure 1.19). In the cited study by Voss and collaborators, the high deformability of the antibodies was reported (they resisted a deformation of more than 20% of their diameter), explaining the conformations they can adopt to bind with as many antigens as possible.

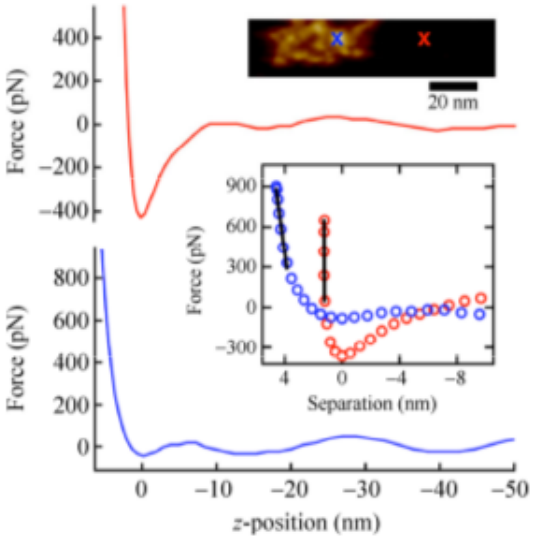

Figure 1.19 – Force–distance curves captured on mica (red curve, top) and on an antibody (blue curve, bottom). Crosses in the topographical image mark the positions at which force–distance curves were acquired. By fitting with the DMT model (see chapter 2) on the black lines in the inset, the moduli were calculated: $E_{mica} = 0.52$ GPa; $E_{antibody} = 2.2$ MPa) [80].

Often normal and anormal tissues or cells are compared in terms of nanomechanical properties to quantify parameters about a disease, in terms of nanomechanical properties. This is the case of normal and "rough eye" phenotype in a fruit fly cornea (*Drosophila melanogaster*) studied by Lavanya Devi and collaborators [81]. Baldwin, Kreplak and Lee studied the mechanism of overload in tendons [82] by mapping the kinked collagen fibrils of normal and overloaded bovine tail tendons, explaining their failure by discrete plasticity.

The influence of adenosine triphosphate (ATP) on the red blood cell membrane was investigated by Picas *et al.* [83]. The modulus and deformation of different parts of the cell membrane were quantified with and without ATP to understand the influence of this molecule on their mechanical behavior, as shown in Figure 1.20. The high deformability of the membranes with ATP explains the blood cells' capability to experience large deformations in narrow capillaries. Encinar extended the study to the influence of ATP on the self-assembly of protein networks on the blood cells membrane [84].

Attempts to quantify properties using modified tips were carried out on biomaterials. Alsteens *et al.* [85], using complex peptide-terminated tip functionalizations, measured the adhesion force on receptors in cell membranes and quantified their dynamic binding strength to the peptide ligands. The method, although being very promising, was reported to be still very challenging, given, for instance, the unknown elasticity of the functionalization system bound with the tip. Álvarez-Ascencio *et al.* made a hair indenter (SEM image shown in Figure 1.21) to evaluate the

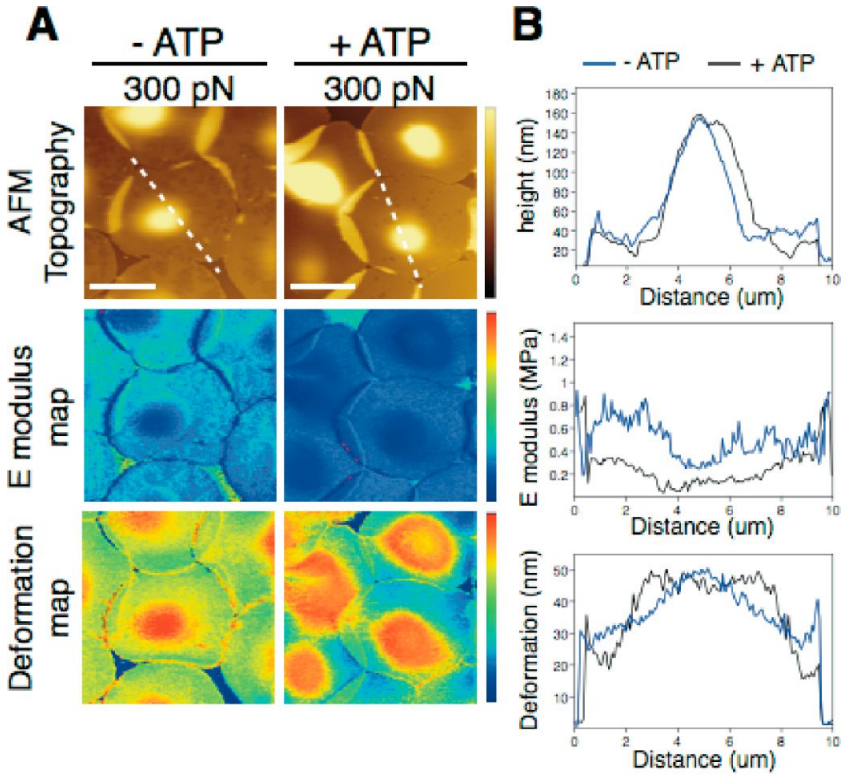

Figure 1.20 – (A) Topographic, local modulus and deformation images of red blood cell with (+) and without (–) ATP. (B) Profile analysis of topographical images, elastic modulus, and deformation map along the white dashed line for ATP-depleted (in blue) and ATP-containing (in black) cells. False color scale is 250 nm for topography, 2.5 MPa for elastic modulus, and 50 nm for deformation. Scale bar is 5 μm. [83].

interaction of the skin with razor-cut hair [86]. They also measured, using PeakForce QNM with a traditional silicon tip, the skin's elasticity modulus to be, in average, 0.4 GPa. With a sharp tip, the skin outermost layer resists up to a $4\,\mu N$ load before showing plasticity.

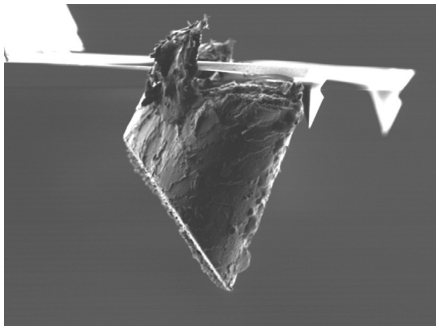

Figure 1.21 – Scanning Electronic Microscopy (SEM) image of the hair indenter used by Álvarez-Ascencio *et al.* [86]. A piece of hair is attached to the cantilever, taking the place of the silicon tip.

As this work also aims to reach a better understanding of the actual meaning of nanomechanical properties, and how they are affected by different parameters, challenging and paradoxical results are among the most important. While imaging living bacteria cells (*Pseudomonas aerug-*

inosa), Smolyakov *et al.* figured out that two equivalent AFM nanomechanical mapping modes (*i.e.* PeakForce QNM from Bruker and Quantitative Imaging from JPK) give different modulus evolutions when increasing the oscillation frequency of the tip [87]. As Quantitative Imaging (QI) showed an increasing modulus of the bacteria with the increasing frequency (expected visoelastic behavior), PeakForce QNM measured decreasing modulus. This is attributed by the authors to creep relaxations, as the frequency ranges for the two modes were not the same (less than 100 Hz for QI and more than 200 Hz for QNM). It highlights the importance of the choice of the parameters, and their adaptation to the studied material. The relative calibration method (detailed in Chapter 2) at a fixed frequency is the most common way to limit the relative influence of unexpected behaviors.

PeakForce QNM mode offers a good tool in the study of biological materials, as it combines quantitative results with a precise force control. It appears however that measured properties on a given material depend significantly on the scanning conditions: imaging in air or in fluid, the tip oscillation frequency, its spring constant... The main parameters and conditions are thus part of the results and have to be detailed to be truly considered as quantitative.

1.3.3 Nanostructured materials

Novel inorganic and organic nano-structured materials are promising in many fields including electronic devices development or drug delivery in medicine. PeakForce QNM provides the same advantages as in biology to study their morphology and properties.

To be able to map the nanoscale elasticity modulus allowed to detect different nanostructures of germanium surfaces irradiated by Bi^+ [88]. It was reported that depending on the irradiation temperature, the surface can form structures from nanoporous sponges to hexagonally ordered nanometric dot patterns. Such dots exhibited a different modulus depending on the irradiation temperature (see Figure 1.22) without any topographic change, revealing that their mechanical properties can be tuned.

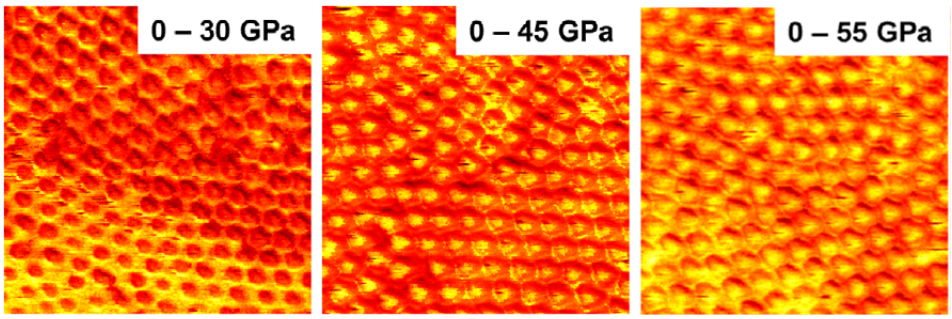

Figure 1.22 – 500×500 nm^2 DMT modulus images of dot–like structures obtained at 280°C (left), 320°C (center) and 340°C (right). The brighter the color, the higher the modulus, the scale range being indicated on each image. It is clear that the dots are stiffer with higher irradiation temperatures [88].

Destsi *et al.* imaged different structures of nanoporous gold [89] and measured average DMT moduli. A layered nanoporous sample exhibited a modulus of 7 GPa and another gold structure with conventional uniform porous morphology exhibited a modulus of 13 GPa. The authors compared their results to litterature data in which the moduli are evaluated using buckling mechanics [90], and found them to be in good accordance, thus validating their calibration and their method: the Young's modulus of a conventional nanoporous gold with the same porosity evaluated by buckling mechanics is around 10 GPa.

As for small biological objects, there are few other means to easily measure the mechanical resistance and stiffness of nanomaterials. For instance, slurries used in thermal energy storage are composed of microcapsules with a diameter in the micrometer range. Their resistance is a critical parameter since they are used in pumping system and submitted to compression forces, and their thermal efficiency depends on their integrity. Quantitative modulus measurements and breaking force experiments were conducted with AFM PeakForce QNM (reported in Table 1.1) and important conclusions were taken on the composition of the shell of the capsules, and the temperature dependance of their mechanical properties [91]. Those conclusions are likely to influence the design of next generations of thermal energy storage slurries.

Temperature $[°C]$	23	45
Needed force to break the capsule $[\mu N]$	11	1.8
Mean Effective Young's modulus value applying 500 nN $[MPa]$	200	50

Table 1.1 – Mechanical properties of Micronal ® DS 5007 X microcapsules reported by Giro-Paloma *et al.* [91]

The stiffness of particles is also critical in drug delivery systems, because it conditions how likely they are absorbed by tumor cells. AFM nanomechanical measurements were thus used to optimize the design of micelles [92] and sol-gel particles [93]. In such particles, Prokopowicz could use adhesion force to identify the drug–loaded domains [94].

The unprecedented versatility and force precision of AFM with PeakForce technology also allowed, in water, to map gas bubbles on a HOPG (Highly Oriented Pyrolytic Graphite) [95]. Their stiffness was measured to be in the 60—120 pN.nm^{-1} range, with small bubbles usually being stiffer than bigger ones (see Figure 1.23. This reveals hints about their physical nature which challenges classical thermodynamics with their time stability.

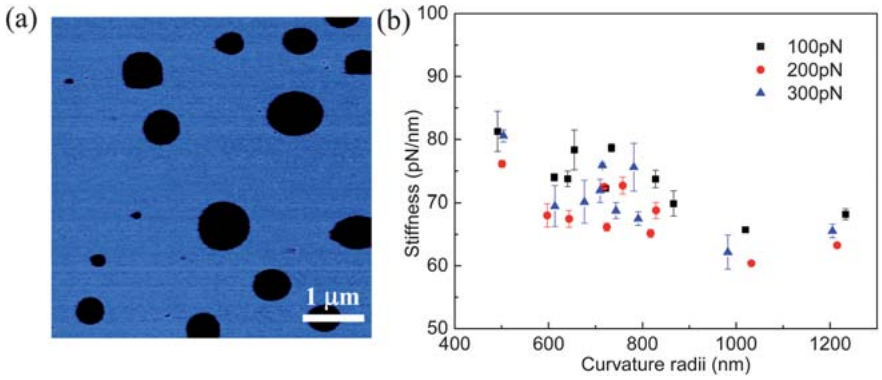

Figure 1.23 – Stiffness image (a) and stiffness versus curvature radii (b) of nano-bubbles, measured with different applied loads [95].The scale bar is not given, but the stiffness measurements of the corresponding bubbles are given in (b).

AFM quantitative mechanical mapping modes allow the direct measurements of mechanical properties of individual microscale and nanoscale objects and nanostructures. Often, results are verified with other methods, often indirect and complex. This leads to a better understanding of materials at this scale, in which there is still a lack of references.

Deformation could be understood as a form of nano-structuration. Ketov *et al.* scanned shear bands on a metallic glass (amorphous zirconium) previously deformed by compression [96]. The results showed a 70% decrease of the DMT modulus of the glass near shear bands, attributed by the authors to the migration of excess free volume and nano-voids. This is an example of how nanomechanics can help understanding the underlying phenomena of the behavior of materials.

1.3.4 Quantitative Nanomechanics in polymer science

Maybe one of the biggest challenge with AFM nanomechanical measurements is to use it to link nanoscale structure and properties to macroscopic behavior of materials. This is a typical issue in polymer science [97]. As the next chapters are specifically dedicated to the study of different polymer and composite systems, the following review is given as a starting point, to explore how nanomechanical measurements by AFM are used in this field, and how they help to understand the behavior of the materials.

Mapping properties of simple polymer systems at the nanoscale

Nanomechanical properties of polymer systems have been extensively studied since the birth of PeakForce QNM and equivalent modes. In fact, many of the first studies used polymers as model materials[5] to define in which conditions the measures are truly quantitative. The comparison between nominal values for Young's modulus, values obtained by classical nanoindentation and AFM–measured values is generally made. Based on such comparisons, Young [98] commented that a good repeatability can only be reached if a great care is taken in the calibration process. Furthermore, when a relative calibration is used[6], the elasticity modulus of the reference sample should be of an order of magnitude close to that of the material studied. Such recommendations allowed the further studies to anticipate the difficulties of this nanoscale characterization method, and helped to make it as robust as possible.

Hydrogels As for biological materials, hydrogels are among the softer polymer systems, and often need an adapted characterization method. As for cells, small objects must be compared using appropriate methods: when Gou *et al.* tried to reproduce the structure of a red blood cell using 3D–printed polyethylene glycol (PEG) hydrogels, they had to use PeakForce QNM mode to compare the mechanical properties of both objects to tune that of the PEG reproduction [99]. On one hand, almost no other characterization method could measure mechanical properties at this scale, and on the other hand, given the softness of hydrogels and cells, very low and controlled force had to be applied.

A very good example of the use of AFM nanomechanical mappings on hydrogels was carried on contact lenses by Chyasnavichyus and collaborators [100]. The cross-section of silicone hydrogels lenses were mapped to verify that the part which is in contact with the eye is softer than the rest. Many interesting observations were made, particularly, it was remarked that measured properties are accurate only when measured on flat surface because the tip–sample contact area remain constant, as calibrated. Furthermore, an explanation to the commonly observed overestimation of the modulus on soft polymers with AFM measurements was proposed: the frequency of the oscillating tip induces a really fast sollicitation, compared to macroscopical tensile test for example. The viscoelastic nature of polymers will thus cause their elasticity modulus to appear

[5] Polystyrene (PS) is almost always used as a model, being an amorphous, homogeneous and common polymer

[6] Relative calibration corresponds to the use of a reference sample of known modulus to adjust calibration parameters, especially the tip radius. See Chapter 2 for more details.

higher with AFM high-frequency sollicitation. It is useful to note that in the mentionned study, the deformations were relatively high for PeakForce measurements, the silicone hydrogel being quite soft: the indentation depth was reported to be in the 20–80 nm range. That implies that the viscoelastic effect is much more effective than in measurements at a more classical 2 nm indentation. It is also important to note that, as seen in chapter 2, the Sneddon contact model is the most appropriate to calculate the local modulus with such high deformations. The authors actually use it manually to quantify the moduli, while using the DMT model to obtain direct qualitative contrast images.

Natural polymers Natural polymers and fibers are increasingly used in the development of new materials, and are also among the oldest used by humanity. They are often exhibiting a particular structure at the nanoscale, it is thus of great interest to anticipate their behavior by knowing their nanomechanical properties.

Paper as a material is still giving informations on the nanoscale phenomena linked to known macroscopic behaviors: by comparing the scannings of cellulose fibers (some being previously submitted to hydrothermal aging), Theodonio *et al.* showed that the embrittlement of aged paper is linked to a nanoscale increase of the modulus of the fibers [101].

Arnould *et al.* emphasized different mechanical properties distributions in flax fibers depending on their age [102]. The observation of distinct regions with different moduli in developing plant stem fibers (see Figure 1.24) implies their progressive development and thickening, as the scan of mature fibers showed no gradient in the cell wall. Previously, the authors successfully validated the method (*i.e.* the detection of modulus gradients in cross-sections of fibers) on the cross-section of aramid fibers (Kevlar), showing a skin-core effect: the outer layer of the fiber exhibited, as expected, a lower modulus. The conclusions on the structure of such fibers could imply a better tuning capability of the properties of composites, using flax fibers at different stages of their development.

Surface treatment As a surface characterization method, AFM is widely used to evaluate the nanoscale effects of surface treatments on polymers, such as ultraviolet (UV) crosslinking [103]. The exposure time is often the analyzed parameter, which has to be adjusted to optimize the treatment. On an epoxy resin based on linseed oil, Dupuis *et al.* evidenced succeeding mechanisms happening during UV exposure [104]. First, the surface DMT modulus is increasing from 1.5 to 3 GPa in average, with an increasing roughness, indicating a successful crosslinking process. Then, from about 750 hours of exposure, a second modulus population is appearing on modulus histograms as shown in Figure 1.25, forming low-modulus zones in the AFM images, testifying the start of a chain-breaking behavior of the treatment.

Influence of time exposure was also studied on polyurethane treated by plasma immersion N_2^+ ion implantation [105]. AFM mappings revealed an increase of the modulus and a decrease of adhesion with increasing treatment time, with the creation of a fractal folded surface structure (shown in Figure 1.26, evidenced by thresholding height AFM images using the Otsu's method [106][7]).

The use of a mask during the treatment allows direct comparison of neat and treated surface: it could be evidenced for instance that UV-ozone treatment on polydimethylsiloxane (PDMS) leads to the formation of a silica layer [107]. Neat PDMS (protected by a mask) could be deformed

[7] The Otsu's method is an automatically performed thresholding technique, transforming a graylevel image into a binary image. It is used here to separate more clearly two height populations in AFM images, revealing the mentionned fractal structures

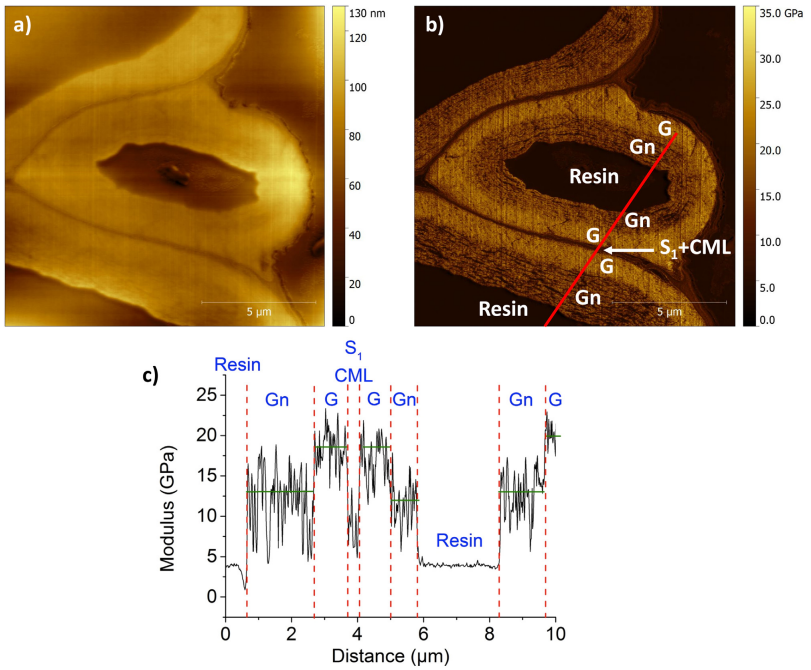

Figure 1.24 – PeakForce-QNM mapping of (a) topography and (b) DMT modulus of the cross-section of developing flax bast fibres extracted from green plant stem and embedded in an acrylic resin. (c) Variation of the indentation modulus along red profile drawn in (b), showing the different parts of the cell walls. Gn corresponds to a young newly deposited layer, G to a mature layer, S_1 to the outer layer of the secondary cell wall and CML to the compound middle lamella [102].

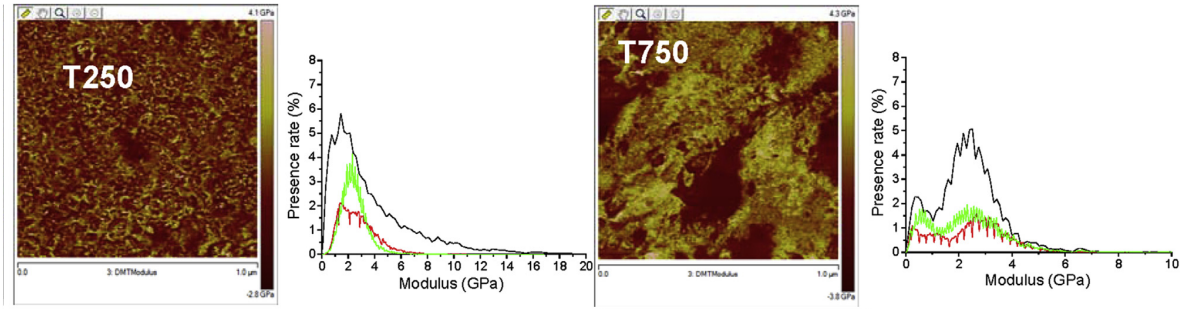

Figure 1.25 – DMT modulus images and corresponding modulus histograms of linseed oil–based epoxy resin aged 250 hours (left) and 750 hours (right) [104].

up to 40 nm by the tip, while treated zones exhibited a low, near null deformation, with a modulus increase from 3-4 MPa to 50 MPa. Using buckling mechanics on wrinkled surfaces, AFM–measured moduli were used to calculate the thickness of the silica layer. In the conditions of the study carried out by Del Campo *et al.*, the created silica layer was determined to be 4.5 μm thick.

Nanomechanical mappings were also used to validate novel UV lithography resins, *i.e.* non-chemically amplified resists, by comparing the properties of nanoscale patterns with those of existing chemically amplified resists [108]. The pattern collapse phenomenon was associated with mechanical properties, in particular the local elasticity modulus, which was measured to verify if it fits in an acceptable range (determined with data on the existing resists).

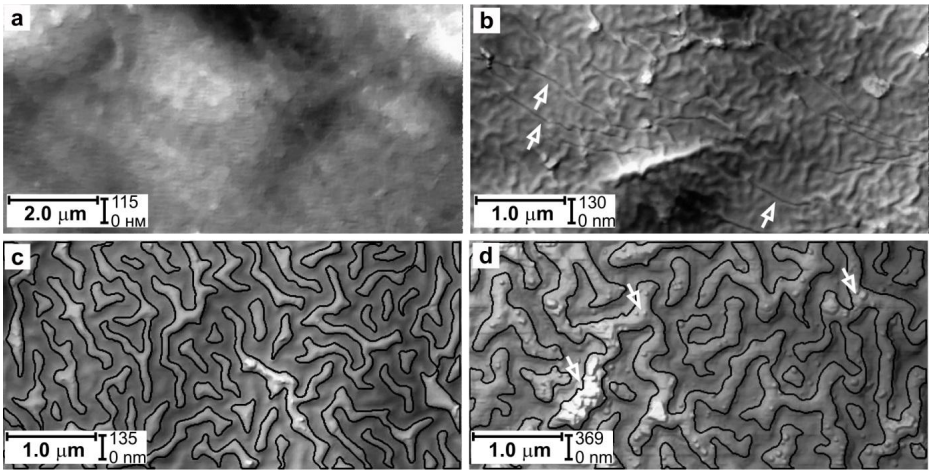

Figure 1.26 – AFM height images of PU: (a) – untreated PU; after plasma immersion N_2^+ ion implantation: (b) – $2 \cdot 10^{15}$ ions/cm^2; (c) – $2 \cdot 10^{16}$ ions/cm^2; (d) – $2 \cdot 10^{17}$ ions/cm^2. In (c) and (d) the fractal structure is evidenced by black lines of constant height [105].

Effects of surface treatments on polyamide 6 (PA6) were extensively studied. Ozone treatments led to a 30% surface DMT modulus drop, attributed to an increase of the solubility of rigid polymer chains on the polymer surface [109]. It was noted that AFM–measured nanoscale adhesion trends should not be extrapolated at the macroscale, since different phenomena enter into account. The adhesion force measured by AFM essentially relates the molecular interactions between the tip and the sample surface, while at the macroscale, other effects such as surface roughness also play a role.Banerjee and collaborators studied PA6 surfaces treated by electron beam [110]. It was reported that when the dose increases, AFM–measured modulus increases while energy dissipation and adhesion decrease. Those trends are attributed to electron-induced crosslinking, restricted segmental mobility and significant reduction of water absorption. The authors observed similar trends of the evolution of properties measured by AFM QNM mode and rheology:

- The DMT modulus, according to the authors, should be correlated with the storage modulus G'
- The dissipation energy is interpreted to be the nanoscale equivalent of the loss factor $tan(\delta)$

Those properties may reflect the same behavior, but a direct link cannot be established between two different scales, since performing measurements at the nanoscale tends to separate each phenomenon, while macroscale measurements aim to understand average effects of many nanoscale and mesoscale phenomena combined.

Phase separation: Copolymers, polymer blends and bitumens

It becomes evident, for many authors, that nanoscale properties and their macroscale counterparts cannot be directly compared even if they are obviously linked. The capability of nanomechanical measurements to separate phenomena and behaviors in the study of single–phased materials and surfaces can be extrapolated to more complex heterogeneous materials. Separate phase characterization and gradients of nanomechanical properties can be evaluated with AFM, opening new paths in the understanding of multiphased materials.

The design of polyurethanes (PU) is a good example as it implies soft and hard segments. Petrovic *et al.* studied with AFM nanomechanical mappings two different formulations, based on the same components: 70%wt of soft segments on one hand, and 50% on the other hand [111]. On AFM PeakForce QNM mappings, the former exhibited a clear phase separation between an homogeneous soft matrix (with a 7 MPa average DMT modulus), essentially composed by soft segments, and heterogeneous nodules, with a higher DMT modulus (*i.e.* 15 MPa in average), thus interpreted as being a mix of soft and hard segments. AFM mappings allowed to conclude that the 50% formulation was more optimized, being far more homogeneous, stiffer (40 MPa in average) and less adhesive. The PU nanostructure could be observed on modulus images, with 15 nm soft (about 45 MPa) and stiff (about 55 MPa) domains, respectively corresponding to soft and hard segments, as shown in Figure 1.27.

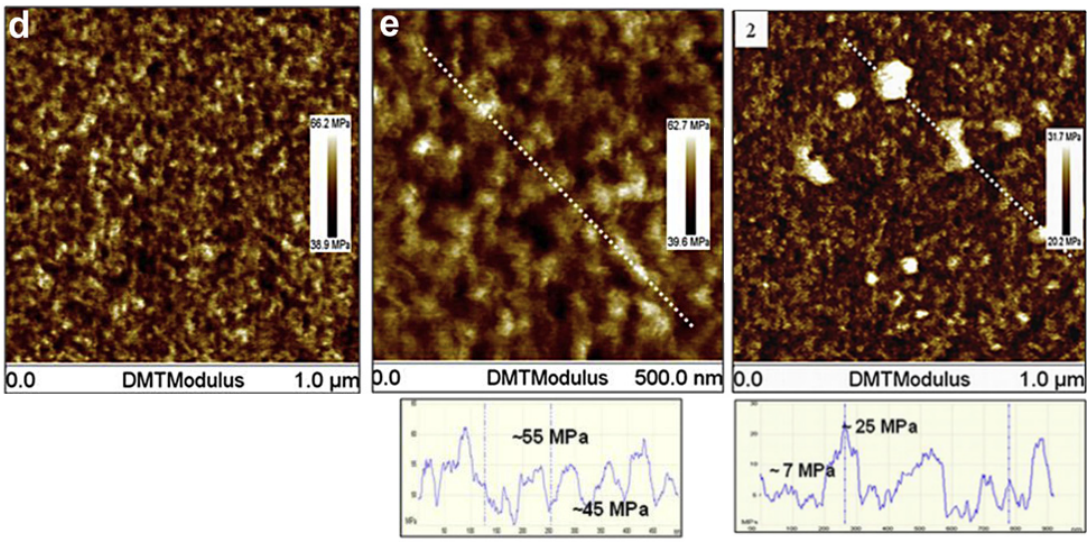

Figure 1.27 – DMT modulus maps of a PU surface containing 50% of soft segments; (d) $1 \times 1\ \mu m^2$; (e) $500 \times 500\ nm^2$) scans with section analysis profile taken along the white dashed line. (2) Similar $1 \times 1\ \mu m^2$ modulus image with profile for a PU containing 70% of soft segments. [111].

Bitumens AFM is an excellent tool in the study of bitumens, since they exhibit a multiphased structure (see Figure 1.28) which is difficult to observe using traditional microscopy techniques.

Fischer [112] and Laurell [113] introduced PeakForce QNM in the study of bitumens, going one step further the understanding of bitumens by quantifying their nanoscale properties. The former analyzed the viscoelastic behavior of bitumens, separating the matrix (Perpetua–phase) and the Peri/Catana phase together. Although no significant DMT modulus difference was reported (the Peri/Catana phase having a 10% higher modulus), the energy dissipation is almost three times higher in the matrix. By analyzing the force curves, it was deduced that the matrix exhibits a non–elastic behavior, but does not show permanent deformation when the same zone is scanned two times: the perpetua phase behaves as a viscous liquid with a relatively short relaxation [112].

Mingwang *et al.* studied various bitumen binder types, and the impact of aging on their microstructure [114]. A decrease of roughness and tip-sample adhesion of each phase, and an increase of DMT moduli on aged bitumens was reported, while the proportion of peri and bee (catana) phase increased or decreased, depending on the bitumen type. This study could help to

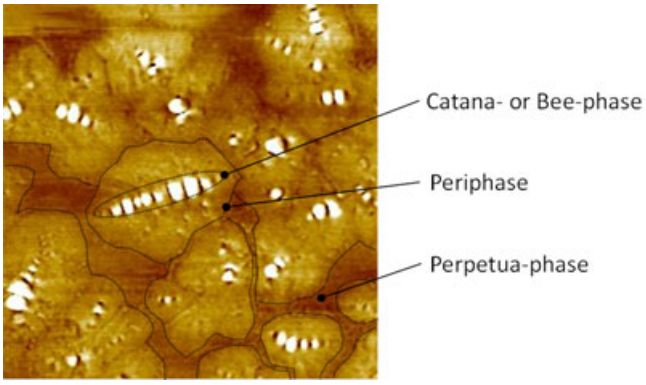

Figure 1.28 – AFM height image showing the different phases of a typical bitumen, (i) Catana phase = bee phase; (ii) peri phase surrounding the bees and (iii) para phase = matrix [112]. The scale of the image is not given, but estimated to be of the order of 10 micrometres.

understand which bitumen types are better suited to conserve their mechanical properties upon aging.

While few analysis methods are well suited to study bitumens, the use of AFM evidenced their structuration at the nanoscale, and the quantitative measurements of nanomechanical properties allowed to unlock scientifical barriers in that particular field.

Blends Immiscible polymer blends are typical multiphased systems. Often, their bulk properties do not follow a simple rule of mixtures, described by the equation 1.1, Y being a macroscopical intensive property of a multiphased blend, Y_i the corresponding property of the individual phase i and f_i its volume fraction.

$$Y = \sum_i f_i \cdot Y_i \tag{1.1}$$

There are several reasons why this rule is almost never followed in blends, particularly:

- This model does not take into account the fact that in a blend, a polymer—sometimes being confined to nanoscale domains—may not behave as it behaves in a bulk state at a macroscopic scale. In equation 1.1, Y_i should represent the property of the polymer as it is in the blend. Furthermore, the phases interact differently according to their relative distribution.

- The influence of the interfaces between phases is extremely important in some cases, especially when compatibilizers are used. Mechanisms such as stress transfer, influencing macroscale Young's modulus, do not occur well if there is a well–defined, poorly interacting interface. The opposite is true for a fuzzy interphase, where entanglement occurs between the polymers of the phases.

AFM nanomechanical measurements provide a response to both problems, by allowing to map local mechanical properties [115, 116, 117] and to measure gradients of properties at interfaces [118]. Wang and collaborators, for example, measured the effect of annealing on the interface between poly(vinyl chloride) (PVC) and poly(caprolactone) (PCL). As shown in Figure 1.29, the interphase becomes substantially thicker when the blend is annealed 50 min at 72°C, hinting molecular diffusion between the phases.

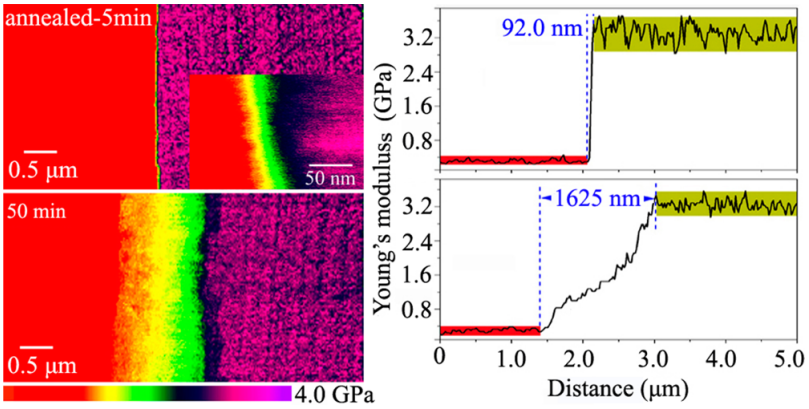

Figure 1.29 – AFM modulus maps of a PVC/PCL sample annealed at 72°C for 5 min (top) and 50 min (bottom) and corresponding modulus profiles across the interface. The annoted size of the transition between the modulus of each phase corresponds to an interdifusion zone [118].

The fact that several properties are measured simultaneously is very useful to investigate slightly different blends (with different volume fractions or different treatments for instance). Wu, Bhattacharya and Morgan used the simultaneous topography, DMT modulus and current mappings (with PeakForce TUNA mode) to quantify the effects of polyhedral oligomeric silsesquioxane (POSS) molecules of different structures and annealing in P3HT[8]/PCBM[9] photovoltaic blends [119]. This allowed the tuning of the structure of the blends to reach improvements in the power conversion efficiency of polymer solar cells at a laboratory scale.

Nanomechanical mappings are thus extremely useful in the study of phase-separated materials, as they allow to explore the interfaces, to measure separately the properties of different components and can help for the modelling of properties of complex systems [120]. One has to keep in mind that when too mechanically different materials are blended, the AFM probe may not be adapted for both [98]. Anyway compromises and strategies to obtain the desired informations can always be found to highlight links between the nanostructure and the properties of heterogeneous materials.

Composites and nanocomposites

As previously mentionned, AFM nanomechanical mappings are of particular interest for the study of heterogeneous materials, as they open the access to the nanoscale structure and local mechanical properties. In composites as in blends, the global behavior of a material is generally not the sum of the behaviors of the different components, weighted by their volume fraction. Therefore, the field of composite materials includes a growing number of AFM nanomechanical studies, leading to a better understanding of both parts: on one hand, the relation between structure and properties of composites, and on the other hand, how AFM should be used for an optimal accuracy and how nanomechanical properties can be interpreted.

The evolution of individual phases properties in composite fillers-matrix systems can thus be evaluated, depending on various factors such as the concentration of fillers [121, 122], their nature [123] or how they are integrated in the matrix (in the case, for example, of *in situ* growing

[8] poly(3-hexylthiophene-2,5-diyl)
[9] [6,6]-phenyl C_{61} butyric acid methyl ester

of zeolites [124]). It is generally remarked that each phase affects each others, sometimes in unexpected ways, such as POSS increasing the modulus of a stiff phosphate glass matrix by hindering its chains movements [125]. As already mentionned, AFM also gives important informations on the dispersion and nature of particles and phases, which can weight their contribution to the overall mechanical behavior [126]. This has been critical in the optimization of formulations and processes of complex materials, for instance for paper coatings containing starch, latex and clay [127]. Figure 1.30 shows the differences of nanoscale properties of such composites paper coatings according to the drying temperature.

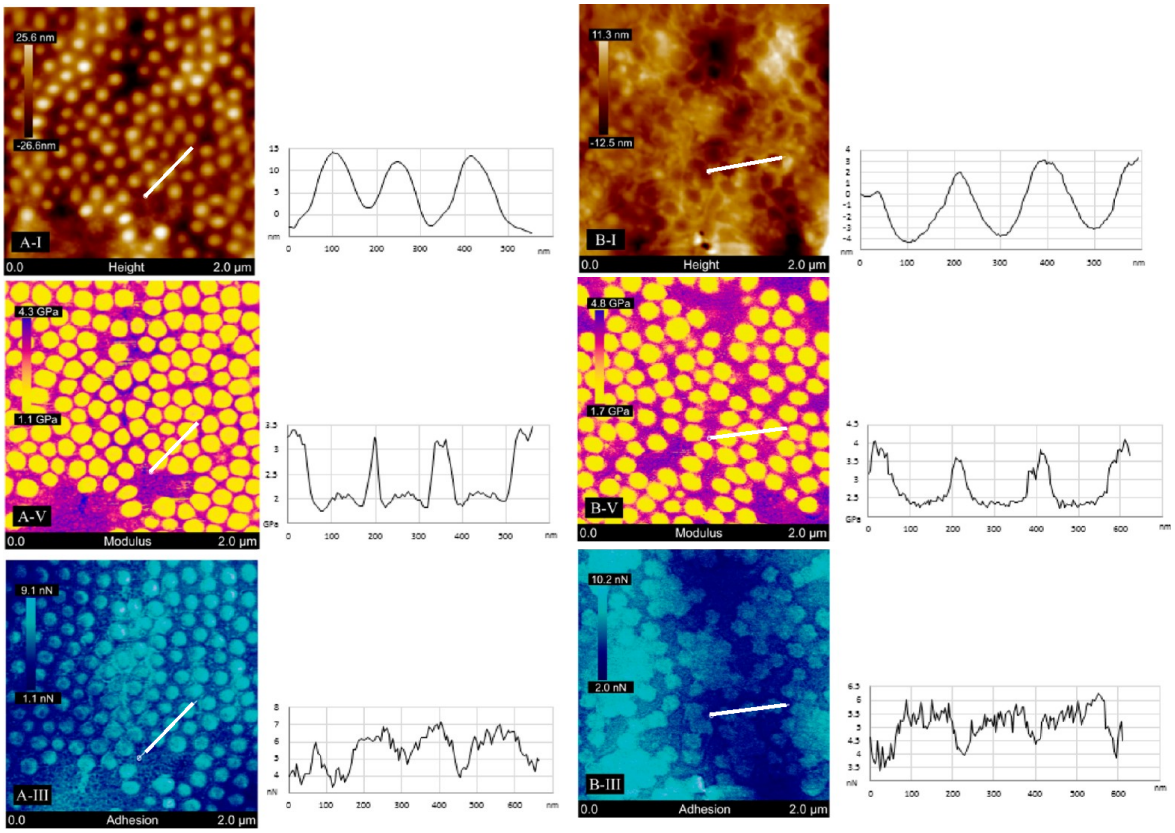

Figure 1.30 – AFM height (top), modulus (center) and adhesion (bottom) maps of a starch/latex paper coating, dried at room temperature (left) and at 105°C for 5 min (right). The softer and more adhesive latex spherical particles sink into the starch matrix when dried at a high temperature, forming pits in the topographical image (top left) while conserving their mechanical properties. The profiles are taken across the white lines [127].

Biocomposites The replacement of traditional oil-based polymers and composites by bio-sourced and/or biodegradable polymers, polymer blends and biocomposites is a current major challenge in material science. The emerging field of biocomposites is of particular interest, since the mechanical properties and processability of many simple biopolymers do not match those of their traditional equivalents. The potential of AFM nanomechanical measurements in the understanding of composites is currently helping the growth of the biocomposites field.

Cellulose is an abundant natural ressource, which is often used as a filler in biocomposites [128]. This complex polymer has been widely studied by AFM, particularly with PeakForce QNM mode [64, 101], thus this approach is relevant to study cellulose–based composites. One im-

mediate use is the evaluation of the structuration and mechanical properties of thin films such as acrylic/cellulose nanowhiskers (CNWs) composite films by Khelifa and collaborators [129]. The authors reported a modulus increase of the film by almost two orders of magnitude when adding 50%wt of CNWs to the acrylic matrix, reaching 11 GPa, which is higher than a pure CNWs film (*i.e.* 9 GPa). They could verify, also by AFM, that it is due to a specific organization of CNWs when blended with the matrix. For such 22 nm ultrathin films, there is hardly other methods to evaluate mechanical properties since the deformation has to be low enough to avoid an unwanted substrate contribution to the calculated modulus.

Furthermore, the mechanical behavior of thin films is sometimes better predicted by nanoscale measurements such as PeakForce QNM AFM mode. Cranston *et al.* measured the Young's Modulus of nanofibrillated cellulose/polyethyleneimine (PEI) multilayer thin films by a method using buckling mechanics[10], obtaining a value of 1.5 GPa [131]. From the Young's modulus of this material in a bulk state (*i.e.* 5.5 GPa), the DMT modulus of different components of the blend measured by PeakForce QNM (*i.e.* 0.85 GPa for cellulose, 0.3 GPa for PEI and an average of 0.8 GPa), they deduced that the mechanical behavior of the film is more similar to that of the nanoscale components than that of the bulk materials.

AFM nanomechanical mappings are particularly efficient at highlighting the crystalline structurations in semicrystalline polymer, as mentionned above. It is also a critical aspect of composite science in the case of a semicrystalline matrix, whose crystallinity and structuration can be affected by the fillers. The crystalline zones are generally evidenced by an increased local modulus [132]. It could be shown, for example, that cellulose nanofibers can increase the crystallinity acting as nucleating agents in polyamide 11 (PA11) nanocomposites, exhibiting a higher structural order than for neat PA11 [133].

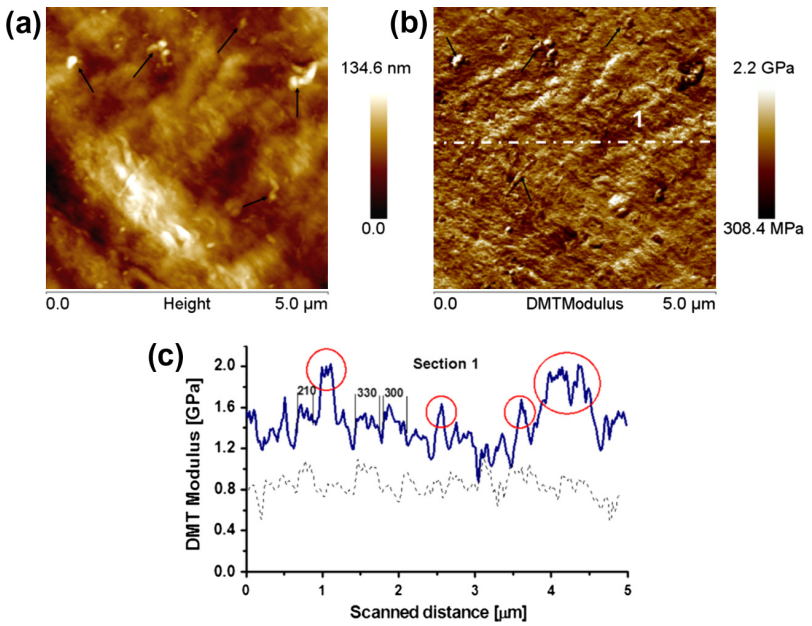

Figure 1.31 – AFM topographical (a) and DMT modulus (b) images of a PA11/cellulose nanofibers composite. (c) modulus profile taken across the white dashed line in (b), represented by the blue solid line. The red circles indicate modulus peaks, hinting the presence of cellulose nanofibers close to the surface. The gray dashed line represents an equivalent DMT modulus profile acquired on neat PA11 [133].

[10]Strain-induced elastic buckling instability for mechanical measurements (SIEBIMM) [130]

Common AFM effects and artifacts in nanomechanical mappings of composites: some authors, studying composites materials, highlighted some effects that are to take into account when mapping similar structures. When working on polyolefines–based composites, Panaitescu, Nicolae and collaborators often reported an overestimation of the expected modulus [134, 135]. This can be attributed to two main factors:

- As reported by Chyasnavichyus *et al.* on silicone hydrogels [100], the viscoelastic nature of polymers plays sometimes an important role. The high oscillation frequency of the tip (typically around 2 kHz) combined with a non–negligible indentation may imply a sollicitation that reflects the glassy state of a polymer, even if it is scanned at a temperature in which it is in its rubbery state.
- The tip radius can change (thus increase) if the tip is worn or contamined. This can happen during calibration and/or scanning. As seen in the next chapter, the tip radius has a direct influence on the calculated modulus. Generally, the nominal value given by the manufacturer is a minimum.

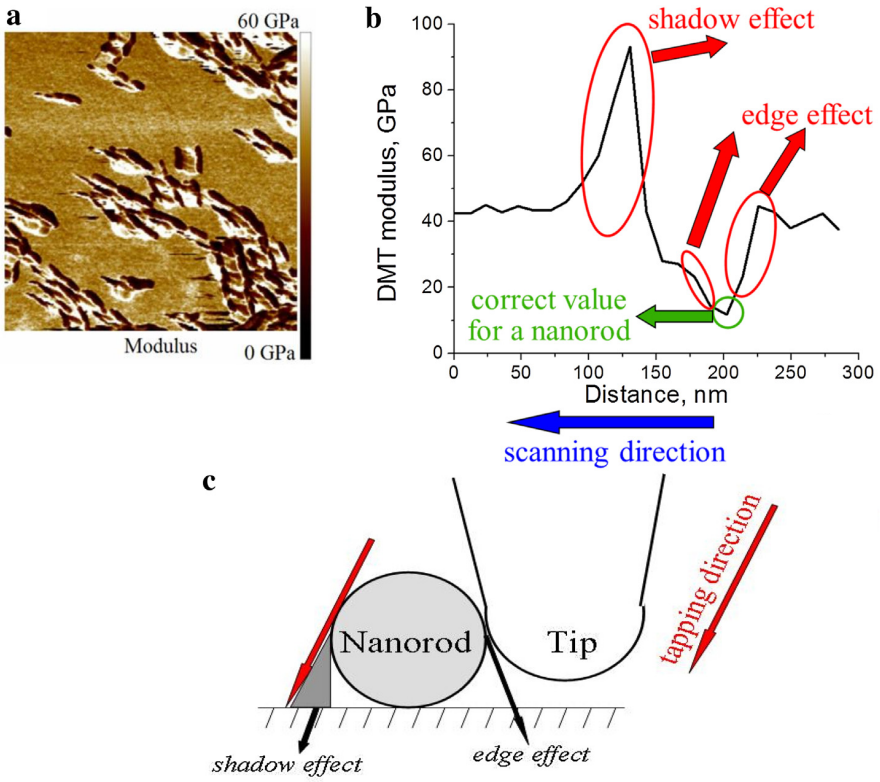

Figure 1.32 – (a) $3 \times 3\ \mu m^2$ DMT modulus images of chitin nanorods deposited on a silica substrate; (b) DMT modulus profile across a nanorod; (c) scheme explaining the modulus variations associated with the edge and shadow effects [136].

Smolyakov *et al.* also observed various effects and artifacts when imaging PS films, chitin nanorods and chitin/silica hybrid nanocomposites [136]:

Edge effect: On chitin nanorods deposited on a silica substrate, the authors observed that an accurate modulus can only be reached in the center of a nanorod, where its tangential surface is relatively perpendicular to the tip movement. This is mainly due to the importance

of the stability of the tip-sample contact area to apply correctly the DMT contact model, discussed in the next chapter. An illustration of this effect is shown in Figure 1.32.

Skin effect: Already documented by Dokukin and Sokolov [35, 137], it was shown that for very low applied force compared to the stiffness of the material, an increase of the modulus is observed, as illustrated in Figure 1.33. It is commonly attributed to a high stress, leading to a non–linear stress-strain regime. One must thus adjust the applied force to reach enough deformation, but taking care of the viscoelastic contribution of polymers in their rubbery state.

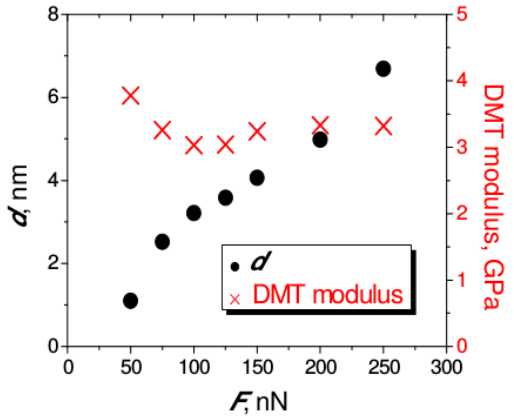

Figure 1.33 – Deformation and modulus versus peak force on a polystyrene film, illustrating the *skin effect* for low applied forces [136].

Shadow effect: On surfaces being almost parallel to the tip movement, the force transferred to the sample is lower than the force setpoint applied by the AFM, leading to an overestimation of the modulus. An illustration for this effect is shown in Figure 1.32. The geometric edge and shadow effects also affect the adhesion and dissipation energy mappings, and are sometimes referred as "topographical effects".

Substrate effect: On thin films or objects, which are often deposited on hard substrates such as silica or glass, high applied forces lead to deformations that are not negligible compared to the object size or film thickness, and to a contribution of the substrate in the measured modulus (generally leading to an overestimation). This effect is depicted in Figure 1.34: on small individual chitin nanorods, when the applied force induces a deformation of 2 nm and more, the DMT modulus begins to increase because of a contribution from the hard substrate.

Those effects and artifacts are to take into account when adjusting the imaging parameters (for force–dependent effects), or when analysing results for geometric artifacts. The knowledge of such effect is a crucial point to reach robust methods for the imaging and result analysis using AFM PeakForce QNM mode and equivalents.

Interfaces As mentionned above, interfaces are critical in the understanding of the structure-properties relationships in composites and nanocomposites. Poor interfaces between fillers and matrix are to be avoided in the design of a composite, and nanomechanical mappings by AFM are efficient at evaluating it. For instance, a local modulus drop in the matrix around the fillers

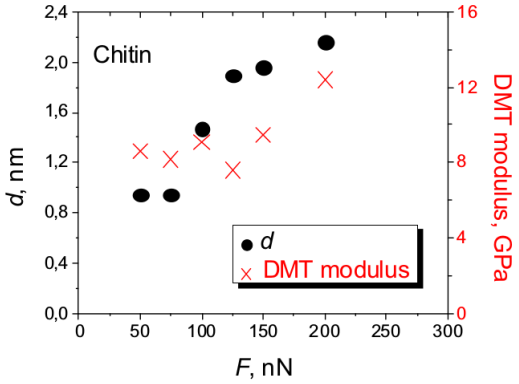

Figure 1.34 – Deformation and modulus versus peak force on isolated chitin nanorods on a silica substrate, illustrating the *substrate effect* for high applied forces [136].

can underline a poor interface, as pointed out by Panaitescu *et al.* in polyethylene/nanosilica composites [138]. The use of relatively small quantities of polyethylene grafted with maleic anhydride (PE-MA) resolved the modulus drop, thus improving the interfacial interaction leading to better overall macroscopical mechanical properties. The authors could also, with PeakForce QNM mappings, point out the different crystallization behaviors of the polyethylene, depending on the composition of the blend or composite: the size of the spherolites in neat PE decreased with PE-MA (See Figure 1.35a and b), while the viscosity induced by the nanosilica particles hindered their formation, leading to a lamellar structure (Figure 1.35c and d).

The gradient of properties, as mentionned for polymer blends [118], is also a relevant parameter in the study of composites interfaces. A thick modulus gradient from one phase to another (*i.e.* a filler) is generally interpreted as a cohesive interphase, as in polyether ether ketone (PEEK)/carbon fibers composites studied by Niu *et al.* [139]. A shrinkage of that interface was reported after ultraviolet and hydrothermal aging, which was interpreted as weakened interactions between matrix and fillers, caused by crosslinking reactions in the polymer. Pakzad *et al.* showed that the gradient of properties (*i.e.* DMT modulus and adhesion) at an interface also depends on the size of the filler in the case of poly(vinyl alcohol) (PVA)/poly(acrylic acid) PAA)/cellulose nanocrystals composites [140]. As shown in Figure 1.36, bigger particles seem to induce a thicker interphase. They also pointed out that the presence of poly(acrylic acid) induced a thinner interphase, and an increased adhesion gradient after heating (thus formation of ester links between the two polymers), because of a lower density of hydrogen bonds between the polymers and the nanocrystals.

Xavier and Bose used AFM nanomechanical mappings to visualize the spatial distribution of chain-end grafted multiwall carbon nanotubes (MWNT) in a polymeric blend [141], not directly imaging the nanotubes but using the fact that the zones where they are in high concentration are stiffer, exhibiting a higher local modulus. Different chain lengths of polystyrene (PS) grafted on the nanotubes implied their different distributions around the interfaces between the PS and the poly(vinyl methyl ether) (PVME), as schematized in Figure 1.37. While high molecular mass PS grafted on MWNTs led to their incorporation in the PS phase, the preferential presence of MWNTs grafted with lower molecular mass PS outside of the PS phase was interpreted as an entropic repulsion, their radius of gyration being too low for this phase, despite having the same chemical nature.

The quantitative mapping of mechanical properties at the interfaces in composites is a unique capability of AFM, allowing to get a better understanding of many promising materials. Since the

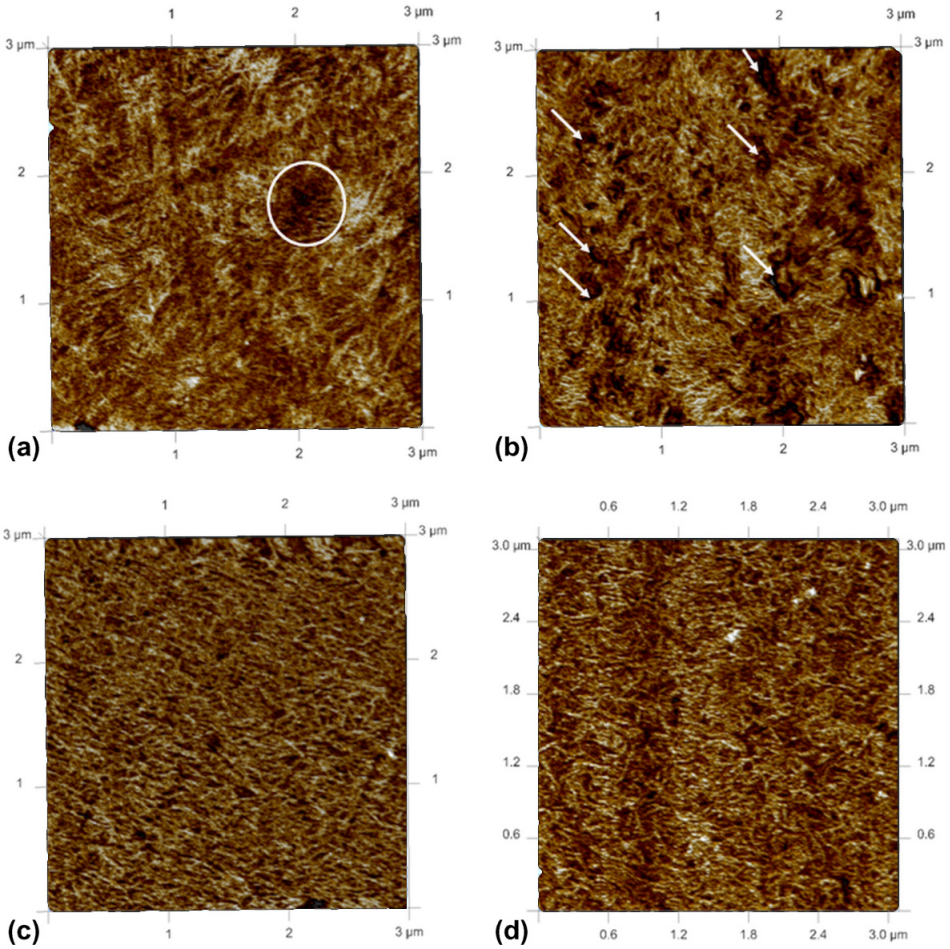

Figure 1.35 – $3 \times 3\ \mu m^2$ DMT modulus images of (a) neat PE; (b) PE-MA; (c) PE with nanosilica (5wt%); (d) PE with PE-MA (5wt%) and nanosilica (5wt%). Circles and arrows mark low-modulus zones. The modulus scale is not given, but moduli are typically in the 200–300 MPa range [138].

first profiles across fiber-matrix interfaces using AFM nanoindentation by Mäder and Gao [24], the mapping of the local modulus and of additional properties such as tip-sample adhesion force and energy dissipation allowed a more complete and more accurate understanding of the role of interfaces and interphases in composite materials.

AFM nanomechanical mappings offer thus an optimal way to evaluate the underlying mechanisms occuring at a local scale in materials such as nanocomposites. Few years of use by scientists highlighted the intrinsic difficulties of the technique, and developed robust methods to avoid them. The measurement of local properties implies the *in situ* scanning of interfaces, which are not easily accessible by traditional characterization methods, but are critical in the understanding of the overall mechanical behavior of polymer blends and composites.

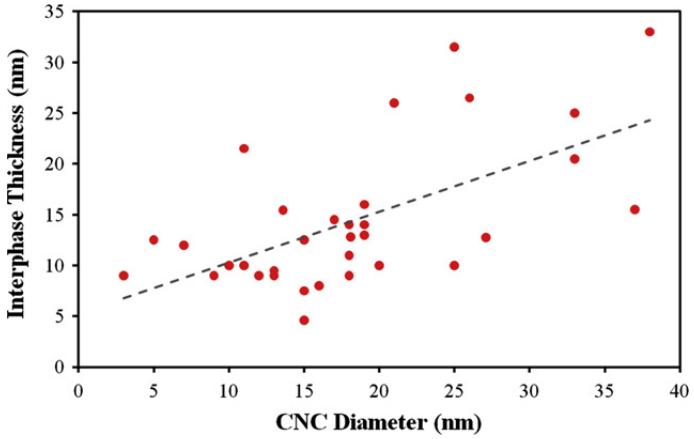

Figure 1.36 – Variation of interphase thickness with the diameter of cellulose nanocrystals in PVA/PAA/cellulose nanocomposites. Red circles show average interphase thickness of individual nanocrystals. The trend line (dashed gray line) shows an increasing trend in the interphase thickness with the nanocrystal diameter. [140].

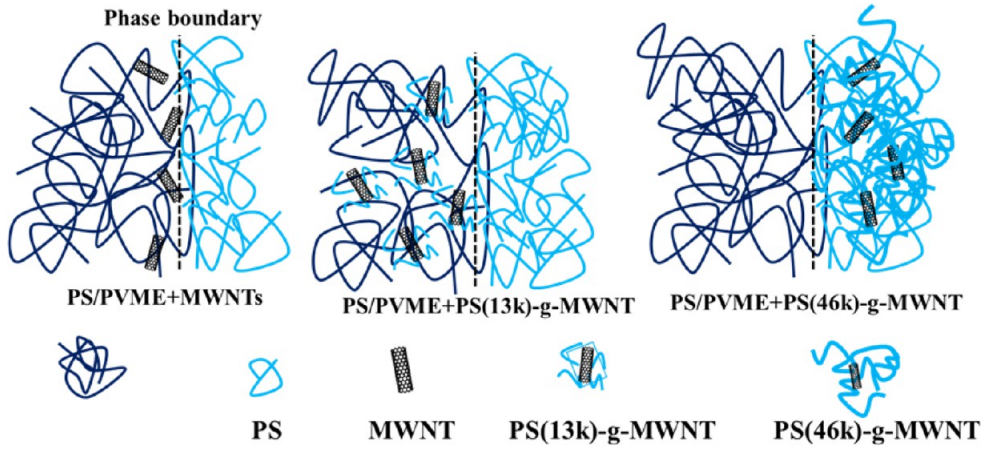

Figure 1.37 – Synthesis of different distributions of MWNTs across a PS—PVME interface depending on wether they are grafted or not, with different PS chain lengths [141].

1.4 Conclusion

The versatility of atomic force microscopy has been leading to the ability to measure local properties of materials at the nanoscale. In particular, novel techniques based on the acquisition of force curves allow now to map mechanical properties such as local elasticity modulus, tip-sample adhesion force or energy dissipation. Although being related to their macroscopic equivalents, these properties do not reflect the macroscopical behavior of bulk materials but local phenomena that participate in it.

The properties mappings have been extensively used to visualize the sub-micrometer structure of many kinds of materials, from cells and proteines to nanocomposites. The use of elasticity, adhesion, dissipation and/or deformation as contrasting informations in AFM images helps to understand how such materials are organized. Nevertheless, beyond simple contrasting, the data measured by AFM nanomechanical mappings are quantitative and reproducible if an appropriate calibration is performed, opening a novel way to study relations between structure and properties,

which is a major purpose of material science.

Quantitative scanning of local mechanical properties allowed advances in fields such as biopolymers or drug delivery systems in medicine. However, some authors have been documenting difficulties associated with quantitative nanomechanical measurements by AFM. Although they often give solutions to bypass them, the AFM operation and data analysis in nanomechanics are not subjected to strong consensus among researchers.

These observations have motivated this work, which aims to propose clear and reproducible methods, applied to novel polymer–based systems, to reach a better understanding of the links between the structure and properties of materials.

Bibliography

[1] G. Binnig, C. F. Quate, and C. Gerber. Atomic force microscope. *Physical Review Letters*, 56:930–933, March 1986.

[2] John E Sader, Julian A Sanelli, Brian D Adamson, Jason P Monty, Xingzhan Wei, Simon A Crawford, James R Friend, Ivan Marusic, Paul Mulvaney, and Evan J Bieske. Spring constant calibration of atomic force microscope cantilevers of arbitrary shape. *Review of Scientific Instruments*, 83(10):103705, 2012.

[3] M Radmacher, RW Tillmann, M Fritz, and HE Gaub. From molecules to cells: imaging soft samples with the atomic force microscope. *Science*, 257(5078):1900–1906, 1992.

[4] Q Zhong, D Inniss, K Kjoller, and VB Elings. Fractured polymer/silica fiber surface studied by tapping mode atomic force microscopy. *Surface Science Letters*, 290(1):L688–L692, 1993.

[5] Bruker Corporation. *MultiMode V8 Instruction Manual*, 2011.

[6] Geoffrey KH Pang, KZ Baba-Kishi, and A Patel. Topographic and phase-contrast imaging in atomic force microscopy. *Ultramicroscopy*, 81(2):35–40, 2000.

[7] S. N. Magonov and M. G. Heaton. Atomic force microscopy, part 6: Recent developments in afm for polymers. *American Laboratory*, 30(10), 1998.

[8] T. Kajiyama, K. Tanaka, S.-R. Ge, and A. Takahara. Morphology and mechanical properties of polymer surfaces via scanning force microscopy. *Progress in Surface Science*, 52(1):1 – 52, 1996.

[9] Dong Wang, Yanhui Liu, Toshio Nishi, and Ken Nakajima. Length scale of mechanical heterogeneity in a glassy polymer determined by atomic force microscopy. *Applied Physics Letters*, 100(25):251905, 2012.

[10] Yi-Hsien Lu, Chih-Wen Yang, and Ing-Shouh Hwang. Molecular layer of gaslike domains at a hydrophobic–water interface observed by frequency-modulation atomic force microscopy. *Langmuir*, 28(35):12691–12695, 2012.

[11] P Maivald, HJ Butt, SAC Gould, CB Prater, B Drake, JA Gurley, VB Elings, and PK Hansma. Using force modulation to image surface elasticities with the atomic force microscope. *Nanotechnology*, 2(2):103, 1991.

[12] S. N. Magonov and D. H. Reneker. Characterization of polymer surfaces with atomic force microscopy. *Annual Review of Materials Science*, 27(1):175–222, 1997.

[13] M. Radmacher, R. W. Tillmann, and H. E. Gaub. Imaging viscoelasticity by force modulation with the atomic force microscope. *Biophysical Journal*, 64(3):735–42, 1993.

[14] K. L. Johnson, K. Kendall, and A. D. Roberts. Surface energy and the contact of elastic solids. *Proceedings of the Royal Society of London A: Mathematical, Physical and Engineering Sciences*, 324(1558):301–313, 1971.

[15] P.-E. Mazeran. *Microscope a force atomique et imagerie mecanique.* PhD thesis, Ecole Centrale de Lyon, 1998.

[16] M. R. Vanlandingham, S. H. McKnight, G. R. Palmese, J. R. Elings, X. Huang, T. A. Bogetti, R. F. Eduljee, and J. W. Gillespie Jr. Nanoscale indentation of polymer systems using the atomic force microscope. *The Journal of Adhesion*, 64(1-4):31–59, 1997.

[17] M. R. Vanlandingham, S. H. McKnight, G. R. Palmese, R. F. Eduljee, J. W. Gillespie, and JR. R. L. McCulough. Relating elastic modulus to indentation response using atomic force microscopy. *Journal of Materials Science Letters*, 16(2):117–119, 1997.

[18] Paramita Mondal, Surendra P Shah, and Laurence Marks. A reliable technique to determine the local mechanical properties at the nanoscale for cementitious materials. *Cement and Concrete Research*, 37(10):1440–1444, 2007.

[19] C Reynaud, F Sommer, C Quet, N El Bounia, and Tran Minh Duc. Quantitative determination of young's modulus on a biphase polymer system using atomic force microscopy. *Surface and interface analysis*, 30(1):185–189, 2000.

[20] Charles A Clifford and Martin P Seah. Quantification issues in the identification of nanoscale regions of homopolymers using modulus measurement via afm nanoindentation. *Applied surface science*, 252(5):1915–1933, 2005.

[21] Igor Zlotnikov, Emil Zolotoyabko, and Peter Fratzl. Nano-scale modulus mapping of biological composite materials: Theory and practice. *Progress in Materials Science*, 2017.

[22] Binyang Du, Ophelia K. C. Tsui, Qingling Zhang, and Tianbai He. Study of elastic modulus and yield strength of polymer thin films using atomic force microscopy. *Langmuir*, 17(11):3286–3291, 2001.

[23] A. Opdahl and G. A. Somorjai. Stretched polymer surfaces: Atomic force microscopy measurement of the surface deformation and surface elastic properties of stretched polyethylene. *Journal of Polymer Science Part B: Polymer Physics*, 39(19):2263–2274, 2001.

[24] E. Mäder and S. L. Gao. Prospect of nanoscale interphase evaluation to predict composite properties. *Journal of Adhesion Science and Technology*, 15(9):1015–1037, 2001.

[25] E. Mäder and S. L. Gao. Characterisation of interphase nanoscale property variations in glass fibre reinforced polypropylene and epoxy resin composites. *Composites Part A: Applied Science and Manufacturing*, 33(4):559 – 576, 2002.

[26] Yang Chen, Cheng Qian, and Naiming Miao. Atomic force microscopy indentation to determine mechanical property for polystyrene–silica core–shell hybrid particles with controlled shell thickness. *Thin Solid Films*, 579:57–63, 2015.

[27] Ming Qiu Zhang, Min Zhi Rong, Han Min Zeng, Stefan Schmitt, Bernd Wetzel, and Klaus Friedrich. Atomic force microscopy study on structure and properties of irradiation grafted silica particles in polypropylene-based nanocomposites. *Journal of applied polymer science*, 80(12):2218–2227, 2001.

[28] Delphine Sicard, Laura E Fredenburgh, and Daniel J Tschumperlin. Measured pulmonary arterial tissue stiffness is highly sensitive to afm indenter dimensions. *Journal of the Mechanical Behavior of Biomedical Materials*, 2017.

[29] Manfred Radmacher, Monika Fritz, Claudia M Kacher, Jason P Cleveland, and Paul K Hansma. Measuring the viscoelastic properties of human platelets with the atomic force microscope. *Biophysical journal*, 70(1):556–567, 1996.

[30] William F Heinz and Jan H Hoh. Spatially resolved force spectroscopy of biological surfaces using the atomic force microscope. *Trends in biotechnology*, 17(4):143–150, 1999.

[31] Takahiro Nitta, Hisashi Haga, Kazushige Kawabata, Kazuhiro Abe, and Takashi Sambongi. Comparing microscopic with macroscopic elastic properties of polymer gel. *Ultramicroscopy*, 82(1):223–226, 2000.

[32] Jan Domke and Manfred Radmacher. Measuring the elastic properties of thin polymer films with the atomic force microscope. *Langmuir*, 14(12):3320–3325, 1998.

[33] Ozgur Sahin, Calvin F Quate, Olav Solgaard, and Abdullah Atalar. Resonant harmonic response in tapping-mode atomic force microscopy. *Physical Review B*, 69(16):165416, 2004.

[34] Etienne Dague, Doan Thanh Lam Le, Sandrine Zanna, Philippe Marcus, Pascal Loubière, and Muriel Mercier-Bonin. Probing in vitro interactions between lactococcus lactis and mucins using afm. *Langmuir*, 26(13):11010–11017, 2010.

[35] Maxim E Dokukin and Igor Sokolov. Quantitative mapping of the elastic modulus of soft materials with harmonix and peakforce qnm afm modes. *Langmuir*, 28(46):16060–16071, 2012.

[36] Peter Schön, Kristóf Bagdi, Kinga Molnár, Patrick Markus, Béla Pukánszky, and G Julius Vancso. Quantitative mapping of elastic moduli at the nanoscale in phase separated polyurethanes by afm. *European Polymer Journal*, 47(4):692–698, 2011.

[37] S Banerjee, N Gayathri, S Dash, AK Tyagi, and Baldev Raj. A comparative study of contact resonance imaging using atomic force microscopy. *Applied Physics Letters*, 86(21):211913, 2005.

[38] Kazushi Yamanaka, Hisato Ogiso, and Oleg Kolosov. Ultrasonic force microscopy for nanometer resolution subsurface imaging. *Applied Physics Letters*, 64(2):178–180, 1994.

[39] U Rabe and W Arnold. Acoustic microscopy by atomic force microscopy. *Applied Physics Letters*, 64(12):1493–1495, 1994.

[40] Jason P Killgore and Donna C Hurley. Pulsed contact resonance for atomic force microscopy nanomechanical measurements. *Applied Physics Letters*, 100(5):053104, 2012.

[41] E Rezaei and JA Turner. Contact resonance afm to quantify the in-plane and out-of-plane loss tangents of polymers simultaneously. *Applied Physics Letters*, 110(10):101902, 2017.

[42] Dalia G Yablon, Anil Gannepalli, Roger Proksch, Jason Killgore, Donna C Hurley, Jean Grabowski, and Andy H Tsou. Quantitative viscoelastic mapping of polyolefin blends with contact resonance atomic force microscopy. *Macromolecules*, 45(10):4363–4370, 2012.

[43] Bruker Corporation. *PeakForce QNM User Guide (Revision E)*, 2011.

[44] Carlos J Gómez and Ricardo Garcia. Determination and simulation of nanoscale energy dissipation processes in amplitude modulation afm. *Ultramicroscopy*, 110(6):626–633, 2010.

[45] B. Pittenger, N. Erina, and C. Su. *Application Note AN128*. Bruker Corporation, 2012. `www.bruker-nano.com`.

[46] Pavel Trtik, Josef Kaufmann, and Udo Volz. On the use of peak-force tapping atomic force microscopy for quantification of the local elastic modulus in hardened cement paste. *Cement and concrete research*, 42(1):215–221, 2012.

[47] Justyna Ciejka, Karol Wolski, Maria Nowakowska, Krzysztof Pyrc, and Krzysztof Szczubiałka. Biopolymeric nano/microspheres for selective and reversible adsorption of coronaviruses. *Materials Science and Engineering: C*, 76:735–742, 2017.

[48] Jiří Škvarla and Juraj Škvarla. An identification of the soft polyelectrolyte gel-like layer on silica colloids using atomic force and electron microscopy. *Ultramicroscopy*, 181:97–106, 2017.

[49] Giovanni M Kelly and Julie NL Albert. Ultrathin film crystallization of poly (ε-caprolactone) in blends containing styrene-isoprene block copolymers: The nano-rose morphology. *Polymer*, 117:295–305, 2017.

[50] Silke Heinen, José Luis Cuéllar-Camacho, and Marie Weinhart. Thermoresponsive poly (glycidyl ether) brushes on gold: Surface engineering parameters and their implication for cell sheet fabrication. *Acta Biomaterialia*, 2017.

[51] Vladimir V Korolkov, Stephanie Allen, Clive J Roberts, and Saul JB Tendler. Green chemistry approach to surface decoration: trimesic acid self-assembly on hopg. *The Journal of Physical Chemistry C*, 116(21):11519–11525, 2012.

[52] Ramona Marina Grigorescu, Florin Ciuprina, Paul Ghioca, Marius Ghiurea, Lorena Iancu, Bogdan Spurcaciu, and Denis Mihaela Panaitescu. Mechanical and dielectric properties of sebs modified by graphite inclusion and composite interface. *Journal of Physics and Chemistry of Solids*, 89:97–106, 2016.

[53] Georgio Kfoury, Jean-Marie Raquez, Fatima Hassouna, Philippe Leclère, Valérie Toniazzo, David Ruch, and Philippe Dubois. Toughening of poly (lactide) using polyethylene glycol methyl ether acrylate: Reactive versus physical blending. *Polymer Engineering & Science*, 55(6):1408–1419, 2015.

[54] Adriana N Frone, Sophie Berlioz, Jean-François Chailan, and Denis M Panaitescu. Morphology and thermal properties of pla–cellulose nanofibers composites. *Carbohydrate Polymers*, 91(1):377–384, 2013.

[55] Jun Zhou, Yingye Jiang, Gaoqing Wu, Weijian Wu, Yang Wang, Kai Wu, and Yonghong Cheng. Investigation of dielectric and thermal conductive properties of epoxy resins modified by core-shell structured ps@ sio 2. *Composites Part A: Applied Science and Manufacturing*, 97:76–82, 2017.

[56] Jing Huang, Jun Wang, Yaxin Qiu, and Defeng Wu. Mechanical properties of thermoplastic polyester elastomer controlled by blending with poly (butylene terephthalate). *Polymer Testing*, 55:152–159, 2016.

[57] Yury Yuryev, Amar K Mohanty, and Manjusri Misra. Hydrolytic stability of polycarbonate/poly (lactic acid) blends and its evaluation via poly (lactic) acid median melting point depression. *Polymer Degradation and Stability*, 134:227–236, 2016.

[58] Qingyang Li, Hao Lu, Juan Cui, Vikas Kumar, Maozhong An, and DY Li. Produce mirror-shining surface of electrogalvanized steel with significantly elevated scratch resistance through combined nanoelectrodeposition and passivation treatment. *Wear*, 376:1707–1712, 2017.

[59] Rebecca L Agapov, James Robbins, Richard Thomas, Dave L Hardman, and Mark D Foster. The effect of fluorosurfactant, copolymer latex, and cross-linker on the surface properties of floor polishes: An investigation using afm with adhesion mapping. *Progress in Organic Coatings*, 76(9):1279–1287, 2013.

[60] Kyle D Anderson, Seth L Young, Hao Jiang, Rachel Jakubiak, Timothy J Bunning, Rajesh R Naik, and Vladimir V Tsukruk. Plasma-enhanced copolymerization of amino acid and synthetic monomers. *Langmuir*, 28(3):1833–1845, 2012.

[61] Jérémy Odent, Philippe Leclère, Jean-Marie Raquez, and Philippe Dubois. Toughening of polylactide by tailoring phase-morphology with p [cl-co-la] random copolyesters as biodegradable impact modifiers. *European Polymer Journal*, 49(4):914–922, 2013.

[62] Jérémy Odent, Jean-Marie Raquez, Philippe Leclère, Franck Lauro, and Philippe Dubois. Crystallization-induced toughness of rubber-modified polylactide: combined effects of biodegradable impact modifier and effective nucleating agent. *Polymers for Advanced Technologies*, 26(7):814–822, 2015.

[63] Farid Khelifa, Marie-Eve Druart, Youssef Habibi, Freddy Bénard, Philippe Leclère, Marjorie Olivier, and Philippe Dubois. Sol–gel incorporation of silica nanofillers for tuning the anti-corrosion protection of acrylate-based coatings. *Progress in Organic Coatings*, 76(5):900–911, 2013.

[64] Denis Mihaela Panaitescu, Adriana Nicoleta Frone, Ioana Chiulan, Angela Casarica, Cristian Andi Nicolae, Marius Ghiurea, Roxana Trusca, and Celina Maria Damian. Structural and morphological characterization of bacterial cellulose nano-reinforcements prepared by mechanical route. *Materials & Design*, 110:790–801, 2016.

[65] Ikjun Choi, Dhaval D Kulkarni, Weinan Xu, Constantinos Tsitsilianis, and Vladimir V Tsukruk. Star polymer unimicelles on graphene oxide flakes. *Langmuir*, 29(31):9761–9769, 2013.

[66] Maria P Sokolova, Michael A Smirnov, Alexander N Bugrov, Pavel Geydt, Elena N Popova, Erkki Lahderanta, Valentin M Svetlichnyi, and Alexander M Toikka. Structure of composite based on polyheteroarylene matrix and zro2 nanostars investigated by quantitative nanomechanical mapping. *Polymers*, 9(7):268, 2017.

[67] Jen-You Chu, Wei-Sheng Hsu, Wei-Ren Liu, Hung-Min Lin, Hsin-Ming Cheng, and Li-Jiaun Lin. A novel inspection for deformation phenomenon of reduced-graphene oxide via quantitative nano-mechanical atomic force microscopy. *Procedia Engineering*, 36:571–577, 2012.

[68] CR Woods, F Withers, MJ Zhu, Y Cao, G Yu, A Kozikov, M Ben Shalom, SV Morozov, MM Van Wijk, A Fasolino, et al. Macroscopic self-reorientation of interacting two-dimensional crystals. *Nature communications*, 7, 2016.

[69] Laura Picas, Pierre-Emmanuel Milhiet, and Jordi Hernández-Borrell. Atomic force microscopy: A versatile tool to probe the physical and chemical properties of supported membranes at the nanoscale. *Chemistry and physics of lipids*, 165(8):845–860, 2012.

[70] Renate Hiesgen, Stefan Helmly, Ines Galm, Tobias Morawietz, Michael Handl, and K Andreas Friedrich. Microscopic analysis of current and mechanical properties of nafion® studied by atomic force microscopy. *Membranes*, 2(4):783–803, 2012.

[71] Winny Fam, Jaleh Mansouri, Hongyu Li, and Vicki Chen. Improving co 2 separation performance of thin film composite hollow fiber with pebax® 1657/ionic liquid gel membranes. *Journal of Membrane Science*, 537:54–68, 2017.

[72] C Daniel Frisbie, Lawrence F Rozsnyai, Aleksandr Noy, Mark S Wrighton, and Charles M Lieber. Functional group imaging by chemical force microscopy. *Science*, pages 2071–2074, 1994.

[73] David Alsteens, Vincent Dupres, Sami Yunus, Jean-Paul Latgé, Jürgen J. Heinisch, and Yves F. Dufrêne. High-resolution imaging of chemical and biological sites on living cells using peak force tapping atomic force microscopy. *Langmuir*, 28(49):16738–16744, 2012.

[74] Jérôme Colson, Laurin Andorfer, Tiina Elina Nypelö, Bernd Lütkemeier, Frank Stöckel, and Johannes Konnerth. Comparison of silicon and oh-modified afm tips for adhesion force analysis on functionalised surfaces and natural polymers. *Colloids and Surfaces A: Physicochemical and Engineering Aspects*, 2017.

[75] Cecile Lara, Simon Gourdin-Bertin, Jozef Adamcik, Sreenath Bolisetty, and Raffaele Mezzenga. Self-assembly of ovalbumin into amyloid and non-amyloid fibrils. *Biomacromolecules*, 13(12):4213–4221, 2012.

[76] Guodong Yang, Lei Liu, Jie Wang, Christian Bortolini, and Mingdong Dong. Light-driven porphyrin modulating fibrillation of hiapp 20–29 peptide. *Journal of Colloid and Interface Science*, 495:37–43, 2017.

[77] Jozef Adamcik, Alexandre Berquand, and Raffaele Mezzenga. Single-step direct measurement of amyloid fibrils stiffness by peak force quantitative nanomechanical atomic force microscopy. *Applied Physics Letters*, 98(19):193701, 2011.

[78] Jozef Adamcik and Raffaele Mezzenga. Study of amyloid fibrils via atomic force microscopy. *Current opinion in colloid & interface science*, 17(6):369–376, 2012.

[79] Kim Sweers, Kees Van Der Werf, Martin Bennink, and Vinod Subramaniam. Nanomechanical properties of α-synuclein amyloid fibrils: a comparative study by nanoindentation, harmonic force microscopy, and peakforce qnm. *Nanoscale research letters*, 6(1):270, 2011.

[80] Agnieszka Voss, Christian Dietz, Annika Stocker, and Robert W Stark. Quantitative measurement of the mechanical properties of human antibodies with sub-10-nm resolution in a liquid environment. *Nano Research*, 8(6):1987, 2015.

[81] AL Lavanya Devi, Upendra Nongthomba, and MS Bobji. Quantitative characterization of adhesion and stiffness of corneal lens of drosophila melanogaster using atomic force microscopy. *journal of the mechanical behavior of biomedical materials*, 53:161–173, 2016.

[82] Samuel J Baldwin, Laurent Kreplak, and J Michael Lee. Characterization via atomic force microscopy of discrete plasticity in collagen fibrils from mechanically overloaded tendons: Nano-scale structural changes mimic rope failure. *Journal of the mechanical behavior of biomedical materials*, 60:356–366, 2016.

[83] Laura Picas, Felix Rico, Maxime Deforet, and Simon Scheuring. Structural and mechanical heterogeneity of the erythrocyte membrane reveals hallmarks of membrane stability. *ACS nano*, 7(2):1054–1063, 2013.

[84] Mario Encinar, Santiago Casado, Alicia Calzado-Martín, P Natale, Álvaro San Paulo, Montserrat Calleja, Marisela Vélez, Francisco Monroy, and Iván López-Montero. Nanomechanical properties of composite protein networks of erythroid membranes at lipid surfaces. *Colloids and Surfaces B: Biointerfaces*, 149:174–183, 2017.

[85] David Alsteens, Moritz Pfreundschuh, Cheng Zhang, Patrizia M Spoerri, Shaun R Coughlin, Brian K Kobilka, and Daniel J Müller. Imaging g protein-coupled receptors while quantifying their ligand-binding free-energy landscape. *Nature methods*, 12(9):845–851, 2015.

[86] Rubén Álvarez-Asencio, Viveca Wallqvist, Mikael Kjellin, Mark W Rutland, Alejandra Camacho, Niklas Nordgren, and Gustavo S Luengo. Nanomechanical properties of human skin and introduction of a novel hair indenter. *Journal of the mechanical behavior of biomedical materials*, 54:185–193, 2016.

[87] G Smolyakov, Cécile Formosa-Dague, C Severac, RE Duval, and E Dague. High speed indentation measures by fv, qi and qnm introduce a new understanding of bionanomechanical experiments. *Micron*, 85:8–14, 2016.

[88] Roman Böttger, Adrian Keller, Lothar Bischoff, and Stefan Facsko. Mapping the local elastic properties of nanostructured germanium surfaces: from nanoporous sponges to self-organized nanodots. *Nanotechnology*, 24(11):115702, 2013.

[89] Eric Detsi, Sergey Punzhin, Jiancun Rao, Patrick R Onck, and Jeff Th M De Hosson. Enhanced strain in functional nanoporous gold with a dual microscopic length scale structure. *Acs Nano*, 6(5):3734–3744, 2012.

[90] Anant Mathur and Jonah Erlebacher. Size dependence of effective young's modulus of nanoporous gold. *Applied physics letters*, 90(6):061910, 2007.

[91] Jessica Giro-Paloma, Camila Barreneche, Mònica Martínez, Boštjan Šumiga, Ana Inés Fernández, and Luisa F Cabeza. Mechanical response evaluation of microcapsules from different slurries. *Renewable Energy*, 85:732–739, 2016.

[92] Tal Stern, Inon Kaner, Neta Laser Zer, Hila Shoval, Dvir Dror, Zakhariya Manevitch, Liraz Chai, Yifat Brill-Karniely, and Ofra Benny. Rigidity of polymer micelles affects interactions with tumor cells. *Journal of Controlled Release*, 257:40–50, 2017.

[93] Magdalena Prokopowicz. Atomic force microscopy technique for the surface characterization of sol–gel derived multi-component silica nanocomposites. *Colloids and Surfaces A: Physicochemical and Engineering Aspects*, 504:350–357, 2016.

[94] Magdalena Prokopowicz. Characterization of low-dose doxorubicin-loaded silica-based nanocomposites. *Applied Surface Science*, pages –, 2017.

[95] Binyu Zhao, Yang Song, Shuo Wang, Bin Dai, Lijuan Zhang, Yaming Dong, Junhong Lu, and Jun Hu. Mechanical mapping of nanobubbles by peakforce atomic force microscopy. *Soft Matter*, 9:8837–8843, 2013.

[96] SV Ketov, HK Nguyen, AS Trifonov, K Nakajima, and DV Louzguine-Luzgin. Huge reduction of young's modulus near a shear band in metallic glass. *Journal of Alloys and Compounds*, 687:221–226, 2016.

[97] Michael E McConney, Srikanth Singamaneni, and Vladimir V Tsukruk. Probing soft matter with the atomic force microscopies: imaging and force spectroscopy. *Polymer Reviews*, 50(3):235–286, 2010.

[98] TJ Young, MA Monclus, TL Burnett, WR Broughton, SL Ogin, and PA Smith. The use of the PeakForce quantitative nanomechanical mapping afm-based method for high-resolution young's modulus measurement of polymers. *Measurement Science and Technology*, 22(12):125703, 2011.

[99] Xiaorong Gou, Meiling Zheng, Yuanyuan Zhao, Xianzi Dong, Feng Jin, Jinfeng Xing, and Xuanming Duan. Mechanical property of peg hydrogel and the 3d red blood cell microstructures fabricated by two-photon polymerization. *Applied Surface Science*, 416:273–280, 2017.

[100] Marius Chyasnavichyus, Seth L Young, and Vladimir V Tsukruk. Mapping micromechanical properties of soft polymer contact lenses. *Polymer*, 55(23):6091–6101, 2014.

[101] Lorenzo Teodonio, Mauro Missori, Dominika Pawcenis, Joanna Łojewska, and Francesco Valle. Nanoscale analysis of degradation processes of cellulose fibers. *Micron*, 91:75–81, 2016.

[102] Olivier Arnould, David Siniscalco, Alain Bourmaud, Antoine Le Duigou, and Christophe Baley. Better insight into the nano-mechanical properties of flax fibre cell walls. *Industrial Crops and Products*, 97:224–228, 2017.

[103] Grégory Mertz, Fatima Hassouna, Philippe Leclère, Abdesselam Dahoun, Valérie Toniazzo, and David Ruch. Correlation between (nano)-mechanical and chemical changes occurring during photo-oxidation of filled vulcanised styrene butadiene rubber (sbr). *Polymer degradation and stability*, 97(11):2195–2201, 2012.

[104] Aurélie Dupuis, François-Xavier Perrin, Amelia Ulloa Torres, Jean-Pierre Habas, Lénaik Belec, and Jean-François Chailan. Photo-oxidative degradation behavior of linseed oil based epoxy resin. *Polymer Degradation and Stability*, 135:73–84, 2017.

[105] Ilya A Morozov, Alexander S Mamaev, Irina V Osorgina, Larisa M Lemkina, Vladimir P Korobov, Anton Yu Belyaev, Svetlana E Porozova, and Marina G Sherban. Structural–mechanical and antibacterial properties of a soft elastic polyurethane surface after plasma immersion n 2+ implantation. *Materials Science and Engineering: C*, 62:242–248, 2016.

[106] Nobuyuki Otsu. A threshold selection method from gray-level histograms. *IEEE transactions on systems, man, and cybernetics*, 9(1):62–66, 1979.

[107] Adolfo del Campo, Aurora Nogales, Tiberio A Ezquerra, and Juan Rodriguez-Hernandez. Modification of poly (dimethylsiloxane) as a basis for surface wrinkle formation: Chemical and mechanical characterization. *Polymer*, 98:327–335, 2016.

[108] Satinder K Sharma, Satyendra Prakash Pal, Pulikanti Guruprasad Reddy, Pawan Kumar, Subrata Ghosh, and Kenneth E Gonsalves. Design and development of low activation energy based nonchemically amplified resists (n-cars) for next generation euv lithography. *Microelectronic Engineering*, 164:115–122, 2016.

[109] Mariusz Kłonica, Józef Kuczmaszewski, Michał P Kwiatkowski, and Janusz Ozonek. Polyamide 6 surface layer following ozone treatment. *International Journal of Adhesion and Adhesives*, 64:179–187, 2016.

[110] Shib Shankar Banerjee, Andreas Janke, Uwe Gohs, Andreas Fery, and Gert Heinrich. Some nanomechanical properties and degree of branching of electron beam modified polyamide 6. *European Polymer Journal*, 88:221–230, 2017.

[111] Zoran S Petrović, DooPyo Hong, Ivan Javni, Natalia Erina, Fan Zhang, and Jan Ilavskỳ. Phase structure in segmented polyurethanes having fatty acid-based soft segments. *Polymer*, 54(1):372–380, 2013.

[112] H Fischer, H Stadler, and N Erina. Quantitative temperature-depending mapping of mechanical properties of bitumen at the nanoscale using the afm operated with peakforce tappingtm mode. *Journal of microscopy*, 250(3):210–217, 2013.

[113] Åsa Laurell Lyne, Viveca Wallqvist, and Björn Birgisson. Adhesive surface characteristics of bitumen binders investigated by atomic force microscopy. *Fuel*, 113:248–256, 2013.

[114] Ming Wang and Liping Liu. Investigation of microscale aging behavior of asphalt binders using atomic force microscopy. *Construction and Building Materials*, 135:411–419, 2017.

[115] Balázs Imre, Dániel Bedő, Attila Domján, Peter Schön, G Julius Vancso, and Béla Pukánszky. Structure, properties and interfacial interactions in poly (lactic acid)/polyurethane blends prepared by reactive processing. *European polymer journal*, 49(10):3104–3113, 2013.

[116] Rodrigo Ortega-Toro, Amparo Muñoz, Pau Talens, and Amparo Chiralt. Improvement of properties of glycerol plasticized starch films by blending with a low ratio of polycaprolactone and/or polyethylene glycol. *Food Hydrocolloids*, 56:9–19, 2016.

[117] T Chinh Ngo, Radostina Kalinova, Damien Cossement, Elise Hennebert, Rosica Mincheva, Rony Snyders, Patrick Flammang, Philippe Dubois, Roberto Lazzaroni, and Philippe Leclère. Modification of the adhesive properties of silicone-based coatings by block copolymers. *Langmuir*, 30(1):358–368, 2013.

[118] Dong Wang, Thomas P Russell, Toshio Nishi, and Ken Nakajima. Atomic force microscopy nanomechanics visualizes molecular diffusion and microstructure at an interface. *ACS Macro Letters*, 2(8):757–760, 2013.

[119] Qi Wu, Mithun Bhattacharya, and Sarah E Morgan. Poss-enhanced phase separation in air-processed p3ht: Pcbm bulk heterojunction photovoltaic systems. *ACS applied materials & interfaces*, 5(13):6136–6146, 2013.

[120] Benjamin Megevand, Sébastien Pruvost, Luanda C Lins, Sébastien Livi, Jean-François Gérard, and Jannick Duchet-Rumeau. Probing nanomechanical properties with afm to understand the structure and behavior of polymer blends compatibilized with ionic liquids. *RSC Advances*, 6(98):96421–96430, 2016.

[121] Achmad Chafidz, Ilias Ali, ME Ali Mohsin, Rabeh Elleithy, and Saeed Al-Zahrani. Atomic force microscopy, thermal, viscoelastic and mechanical properties of hdpe/caco3 nanocomposites. *Journal of Polymer Research*, 19(4):9860, 2012.

[122] Shiqiang Song and Yong Zhang. Carbon nanotube/reduced graphene oxide hybrid for simultaneously enhancing the thermal conductivity and mechanical properties of styrene-butadiene rubber. *Carbon*, 2017.

[123] Emmanuel O Ogunsona, Manjusri Misra, and Amar K Mohanty. Impact of interfacial adhesion on the microstructure and property variations of biocarbons reinforced nylon 6 biocomposites. *Composites Part A: Applied Science and Manufacturing*, 98:32–44, 2017.

[124] Subhrakanti Chakraborty, Bo Wang, and Prabir K Dutta. Tolerance of polymer-zeolite composite membranes to mechanical strain. *Journal of Membrane Science*, 518:192–202, 2016.

[125] Kyoungtae Kim, Todd M Alam, Joseph D Lichtenhan, and Joshua U Otaigbe. Synthesis and characterization of novel phosphate glass matrix nanocomposites containing polyhedral oligomeric silsesquioxane with improved properties. *Journal of Non-Crystalline Solids*, 463:189–202, 2017.

[126] Z Derbali, A Fahs, J-F Chailan, IV Ferrari, ML Di Vona, and P Knauth. Composite anion exchange membranes with functionalized hydrophilic or hydrophobic titanium dioxide. *International Journal of Hydrogen Energy*, 2017.

[127] Majid Sababi, John Kettle, Hille Rautkoski, Per M Claesson, and Esben Thormann. Structural and nanomechanical properties of paperboard coatings studied by peak force tapping atomic force microscopy. *ACS applied materials & interfaces*, 4(10):5534–5541, 2012.

[128] Qiaolian Lv, Chunjiang Xu, Defeng Wu, Zhifeng Wang, Ruyue Lan, and Lisheng Wu. The role of nanocrystalline cellulose during crystallization of poly (ε-caprolactone) composites: Nucleation agent or not? *Composites Part A: Applied Science and Manufacturing*, 92:17–26, 2017.

[129] Farid Khelifa, Youssef Habibi, Philippe Leclère, and Philippe Dubois. Convection-assisted assembly of cellulose nanowhiskers embedded in an acrylic copolymer. *Nanoscale*, 5(3):1082–1090, 2013.

[130] Christopher M Stafford, Christopher Harrison, Kathryn L Beers, Alamgir Karim, Eric J Amis, Mark R VanLandingham, Kim Ho-Cheol, Willi Volksen, Robert D Miller, and Eva E Simonyi. A buckling-based metrology for measuring the elastic moduli of polymeric thin films. *Nature materials*, 3(8):545, 2004.

[131] Emily D Cranston, Mohamed Eita, Erik Johansson, Julia Netrval, Michaela Salajková, Hans Arwin, and Lars Wågberg. Determination of young's modulus for nanofibrillated cellulose multilayer thin films using buckling mechanics. *Biomacromolecules*, 12(4):961–969, 2011.

[132] Laura Lopez-Figueras, Nuria Navascues, and Silvia Irusta. Polycaprolactone/mesoporous silica mcm-41 composites prepared by in situ polymerization. *Particuology*, 30:135–143, 2017.

[133] Denis Mihaela Panaitescu, Adriana Nicoleta Frone, and Cristian Nicolae. Micro-and nano-mechanical characterization of polyamide 11 and its composites containing cellulose nanofibers. *European Polymer Journal*, 49(12):3857–3866, 2013.

[134] Denis Mihaela Panaitescu, Zina Vuluga, Constantin Radovici, and Cristian Nicolae. Morphological investigation of pp/nanosilica composites containing sebs. *Polymer Testing*, 31(2):355–365, 2012.

[135] Francois Xavier Perrin, Denis Mihaela Panaitescu, Adriana Nicoleta Frone, Constantin Radovici, and Cristian Nicolae. The influence of alkyl substituents of poss in polyethylene nanocomposites. *Polymer*, 54(9):2347–2354, 2013.

[136] Georgiy Smolyakov, Sébastien Pruvost, L Cardoso, B Alonso, E Belamie, and Jannick Duchet-Rumeau. Afm peakforce qnm mode: Evidencing nanometre-scale mechanical properties of chitin-silica hybrid nanocomposites. *Carbohydrate polymers*, 151:373–380, 2016.

[137] Maxim E Dokukin and Igor Sokolov. On the measurements of rigidity modulus of soft materials in nanoindentation experiments at small depth. *Macromolecules*, 45(10):4277–4288, 2012.

[138] Denis Mihaela Panaitescu, Adriana Nicoleta Frone, and Ilie Catalin Spataru. Effect of nanosilica on the morphology of polyethylene investigated by afm. *Composites Science and Technology*, 74:131–138, 2013.

[139] Yi-Fan Niu, Ying Yang, Sai Gao, and Jia-Wei Yao. Mechanical mapping of the interphase in carbon fiber reinforced poly (ether-ether-ketone) composites using peak force atomic force microscopy: Interphase shrinkage under coupled ultraviolet and hydro-thermal exposure. *Polymer Testing*, 55:257–260, 2016.

[140] Anahita Pakzad, John Simonsen, and Reza S Yassar. Gradient of nanomechanical properties in the interphase of cellulose nanocrystal composites. *Composites Science and Technology*, 72(2):314–319, 2012.

[141] Priti Xavier and Suryasarathi Bose. Nanomechanical mapping, hierarchical polymer dynamics, and miscibility in the presence of chain-end grafted nanoparticles. *Macromolecules*, 49(3):1036–1048, 2016.

Chapter 2

Performing mechanical measurements using AFM

Contents

2.1 Introduction

To quantify a property of a material at a given point means to associate it with an absolute value. It implies that if the measurement is made again with the same method and in the same conditions, the measured value should be the same within a reasonable uncertainity range. It is very challenging at nanoscale in the case of AFM nanomechanical mappings, because many parameters cannot be evaluated directly and the measurements are very sensitive to external conditions. To develop methods to reach a good reproductibility is thus of major interest, as it allows to give the measured data a meaning.

As seen in the previous chapter, AFM nanomechanical measurements are based on force curves, which are obtained by an indentation process, generally in the elastic regime of the characterized material. Measuring properties such as the local elasticity modulus requires to make some assumptions, particularly about the contact geometry (which, at nanoscale, cannot be exactly known) and about the general behavior of the material. Consequently, quantitative nanomechanical measurements depend on the use of different models based on contact mechanics.

To reach reproducible measurements also requires particular operation methods, performed with extreme care. As AFM is made to be able to characterize a broad range of different materials, the conditions have to be adapted to each one, especially for nanomechanical imaging.

Theoretical basis, especially contact mechanics and modeling, will be covered in the following sections. The different relevant theories and their respective application domains will be described. Then, the practical operation of the microscope will be treated. The main features of the Quantitative NanoMechanics^{TM} (QNM) mode and the required calibration steps prior to each session will be explained. Finally the theoretical and practical conditions to get quantitative measurements with AFM will be discussed.

2.2 Models for tip–sample contact

The elasticity modulus does not depend only on the data accessible with the AFM (force and position of the tip); The geometry of the tip–sample contact must also be known. According to Hooke's law in its general form,

$$E = \frac{\sigma}{\epsilon} \tag{2.1}$$

E representing a modulus, σ the stress, ε the strain. The stress, being a ratio of a force to a surface, depends on this geometry.

In order to apply this to a tip–sample geometry, some assumptions have to be made. The contact mechanics allowed the development of several theories that can be applied to different configurations, like the widely known Oliver and Pharr model for nanoindentation [1]. Many models can be applied to the measurement of local modulus by an AFM tip. The models differ mainly between themselves by how they take into account the adhesion forces and by the tip geometry considered [1]. They allow thus to describe several types of mechanical behaviors and therefore several types of materials. The main contact models used in AFM nanomechanics are described below.

2.2.1 Hertz theory

At the end of the nineteenth century, Hertz [2] was the first to describe the distribution of local stresses caused by the contact of two curved surfaces deforming each other in their elastic domain.

In order to model the contact point between the AFM tip and a sample surface, two spheres are thus considered, of respective radius R_1 and R_2 [2], Young's modulus E_1 and E_2, and Poisson's ratios ν_1 and ν_2. The reduced modulus E^* is the modulus equivalent to the system at the contact point. It is defined by equation 2.2:

$$\frac{1}{E^*} = \left(\frac{1-\nu_1^2}{E_1}\right) + \left(\frac{1-\nu_2^2}{E_2}\right) \tag{2.2}$$

In the same way, an equivalent radius R^* is defined (equation 2.3), without real physical meaning but useful to the definitions of the models. If R_1 tends towards infinity (*i.e.* to describe a flat sample surface), R^* tends towards R_2, which is then the tip's radius of curvature.

$$\frac{1}{R^*} = \frac{1}{R_1} + \frac{1}{R_2} = \frac{R_1 + R_2}{R_1 R_2} \tag{2.3}$$

The Hertz model is based on the following assumptions:

- The material is isotropic.
- All the deformations are in the elasticity domain of the material.
- The elasticity is linear.
- The normal force F_{normal}, pushing the solids 1 and 2 against each other, follows the same direction than the straight line defined by the centers of the two spheres.

[1] In the Hertz [2], DMT [3] and JKR [4] models, the extremity of the tip is considered to be spherical. In the Sneddon model [5], the tip is considered to be conical.

[2] One of the spheres, corresponding to the sample, can be considered then as a semi-space (hence a plane surface) by extending its radius towards infinity.

- There is no friction nor adhesion.

Then the contact surface can be defined. It is a disc whose area equals πa^2 where a is the contact radius. The model states:

$$a = \sqrt[3]{\frac{3}{4}\frac{F_{12} \cdot R^*}{E^*}} \tag{2.4}$$

The relation is valid only if $R_1 \gg a$ and $R_2 \gg a$.

If d is the penetration, defined by how much the centers of each spheres get closer from each other, starting from the point where they are just in contact. In the case of tip–sample contact in atomic force microscopy, this quantity represents the indentation.

$$d = \frac{a^2}{R^*} \tag{2.5}$$

Then relation 2.4 leads to:

$$F_{normal} = \frac{4}{3}E^*\sqrt{R^* d^3} \tag{2.6}$$

If the sphere 1 becomes the sample surface and the sphere 2 the extremity of the AFM tip, R^* tends towards R_2 which can be renamed R_{tip}, tip's radius of curvature. This data is evaluated during a calibration step (see section 2.3.2). The force and the indentation being known, E^* can be deduced from equation 2.6.

2.2.2 Derjaguin-Muller-Toporov (DMT) model

The Hertz model, however, does not take into account the adhesion forces. The works of Derjaguin, Muller and Toporov [3] established a model in which such attractive forces act *outside* the contact (which is repulsive). The contact remains hertzian and these adhesive forces are not able to deform the materials. The assumptions of the Hertz model are always applied, and viscoelasticity is neglected.

The DMT relation is thus similar to the relation 2.6, with the addition of the adhesive term F_{adh} :

$$F_{normal} = \frac{4}{3}E^*\sqrt{R^* d^3} + F_{adh} \tag{2.7}$$

As for the Hertz model, considering the tip–sample contact, R^* tends towards R_{tip}. The adhesion force during each contact cycle is directly accessible in AFM Peak Force mode via the force curves. Figure 2.1 illustrates the tip–sample contact for a hertzian model. The condition $R_{tip} \gg a$ still stands.

The DMT model is currently the most used in atomic force microscopy for the calculation of the local elastic modulus. It is, with the Sneddon model [5], the only model which is implemented in Bruker's PeakForce QNM mode, in the version used in this work. It allows the direct calculation of the DMT modulus (or Sneddon modulus) in an AFM channel while scanning.

2.2.3 Johnson-Kendall-Roberts (JKR) model

The model introduced by Johnson, Kendall and Roberts [4] describes a non-hertzian sphere-sphere contact (or sphere-plane as described above). Unlike the DMT model, the attractive adhesive forces *inside* the contact zone are taken into account and the exterior forces are neglected.

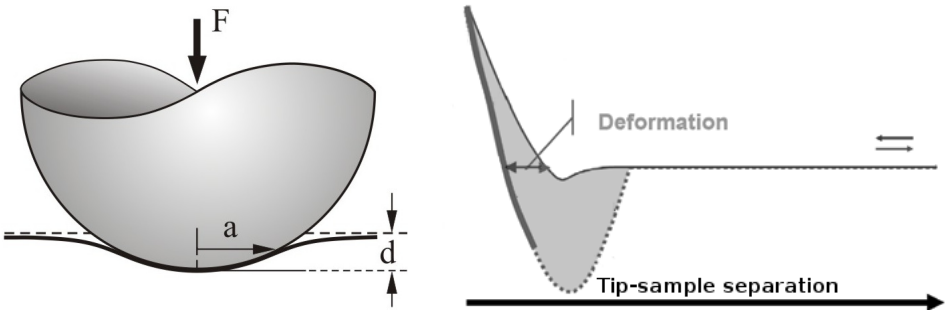

Figure 2.1 – Left: scheme of the tip–sample contact as described by Hertz and DMT models. Right: AFM force curve showing the deformation zone, corresponding to d on the scheme. It is worth noting that the actual deformation measured with the AFM also takes into account the *Deformation fit region* or *Deformation Force level*, which is a percentage (by default 85%) of the full deformation [6].

The JKR model predicts an **increase of the contact radius** a when the interaction is in the repulsive domain, as shown in Figure 2.2 (The figure is taken from the original publication describing the model [4]).

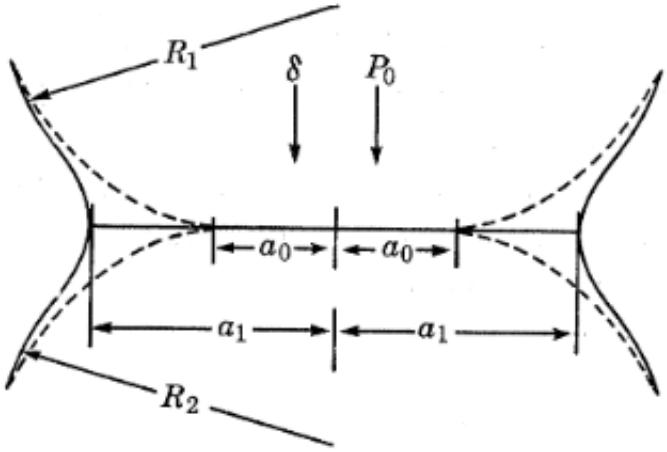

Figure 2.2 – Sphere-sphere contact as predicted by the JKR model. The dashed lines represent the contact of the spheres for a hertzian model, and a_0 stands for the correspoding radius. The contact radius a_1 is the one predicted by the JKR model.

An **adhesive neck** forms when the two objets separate. Figure 2.3 illustrates this phenomenon in the case of one sphere (in black) has an infinite stiffness and the other (in gray) has an infinite radius, to apply the model to the tip–sample contact. The indentation d can thus be negative and the contact radius a is not null when the two spheres separate.

The model gives rise to more complex relationships linking the forces, the properties and the variables of the contact (contact radius and indentation). Using the same notations as above, if F_{normal} is the normal force pressing the spheres against each other (thus equivalent to the force that the tip is applying on the sample surface) and F_{adh} the adhesion force, the contact radius is given by

$$a = \sqrt[3]{\frac{3}{4}\frac{E^*}{R^*}\left(F_{normal} + 2F_{adh} + 2\sqrt{F_{adh}(F_{normal} + F_{adh})}\right)} \tag{2.8}$$

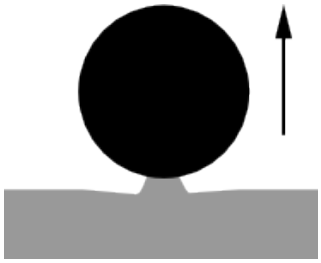

Figure 2.3 – Formation of an adhesive neck when the surfaces separate, as predicted by the JKR contact model.

The indentation d is given by

$$d = \frac{a^2}{R^*} - \sqrt{\frac{4}{3}\frac{aF_{adh}}{E^*R^*}} \tag{2.9}$$

By combining the equations 2.8 and 2.9, the contact radius a can be eliminated and a relation linking the forces, the radius, the indentation and the equivalent modulus can be obtained.

The JKR model was developed from observations on gelatin and rubber spheres. It is thus particularly applicable to soft materials, not only because of their stiffness but also because of their adhesion behavior. However, it is not implemented in the version 8 of Nanoscope, the software controlling AFM PeakForce QNM, which is used in this work.

2.2.4 Sneddon model

When the materials studied tend to be highly deformed by an AFM tip, in particular soft biological samples [7] or polymer hydrogels [8], theories assimilating the tip of the AFM tip to a sphere are no longer valid. In those cases, the Sneddon model [5], which describes the contact between a rigid cone and an infinite semi-space, is relevant since it is more accurate for important indentations (*i.e.* more than 30 nm). Adhesive forces are neglected. Figure 2.4 illustrates the considered geometry.

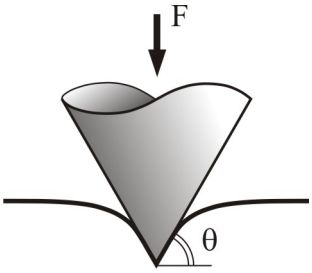

Figure 2.4 – Scheme of the tip–sample contact as described by the Sneddon model.

The model stands, for total indentation:

$$d = \frac{\pi}{2} a \cdot tan(\theta) \tag{2.10}$$

For the corresponding force, considering E the local Young's modulus and ν the Poisson's ratio of the surface, admitting $E_{tip} \gg E$:

$$F_{normal} = \frac{\pi a^2 E}{1-\nu^2} \cdot tan(\theta) = \pi a^2 E^* \cdot tan(\theta) \tag{2.11}$$

The relation binding force, deformation and modulus is thus:

$$F_{normal} = \frac{4E^*}{\pi \cdot tan(\theta)} \cdot d^2 \tag{2.12}$$

Relation 2.12 allows to obtain the local modulus on the basis of the force and deformation data, provided that the tip angle θ is known. Tips with a precisely known angle, specifically designed for the use of the high indentation Sneddon model, are currently marketed.

2.2.5 Model choice and transitional theories

Relations 2.6, 2.7, 2.8 and 2.9, or 2.12 allow to obtain—according to the selected model—the local modulus when an indentation is performed, from force (applied force and adhesive force) and deformation data, measurable at each point of an AFM image with the PeakForce QNM mode. These models exist because it is impossible to know the exact geometry of the actual contact for any tip and at any point on a surface. Each one therefore applies as an approximation in particular cases.

Sphere or cone As explained above, the Sneddon model only applies when the tip is assimilable to a cone, *i.e.* if the radius of curvature of the tip is negligible, compared to of the depth of indentation. For other models, the tip is considered to be spherical (at its extremity) and the condition $R_{tip} \gg a$ must be respected (radius of contact negligible in front of the radius of curvature of the tip).

The choice between JKR and DMT models[3] is thus critical for low–indentation modulus measurements (*i.e.* in the 2—5 nm indentation range). After having long been rival theories, it was gradually admitted that they simply applied to distinct cases. Tabor [9], particularly, was one of the first to consider different scenarios, introducing the influence of stiffness and roughness of each surface in the choice of the more relevant model. He pointed that the adhesion is not only determined by the intrinsic properties of the materials in contact but also by the roughness of the surfaces, which can dramatically modify the adhesion. He showed then that both JKR and DMT theories can be validated experimentally, depending on the adhesion behavior of the solids in contact.

Maugis transition and areas of validity of models First formulas evaluating the type of sphere-plane contact were introduced by Muller *et al* [10], and then, inspired by those of Dugdale [11], Maugis' works [12] have finally made it possible to consider defined areas of use of each model. A parameter, λ, is introduced in order to describe the different intermediate behaviors between the areas of application of DMT and JKR models. Considering now the contact between a sphere of radius R and a plane, this parameter is defined by the relation 2.13:

$$\lambda = 2\sigma_0 \sqrt[3]{\frac{9R}{16\pi w E^{*2}}} \tag{2.13}$$

where w represents the adhesion work defined by Bradley [13] (equation 2.14) and σ_0 the maximal stress defined in equation 2.15, ξ_0 being the interatomic equilibrium distance.

$$w = \frac{F_{adh}}{2\pi R} \tag{2.14}$$

[3] The Hertz model is no longer mentionned : it is equivalent to the DMT model with a zero adhesion force.

$$\sigma_0 = \frac{16}{9\sqrt{3}} \frac{w}{\xi_0} \tag{2.15}$$

Then, for a given situation (materials and geometry), if $\lambda \ll 10^{-2}$, the contact is better predicted by the DMT theory. If $\lambda \gg 3$, on the contrary, the JKR model is the most appropriate to describe the situation.

Maugis uses λ to link adimensioned expressions of the force, of the contact radius and of the indentation, thus creating a complex transitional model between JKR and DMT theories. Unfortunately, the model remains theoretical and is still not used in practice for AFM measurements.

The Maugis transition was then completed, in particular by Johnson and Greenwood [14]. Numerous attempts to bring the theories together, giving to each one its domain of application, have appeared [15, 16]. Johnson and Greenwood [15] established a map (Figure 2.5) which indicates the most appropriate model, according to the parameter λ and the intensity of the applied loads.

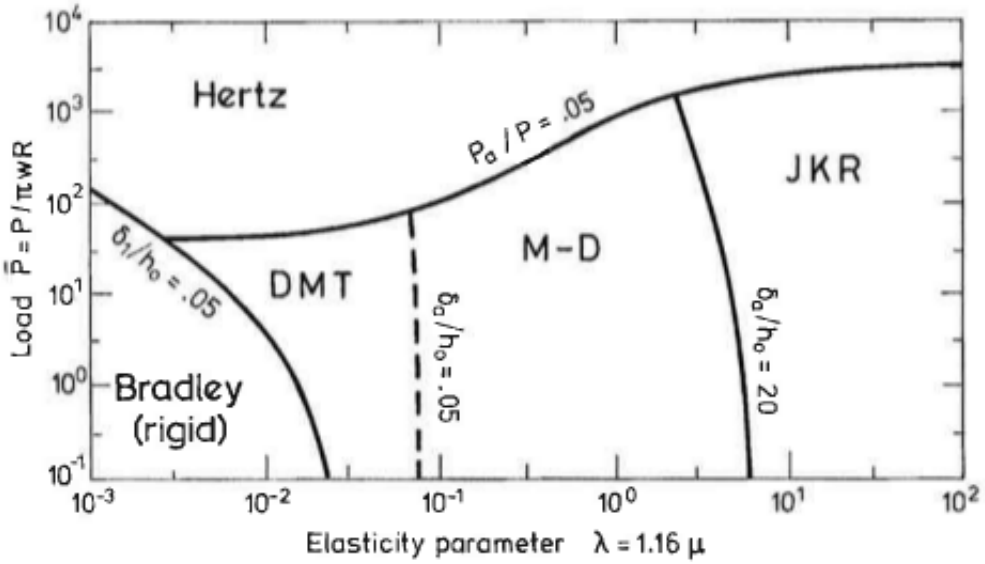

Figure 2.5 – Johnson and Greenwood's models map [15]. M-D refers to the Maugis transition (Maugis-Dugdale)

In AFM, with forces (P) of about ten nN and radii (R) of about ten nm, the relevant area is the bottom of the map. In the case of polymers, with deformations of the order of a few nanometers (therefore for a pseudo-spherical contact), λ is of the order of 1 [17], thus in a domain ideally described by the transitional Maugis theory.

2.2.6 Real tip–sample contact on polymers

External factors and contact models

For typical polymers having a modulus in the 10 MPa—10 GPa range, attempts were made to define the right model and conditions to quantify local mechanical properties by AFM. Dokukin *et al.* emphasized several challenges caused by the scale and the unpredicted factors of a real tip–sample contact on reference polymer surfaces (*i.e.* 2.7 GPa polystyrene films and 0.6–0.7 GPa polyurethane) [18, 19]. By measuring and using the actual tip radius for each experiment (see

"Absolut method" in section 2.3.2), they showed that an overestimation of the modulus is unavoidable. Furthermore, although the higher modulus of the PS implies a lower λ parameter than for the PU, the DMT model was found to fit better the modulus of the latter, while the modulus of the polystyrene was betterpredicted by the JKR theory. Finally, the authors managed to get consistent quantitative results by sacrificing the AFM resolution, using dull probes (with tip radii of more than 200 nm).

Scale One way to explain such difficulties is to consider that the reference moduli that are often compared to AFM values are obtained by other methods corresponding to higher scales. Even traditional nanoindentation, with typical indentation depths of several hundreds of nanometers, is not sensitive to the same local phenomena and molecular interactions as the AFM is. Consequently, the properties measured at different scales *do not have the same meaning*, and it can be normal to obtain values that do not match.

Humidity The real contact between tip and sample exhibits additional factors that deserve consideration, although difficult to integrate to contact models. One of those issues is ambient humidity when using AFM in air, forming a contact-modifying water meniscus. This phenomenon does not modify the different theories of the contact and their fields of application but can modify the radius of contact [17].

Real geometry Another important factor is the actual geometry of the tip, which is never perfectly spherical. These two main factors affect the value and the definition of the tip radius for the spherical contacts. One way to bypass this is to define an **equivalent radius** for a given tip in given conditions, which has to be determined prior to each session in QNM mode, and entered in the controlling software to be taken into account in the measurements. This approach consists in deducing this virtual radius by scanning a standard surface whose modulus is precisely known, and then by adjusting the radius in the software so that the AFM measures the right modulus value. This protocol, called relative calibration of the tip radius, is detailed in section 2.3.2.

Viscoelasticity Despite an extremely small scale, the visco-elastic behavior of polymers can also distort the calculation of moduli. This problem is partly solved by managing the synchronization times of the device, detailed in section 2.3.2. Although this effect is often neglected because of very reduced deformation amplitudes, it is at least necessary to specify the oscillation frequency of the AFM probe when presenting results[4].

Concluding remarks and discussions Considering such factors, the method described in the next section was established to get reproducible quantitative results, taking into account the factors cited above.

Regarding the contact model to use in polymer science, a debate between JKR and DMT is still ongoing. As a general rule of thumbs, it can be considered that the stiffer the scanned sample is, the better it is described by the DMT model, while the softer and more adhesive it is, the closer it gets from a JKR–type bevavior. However, this is not always true and unexpected results can still appear [18]. Furthermore, for non–homogeneous samples, blends and composites, the optimal model can vary depending on the phase or on the scanned zone.

[4] Typically about 2 kHz in PeakForce QNM mode.

It is thus chosen to use the DMT model, that is directly calculated during AFM imaging in the current version of the control software (see section 2.3.1), allowing faster acquisition of relevant data, thus more AFM images to reach more significant conclusions.

2.3 AFM operation principle

The following section presents the experimental conditions and general methods used in this work. The methodology is inspired by the existing AFM manuals [6, 20] and by discussions with other AFM users.

2.3.1 Hardware, software and supply

Many AFM elements have to be specific to the studied materials, to the scale of the observations, and obviously to the type of measurements (*i.e.* the AFM mode). The AFM setup used in his work is described below.

AFM configuration

All the AFM mappings and measurements in this work were carried out using the following configuration (from Bruker Corporation):

Microscope: Multimode 8 Scanning Probe Microscope

Controller: Nanoscope V

Software version: Nanoscope, version 8

Scanner: AS-130VLR ("Scanner J" vertical)

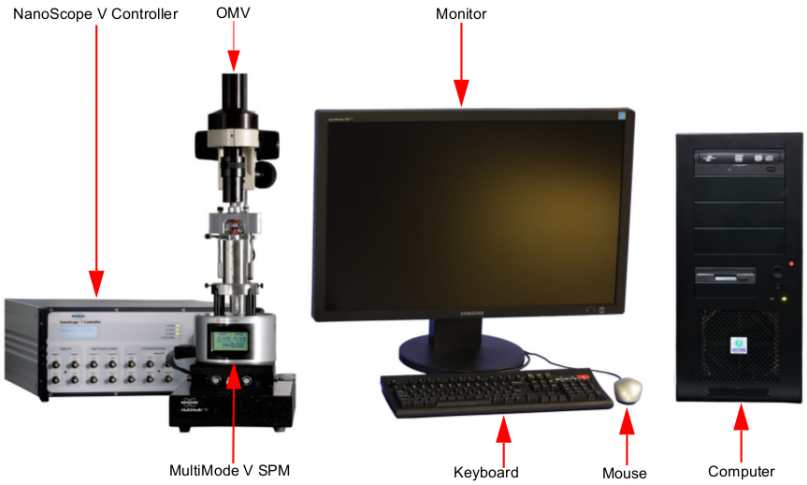

Figure 2.6 – Complete hardware setup. OMV stands for the optical viewing system [20].

Image analysis software

The following software was used for AFM image and force curves analysis:

- Gwyddion v. 2.34
- NanoScope Analysis v. 1.50 (Bruker)
- AtomicJ v. 1.7.2 [21]

Probe choice

The AFM probes, having a short lifetime of few scans in normal operating conditions, have to be changed frequently. Furthermore, the spring constant of their cantilever has to be adapted to the scanned material, especially in the case of mechanical measurements, as in PeakForce QNM mode. The general correspondance between Bruker's probes and the stiffness of the scanned material is shown in Figure 2.7. In the studies presented in the next chapters, TAP150A (nominal spring constant[5] $5N/m$) and RTESPA probes (nominal spring constant: $50N/m$) were mainly used.

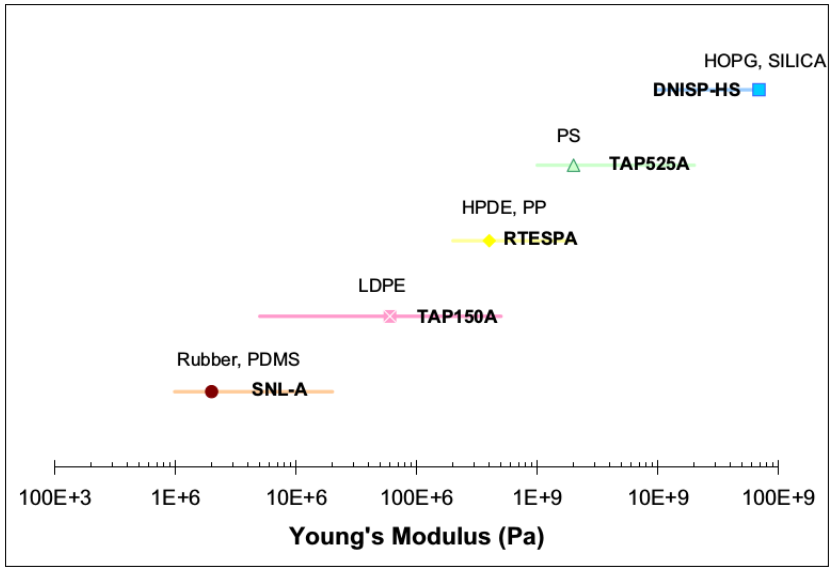

Figure 2.7 – Modulus range covered by various probes from Bruker. The modulus of typical reference samples for each range is indicated as well [6].

2.3.2 Calibration

In order to reach quantitative measurements, according to the contact model used, a calibration step must be performed prior to any session. This concerns principally the tip and its position in the tip holder. Three main parameters need to be calibrated and given to the software to allow the calculations of the local mechanical properties from the force curves:

[5] The nominal spring constant gives an idea of the order of magnitude of the spring constant of a given probe. However, its real spring constant may be significantly different from the nominal value, thus the importance of a right calibration step, described in section 2.3.2.

- The **deflection sentitivity**, in other words the link between a given deflection of the cantilever induced by a contact and the corresponding movement of the laser on the photodiode. The calibration is performed with a parallel calibration of the time synchronization of the setup.

- The **spring constant** of the cantilever, which affects the local contact load between the tip and the sample, for a same vertical displacement of the piezo.

- The **tip radius** (radius of curvature of the extremity of the tip), involved in the equation 2.3, allowing to calculate the local modulus for every contact model where a sphere-plane geometry is considered.

The calibrations steps for those parameters are detailed below.

Deflection sensitivity and time synchronization

The first calibration step is to tune the deflection sensitivity, giving the relation between the deflection of the cantilever when the probe is pushed down on the hard sample and the corresponding movement of the laser recorded by the photodiode. It is determined by the tip and the position of the laser and of the photodiode in a particular configuration. After this step, the exact position of the tip at each moment is precisely known, allowing to perform the following calibration steps.

A clean sapphire sample is generally used, since its stiffness can be considered to be infinitely higher than that of any cantilever.

After this step, the position of the laser must not be changed. To change the sample, it is generally preferred to remove carefully the whole scanner head, instead of removing only the tip holder. This avoids slight changes in the relative position of the laser and the cantilever, which can change the deflection behavior.

Static calibration (Ramp mode) This first step corresponds to the method described in the section 4.3 of the PeakForce QNM user guide [6]. One force curve is acquired on a point of the hard sample.

Since the sapphire allows no (or negligible) indentation, the contact zone corresponds to a pure characteristic of the cantilever. This zone in manually selected, as shown in Figure 2.8. It can be considered then that the value of the deflection sensitivity is known, and has been entered in the software. The operation has to be repeated a few times for reproductibility.

Dynamic calibration (Scan mode) The static calibration gives the true value of the deflection sensitivity, but it has to be verified if it is well taken into account in a scanning situation, in which the movements of the cantilever are faster than in the static calibration. Some new parameters enter into account, and their values have to be tuned so that the value of the "dynamic" deflection sensitivity matches the one calculated previously in ramp mode.

This step is not mentionned in the manual corresponding to the version 8 of the Nanoscope software, and is inspired by discussions about the improvements made (or planned) in the next versions.

While scanning the sapphire sample as if it was a normal sample (applying the same force

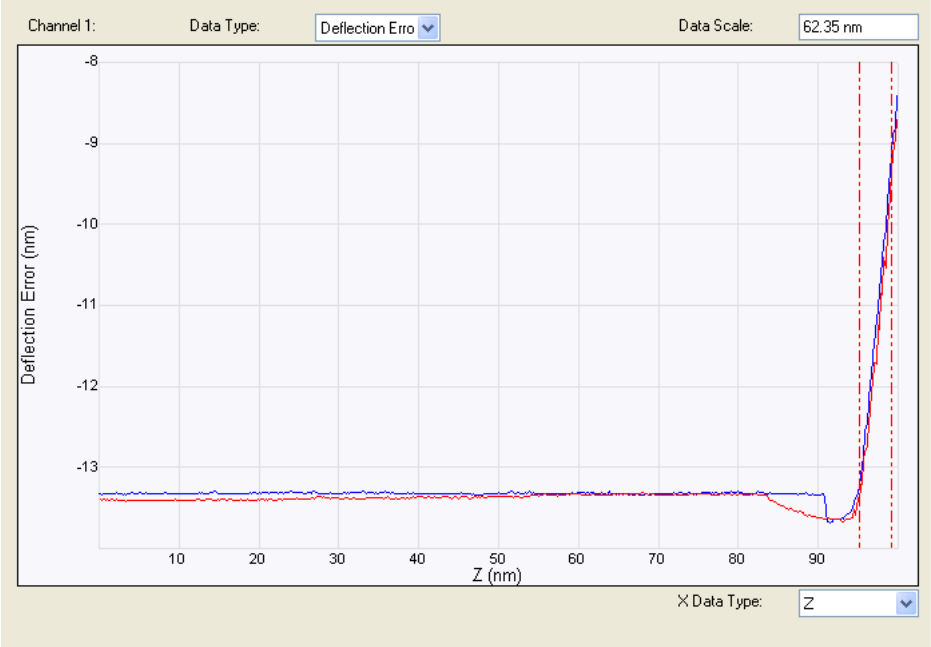

Figure 2.8 – Force curve acquired on a hard sample for the calibration of the deflection sensitivity. The vertical red dashed lines define the zone used for the calculation of the deflection sensitivity [6].

as in the previous step in ramp[6]), if the force curves are adjusted in the right way[7], it has to be verified that the *dynamic* deflection sensitivity (obtained by clicking "Update Sensitivity" in the force curve windows) is less than 10% different from the one calculated in ramp mode. If not, a parameter, *Drive3 Amplitude Setpoint*[8], has to be adjusted until the two deflection sensitivities match.

Once it is done, the value of the time synchronization parameter, *Sync Distance New*, has to be noted before the withdrawal of the tip. This value will be used in all the further scans but has to be entered again in the software each time the tip is engaged.

Spring constant of the cantilever

To know exactly the tip–sample interaction force between the tip and the sample, the spring constant of the cantilever must be known.

There are many ways to determine this spring constant k_{tip}, as described by Ohler [22], but the most reliable and convenient are the Thermal Tune method [23] and the Sader method [24, 25]. In both methods the cantilever must be free (not engaged on a sample).

Thermal Tune This is the default method, adapted for any kind of soft cantilever (*i.e.* $k_{tip} < 1\ N/m$) [22]. The probe is modelled as a harmonic oscillator and the brownian fluctuations of the cantilever are recorded. Hutter *et al.* evidenced the link between the spring constant k_{tip}, the thermal energy k_bT and the mean square vertical displacement of the cantilever $\langle z_c^2 \rangle$,

[6] The peak force is called *PeakForce setpoint* in scan mode, and *Trig threshold* in ramp mode.

[7] The approach curve and the withdrawal curve must be superimposed, except possibly in the adhesion zone. It is done by using *Auto config* or by adjusting manually the time synchronization.

[8] Accessible through *Calibrate*>*Property maps* in Nanoscope v. 8.15.

shown in equation 2.16 [23]. k_b is the Boltzmann constant and T the temperature.

$$k_{tip} = \frac{k_b T}{\langle z_c^2 \rangle} \tag{2.16}$$

By analyzing the vertical thermal oscillations of the cantilever in the frequency domain, it is possible to measure $\langle z_c^2 \rangle$ by integrating the area under the peak of the fundamental mode, then k_{tip} can be calculated.

Various further studies evidenced that this equation tends to overestimate the spring constant, mainly due to the fact that the cantilevers do not behave as ideal spring, and to artifacts linked with the optical detection system (laser and photodiode). This led to the determination of correction factors which are proper to each type of scanner. Such factors are taken into account in the AFM software and the spring constant is directly calculated when the peak of the fundamental mode is identified and the right temperature is given.

It was found that even for probes of the TAP150A type, widely used in this work and having a nominal spring constant of $5N/m$, the Thermal Tune method gives the most reproducibe results.

Sader method The Sader method [24] is adapted to stiffer cantilevers such as those of the RTESPA probes. It is adapted only for a rectangular cantilever, since the model requires its length and its width, generally measured via optical microscopy. The method is then similar to the thermal tune method, but takes into account the density and viscosity of air (or the fluid in which the probe oscillates) and the quality factor Q of the peak of the fundamental mode of the thermal oscillations of the cantilever.

The Sader method is used in this work for RTESPA probes. A java applet allows to calculate the spring constant on Sader's website [26] from the data mentionned above.

The challenge of the development of methods to measure spring constants of AFM cantilevers is to minimize the uncertainities, which are sometimes linked to the conditions of manipulation. A recent study by Schillers *et al.* shows that the use of a vibrometer to measure k_{tip} before measuring the deflection sensitivity[9] gives better results that the methods mentionned above for the imaging of cells and soft matter in liquids [27].

Anyway, the methods used in this work (*i.e.* Thermal tune and Sader method) are still the known methods with the lowest uncertainities for the type of probes used for the imaging of materials in air [22].

Tip radius

The last calibration step to be able to calculate local mechanical properties is related to the shape of the end of the tip. If it is considered to be spherical in the selected contact model (in other words, if low deformations are expected), then this step is necessary. There are two ways of calibrating the tip radius R_{tip}, the *absolute* method and the *relative* method, both detailed in the PeakForce QNM manual [6].

Absolute method This method consists in measuring directly the tip end radius, by scanning a tip calibration artifact sample. This type of sample exhibits a very high roughness, due to features which are sharper than the AFM tip. While scanning the topography of those features, the resulting AFM image do not reveal the exact morphology of the sample, but the shape of the tip. Such an image of a roughness sample is shown in Figure 2.9.

[9] Which is then adjusted to measure the same spring constant as in vibrometry using thermal tune.

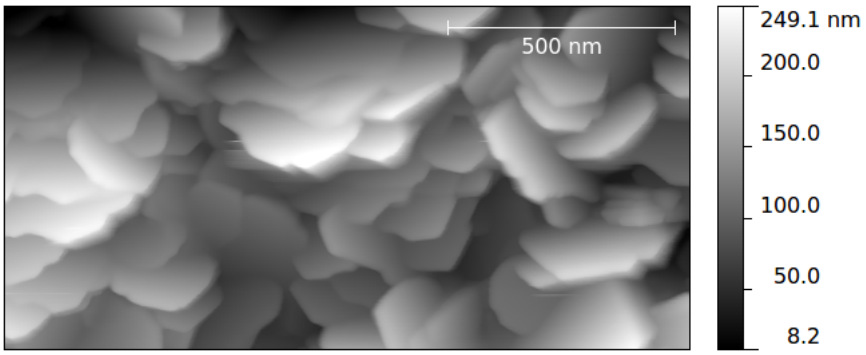

Figure 2.9 – Typical AFM height image of an artifact sample (polycrystalline titanium, ref. #RS from Bruker). The peaks of the sample are generally sharper than the AFM tip scanning them, so their shape in the AFM image actually reflects the shape of the tip.

The Nanoscope Analysis software provides a tool to perform the tip radius calculation, by automatically choosing the appropriate peaks and by estimating if the tip is blunt or not (or, at least, in an appropriate shape to use the sphere–plane contact models). An estimation of the tip radius is given and can then be entered to the Nanoscope software to have the local modulus directly calculated in the corresponding channel.

The absolute method can be applied in different ways, if other ways to calculate directly the tip radius are available. Some authors, for instance, used high resolution scanning electron microscopy images of tips to evaluate their radius [28].

Although being theoretically accurate and quite straightforward, this method is decreasing in popularity because of the accumulation of error factors that are not compensated, and that are impossible to evaluate. The most important error factor is the fact that the tip apex is never perfectly spherical.

Relative method The method used in ths work is the relative one. The tip radius here is not directly measured, but evaluated by scanning a sample of known modulus and by adjusting R_{tip} until this modulus is measured by the AFM. The advantage of such method is that many previously mentionned error factors are bypassed, because the real modulus of the reference sample is used. There are however several points of this calibration method that deserve discussion, and a great care in the operation and interpretations is required to be able to consider the measurements quantitative.

- The calculated **tip radius is here virtual** and relative to the conditions in which it is determined. The local mechanical measurements can be considered quantitative *only if the tip–sample contact geometry on the reference sample is similar on the studied samples.* Otherwise, the virtual tip radius does not have any physical meaning, and this leads to wrong calculations of mechanical properties. It is thus often advised to choose a reference sample with an elasticity modulus close to that of the studied sample, but the most important is to adjust the applied force (*PeakForce Setpoint* in QNM mode on Bruker systems) so that the deformation matches reasonably the one obtained on the reference sample.

- The **Young's modulus of the reference** sample's surface is usually known by nanoindentation measurements, which corresponds to a mechanical measurement at a larger scale,

using different models such as the Oliver and Pharr model [1]. As already mentionned in section 2.4.2, the assumption of scale equivalence seems fair for homogeneous materials. For the nanomechanical imaging of polymers, the reference samples have thus to be amorphous, isotropic and as flat as possible. In this work, a polystyrene film provided by Bruker is used as a reference sample, with a nominal modulus of 2.7 GPa. For the imaging of relatively soft samples in the 10—50 MPa range, a confirmation of the tip radius is performed on a softer reference sample provided by Bruker, a polydimethylsiloxane gel sample with a nominal modulus of 3.5 MPa, if the probe's cantilever is soft enough to reach the adequate deformation on this sample.

A typical DMT modulus image and DMT modulus histogram of a reference polystyrene film is shown in Figure 2.10. In this case, the tip radius is already tuned: the modulus distribution is centered around the reference value of 2.7 GPa.

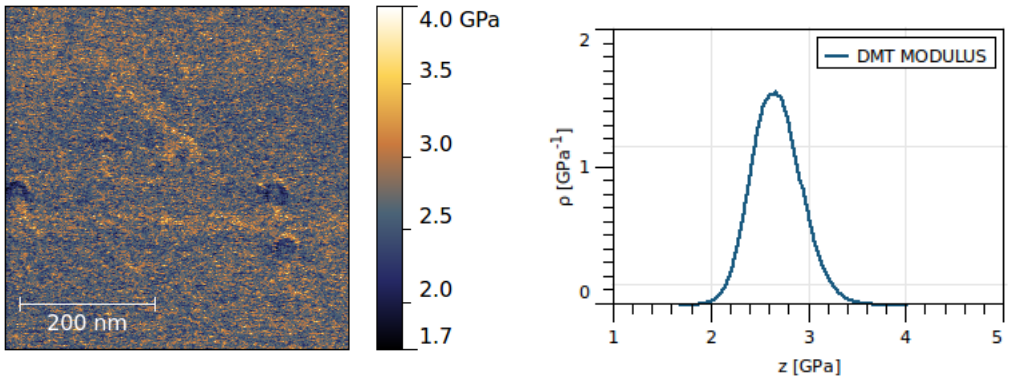

Figure 2.10 – DMT modulus image of a reference sample (polystyrene (PS) film from Bruker, left) and corresponding modulus distribution (right).

2.4 Discussions about quantitative measurements

2.4.1 Considerations about the Poisson's ratio

After the calibration, the last step to reach true quantitative measurements is to enter the Poisson's ratio of the scanned material[10], since it is used in equation 2.2, on which most contact models are based. This may be the most challenging part, since the imaging of heterogeneous materials such as polymer blends or composites, but also semicrystalline polymers implies necessarily significant changes in the real Poisson's ratio within a single image.

Since it is impossible to predict such local Poisson's ratios, at a nanoscale and often confined, it is chosen here to consider a fixed Poisson's ratio of 0.3, which is a reasonable average value for common polymers, for all experiments at the nanoscale. Thus the local modulus (generally the DMT modulus, E_{DMT}) considered in this work *includes* the potential shift of the Poisson's ratio from its default value of 0.3. As a worst-case scenario, this means that if a scanned zone has a *real* Poisson's ratio of 0.5 instead of the considered value of 0.3, the local modulus would be overestimated by 15%, according to equation 2.2.

[10] Note: it is also important to do so with the reference sample in the case of a relative calibration of the tip radius.

2.4.2 Definition of the local modulus

The main reference sample used in the relative calibration process is a polystyrene (PS) film, which modulus (usually 2.7 GPa) is determined by nanoindentation. The PS being amorphous and homogeneous, this is assumed that the mesoscopic scale modulus (given by nanoindentation, which can be considered equivalent to a macroscopic modulus) and the nanoscale modulus can be considered to be the same. Although some authors evidenced slight caracteristic heterogeneities at the nanoscale, even for amorphous PS [29], the assumption of scale equivalence seems fair enough for the reference sample, given the amorphous nature of PS (the lenghtscale and amplitude of heterogeneities documented by Wang *et al.* in PS can be considered negligible in nanomechanical measurements since it was never observed using PeakForce QNM and equivalent techniques). However, it is the only case where the elastic modulus can be considered to be equivalent at every scale: while a macroscale modulus reflects the average of molecular interactions, heterogeneities and sometimes defects in a bulk material, a local modulus measured by AFM only traduces the mechanical behavior of a zone of few square nanometers. Therefore, a difference between local and macroscopic Young's modulus can be expected, particularly for heterogeneous materials.

An example is the poly(-butylene-adipate-*co*-terephthalate) (PBAT), a crystalline copolyester, usually exhibiting a macroscopic Young's modulus from tensile tests in the 40—50 MPa range [30]. As described in the next chapters, the local modulus of PBAT measured by AFM is varying in the 50–200 MPa range in average. While the order of magnitude is conserved, this shows that the modulus is not necessarily equivalent through the scales.

Furthermore, the macroscopic and the local modulus of materials such as bulk polymers can differ because of the scale of the measure. Such polymer can have different local properties at the interface with the air, because of the spatial organization of the chains that are less constrained by each other in such zones. In AFM nanomechanical mappings, the scanned depth is typically few radii of gyration of the chain's atoms, which corresponds to the depth of those zones. Therefore, although some comparisons are made between the properties at different scales, the concepts of "local (nanoscale) modulus" and "macroscopical modulus" mean distinct things.

The local modulus used in this work, measured by AFM at each pixel of a modulus map can thus be defined. It is calculated using the DMT model (as well as the adhesion force), and is relative to the modulus of a reference sample (generally 2.7 GPa polystyrene). The conditions to obtain quantitative measurements, respecting as well as possible all the assumptions mentionned above, are detailed in section 2.4.3.

2.4.3 Ideal conditions for quantitative measurements

To be able to make absolute quantitative measurements with AFM nanomechanical mappings using force curves means:

- To apply the right contact model for each modulus or adhesion measurement, *i.e.* for each pixel of an AFM image.

- To make sure that the assumptions that are necessary to apply a given model are reasonably respected. For instance, if it is intended to apply the Hertz or the DMT model, it is important to make sure that the tip radius R_{tip} is by far larger than the contact radius a.

In polymer science[11], this would mean, using the currently applied models, to be able to calculate the λ parameter (equation 2.13) at each point, allowing to choose the appropriate one between JKR and DMT. It would be also useful to be able to apply the Maugis-Dugdale transitional model, which is still challenging.

If an *absolute quantitativity* of the technique is still a challenge, methods such as relative calibration allow to obtain quantitative measurements if some conditions are respected. To be able to stick to the assumptions made to use one contact model, the contact geometry must be equivalent in the tip radius calibration step and in the scanning of the studied samples. If the applied force may vary, **the deformation have to stay in the same range** during all the experiment. This should guarantee the conservation of the contact geometry. The deformation maps can also help to identify where the other measured properties are valid or not.

The **mechanical properties** of the studied sample should not be too different from those of the reference sample, typically remaining within the same order of magnitude for the local modulus. This limit can be exceeded, but in this case the validity is generally confirmed with a different reference sample.

Finally, the **probe wear** must be prevented. It is common to observe a sudden increase of the average adhesion force during scanning, as shown in Figure 2.11 with the horizontal adhesion steps. This is caused by a change of the contact geometry, due to damage or pollution of the tip apex. The tip radius has to be calibrated once again. To avoid this, when a really fine resolution is not needed, the tip is *stabilized* before the calibration. This can be done by scanning the hard sample later used to calibrate the deflection sensitivity: several scans are done[12] until the adhesion force is perfectly stable. Tips with a radius of approximately 20 nm are generally much less damaged during the scans.

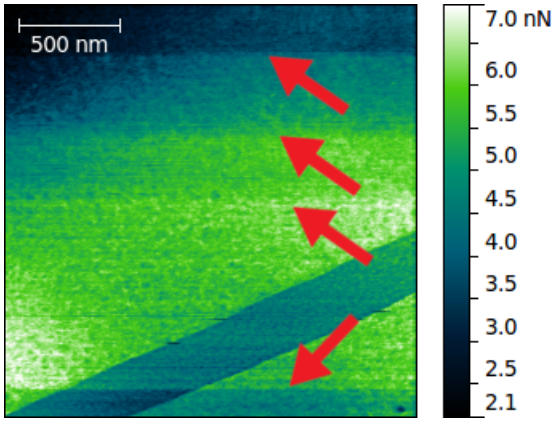

Figure 2.11 – AFM adhesion map showing hints of tip modification. The horizontal sudden adhesion steps marked by red arrows correspond, if they are not visible on any other channel, to moments in the scan in which the contact geometry changed, because of tip damage or pollution.

By respecting these conditions, it has been possible to perform quantitative and reproducible measurements on most samples.

[11] Excepting really soft polymers such as hydrogel, on which force curves are usually studied using Sneddon's model due to large indentations [8].

[12] The PeakForce Setpoint or equivalent, *i.e.* the maximal applied force, has to be equivalent or slightly higher than the further applied force, used when scanning the studied samples.

2.5 Conclusion

Nanomechanical measurements using an atomic force microscope are made possible by the application of theoretical models from contact mechanics, modeling the tip–sample contact. According to the mechanical properties of the sample and the way the AFM is operated, the geometry and the behavior of this contact may vary. Consequently, several contact models are available to describe each case.

To be able to choose and to apply the most appropriate contact model and to respect the corresponding assumptions are the keys to quantitative measurements for a given studied material. It is also essential to adapt the choice of the probe: the cantilever has to be chosen appropriately to be stiffer than the studied samples, but not too much to remain responsive and sensitive. Then the calibration of the probe is mandatory, prior to any quantitative measurement. The deflection sensitivity and the spring constant of the cantilever have to be known precisely, along with the radius of curvature of the tip apex.

Nevertheless, external factors have also to be taken into account to avoid accumulated errors in such a sensitive technique. This is why the last calibration step, the evaluation of the tip radius, is usually performed indirectly, by scanning a reference sample of known modulus. This bypasses many error factors, but implies to scan all the samples of the session with a great care to stick to the same conditions as during the calibration. Then quantitative and reproducible measurements can be achieved.

One has to keep in mind that the properties at this scale, and particularly the elasticity modulus, are only equivalent to their counterparts at the macroscopic scale in the case of amorphous, homogeneous and isotropic materials. Sometimes, materials behave very differently at the nanoscale, and to study how and why is the major interest of such a technique.

Bibliography

[1] Warren Carl Oliver and George Mathews Pharr. An improved technique for determining hardness and elastic modulus using load and displacement sensing indentation experiments. *Journal of materials research*, 7(6):1564–1583, 1992.

[2] H.R. Hertz. Ueber die beruehrung elastischer koerper (on contact between elastic bodies). *Gesammelte Werke (Collected Works)*, 1:155, 1895.

[3] B.V Derjaguin, V.M Muller, and Yu.P Toporov. Effect of contact deformations on the adhesion of particles. *Journal of Colloid and Interface Science*, 53(2):314 – 326, 1975.

[4] K. L. Johnson, K. Kendall, and A. D. Roberts. Surface energy and the contact of elastic solids. *Proceedings of the Royal Society of London A: Mathematical, Physical and Engineering Sciences*, 324(1558):301–313, 1971.

[5] Ian N. Sneddon. The relation between load and penetration in the axisymmetric boussinesq problem for a punch of arbitrary profile. *International Journal of Engineering Science*, 3(1):47 – 57, 1965.

[6] Bruker Corporation. *PeakForce QNM User Guide (Revision E)*, 2011.

[7] Delphine Sicard, Laura E Fredenburgh, and Daniel J Tschumperlin. Measured pulmonary arterial tissue stiffness is highly sensitive to afm indenter dimensions. *Journal of the Mechanical Behavior of Biomedical Materials*, 2017.

[8] Marius Chyasnavichyus, Seth L Young, and Vladimir V Tsukruk. Mapping micromechanical properties of soft polymer contact lenses. *Polymer*, 55(23):6091–6101, 2014.

[9] D Tabor. International conference on colloids and surfaces surface forces and surface interactions. *Journal of Colloid and Interface Science*, 58(1):2 – 13, 1977.

[10] V.M Muller, V.S Yushchenko, and B.V Derjaguin. On the influence of molecular forces on the deformation of an elastic sphere and its sticking to a rigid plane. *Journal of Colloid and Interface Science*, 77(1):91 – 101, 1980.

[11] D.S. Dugdale. Yielding of steel sheets containing slits. *Journal of the Mechanics and Physics of Solids*, 8(2):100 – 104, 1960.

[12] Daniel Maugis. Adhesion of spheres: The JKR-DMT transition using a dugdale model. *Journal of Colloid and Interface Science*, 150(1):243 – 269, 1992.

[13] R.S. Bradley M.A. Lxxix. the cohesive force between solid surfaces and the surface energy of solids. *The London, Edinburgh, and Dublin Philosophical Magazine and Journal of Science*, 13(86):853–862, 1932.

[14] K.L. Johnson and J.A. Greenwood. A maugis analysis of adhesive line contact. *Journal of Physics D: Applied Physics*, 41(15):155315, 2008.

[15] K.L. Johnson and J.A. Greenwood. An adhesion map for the contact of elastic spheres. *Journal of Colloid and Intarface Science*, 192(1):326–333, 1997.

[16] E Barthel. Adhesive elastic contacts – JKR and more. *J. Phys. D: Appl. Phys.*, 41:163001, 2008.

[17] P.-E. Mazeran. *Microscope a force atomique et imagerie mecanique.* PhD thesis, Ecole Centrale de Lyon, 1998.

[18] Maxim E Dokukin and Igor Sokolov. Quantitative mapping of the elastic modulus of soft materials with harmonix and peakforce qnm afm modes. *Langmuir*, 28(46):16060–16071, 2012.

[19] Maxim E Dokukin and Igor Sokolov. On the measurements of rigidity modulus of soft materials in nanoindentation experiments at small depth. *Macromolecules*, 45(10):4277–4288, 2012.

[20] Bruker Corporation. *MultiMode V8 Instruction Manual*, 2011.

[21] Paweł Hermanowicz, Michał Sarna, Kvetoslava Burda, and Halina Gabryś. Atomicj: An open source software for analysis of force curves. *Review of Scientific Instruments*, 85(6):063703, 2014.

[22] B Ohler. Practical advice on the determination of cantilever spring constants. veeco instruments inc, 2007.

[23] Jeffrey L Hutter and John Bechhoefer. Calibration of atomic-force microscope tips. *Review of Scientific Instruments*, 64(7):1868–1873, 1993.

[24] John E Sader, Ian Larson, Paul Mulvaney, and Lee R White. Method for the calibration of atomic force microscope cantilevers. *Review of Scientific Instruments*, 66(7):3789–3798, 1995.

[25] John E Sader, Julian A Sanelli, Brian D Adamson, Jason P Monty, Xingzhan Wei, Simon A Crawford, James R Friend, Ivan Marusic, Paul Mulvaney, and Evan J Bieske. Spring constant calibration of atomic force microscope cantilevers of arbitrary shape. *Review of Scientific Instruments*, 83(10):103705, 2012.

[26] John E Sader. http://sadermethod.org.

[27] Hermann Schillers, Carmela Rianna, Jens Schäpe, Tomas Luque, Holger Doschke, Mike Wälte, Juan José Uriarte, Noelia Campillo, Georgios PA Michanetzis, Justyna Bobrowska, et al. Standardized nanomechanical atomic force microscopy procedure (snap) for measuring soft and biological samples. *Scientific Reports*, 7, 2017.

[28] Magdalena Prokopowicz. Atomic force microscopy technique for the surface characterization of sol–gel derived multi-component silica nanocomposites. *Colloids and Surfaces A: Physicochemical and Engineering Aspects*, 504:350–357, 2016.

[29] Dong Wang, Yanhui Liu, Toshio Nishi, and Ken Nakajima. Length scale of mechanical heterogeneity in a glassy polymer determined by atomic force microscopy. *Applied Physics Letters*, 100(25):251905, 2012.

[30] Sébastien Livi, Valeria Bugatti, Bluma Guenther Soares, and Jannick Duchet-Rumeau. Structuration of ionic liquids in a poly (butylene-adipate-co-terephthalate) matrix: its influence on the water vapour permeability and mechanical properties. *Green Chemistry*, 16(8):3758–3762, 2014.

Chapter 3

AFM study: Compatibilization of PBAT/PLA blends with ionic liquids

Contents

This chapter corresponds to a paper published in RSC Avdances *in 2016 under the title "Probing nanomechanical properties with AFM to understand the structure and behavior of polymer blends compatibilized with ionic liquids".*

Abstract

PeakForce QNM AFM mode was used to investigate the nanoscale mechanical properties of poly(butylene-adipate-*co*-terephtalate)/poly(lactic acid) (PBAT/PLA) blends successfully compatibilized with phosphonium-based ionic liquids (ILs). This novel AFM mode allowed to evidence the phase structuration and also emphasized the effect of the ionic liquids on the mechanical behavior at nanoscale of the polymer phases and interfaces. On one hand, phosphonium-chloride IL (il-Cl) was shown to play an efficient role as interfacial agent, *i.e.*, acting for a finer dispersion of PLA nodules in PBAT continuous matrix. On the other hand, phosphonium-phosphinate IL (il-TMP), leads to PLA dispersed phase as fibrils and locates as an interphase layer between the two polymers. Adhesion force mappings confirmed that ILs are mainly localized at the interfaces between the two polyesters. The PeakForce QNM AFM study allowed to propose complete models for the compatibilization mechanism allowing to establish relationships between the nanoscale structure and the macroscopic mechanical properties of these blends.

3.1 Introduction

Understanding the link beyond compatibilization at molecular scale and macroscopic physical properties is an extremely important challenge in polymer and composite science, as it gives tools for formulation and processing to target final properties.

The Atomic Force Microscope (AFM) [1] is a powerful tool for its ability to reach a nanometric resolution on surfaces, using the interaction of a sharp tip with the sample [2]. Since the emergence of the Tapping Mode, in which the tip comes into an intermittent contact with the scanned surface, preventing it from fast damage, the technique became viable to study soft matter, and especially polymers [3].

The introduction of the force curve, relating tip-sample distance and interaction force (Figure 3.1) acquired for each contact, opened a new field in nanomechanics [4, 5] as it gives access to physical properties such as mechanical stiffness [6], adhesion force, or dissipated energy at the nanoscale. Nevertheless, this method usually required long acquisition time and heavy data processing. More recently, Bruker AXS (CA, USA) developped the PeakForce Quantitative NanoMechanics (QNM) mode [7] and integrated this technology into an AFM scan mode, allowing to take full profit from the recordings as well as mapping simultaneously topography and mechanical properties.

AFM QNM mode became an unavoidable tool to understand the mechanical behavior and structure of polymers at the nanoscale [8, 9, 10, 11]. Such a mode was applied to explain how the properties of polymers change after physical and chemical treatments [12, 13, 14] or for investigating the interfaces between polymers [15]. Significant advances could also be made in the understanding of interfacial interactions in polymer blends, composites and nano-composites [16, 17, 18, 19, 20].

Bio-based composites and blends start to be intensively investigated according to the growing interest for renewable resources. AFM with QNM mode was used for the better understanding of the behavior of polycaprolactone [10] or poly(lactic acid) [21, 22]–based materials and composites containing cellulose nanofibers [23, 24, 21] and nanocrystals [25, 26] or chitin [8].

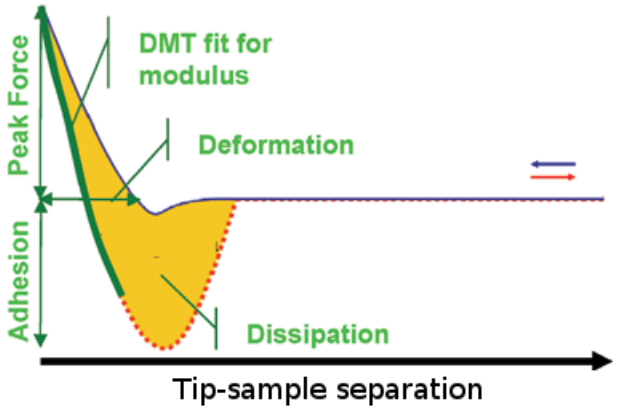

Figure 3.1 – Typical AFM Force curve with accessible mechanical data, adapted from Bruker's Application Note #128 [7] (image reproduced with the kind authorization of Bede Pittenger)

Poly(lactic acid) (PLA) is a good candidate to replace many commodity oil-based polymers [27]. However, due to its brittle nature, many routes were considered to improve its mechanical properties, and a promising one is to design blends by combining PLA with a more impact-resistant polymer [28, 29]. PLA blended with poly(butylene-adipate-*co*-terephtalate) (PBAT), a flexible aliphatic-aromatic copolyester, is today widely investigated [30, 31, 32] as a promising material for various applications such as food packaging and compostable films for agriculture.

Phosphonium ionic liquids were already identified to display favorable interactions with PBAT [33, 34, 35] and were selected in a previous study [36] as efficient interfacial agents, *i.e.* compatibilizers, for PBAT/PLA blends. In this chapter, AFM nanomechanical mappings are carried out for those blends in order to investigate the underlying mechanisms involved in that novel route of polymer compatibilization. This chapter aims to propose a quite simple method to evaluate microstructure, interfaces and interactions at the nanoscale.

3.2 Experimental

3.2.1 PBAT/PLA blends

Materials used in this study were prepared as described by Lins *et. al.* [36]. Poly(lactic acid), PLA 2002D (1.5–2% of D isomer) was obtained from NatureWorks® LLC Co. (USA). Poly(butylene-adipate-co-terephtalate) (PBAT) was supplied by BASF Co. (Germany) under the trade name of Ecoflex®. Two ILs based on the same phosphonium cation (*i.e.* trihexyltetradecyl phosphonium) with two different anions (*i.e.* chloride denoted il-Cl and bis-2,4,4-(trimethylpentyl)phosphinate, also denoted il-TMP) were provided by Cytec Industries Inc. The structures of the polymers and ionic liquids are summarized in Table 3.1.

All the blends were extruded and injected for tensile test samples. The PBAT:PLA weight ratio was 80:20 and 1 wt% of ionic liquid was added in the corresponding blends. Table 3.2 summarizes their main tensile properties (Young's modulus E and strain at break ε_{max}).

3.2.2 AFM measurements

The AFM measurements were carried out using a Bruker Multimode 8 scanning probe microscope with a Nanoscope V controller under ambient conditions. The PeakForce QNM (Quantitative NanoMechanics) mode was used, allowing the simultaneous recording of topography and force

Table 3.1 – Designation and structure of the components considered in this study

Nomenclature	Chemical Structure
Polymers :	
PBAT	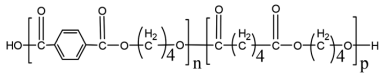
PLA	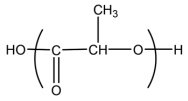
Ionic Liquids :	
il-Cl	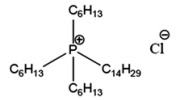
il-TMP	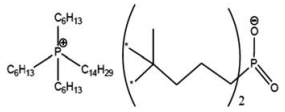

Table 3.2 – Tensile properties of the blends measured by Lins *et al.*[36]

	Young's Modulus [MPa]	Strain at break [%]
PBAT	41	894
PBAT/PLA	115	540
PBAT/PLA/il-Cl	140	1000
PBAT/PLA/il-TMP	165	910

curves for each pixel. By applying a model for the tip-sample contact, the mechanical properties of the scanned surface, such as local modulus and adhesion were mapped. Here the Derjaguin-Müller-Toporov (DMT) [37] model was used, leading to equation 3.1.

$$F = \frac{4}{3} E^* \sqrt{R d^3} + F_{adh} \tag{3.1}$$

where F is the applied force, F_{adh} the adhesion force, R the tip radius,d the tip-sample distance and E^* the reduced modulus. The latter modulus is defined by equation 3.2.

$$\frac{1}{E^*} = \left(\frac{1-\nu_1^2}{E_1}\right) + \left(\frac{1-\nu_2^2}{E_2}\right) \tag{3.2}$$

Subscripts 1 and 2 represent each material in contact (*i.e.* the studied sample and the silicon tip), each one with a modulus, E_i, and Poisson's ratio, ν_i.

The TAP150 probe, with a nominal spring constant of 5 N/m, was used. Its deflection sensitivity was measured on a hard sapphire surface. The spring constant was calibrated by thermal tuning method and the tip radius was evaluated by the relative method [38] on Bruker's polystyrene standard reference sample.

3.2.3 Sample preparation

For AFM observation, a clean surface of a representative part of the sample had to be obtained. Surface preparation using a microtome operating at -100°C was inefficient in this case. In fact, AFM imaging showed highly deformed structures on the surfaces and no correspondence

with previous analyses of the morphologies analyzed by Transmission Electron Microscopy [36]. Cryofractured surfaces were therefore considered. Surfaces for AFM observation were prepared by breaking tensile coupons after cooling them in liquid nitrogen for 10 minutes. The tensile samples were hit in their middle part in order to locate the fracture in the central section which is a representative surface of the bulk morphology of the material.

3.2.4 DSC measurement

DSC measurements of the neat polymers and blends were performed using a Q10 (from TA Instuments) from -70 to 200°C. The samples were kept for 1 min at 200°C to erase the thermal history before being heated or cooled at a rate of 10 $K.min^{-1}$ under nitrogen flow (50 $mL.min^{-1}$). The glass temperature, T_g, was measured at the maximum of the derivative of the heat flow at the heat capacity change. The melting temperature, T_m, was measured from the maximum of the endothermic peak during heating. The crystallinity ratio, χ_{PBAT} [%], of PBAT/PLA blends was calculated from the melting enthalpy of fully crystalline PBAT, i.e. 114 $J.g^{-1}$ [39].

Table 3.3 – Melting and crystallization temperatures of neat PLA, PBAT, PBAT/PLA blends and PBAT/PLA blends with IL addition

Blend	T_g (°C) *PBAT*	T_g (°C) *PLA*	T_m (°C) *PBAT*	T_m (°C) *PLA*	ΔH_c [J/g]	ΔH_m [J/g]	χ_c [%] *PBAT*
PBAT	-34	—	121	—	17	14	13
PLA	—	63	—	—	—	—	—
PBAT/PLA	-28	61	119	—	9	15	13
PBAT/PLA/il-Cl	-29	60	122	—	15	8	7
PBAT/PLA/il-TMP	-28	57	124	150	16	4	3

3.3 Results and discussions

3.3.1 Thermal behavior of neat polymers and PBAT/PLA blends

DSC traces for the neat polymers, PBAT/PLA and PBAT/PLA/ILs blends are presented in Figure 3.2. DSC results, with calculated crystallinity ratio for the PBAT phase are shown in Table 3.3.

Comparing the PBAT/PLA blends with and without ILs, the main effects of the ILs relates to a decrease in PBAT crystallinity (-6 and -10% with il-Cl and il-TMP, respectively). In the case of PBAT/PLA/il-TMP, two types of PLA crystalline phases evidenced from two endothermic peaks close to 150°C, *i.e.* the ionic liquids induced crystalline morphisms.

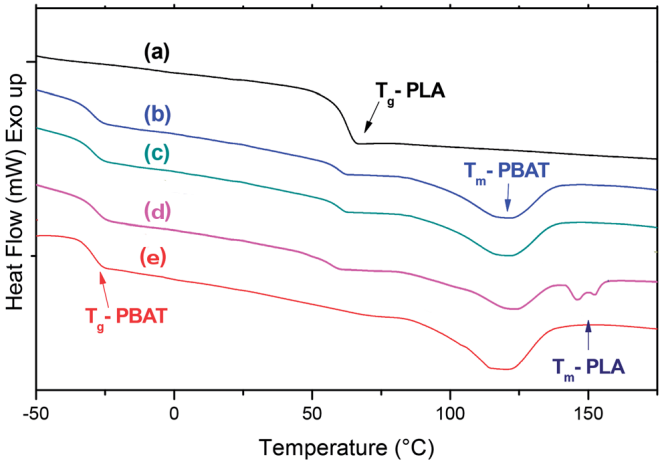

Figure 3.2 – DSC thermograms of (a) PLA, (b) PBAT/PLA, (c) PBAT/PLA/IL-Cl, (d) PBAT/-PLA/IL-TMP and (e) PBAT (heating rate: 10 K.min^{-1}).

3.3.2 Effects of ILs on the morphology of PBAT/PLA blends

The mapping of the DMT modulus shows a clear mechanical contrast in between the two polymer phases, *i.e.* PBAT and PLA, in the blends. For all the studied samples, two phases were clearly distinguished as PBAT is substantially softer (macroscopic Young's modulus : 40-50 MPa) compared to PLA (which exhibit a bulk Young's modulus of 3.5 GPa) [36].

Figure 3.3 shows 3.5×3.5 μm^2 maps of each blend surface, with on top the topographic scan and at the bottom the DMT modulus maps. On the latter ones, orange-white areas, relating to high DMT modulus values, correspond to the PLA phase, while the dark blue areas correspond to

the PBAT low-modulus matrix. The effect of the addition of ionic liquids on the microstructure of the blends was emphasized.

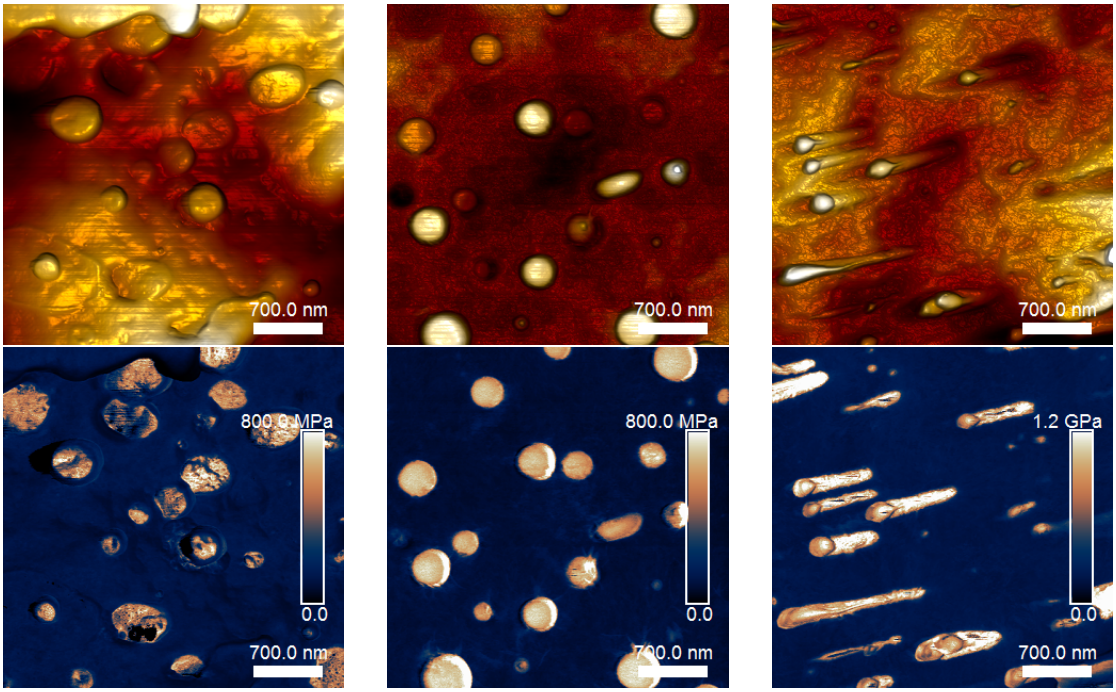

Figure 3.3 – AFM Height (top) and DMT Modulus (bottom) maps of a $3.5 \times 3.5\ \mu m^2$ region of a: (left) PBAT/PLA sample; (center) PBAT/PLA/il-Cl sample; (right) PBAT/PLA/il-TMP sample

In fact, the morphology of the PBAT/PLA neat blend (Figure 3.3—left) is common for blends based on non-miscible or only slightly miscible polymers, *i.e.* irregularly shaped PLA particles having a broad distribution of particle sizes. The addition of il-Cl (Figure 3.3—center) leads to more uniform and more spherical PLA droplets, while il-TMP–modified blend displays a PLA phase shaped as fibrils. These morphology features are in agreement with the previous studies by TEM of such blends [36].

The average particle size for each blend is summarized in Table 3.4. More than 40 nodules over several images were measured in their 2 dimensions (largest and lowest diameter), to achieve a statistical accuracy. In the case of the blend containing il-TMP, only the shortest dimension, *i.e.* the diameter of the fibril, was taken into account.

Table 3.4 – Average particle size of PBAT/PLA blends measured with AFM

Blend	Average particle size [nm]	Standard deviation [nm]
PBAT/PLA	357	196
PBAT/PLA/il-Cl	300	112
PBAT/PLA/il-TMP	250	96

The compatibilization mechanism is highlighted, first by the reduction of the average nodule or fibril diameter from more than 350 nm to 300 nm with the addition of il-Cl, and to 250 nm with il-TMP. In addition, the reduction of the standard deviation by almost a factor 2 with the addition of both ionic liquids shows a clear influence on homogeneity, *i.e.* a successful

compatibilization. Previous TEM results [36] show nodules sizes and dispersions within the same order of magnitude.

3.3.3 Effect of ILs on the mechanical properties of individual phases

Quantitative results of the DMT modulus on an AFM scan can be presented as modulus distributions, or histograms, of that modulus. Figure 3.4 shows typical DMT modulus distribution recorded on a single scan, for neat PBAT, PBAT/PLA and PBAT/PLA/ils blends.

In each case, the first narrow low-modulus peak corresponds to the quite homogeneous PBAT matrix. In the blends, another peak, lower in amplitude, appears at a higher DMT modulus (at about 1 GPa). It corresponds to the PLA dispersed phase.

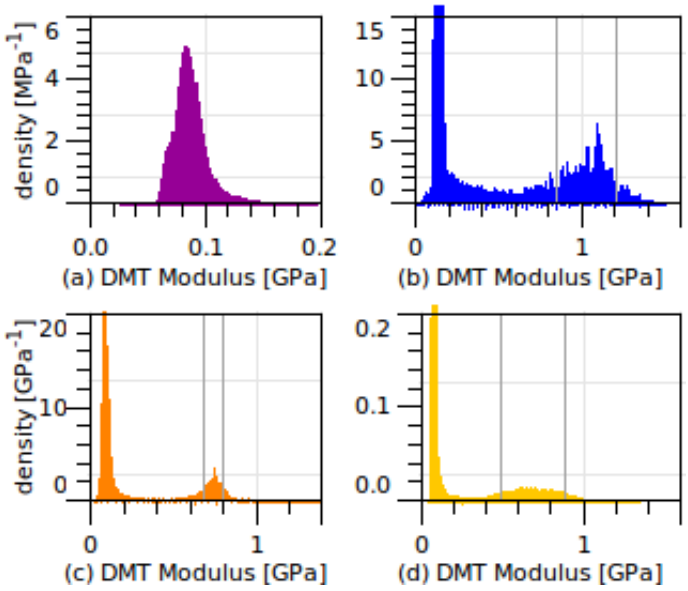

Figure 3.4 – Typical statistical distributions of the DMT modulus in (a) PBAT, (b) PBAT/PLA, (c) PBAT/PLA/il-Cl, and (d) PBAT/PLA/il-TMP blends. The dark gray vertical lines on (b), (c), and (d) represent the full width at half maximum of the peaks corresponding to the PLA phase.

As the shape of the distribution strongly depends on the scan path, *i.e.* on the proportion of each component encountered along the scan, no general conclusion can be taken from those single distributions. However, modulus values could be obtained separately for each phase by fitting each distribution peak with a gaussian curve. This was done on 6 scans at least for each blend, giving quantitative DMT modulus data on the phases.

PBAT phase (matrix).

Figure 3.5 shows the average DMT modulus (and standard deviations) obtained for neat PBAT and the blends by fitting the PBAT distribution peak.

First, it is interesting to notice that the neat PBAT DMT modulus obtained by AFM-QNM (*i.e.* 100 MPa) does not correspond to the Young's Modulus obtained from tensile tests (*i.e.* between 40 and 50 MPa [36, 33]). This difference issues from the fact that both moduli should be considered differently. In fact, the DMT modulus is measured very locally, while the Young's modulus considers a large volume of matter. Such a difference between nano- and macroscopic moduli was already reported in the litterature. For example, Perrin *et. al.* [17] observed larger

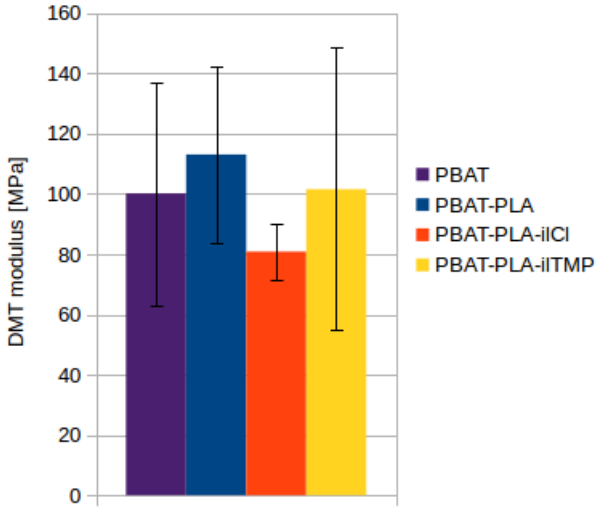

Figure 3.5 – Average DMT modulus for the PBAT phase of each blend and neat PBAT

moduli on PE-POSS nanocomposites when measured with AFM (ranging from 160 to 240 MPa) than with a tensile test (ranging from 105 to 125 MPa).

Nevertheless, from the comparison between the DMT moduli of the PBAT in the neat PBAT and in blends, the PBAT matrix of the PBAT/PLA blend seems to be slightly stiffer (+10%). This phenomenon can be attributed to a partial miscibility of PLA into the PBAT matrix which is confirmed by the increase of the glass transition temperature of the PBAT phase (Table 3.3) from -34°C to -28°C when PBAT is blended with PLA.

In contrast, the addition of 1% of il-Cl to the blend induced a decrease of the DMT modulus of the PBAT matrix. This change can be explained by a lower effect of the crystalline phase of this polyester as the ionic liquid hinders the nucleation of crystallization. In fact, the PBAT phase crystallinity rate decreases with the introduction of ionic liquids (Table 3.3). The lowest modulus value, obtained for the il-Cl modified blend, could be explained by the better interactions of this ionic liquids in PBAT compared to il-TMP modified one.

PLA phase.

DMT moduli for the PLA dispersed phase in the various PBAT/PLA blends are reported Figure 3.6.

The addition of ionic liquids tends to decrease the average PLA DMT modulus in the same order of magnitude for both ILs. Very slight plasticization was reported by Lins et. al. (Table 3.3), as a 1K decrease of the glass transition with the addition of il-Cl and 4K decrease with il-TMP. This phenomenon is in agreement with the previous conclusions. In fact, more favorable interactions of il-Cl with PBAT were observed, and on the opposite, il-TMP and PLA have better interactions.

Considering the gaussian fits of the PLA peak, the average full width at half maximum height is about 400 MPa for both PLAT/PLA and PBAT/PLA/il-TMP. For the non-modified PBAT/PLA blend, the broadness of the distribution peaks issued from the irregular shape of the nodular dispersed PLA phase. For the il-TMP modified blend, the existence of a crystalline PLA structure induces a more complex mechanical response, thus a broader distribution of DMT moduli. In the case of PBAT/PLA/il-Cl, narrower peaks (the average full width at half maximum

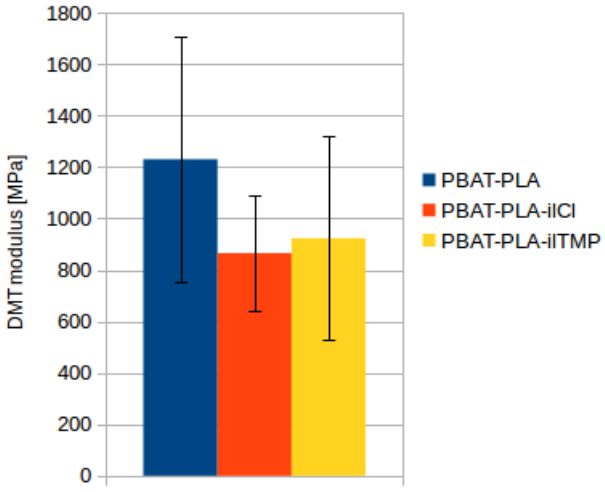

Figure 3.6 – Average DMT modulus for the PLA dispersed phase in each type of PBAT/PLA blends

decreases to 160 MPa) are the signature of a more homogeneous organization of the amorphous PLA phase.

Effect of il-TMP on PLA crystallinity : As shown by DSC results (Table 3.3), a crystalline structure appeared in the PLA phase of the blend containing il-TMP. A DMT modulus profile taken across a PLA fibril is shown in Figure 3.7. The low-modulus PBAT phase, the interfaces/phases (see next section), and the PLA phase (with a modulus higher than 600 MPa) can be easily identified. Nevertheless, the center of the PLA zone exhibits an even higher modulus, close to 1 GPa. The evidenceded crystalline structures having a melting point close to 150°C, is thus localized in the center of the fibril.

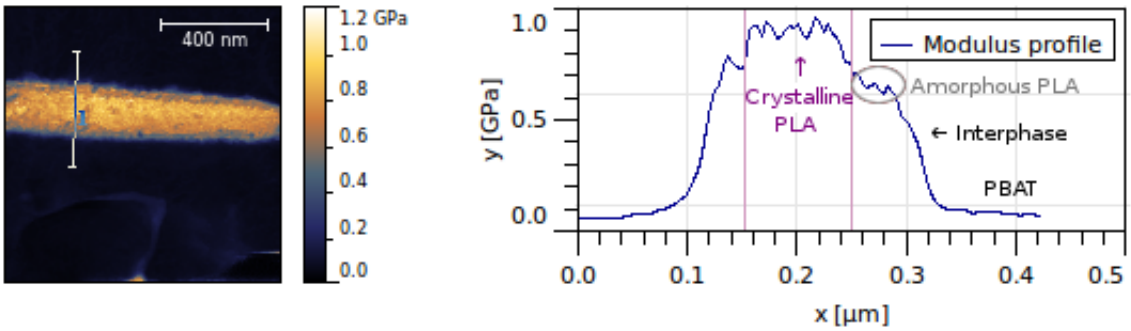

Figure 3.7 – DMT modulus map of a zone containing a PLA fibril in the PBAT/PLA/il-TMP blend, and corresponding modulus profile taken along the fibril section.

To summarize : on the one hand, the addition of ionic liquids tends to reduce the DMT modulus of the PLA phase in PBAT/PLA blends, but on the other hand, it leads to an opposite effect on the mechanical behavior at macroscale. In fact, the addition of 1% il-Cl induces an increase of the Young's modulus of +20%, and the same amount of il-TMP induces a +45% increase. In addition, the strain at break is about two times higher than for the neat PBAT/PLA in both IL-modified blends. Therefore, there is other factors of strengthening induced by ionic

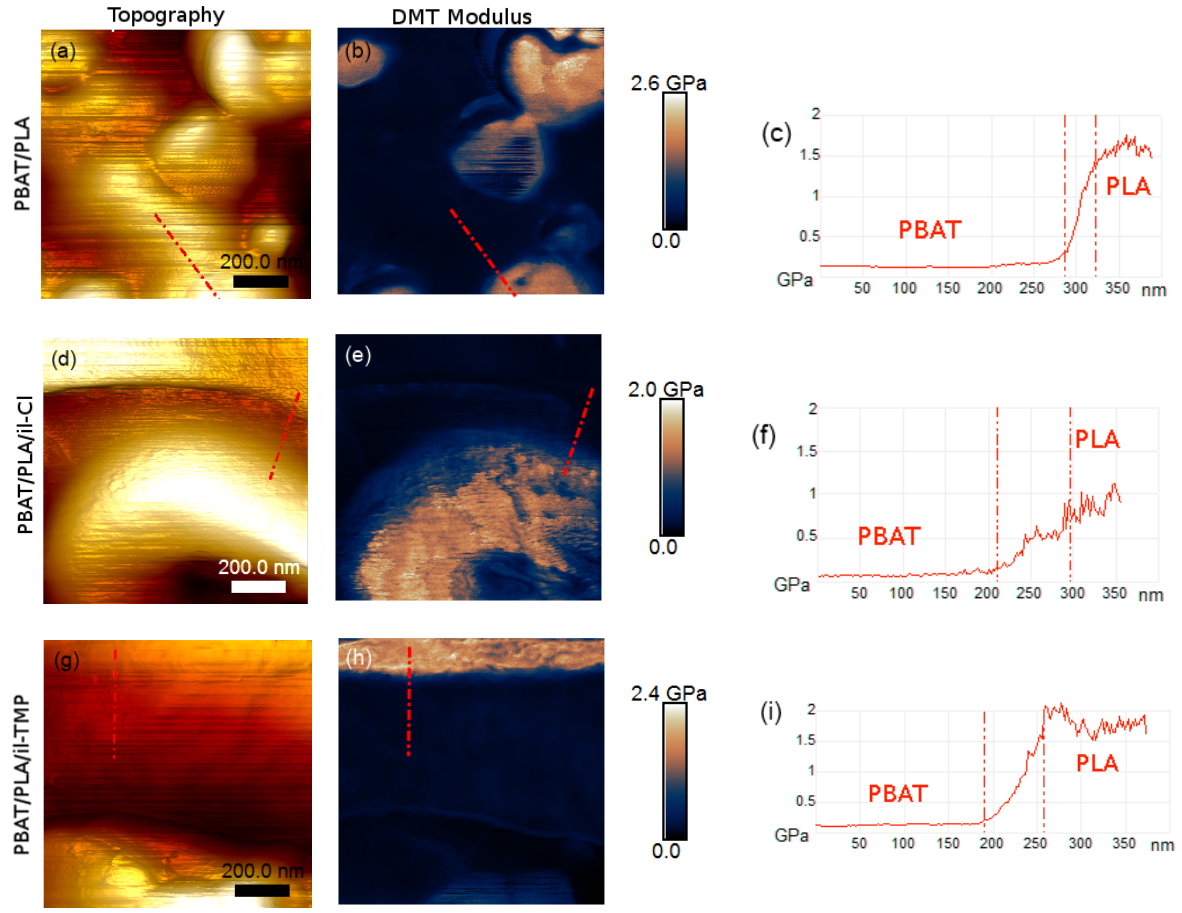

Figure 3.8 – AFM 1×1 μm^2 topography (left) and DMT modulus (center) images with corresponding modulus profiles for PBAT/PLA : (a), (b) and (c); PBAT/PLA/il-Cl : (d), (e) and (f); PBAT/PLA/il-TMP : (g), (h) and (i). The modulus profile are taken following the red dashed line in (b), (e) and (h).

liquids. Obviously, the microstructuration of the blends, particularly in the case of the PLA fibrils generated from the use of il-TMP, plays an important role on the macroscopic Young's Modulus. Nevertheless, such an improvement could not be totally explained by the geometrical description of the dispersed phase, *i.e.* size and shape distributions. As a consequence, a special attention could be paid on the interface between the two polymers which is reported in the following section. Interpretations are discussed in section 3.3.5.

3.3.4 Effect of ILs on the interfaces

Extent of interfacial zone from DMT modulus changes.

It was chosen to define the interfacial zone or interphase between PBAT and PLA phases from the changes of the DMT modulus, *i.e.* the extent of the transition corresponding to the change of the DMT modulus between two stable values. Along a profile (see Figure 3.8 for examples of various profiles), the thickness of this interfaciel zone can be measured, and the DMT modulus transition can be considered as linear which can be quantified from the slope of DMT modulus vs. distance curve, dE_{DMT}/dx (where x is the distance). This slope relates to the degree of local

miscibility of the two phases (the lower slope value corresponds to the higher miscibility) and defines the interfacial zone or interphase thickness. Along more than 20 profiles for each blend, interface thicknesses and DMT modulus slopes were measured. The average results are reported in Table 3.5.

Table 3.5 – Average interface thickness and DMT modulus slope for each blend

Blend	Interphase thickness [nm]	dE_{DMT}/dx [MPa/nm]
PBAT/PLA	43 ± 17	32 ± 11
PBAT/PLA/il-Cl	88 ± 38	13 ± 8
PBAT/PLA/il-TMP	63 ± 19	22 ± 12

Clearly, the addition of ionic liquids tends to make the interfaces thicker compared to neat PBAT/PLA interfacial zone. il-TMP addition leads to interphases which are +45% thicker while il-Cl induces two times thicker interphase, in comparison with the non-modified PBAT/PLA blend. The lower DMT modulus slope indicates that the phases may be locally miscible because of the ionic liquid which is probably located in the interfaciel zone. Thus, one can propose that an interphase is generated from the localization of the IL in between the two phases.

This structuration of IL-modified blends may be the key process to explain the improvements observed at the macroscopic scale, *i.e.* increase of both Young's modulus and strain at break. Macromolecular mechanisms governing the interphase behavior will be discussed later.

Localization of ionic liquids in the PBAT/PLA blends.

The previous results suggest that the ionic liquids are localized at the interface. To confirm this idea, the same images and profile lines shown in Figure 3.8 are presented in Figure 3.9 with adhesion force maps instead of DMT modulus images. On the profiles the marks are the same as in Figure 3.8, quantifying the interphase thickness from the length of the DMT modulus step change.

It is important to notice that the measured adhesion force can be highly influenced by the topographic variations : the contact area between tip and sample may increase, inducing a locally higher measured adhesion force, only caused by topography. Therefore, the adhesion analysis was always done along profiles in which the topography remains flat enough to avoid significant modifications of the tip-sample contact area. An example of this effect is noticeable in Figure 3.9 (b) : on the right side of the scan, some zones display high adhesion while there is nothing more than PBAT and PLA. Those areas correspond in Figure 3.9 (a) to steep height variations influencing the adhesion measure.

In the PBAT/PLA blend (Figure 3.9 (a), (b) and (c)), the adhesion force varies as a step through the interphase. The PLA phase being less adhesive (or less likely to interact with the AFM tip), the adhesion force drops just before the DMT modulus step (see Figure 3.8 (c), using the same markers as in Figure 3.9). PBAT displays adhesion between 15 and 20 nN with the AFM tip as PLA leads to a value close to 10 nN.

In the blend containing il-Cl, a 150 nm wide adhesive zone is visible in Figure 3.9 (f). This one is almost two times larger than the modulus-defined interphase (see markers). Since no other component is present in the blend, and both PBAT and PLA do not exceed 20 nN of adhesion, such an observation confirms the presence of il-Cl at the interface. One can notice that the adhesion phenomenon tends to be localized on the PBAT side which confirms better interactions of il-Cl with PBAT than PLA as reported previously.

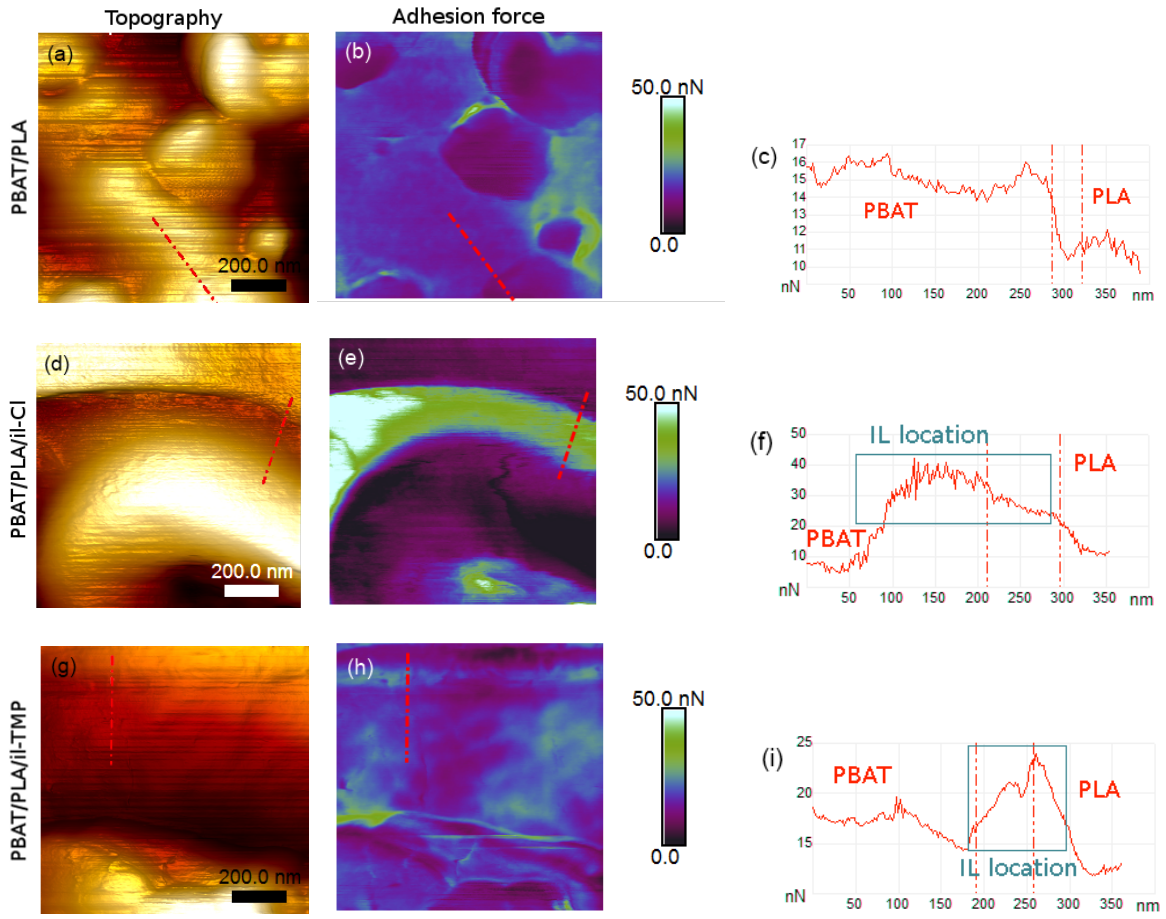

Figure 3.9 – AFM $1 \times 1\ \mu m^2$ topography (left) and adhesion (center) images with corresponding profiles for PBAT/PLA : (a), (b) and (c); PBAT/PLA/il-Cl : (d), (e) and (f); PBAT/PLA/il-TMP : (g), (h) and (i). The adhesion profile are taken following the red dashed line in (b), (e) and (h) and the analyzed zones are the same as in Figure 3.8.

As shown in Figure 3.9 (h) and (i), the PBAT/PLA blend containing il-TMP also exhibits an adhesion peak at the interface between PBAT and PLA which is weaker than in the previous case. The adhesion maximum is, for this il-TMP modified blend, localized on the PLA side of the interphase. Again, this observation confirms the better interactions of il-TMP phosphinate anion with PLA than PBAT as reported previously. According to the increase of the PLA crystallinity in the il-TMP modified PBAT/PLA blend, one can suppose that a small fraction of the ionic liquid is also located into the PLA phase.

In summary, the study of adhesion confirms a preferential localization of ILs in the interphase between the two components of the blend. Low amount of the ionic liquids may also be localized into one polymer phase, depending on the affinity of the IL with one polymer component.

3.3.5 Discussions

In the non-compatibilized PBAT/PLA blend, the poor interactions between PBAT matrix and PLA dispersed phase leads to interfaces which act as weak components under mechanical stress application. As an ionic liquid is added to such a blend, this one localizes at the interface and plays the role of interfacial agent interacting with both polymers. However, il-Cl and il-TMP

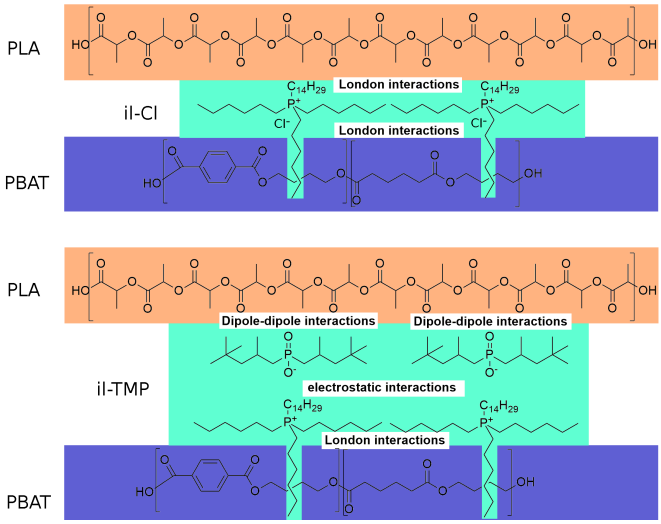

Figure 3.10 – Schematic representation of interactions between PLA and PBAT with the addition of IL-Cl (top) and il-TMP (bottom)

exhibit different behaviors indicating that the counter anion, chloride or phosphinate, leads to specific interactions with one of the polyester, *i.e.* PLA or PBAT.

In the case of il-Cl, the large influence on the interphase thickness is in agreement with the fact that the PBAT/PLA/il-Cl blend displays the highest strain at break (i.e. 1,000%). In fact, due to its small size, the chloride anion can easily be attracted by its counterpart, *i.e.* the phosphonium cation, and more specifically the central phosphorous, and do not play a relevant role in the compatibilization process (see Figure 3.10). One can emphasize the important role of the aliphatic chains of the cation which could interact with the alkyl segments in PBAT (Figure 3.1). Such an hypothesis is consistent with its preferential presence on the PBAT side of the interface. According to its better affinity with PBAT than the PLA polymer, the phosphonium cation allows a better local miscibility of the phases (hence the increased interphase extent), leading to a diffuse interphase resulting in continuous interactions of the chains under strain.

Il-TMP seems to have a lower influence on the miscibility and as a consequence on the mechanical behavior at large strains, *i.e.* on the strain at break. The stiffness (Young's modulus) of the PBAT/PLA/il-TMP is improved due to the fibrillar shape of the PLA phase. At the molecular scale, the structure of the TMP anion makes it more likely to form Keesom interactions with the ester groups of both polymers (see Figure 3.10). As PLA has a higher density of ester groups, il-TMP has to be preferentially located on the PLA side of the interphase. As a consequence, the interface may consist then in a cationic outer layer, interacting with the alkyl segments of PBAT, and an anionic inner layer, interacting with the ester groups of PLA. Furthermore, the inner phosphinate layer may have an influence on the organization of PLA chains which can explain the crystalline structure in the bulk of the fibril.

Figure 3.11 summarizes the proposed molecular structures for each blend.

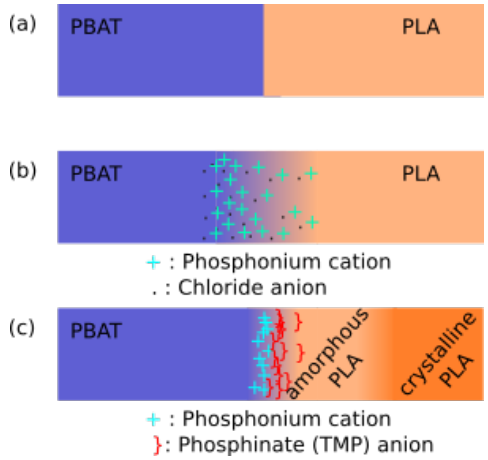

Figure 3.11 – Schema of the interface structure for (a) PBAT/PLA, (b) PBAT/PLA/il-Cl and (c) PBAT/PLA/il-TMP

3.4 Conclusions

Nanomechanical properties mapping of PBAT/PLA blends compatibilized with ionic liquids were performed, exploring the differences induced by the nature of the counter anion for a given phosphonium–based ionic liquid. AFM QNM mode constitutes an outstanding method to understand the nanoscale structure and to investigate interfacial interactions involved in the compatibilization process, without requiring delicate sampling. The macroscopic mechanical properties improvement was successfully explained from molecular and nanoscale phenomena observed with AFM.

The mechanical stiffness contrast gave access to the different induced nanostructures. Non-compatibilized blends exhibited an irregular nodular organization of the dispersed PLA phase, while with the addition of 1% phosphonium-based ionic liquid, the distribution of particle sizes became narrower. From the addition of a chloride anion, regular spherical PLA droplets of about 300 nm in diameter were observed. With the phosphinate (TMP) anion, regular PLA fibrils were formed. A crystalline PLA structure induced by il-TMP and identified using DSC was observed and localized in the bulk of the PLA fibrils.

Quantitative DMT modulus mappings highlighted a decrease of the nanoscale DMT modulus of both phases with the addition of ionic liquids, especially with il-Cl. Consequently, the Young's modulus (which is measured at the macroscale) increase could be explained by more favorable interfacial interactions between PBAT and PLA mediated by the ionic liquid. DMT modulus and adhesion data analysis confirmed this assumptions. il-Cl leds to a two times thicker interphase inducing a better local miscibility of PBAT and PLA phases, explaining the improvement of the macroscopic mechanical properties such as the strain at break. Il-TMP induced a slighter effect on the local miscibility, but formed an interface layer ensuring interactions with both polymers. Adhesion force mapping confirmed the preferential presence of ionic liquids at the interface (but in a different side of the interface for il-TMP and il-Cl). Ionic liquids were also localized in the polymer phases in a lower concentration which could contribute to modify the crystalline structures. In fact, both il-Cl and il-TMP led to a reduction of the PBAT crystallinity, while il-TMP helped the nucleation of a crystalline structure into the PLA fibrils. In addition to the basic understanding of the morphology of these specific polymer blends, this study confirms that ionic liquids can offer new routes for compatibilization of polymer blends.

The PeakForce QNM AFM mode was revealed to be a powerful tool to access to the very local mechanical properties with a remarkably easy sample preparation. The method described in this chapter opens a new path for a better understanding of the nanoscale behavior of blends and composites, *i.e.* to design and tailor their functional properties from nanoscale.

Bibliography

[1] G. Binnig, C. F. Quate, and C. Gerber. Atomic force microscope. *Physical Review Letters*, 56:930–933, March 1986.

[2] Jian Zhong and Juan Yan. Seeing is believing: atomic force microscopy imaging for nanomaterial research. *RSC Adv.*, 6:1103–1121, 2016.

[3] Q Zhong, D Inniss, K Kjoller, and VB Elings. Fractured polymer/silica fiber surface studied by tapping mode atomic force microscopy. *Surface Science Letters*, 290(1):L688–L692, 1993.

[4] M. R. Vanlandingham, S. H. McKnight, G. R. Palmese, J. R. Elings, X. Huang, T. A. Bogetti, R. F. Eduljee, and J. W. Gillespie Jr. Nanoscale indentation of polymer systems using the atomic force microscope. *The Journal of Adhesion*, 64(1-4):31–59, 1997.

[5] M. R. Vanlandingham, S. H. McKnight, G. R. Palmese, R. F. Eduljee, J. W. Gillespie, and JR. R. L. McCulough. Relating elastic modulus to indentation response using atomic force microscopy. *Journal of Materials Science Letters*, 16(2):117–119, 1997.

[6] Feng Zhao, Yudong Huang, Li Liu, Yongping Bai, and Liwei Xu. Formation of a carbon fiber/polyhedral oligomeric silsesquioxane/carbon nanotube hybrid reinforcement and its effect on the interfacial properties of carbon fiber/epoxy composites. *Carbon*, 49(8):2624 – 2632, 2011.

[7] B. Pittenger, N. Erina, and C. Su. *Application Note AN128*. Bruker Corporation, 2012. `www.bruker-nano.com`.

[8] G. Smolyakov, S. Pruvost, L. Cardoso, B. Alonso, E. Belamie, and J. Duchet-Rumeau. {AFM} peakforce {QNM} mode: Evidencing nanometre-scale mechanical properties of chitin-silica hybrid nanocomposites. *Carbohydrate Polymers*, 151:373 – 380, 2016.

[9] T J Young, M A Monclus, T L Burnett, W R Broughton, S L Ogin, and P A Smith. The use of the peakforce tm quantitative nanomechanical mapping afm-based method for high-resolution young's modulus measurement of polymers. *Measurement Science and Technology*, 22(12):125703, 2011.

[10] Dong Wang, Yanhui Liu, Toshio Nishi, and Ken Nakajima. Length scale of mechanical heterogeneity in a glassy polymer determined by atomic force microscopy. *Applied Physics Letters*, 100(25), 2012.

[11] Peter Schön, Kristóf Bagdi, Kinga Molnár, Patrick Markus, Béla Pukánszky, and G. Julius Vancso. Quantitative mapping of elastic moduli at the nanoscale in phase separated polyurethanes by {AFM}. *European Polymer Journal*, 47(4):692 – 698, 2011. Designer polymers: Controlled synthesis, structure-property relationships and applications (Dedicated to Professor Nikos Hadjichristidis in recognition of his contribution to polymer science).

[12] Mariusz Kłonica, Józef Kuczmaszewski, Michał P. Kwiatkowski, and Janusz Ozonek. Polyamide 6 surface layer following ozone treatment. *International Journal of Adhesion and Adhesives*, 64:179 – 187, 2016.

[13] Ilya A. Morozov, Alexander S. Mamaev, Irina V. Osorgina, Larisa M. Lemkina, Vladimir P. Korobov, Anton Yu Belyaev, Svetlana E. Porozova, and Marina G. Sherban. Structural–mechanical and antibacterial properties of a soft elastic polyurethane surface after

plasma immersion n2+ implantation. *Materials Science and Engineering: C*, 62:242 – 248, 2016.

[14] Marius Chyasnavichyus, Seth L. Young, and Vladimir V. Tsukruk. Mapping micromechanical properties of soft polymer contact lenses. *Polymer*, 55(23):6091 – 6101, 2014.

[15] Dong Wang, Thomas P. Russell, Toshio Nishi, and Ken Nakajima. Atomic force microscopy nanomechanics visualizes molecular diffusion and microstructure at an interface. *ACS Macro Letters*, 2(8):757–760, 2013.

[16] Denis Mihaela Panaitescu, Zina Vuluga, Constantin Radovici, and Cristian Nicolae. Morphological investigation of pp/nanosilica composites containing {SEBS}. *Polymer Testing*, 31(2):355 – 365, 2012.

[17] Francois Xavier Perrin, Denis Mihaela Panaitescu, Adriana Nicoleta Frone, Constantin Radovici, and Cristian Nicolae. The influence of alkyl substituents of {POSS} in polyethylene nanocomposites. *Polymer*, 54(9):2347 – 2354, 2013.

[18] Denis Mihaela Panaitescu, Adriana Nicoleta Frone, and Ilie Catalin Spataru. Effect of nanosilica on the morphology of polyethylene investigated by {AFM}. *Composites Science and Technology*, 74:131 – 138, 2013.

[19] Shib Shankar Banerjee, Kotnees Dinesh Kumar, Arun K. Sikder, and Anil K. Bhowmick. Nanomechanics and origin of rubber elasticity of novel nanostructured thermoplastic elastomeric blends using atomic force microscopy. *Macromolecular Chemistry and Physics*, 216(15):1666–1674, 2015.

[20] Laida Cano, Junkal Gutierrez, and Agnieszka Tercjak. Enhancement of the mechanical properties at the macro and nanoscale of thermosetting systems modified with a polystyrene-block-polymethyl methacrylate block copolymer. *RSC Adv.*, 5:102085–102095, 2015.

[21] Adriana N. Frone, Sophie Berlioz, Jean-François Chailan, and Denis M. Panaitescu. Morphology and thermal properties of pla–cellulose nanofibers composites. *Carbohydrate Polymers*, 91(1):377 – 384, 2013.

[22] Balázs Imre, Dániel Bedő, Attila Domján, Peter Schön, G. Julius Vancso, and Béla Pukánszky. Structure, properties and interfacial interactions in poly(lactic acid)/polyurethane blends prepared by reactive processing. *European Polymer Journal*, 49(10):3104 – 3113, 2013.

[23] Emily D. Cranston, Mohamed Eita, Erik Johansson, Julia Netrval, Michaela Salajková, Hans Arwin, and Lars Wågberg. Determination of young's modulus for nanofibrillated cellulose multilayer thin films using buckling mechanics. *Biomacromolecules*, 12(4):961–969, 2011. PMID: 21395236.

[24] Denis Mihaela Panaitescu, Adriana Nicoleta Frone, and Cristian Nicolae. Micro- and nano-mechanical characterization of polyamide 11 and its composites containing cellulose nanofibers. *European Polymer Journal*, 49(12):3857 – 3866, 2013.

[25] Farid Khelifa, Youssef Habibi, Philippe Leclere, and Philippe Dubois. Convection-assisted assembly of cellulose nanowhiskers embedded in an acrylic copolymer. *Nanoscale*, 5:1082–1090, 2013.

[26] Anahita Pakzad, John Simonsen, and Reza S. Yassar. Gradient of nanomechanical properties in the interphase of cellulose nanocrystal composites. *Composites Science and Technology*, 72(2):314 – 319, 2012.

[27] M. Vert, G. Schwarch, and J. Coudane. Present and future of pla polymers. *Journal of Macromolecular Science, Part A*, 32(4):787–796, 1995.

[28] Kelly S. Anderson, Shawn H. Lim, and Marc A. Hillmyer. Toughening of polylactide by melt blending with linear low-density polyethylene. *Journal of Applied Polymer Science*, 89(14):3757–3768, 2003.

[29] Chang-Hong Ho, Chau-Hui Wang, Chin-I. Lin, and Yu-Der Lee. Synthesis and characterization of tpo–pla copolymer and its behavior as compatibilizer for pla/tpo blends. *Polymer*, 49(18):3902 – 3910, 2008.

[30] Hua Yuan, Zhiyong Liu, and Jie Ren. Preparation, characterization, and foaming behavior of poly(lactic acid)/poly(butylene adipate-co-butylene terephthalate) blend. *Polymer Engineering & Science*, 49(5):1004–1012, 2009.

[31] Mukesh Kumar, S. Mohanty, S.K. Nayak, and M. Rahail Parvaiz. Effect of glycidyl methacrylate (gma) on the thermal, mechanical and morphological property of biodegradable pla/pbat blend and its nanocomposites. *Bioresource Technology*, 101(21):8406 – 8415, 2010.

[32] Racha Al-Itry, Khalid Lamnawar, and Abderrahim Maazouz. Improvement of thermal stability, rheological and mechanical properties of pla, {PBAT} and their blends by reactive extrusion with functionalized epoxy. *Polymer Degradation and Stability*, 97(10):1898 – 1914, 2012. 3rd International Conference on Biodegradable and Biobased Polymers (BIOPOL-2011) - Strasbourg 2011.

[33] Sebastien Livi, Valeria Bugatti, Bluma Guenther Soares, and Jannick Duchet-Rumeau. Structuration of ionic liquids in a poly(butylene-adipate-co-terephthalate) matrix: its influence on the water vapour permeability and mechanical properties. *Green Chem.*, 16:3758–3762, 2014.

[34] Sebastien Livi, Gabriela Sar, Valeria Bugatti, Eliane Espuche, and Jannick Duchet-Rumeau. Synthesis and physical properties of new layered silicates based on ionic liquids: improvement of thermal stability, mechanical behaviour and water permeability of pbat nanocomposites. *RSC Adv.*, 4:26452–26461, 2014.

[35] Sebastien Livi, Valeria Bugatti, Manuel Marechal, Bluma G. Soares, Guilherme M. O. Barra, Jannick Duchet-Rumeau, and Jean-Francois Gerard. Ionic liquids-lignin combination: an innovative way to improve mechanical behaviour and water vapour permeability of eco-designed biodegradable polymer blends. *RSC Adv.*, 5:1989–1998, 2015.

[36] Luanda C. Lins, Sebastien Livi, Jannick Duchet-Rumeau, and Jean-Francois Gerard. Phosphonium ionic liquids as new compatibilizing agents of biopolymer blends composed of poly(butylene-adipate-co-terephtalate)/poly(lactic acid) (pbat/pla). *RSC Adv.*, 5:59082–59092, 2015.

[37] B.V Derjaguin, V.M Muller, and Yu.P Toporov. Effect of contact deformations on the adhesion of particles. *Journal of Colloid and Interface Science*, 53(2):314 – 326, 1975.

[38] Bruker Corporation. *PeakForce QNM User Guide (Revision E)*, 2011.

[39] Ricard Herrera, Lourdes Franco, Alfonso Rodríguez-Galán, and Jordi Puiggalí. Characterization and degradation behavior of poly(butylene adipate-co-terephthalate)s. *Journal of Polymer Science Part A: Polymer Chemistry*, 40(23):4141–4157, 2002.

Chapter 4

AFM study: Structuration of ionic liquids in PBAT

Contents

This chapter corresponds to a paper currently submitted under the title "Advanced characterization of the structuration of ionic liquids in a copolyester using atomic force microscopy".

Abstract

The influence of the addition in small amounts (2wt%) of two phosphonium–based ionic liquids (ILs) on the nanostructuration and mechanical properties of a poly(butylene-adipate-*co*-terephtalate) (PBAT) matrix was investigated using complementary approaches. Advanced characterization techniques, *i.e.* dielectric spectroscopy and nanomechanical characterizations using atomic force microscopy (PeakForce QNM mode, Bruker) were used along X-ray diffraction, differential scanning calorimetry and dynamic mechanical analysis to explain the mechanical (tensile) properties of each blend. The semicrystalline matrix was found to have a spherulitic structure, with crystalline lamellae composed of butylene terephtalate units. In one case, the addition of an immiscible phosphonium-phosphinate ionic liquid (il-TMP) to the matrix, inducing a 33% increase of the strain at break, was found via AFM to induce a nodular microstructure with dissipative effects and smooth nodule-matrix interphases. In the other case, a phosphonium-chloride ionic liquid (il-Cl) generated a complex structuration effect on the matrix: being miscible in the amorphous phases, it increases the chain mobility, as would do a plasticizer, of the mobile amorphous phase (MAF) consisting of free polymer chains, while it hinders the relaxation, thus chain movements, of the rigid amorphous phase (RAF), *i.e.* PBAT chains that are partially anchored in the crystalline phase, or confined between crystalline lamellae. This double effect induced a moderate macroscopic Young's modulus drop (less than -20%) with a +60% increase of the strain at break, and almost no influence on thermal properties. AFM *in situ* mechanical measurements, along with dielectric spectroscopy, allowed to propose complete mechanisms for the ILs-matrix interactions, highlighting the potential of such additives for the tuning of the properties of polymers.

4.1 Introduction

In polymer science, developing ways to design, tailor and adjust properties of existing materials is a major challenge. The main routes to modify such properties are via the processing of the polymer, by acting on its physical structuration and/or on phenomena such as phase separation, or via the formulation with additives, adding physical or chemical interactions that can modify the final properties.

The use of ionic liquids (ILs) represents a novel route to modify the structure and properties of polymers [1]. The numerous existing cation-anion combinations make them suitable for various applications: they have been used as plasticizers [2, 3, 4], solvents for cellulose [5], intercalating agents for bio/nanocomposites with clays [6], compatibilizers for biopolymer blends [7], as well as reagents and parts of thermoset networks [8]. Ionic liquids have also shown promising capabilities for the nanostructuration of polymer systems such as fluorinated copolymers, in which a tunable effect on the crystallization behavior, on the dispersion morphology and on the crystalline phase structure have been reported by Yang *et al.* [9].

This has been particularly useful in the field of biopolymers, where the capability to modify the properties is a critical issue: in order to propose an alternative to traditional oil–based polymers, the goal is to be able to tune the properties of biopolymers to obtain materials that are equivalent.

A key to that issue is to understand completely the mechanisms that link formulations and processes to functional properties, at every scale of the material. Atomic Force Microscopy [10] is a particularly useful tool to investigate the properties of materials at nanoscale with an outstanding resolution. The intermittent contact of an extremely sharp tip with the sample surface allows to gather informations about its local properties [11], and the capability to acquire force curves [12, 13] led recently to the development of PeakForce QNM (Bruker, USA), an AFM mode allowing a high–resolution mapping of mechanical properties of surfaces [14].

This has already allowed promising results for the understanding of the structure-properties links of polymers [15, 16]. The technique gives access to the mechanical behavior at a nanoscopic scale, by mapping properties such as the tip-sample adhesion force, the local elastic modulus or the energy dissipation. A better understanding and vizualization of various phenomena could be achieved, for instance the creation via annealing of an interphase between two blended immiscible polymers [17], or the surface properties changes due to surface treatments [18] or photo-oxidation [19].

In this study, the effects of some phosphonium–based ionic liquids on a biodegradable matrix are investigated. The poly(butylene-adipate-*co*-terephtalate) (PBAT) is an aliphatic-aromatic copolyester used in various forms, from films to fibers [20] in fields such as medicine, agriculture and food packaging [21]. The use of PBAT has been revealed to be very promising in fully biodegradable blends [22, 23] and composites [24]. In those particular fields, phosphonium ionic liquids have also already shown a good potential with PBAT, for their compatibilizing and/or intercalating properties to design nanocomposites with clays [25, 26], lignine [27] and blends with PLA [7, 28].

Given the wide field of applications of the PBAT/ILs combinations, it is proposed in the present work to go deeper in the characterization of their mutual interactions, choosing two ILs that are already known for their different behavior when blended with PBAT. As a starting point, it is chosen to focus on the modification of tensile mechanical properties induced by the addition of 2wt% of a ionic liquid, as reported by Livi *et al.* [29] and represented in Figure 4.1. The further analysis aims to explain, for both ionic liquid, its effect on the matrix to reach such modifications of mechanical properties: an increase of the strain at break, from 510% (neat PBAT) to 810% and 680% with il-Cl and il-TMP, respectively, and a modulus drop from 47 to 40 MPa with il-Cl.

AFM nanomechanical mappings already demonstrated their capabilities to highlight the link between structure and properties on both biopolymers [30, 31, 32] and polymer structures blended with ionic liquids [33, 28]. The combination of this technique with dielectric spectroscopy having shown promising results for polymer–based materials [34], it is used here to elucidate the interaction between PBAT and the ILs and propose an action mechanism.

4.2 Experimental

4.2.1 PBAT/ILs blends

Poly(butylene-adipate-co-terephtalate) (PBAT) was supplied by BASF Co. (Germany) under the trade name of Ecoflex®. It is a statistical copolymer with 50% butylene adipate (PBA) and 50% butylene terephtalate (PBT) segments.

The two ionic liquids based on a trihexyltetradecyl phosphonium cation with two different anions (*i.e.* chloride denoted il-Cl and bis-2,4,4-(trimethylpentyl)phosphinate denoted il-TMP) were provided by Cytec Industries Inc. They are in a liquid state at ambient temperature and

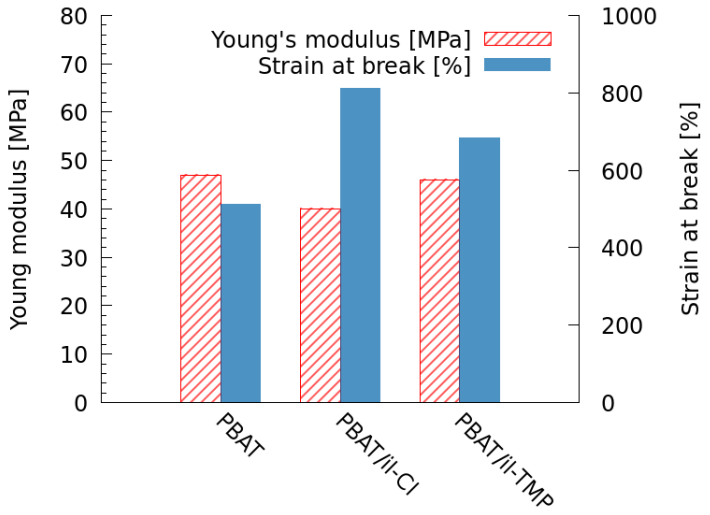

Figure 4.1 – Tensile properties of the blends measured by Livi et al. [29]

at any temperature range used in this study. The chemical structures of the matrix and ionic liquids are summarized in Table 4.1.

Table 4.1 – Designation and structure of the components considered in this study

Nomenclature	Chemical Structure
PBAT matrix:	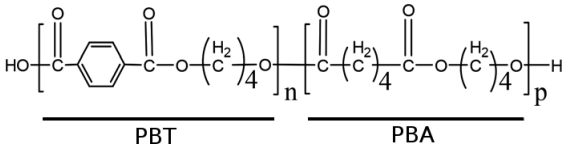
Ionic Liquids:	
il-Cl	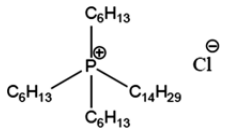
il-TMP	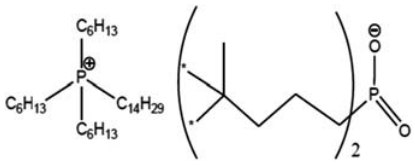

Processing of PBAT with and without ILs

All the samples used in this study were prepared by twin screw extrusion and injection molding, as a simple and scalable process. Ionic liquids were introduced in low amounts (2% wt) and the blends were processed at 160°C and 100 rpm with a 100 rpm rotation for about 3 minutes (the same was done for the neat PBAT matrix) using a 15 g–capacity DSM micro-extruder (Midi 2000 Heerlen, NL) [29].

Dielectric spectroscopy samples The samples used for dielectric spectroscopy were injected into a 1 mm thick disk mold (diameter: 32.5 mm) at 60°C. Circular gold electrodes were sputtered on both sides of the samples using a mask (diameter: 25 mm), applying 30 mA during 300 s for each side.

AFM, DMA and XRD samples The samples used for DMA, XRD and AFM characterizations were obtained from dumbbell-shaped specimens, injected the same way as for the disks described above. For XRD, the wide extremities were used, while for AFM and DMA samples the center beam was preferred.

The surfaces for AFM mappings were prepared via microtomy at -130°C along the cross-section of the beams to get a smooth surface without affecting the microstructure.

Density measurements

Volumetric mass density measurements were performed using an hydrostatic weighing system provided by Mettler Toledo, used on a Mettler Toledo precision weighing scale. The samples are precisely weighed in air and in water, and the volumetric mass ρ_{sample} is given by equation 4.1. All the samples studied here have a higher density than water, so their weight in water can be measured.

$$\rho_{sample} = \frac{\rho_{water}}{1 - \frac{m_w}{m_{air}}} \tag{4.1}$$

Where ρ_{water} is the volumetric mass of water at room temperature (998.29 kg.m^{-3} at 20°C), m_w the weight of the sample in water and m_{air} the weight of the dry sample in air.

4.2.2 Atomic Force Microscopy

The AFM mappings were carried out using a Multimode 8 scanning probe microscope (Bruker, Santa Barbara, USA) with a Nanoscope V controller under ambient conditions. To map mechanical properties such as local modulus and adhesion forces, the PeakForce QNM mode (Quantitative NanoMechanics) was used. Mechanical properties such as adhesion force and local modulus could be mapped, by applying the Derjaguin-Müller-Toporov (DMT) contact theory to model the geometry and behavior of the tip-sample contact [35]. The Johnson-Kendall-Roberts model (JKR) could also be used [36], but the most relevant for polymers is a theoretical transitory model between JKR and DMT which is not numerically applicable [37, 38]. The DMT model is implemented in the AFM software and, being relevant for the purpose of this study, it is chosen here. The contact modulus E^* is defined by equation 4.2.

$$\frac{1}{E^*} = \left(\frac{1-\nu_1^2}{E_1}\right) + \left(\frac{1-\nu_2^2}{E_2}\right) \tag{4.2}$$

where E_1 and E_2 represent the modulus of the silicon tip and of the sample surface, respectively, while ν_1 and ν_2 represent their respective Poisson's ratio. The DMT model predicts the relation given by equation 4.3, allowing to calculate mechanical properties at each pixel of an AFM image.

$$F = \frac{4}{3}E^*\sqrt{Rd^3} + F_{adh} \tag{4.3}$$

where F is the applied force, F_{adh} the adhesion force, R the tip radius, d the tip-sample distance and E^* the equivalent contact modulus.

The Al-coated[1] TAP150 probe with an aluminium coating was used (nominal spring constant: 5 N/m). Prior to each measurements session, the deflection sensitivity was measured on a hard sapphire surface. The spring constant was calibrated using a thermal tuning method and the tip radius was evaluated using a reference sample of known modulus (amorphous and homogeneous polystyrene film), as suggested by the *relative calibration* method [14].

4.2.3 X-ray diffraction

Wide angle X-Ray diffraction (WXRD) analysis was carried out using a X-Ray diffractometer (D8 Advance, Bruker, USA) with a Cu radiation source operated at 40 kV and 40 mA.

The diffractograms were treated using Fityk (version 1.2.1) [39]. Each peak was fitted using a gaussian or pseudo-Voigt profile[2] to gather every parameter to apply Scherrer's equation:

$$d = \frac{K\lambda}{\beta.cos(\theta)} \tag{4.4}$$

λ being the X-ray wavelength (for a copper source, $\lambda = 1.5418$ Å), β the full width at half maximum of the peak and θ being Bragg's angle. K is a dimensionless factor linked to the shape of the crystallites. Its value for polybutylene terephtalate (PBT) is usually fixed at 0.89 or 0.9 by most authors [40, 41]. This value should only concern crystallites with a spherical shape, and other values were documented for each crystalline directions of simple crystallites shapes (*i.e.* cubic, octahedral and tetrahedral) [42]. The reported values for K are typically in the 0.7—2.0 range. Anyway, the PBT crystallizes with a triclinic unit cell [43, 44], and no clue of the exact crystalline shape is available. In this case, it is chosen to keep the value of 0.89 for K, as a first estimation, keeping in mind that the results for d can be under-estimated.

4.2.4 Dynamic Mechanical Analysis (DMA)

Uniaxial torsion DMA was performed using Dynamic Mechanical Thermal Analyzer (Ares G2, TA Instruments, USA), at fixed frequency of 1 Hz and heating rate of 3°C/min using specimens of dimensions 25 mm×4 mm×2 mm in a temperature range of -80 to 80°C applying a 0.1% imposed strain.

4.2.5 Differential Scanning Calorimetry (DSC)

DSC measurements were performed using a Q20 (from TA Instuments, USA) from -70 to 170°C using a Chiller cooling system. The samples were kept for 2 min at 200°C to erase their thermal history before being cooled and then heated at a 10°C/min rate under a nitrogen flow (50 mL/min). The glass temperature (T_g) was measured at the maximum of the derivative of the heat flow signal when the glass transition step occurs, in the heating phase. The crystallinity χ_c of PBAT was calculated with the heat of melting of fully crystalline for PBAT, evaluated by Herrerra *et al.* to be 114 $J.g^{-1}$.

4.2.6 Dielectric spectroscopy

The dielectric analysis measurements were carried out using a ModuLab XM system (Solartron analytical-AMETEK, USA). Each sample underwent two cycles with isothermal frequency sweeps from 10^6 to 10^{-2} Hz performed every 3°C from -70 to 60°C, applying a $5V - RMS$ voltage.

[1] Some AFM probes are coated with aluminium to optimize the laser deflection.

[2] The pseudo-Voigt fit was only used for the $\bar{1}01$ peak. See Table 4.2 and Figure 4.3.

The results were analyzed using WinFit (Novocontrol, Germany). The transitions associated with relaxations or conductivity were fitted using Havriliak-Negami plots and the obtained fit parameters were used to calculate the activation energy. The Havriliak-Negami equation [45] stands:

$$\bar{\varepsilon_r}(f) = \varepsilon_\infty + \frac{\Delta\varepsilon}{(1+(2\pi f\tau)^\alpha)^\beta} \tag{4.5}$$

where f is the frequency, $\bar{\varepsilon_r}(f)$ is the complex permittivity, ε_∞ the permittivity at infinite frequency, $\Delta\varepsilon = \varepsilon_0 - \varepsilon_\infty$ with ε_0 the permittivity at low frequency, and τ is the relaxation time of the material at the considered temperature. α and β are the Havriliak-Negami shape parameters and are comprised between 0 and 1. Adjusting those parameters to obtain a proper fit of a relaxation allows, via the specific relaxation time τ at different temperatures, to calculate the activation energy E_A associated with it applying an Arrhenius law[3], given in eqn 4.6.

$$\tau(T) = \tau_\infty \cdot exp(\frac{-E_A}{k_B T}) \tag{4.6}$$

Where τ_∞ is a constant (relaxation time at an infinite temperature, in s), k_B the Boltzmann constant and T the temperature in Kelvins. The same equation stands replacing τ by σ_0, the direct current (DC) conductivity (here measured at very low frequency, *i.e.* 0.01 Hz), to calculate the activation energy associated with the conduction phenomenon.

4.3 Result and discussions

4.3.1 Morphological and thermal characterization

Densities

The volumetric mass density was measured to be 1.217 ± 0.001 g.cm^{-3} for every sample. Since no significant change is observed, it can be considered that the macroscopical organization of the PBAT polymer chains remains unchanged by the presence of ionic liquids.

Microstructures

Figure 4.2 shows AFM micrographs of the microstructure of the three systems, with height and DMT modulus mappings. First, while il-Cl seems to be miscible in the PBAT matrix without changing its apparent structure, il-TMP forms nodules and is at least partially immiscible in PBAT. This is consistent with the morphologies observed in transmission electron microscopy by Livi *et al.* [29]. The apparent holes in topographic images of the PBAT/il-TMP system and the fact that these features display a low modulus is also consistent with the idea of ionic liquid nodules.

The AFM DMT modulus images of the three blends also suggest a common crystalline organization in a lamellar form, creating spherulites at a larger scale. A more detailed view of the lamellae in AFM is given further. DMT modulus images already proved their efficiency to identify and characterize crystalline lamellar structures [32].

[3] All the measurements gave a linear relation between $ln(\tau)$ and $1/T$, justifying the application of the Arrhenius law and not the VTF (Vogel-Fulcher-Tammann) law.

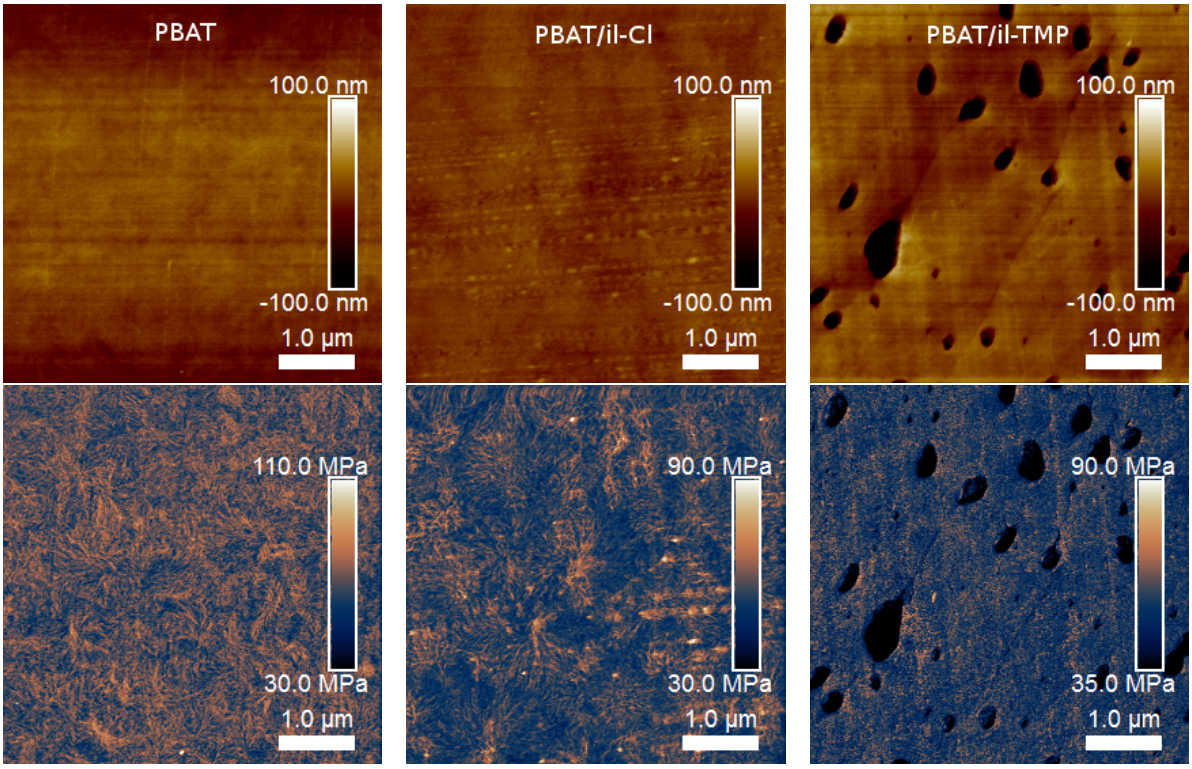

Figure 4.2 – AFM height (top) and DMT Modulus (bottom) maps of a $5 \times 5\ \mu m^2$ region of a: (left) PBAT sample; (center) PBAT/il-Cl sample; (right) PBAT/il-TMP sample

Crystalline structure

The degree of crystallinity of the blends was measured to be $14 \pm 1\%$ in DSC for all the blends without significant difference due to the presence of ionic liquids. A XRD analysis was carried out, revealing the main peaks associated with the crystalline directions for the three systems, displayed in Figure 4.3.

The peaks correspond to those observed by Briber and Thomas for the PBT homopolymer [46]. The fact that the crystalline domains in PBAT are composed of PBT units is confirmed by Herrera *et al.* [47] and by Kuwabara [48].

To estimate the size of the corresponding crystallites, Scherrer's equation was applied to each peak. The results are summarized in Table 4.2.

Table 4.2 – Main PBT crystalline directions observed in the PBAT/ILs blends and corresponding estimated domain sizes obtained with the application of Scherrer's equation (eqn 4.4).

	d [nm]				
Orientation	$0\bar{1}1$	010	$\bar{1}01$	100	$1\bar{1}1$
PBAT	8.1	13.5	3.0	10.3	6.5
PBAT/il-Cl	9.0	14.2	2.7	11.2	6.7
PBAT/il-TMP	7.4	12.4	3.7	9.3	5.9

Given the uncertainity associated to the peak fitting in XRD, due to the preponderance of the amorphous phase, the difference in the sizes of the crystallites between the blends are irrelevant.

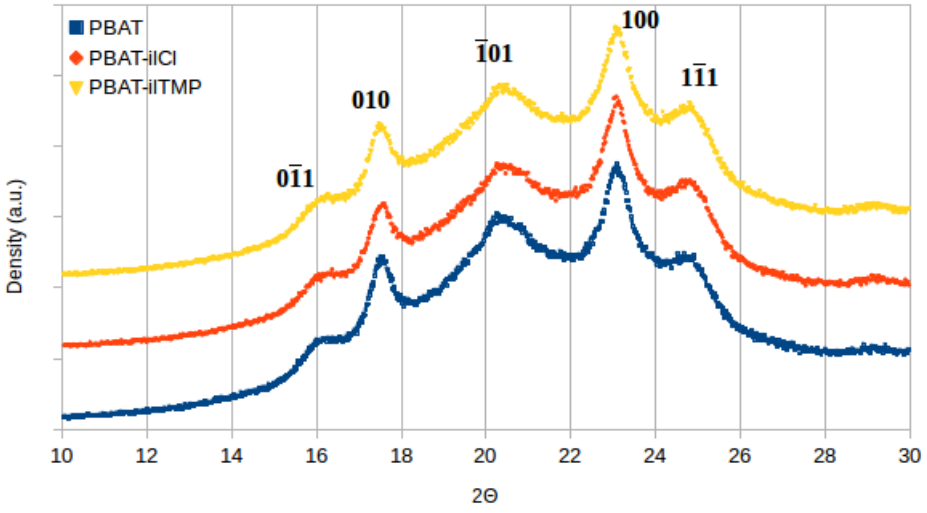

Figure 4.3 – WAXS scans of neat PBAT and PBAT/ILs blends. Each peak corresponds to a PBT crystalline direction, according to the study of Briber and Thomas[46].

It is thus considered that there is no major observable variation of the size of the crystallites caused by the ionic liquids. Such crystallites are observable in AFM, by scanning parts of the spherulites as in Figure 4.4.

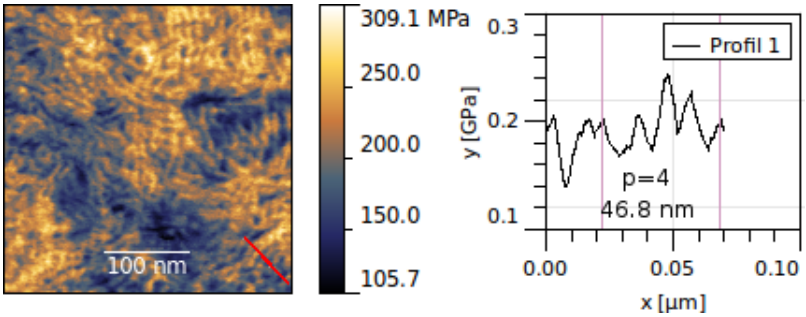

Figure 4.4 – $350 \times 350nm$ AFM DMT modulus map of a PBAT surface exhibiting crystalline lamellae, and corresponding modulus profile taken along the red line, perpendicularly to the direction of the lamellae. Crystalline lammelae correspond to the modulus peaks.

A red profile is drawn perpendicularly to the lamellae, and 4 modulus peaks (corresponding to stiff PBT crystallites) are identifiable between the purple vertical lines (representing a distance of 46.8 nm). This means an average spacing of less than 12 nm between the lamellae in this case, of the same order of magnitude as their estimated dimensions given in Table 4.2. This suggests that the amorphous chains stacked between lamellae are quite confined, as confirmed further.

Thermomechanical relaxations

The DMA analysis was carried out on the blends to identify the thermal transitions of the three systems. The evolution of the storage modulus and of the loss modulus across the temperature range (-80 to 80°C) is shown in Figure 4.5.

The storage modulus drop around -30°C, associated with a peak in the losses, is very likely to correspond to the α transition of the blends, passing from a glassy state at low temperatures

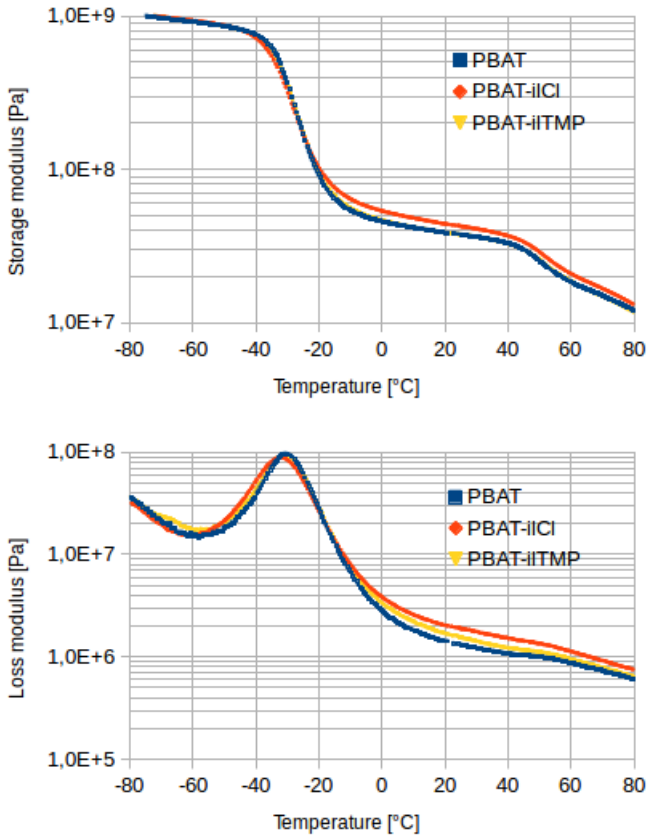

Figure 4.5 – Variation of the storage modulus (top) and of the loss modulus (bottom) of PBAT and PBAT-ILs blends with temperature at 1 Hz

to a rubbery state. The α transition temperature T_α can be defined by the temperature at the maximum of the loss modulus peak.

The results are summarized in Table 4.3. They are in good accordance with the glass transition temperatures obtained by DSC, which also correspond well to the results reported by Livi *et al.* [29].

No significant drop of the glass transition temperature is observed. Those results are not likely to correlate any placticization effect induced by the ionic liquids. Even if such a slight effect is possible (-2°C in the T_α of the PBAT/il-Cl blend, but not confirmed in DSC), it cannot explain the big modifications of mechanical properties induced by the addition of 2wt% il-Cl.

A second transition can be observed on the DMA curves around 50°C, with a slight drop of both moduli. This can be associated with an α' interfacial relaxation. Since it can be observed

Table 4.3 – Transition temperatures observed in DMA (from the loss peak) and DSC analysis. All the values are given with ±1°C.

Blend:	T_α (DMA) [°C]	T_g (DSC) [°C]
PBAT	-30.5	-35.1
PBAT/il-Cl	-32.4	-35.0
PBAT/il-TMP	-30.8	-36.0

in all the blends and not only PBAT/il-TMP, the corresponding interface is likely to be the one between the crystalline phase and the amorphous phase, and/or an amorphous interphase between crystalline lamellae, as reported in P(VDF-CTFE)[4]/ILs blends by Yang *et al.* [9].

Summary of the morphological, thermal and mechanical characterizations

The routine characterizations techniques described above showed that, except for the il-TMP nodules, no significant difference of the organization of the matrix is induced by the ionic liquids: the density, the crystallinity (degree and structure) and the thermal/thermomechanical properties remain almost unchanged by the addition of 2wt% of a ionic liquid.

It is thus proposed to explore deeper the interactions between phases and within the phases, using nanomechanical data measured in AFM and dielectric spectroscopy to answer the appearing problem: how 2wt% of a ionic liquid can significantly change the mechanical properties of the matrix (increase of the strain at break with, for il-Cl, a small decrease of the Young's modulus) without affecting the other bulk properties ?

4.3.2 Elucidating the mechanisms of interactions of ILs with the PBAT matrix

Dielectric spectroscopy and nanomechanical analysis

Dielectric spectroscopy An example of the spectra obtained for the relative dielectric permittivity ε_r' and the corresponding loss ε_r" at two temperatures is given in Figure 4.6. For all the blends, three phenomena were evidenced: the α and α' relaxations, and conductivity at low frequencies and/or high temperatures.

On the left curve, the permittivity spectra at -22°C displays a slight peak in ε_r" around 100 Hz, which corresponds to the α relaxation. For PBAT/il-Cl, this peak is merged into the conduction slope, but is still identifiable. The activation energies calculated from the Havriliak-Negami fits parameters for the blends are summarized in Table 4.4, obtained from Arrhenius plots shown in Figure 4.7. Although the value of the activation energy for the alpha relaxation of PBAT/il-TMP could not be calculated properly, no major difference is expected, as between the neat PBAT and PBAT/il-Cl (less than 3%), since the corresponding relaxation occurs almost at the same temperature for all the blends, as observed in DMA and DSC.

Table 4.4 – Activation energies (E_A) of each phenomena observed in dielectric spectroscopy. All the values are given in $kJ.mol^{-1}$

E_A of:	α **relaxation**	α' **relaxation**	**Conductivity**
PBAT	232.6	72.4	69.4
PBAT/il-Cl	239.0	82.8	80.7
PBAT/il-TMP	-[5]	72.4	67.0

In the diagrams of Figure 4.6 (right), the real and imaginary parts of the complex permittivity of the three blends at 50°C (323 K) are shown with their frequency dependence. ε" (bottom right) mostly reveals an important conduction phenomenon in the three cases, much more important for the blend with il-Cl and also relevant for the PBAT/il-TMP system. This can be explained

[4] Poly(vinylidene fluoride-*co*-chlorotrifluoroethylene)

[5] This value was not calculated because the corresponding relaxation could not be fitted properly, due to overlapping phenomena (conduction) in the frequency domain.

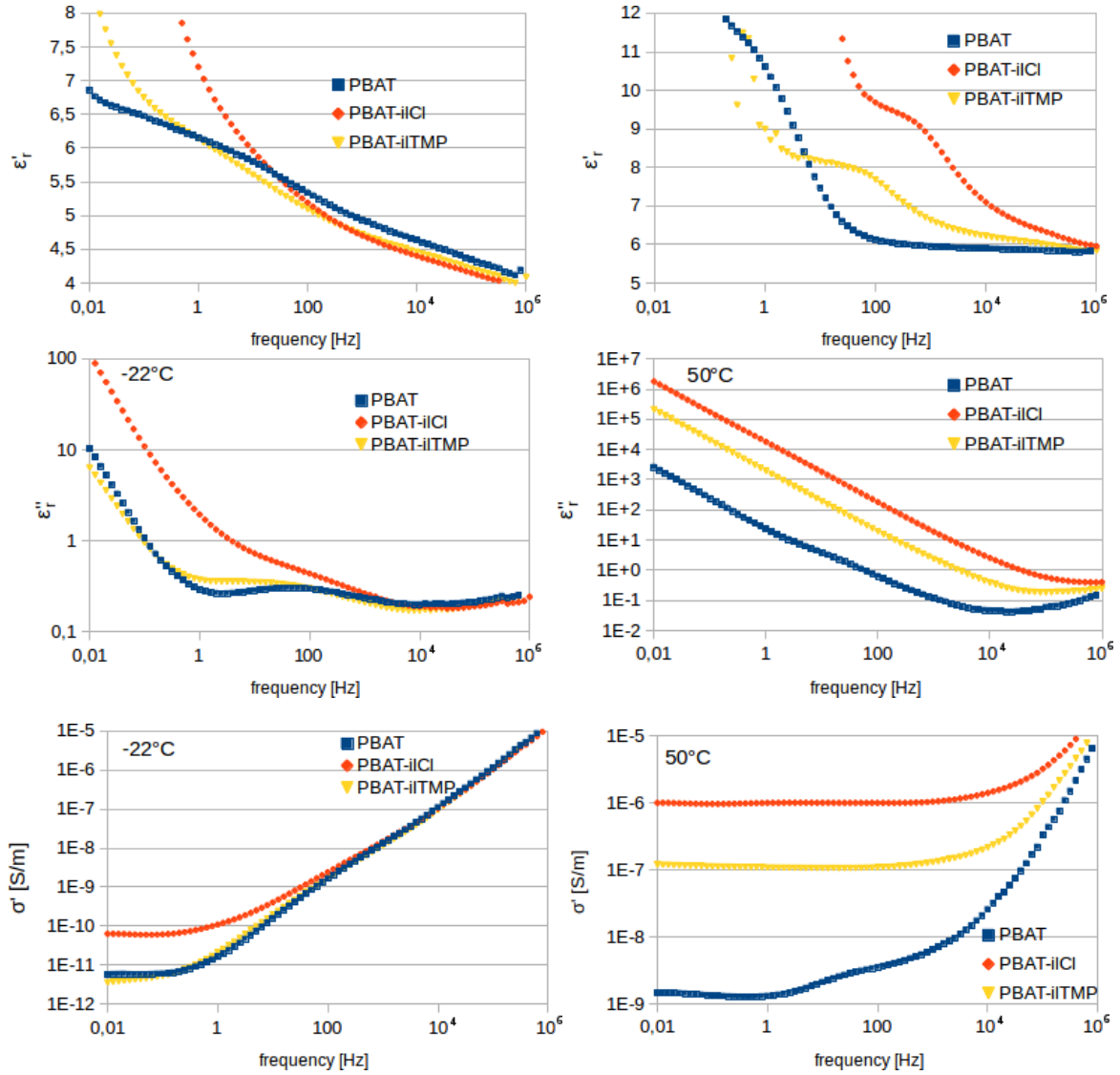

Figure 4.6 – Relative dielectric permittivity (top), loss (middle) and real conductivity (bottom) versus frequency, at -22°C (left) evidencing the α relaxation around 100 Hz and at 50°C (right) showing conduction and the α' relaxtion. The latter corresponds to the conductivity step around 100 Hz for PBAT, and is overlapped by the conduction for the other blends (It corresponds anyway to the steps in ε_r' and could be fitted properly).

by ionic conductivity, first induced by impurities in the PBAT matrix, and by the ionic liquids in the blends. The miscibility of il-Cl and the smaller size of the chloride anion correlates higher conduction losses for PBAT/il-Cl.

If the α' relaxation peak at 50°C is almost totally masked by the conductivity slopes in the imaginary permittivity spectrum (loss) in Figure 4.6, the ε' spectrum (top right) reveals a step for the three systems, which corresponds to this relaxation. This may reflect the confined part of the amorphous phase, *i.e.* the chains that are confined between the crystalline lamellae or anchored in the crystalline phase, often called rigid amorphous phase or fraction (RAF) [9]. In other words, this reflects the interface between the amorphous and crystalline phases. The

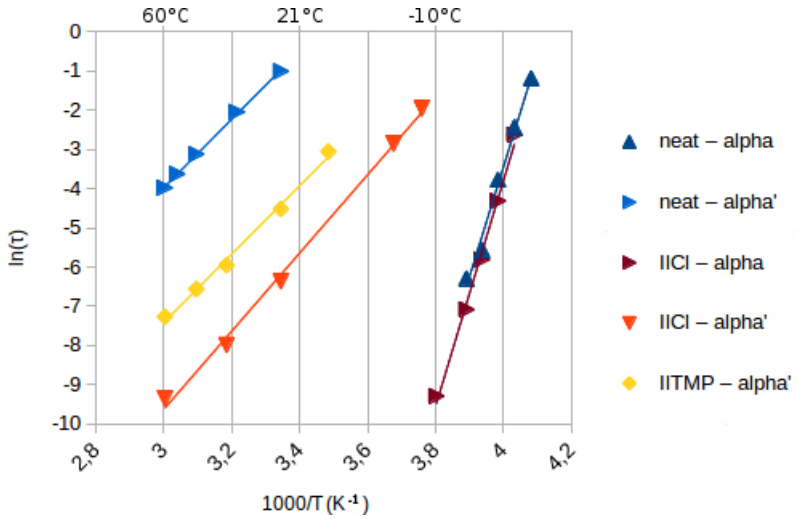

Figure 4.7 – Arrhenius plots for the described relaxations. All linear regression fits are obtained with a squared correlation coefficient superior to 0.99. Similar results were obtained for the conductivities.

broadness of the corresponding loss peak in DMA and in dielectric spectroscopy, reason why it is almost masked in both cases by other phenomena, confirms this idea, as described by Alegria and Colmenero [49].

The PBAT polymer, having a relatively low crystallinity (*i.e.* between 10 and 15% [47, 29]), fits well in the category of semicrystalline polymers that are likely to form such an interfacial amorphous phase (RAF), distinct from the fully free chains of the main amorphous phase, denoted mobile amorphous fraction (MAF) [50]. Furthermore, the formation of a rigid amorphous phase was already reported for the PBT polymer [51]. The two amorphous zones can be observed in Figure 4.4, where dark blue domains correspond to the MAF (represented by the α relaxation) and the inter-lamellar amorphous regions (for instance the darker strips in the orange crystalline zones) correspond to the RAF (represented by the α' relaxation).

In terms of activation energy (Table 4.4), both ionic conductivity and α' relaxation reveal the same trend: on one hand, those phenomena in neat PBAT and in PBAT/il-TMP seem to require the same activation energy. This is consistent with the fact that il-TMP is immiscible (or very slightly miscible) in the PBAT matrix. The same matrix is characterized for neat PBAT and PBAT/il-TMP, the nodules having almost no influence in the dielectric response, except that they increase the ionic conductivity.

On the other hand, both the conduction and the α' relaxation require around 15 to 20% more energy in the blend with 2wt% il-Cl (even if the number and size of its charge carriers make it more conductive than the other blends). The ionic liquid may thus play a role in the interfacial amorphous zone between the PBT–rich crystalline phase and the rest of the amorphous phase.

This observation for PBAT/il-Cl cannot be directly correlated with the tensile mechanical properties summarized in Figure 4.1: interfacial relaxation and conduction phenomena require more energy in this blend while it is mechanically softer and with a higher strain at break. This necessarily hints the coexistence of various different (but certailny interdependent) mechanisms induced by the ionic liquid. They are discussed in the following section.

Nanomechanical analysis An AFM nanomechanical analysis was carried out over a large number of images for every system to evaluate what are the nanoscale mechanisms that explain

such modifications of macroscopical properties, unexpected dielectric spectroscopy results and almost no substancial difference in other physical properties.

First, the DMT moduli from mappings such as those presented in Figure 4.2 were gathered into distributions. Figure 4.8 displays such representative diagrams for the three blends.

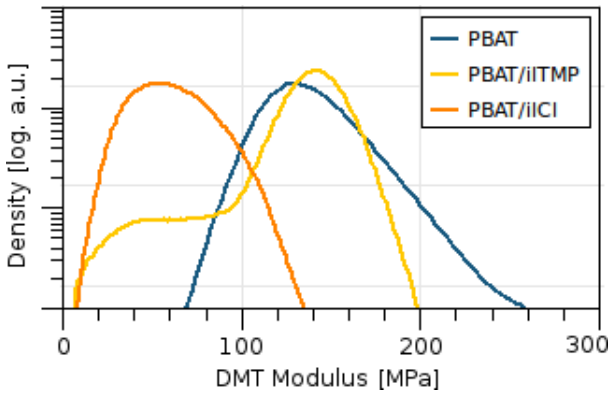

Figure 4.8 – Representative logarithmic distributions of DMT modulus over AFM images for each blend. The vertical axis represents the density of probability associated with each modulus value in modulus mappings.

With the support of additional AFM nanomechanical data, a synthesis of the effects of the two different ionic liquids on the PBAT matrix are discussed in the following sections.

Effect of il-TMP

In Figure 4.8, the main peaks of the neat PBAT and of the PBAT/il-TMP blend are centered around 140 MPa, which correlate the fact that the continuous matrix in PBAT/il-TMP behaves similarly to the neat PBAT.

Although the reported low miscibility may limit any effect of the il-TMP on the matrix [52], in the distribution in Figure 4.8, the PBAT/il-TMP system also exhibit a low modulus shoulder that corresponds to the softer il-TMP nodules. It is a continuous shoulder and not a distinct peak, suggesting the existence of transitional zones between ionic liquid nodules and PBAT matrix, *i.e.* an interphase.

In Figure 4.9, the same profile is taken across the height image and the DMT modulus image. The region between the two vertical dashed blue lines on the height profile can be interpreted as the matrix edge, close to the interface with the nodule, since there is no significant height variation with the rest of the matrix.

However, in that zone of about 40 nm, a DMT modulus transition can be observed into the polymer matrix. This can be interpreted as an interphase constituted by free dangling segments of the polymer chains from the matrix, explaining the smooth modulus transition. The neat PBAT modulus is quickly restored when going further into the matrix, due to the immiscibility of the ionic liquid.

It is known that phosphonium cation and phosphinate anions are among the most basic ions used in ionic liquids [53, 54]. Studies reports that basic ionic liquids are good catalysts for depolymerisation of polyesters structurally similar to the PBAT, for instance poly(lactic acid) [55] and polyethylene terephtalate [56, 52]. This may also affect the aspect of the interphases, but it couldn't be confirmed experimentally.

Figure 4.10 displays a mapping of the dissipated energy at each tip-sample contact, for

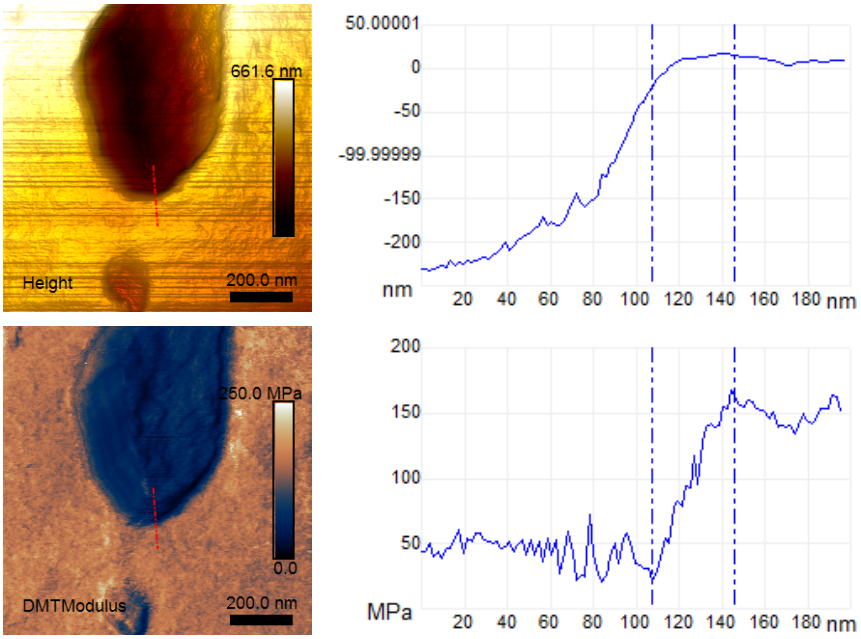

Figure 4.9 – AFM $1 \times 1\ \mu m^2$ topography (top) and DMT modulus (bottom) images of a PBAT/il-TMP surface with corresponding profiles, taken following the red dashed line.

the PBAT/il-TMP blend. It can be clearly observed that the nodules (or the corresponding interphases) correspond to zones where more energy can be dissipated. The macroscopical strain at break of this blend increased by 33% for this blend compared to the neat PBAT, according to Livi *et al.* [29] (This can be explained by the fact that the blend can store more energy under stress due to its IL nodules, which can hinder the crack propagation, thus increasing the strain at break while the continuous matrix keeps the Young's modulus of the neat PBAT.

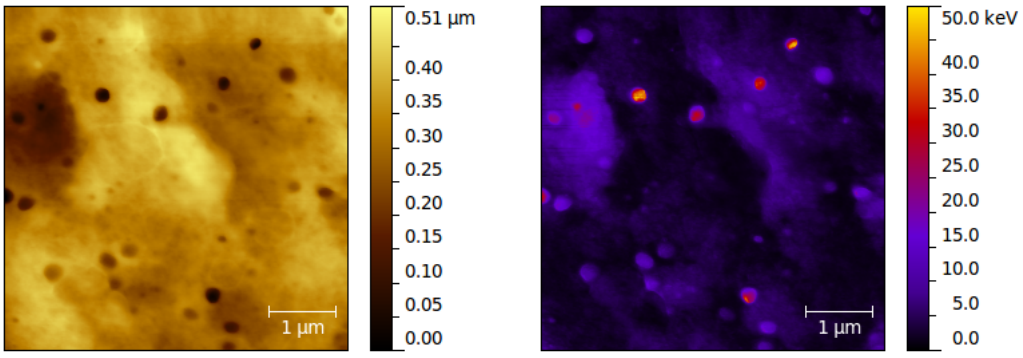

Figure 4.10 – Topography (left) and dissipation energy (right) AFM nanomechanical mappings of the PBAT/il-TMP blend, revealing the dissipative nature of the nodules.

Effect of il-Cl

As shown in Figure 4.8, PBAT/il-Cl exhibits a DMT modulus distribution centered around 60 MPa, which is less than the half of the equivalent for the other blends. This trend is observed

for all the recorded mappings. In tensile tests, the modulus drops only by 18% with the addition of 2wt% of il-Cl, and as seen above, this cannot be only explained by a plasticization effect (no significant variation of the T_g is observed in DSC measurements). As il-Cl seems totally miscible with the matrix, an attempt to localize it can be made using adhesion mappings, as already done in a previous study on PBAT/PLA/ILs blends [28].

First, different zones of the PBAT matrix have to be identified. As seen with the XRD analysis, the crystalline phase of the PBAT matrix is composed by stiff PBT units. The amorphous phase, which is majoritary, may consist mostly in butylene adipate segments, along with the rest of the butylene terephtalate. In DMT modulus images, spherulites are easily identifiable. Finally, an intermediate amorphous phase (RAF), characterized by the α' relaxation, was also identified by dielectric spectroscopy and DMA.

In Figure 4.11, based on their shape, some obvious spherulites were marked in red on the DMT modulus images for PBAT/il-Cl and neat PBAT, and the mask was reported on the adhesion mappings. It is worth noting that the spherulites may not only be constituted by the crystalline phase, but also by inter-lamellar rigid amorphous zones.

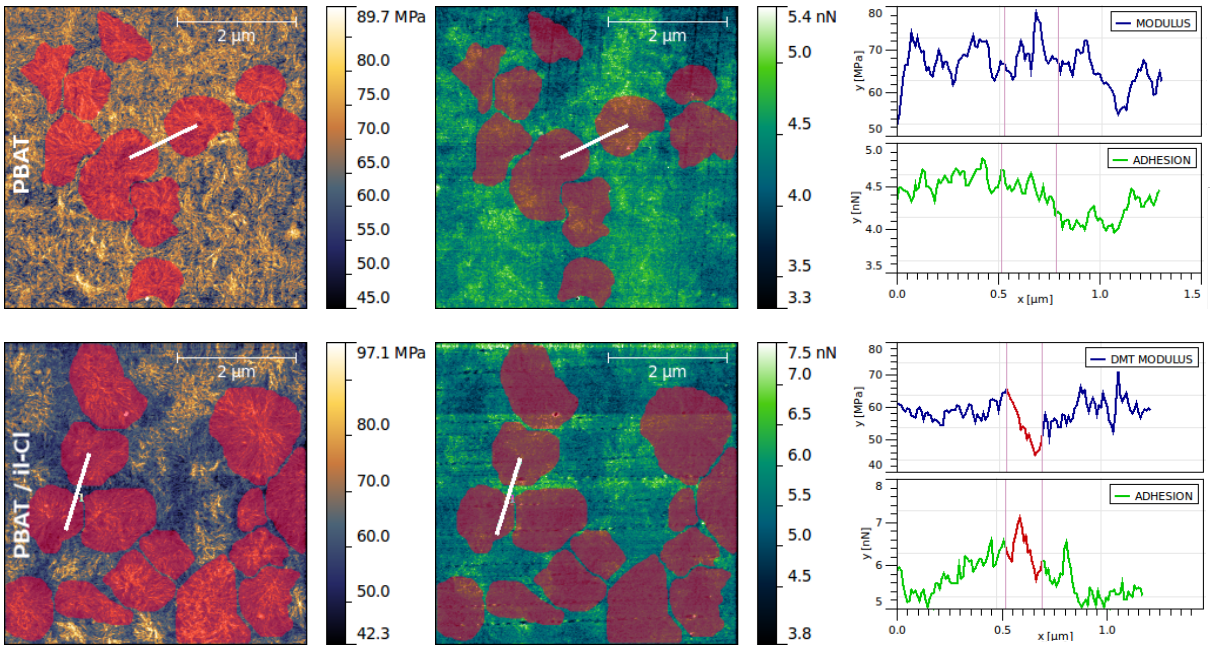

Figure 4.11 – AFM $5\times5\ \mu m^2$ DMT modulus (left) and adhesion (center) images with corresponding profiles (right) for neat PBAT (top) and PBAT/il-Cl (bottom). The profiles are taken following the white lines in the images, and the vertical purple lines on the profiles correspond to the gaps between zones marked in red. Some (but not all) clearly identifiable spherulites are marked in red in the images.

The crystalline zones being identified, it can be observed that PBAT and PBAT/il-Cl follow different trends:

- On the one hand, for the neat PBAT, the lamellar crystallinity seems to be the only contrast factor in the DMT modulus image. Between the purple vertical lines in the profiles in Figure 4.11, a zone between spherulites that corresponds to the amorphous phase, no significant difference with the rest of the profile is visible in adhesion.
- On the other hand, for the PBAT/il-Cl blend, a clear difference can be seen between zones

with crystalline phase (*i.e.* spherulites, marked in red) and zones between spherulites (mainly corresponding to the MAF), that exhibit a lower local modulus and higher adhesion. This can be observed in the profiles, where the part of the curves that corresponds to the amorphous zone between spherulites is marked in dark red, displaying a modulus drop and an adhesion peak. The fact that adhesions forces reaching values that are not observed on the neat PBAT[6] hints the presence of another component, *i.e.* the ionic liquid. The adhesion mappings reveal thus that il-Cl may be preferentially located in the amorphous phase of the PBAT matrix.

Based on such observations, an explanation of the complex effect of il-Cl on the PBAT matrix can be made. First, the ionic liquid, located mostly in the amorphous phase of the PBAT, tends to increase drastically the chain mobility at the nanoscale in the MAF, explaining the local (DMT) modulus drop observed in AFM, compared to that of the other systems (see Figure 4.8).

The il-Cl should obviously be present not only in the MAF but also in the RAF, given its effect on the α' relaxation. The polymer chains being much more constrained in this phase, the ionic liquid may act differently and reduce even more their movement capability, thus making the relaxation of this zone requiring more energy (dielectric data). This may represent a gain in stiffness at a higher scale than what is observed in AFM, counterbalancing the dramatic drop in the nanoscale modulus, explaining a lesser drop in the macroscopic scale Young's modulus. From this point of view, the ionic liquid has the same role as a filler functionalization, but with the crystalline phase.

This can also be explained by a cooperation effect between the ions of il-Cl and the polymer chains, due to dipole-dipole and/or ionic interactions, that should be much more present than in the neat blend. These interactions are also highlighted by the conductivity data: if the conductivity is more important in the PBAT/il-Cl blend, the energy required to activate the conduction is much higher than in the other systems.

The phosphonium-chloride ionic liquid have thus a double effect on the PBAT matrix: on one hand it acts like a local plasticizer, increasing the chain mobility in the MAF phase (thus increasing the global strain at break), but on the other hand it forms strong cooperating interactions, particularly in the interfacial RAF phase, compensating some effects induced by the gain in chain mobility and limiting the Young's modulus decrease.

4.4 Conclusions

The effects of the introduction of a small amount (2wt%) of two different phosphonium ionic liquids on the structure and mechanical properties of a PBAT copolyester have been investigated using advanced characterization techniques, and in particular AFM nanomechanical imaging. This method allows, via the simultaneous acquisition of several images of the same surface, high resolution mappings of different mechanical properties such as the local elasticity modulus, the tip-sample adhesion force and the energy dissipation. By this way, the nanostructure of a material is explored from unusual points of view, allowing to go deeper into the understanding of the molecular organization of the studied polymers, and the way they are modified, here by ionic liquids.

The tensile mechanical properties of the PBAT matrix were affected by both ionic liquids: while the addition of a phosphonium-phosphinate ionic liquid, denoted il-TMP, increased the

[6]It is worth noting that to compare adhesion forces quantitatively from an image to another, the images in Figure 4.11 were acquired in the same session with the same tip.

strain at break of the matrix by 33% without affecting the Young's modulus, the same amount of il-Cl, a phosphonium-choride IL, increased the strain at break by 60% and reduced the modulus from 47 to 40 MPa. However, no substantial modification of the density, of the crystalline structure and of thermal properties (*i.e.* the glass transition temperature and the crystallinity) were recorded.

The same crystalline structure was identified in the three systems, consisting in lamellae constituted by PBT segments. Two amorphous phases were identified by dielectric spectroscopy according to their relaxation behavior: the mobile amorphous fraction (MAF) and the rigid amorphous fraction (RAF). The former consists in fully free polymer chains in relatively large amorphous domains while the latter represents the constrained chains between crystalline lamellae or at the crystalline/amorphous interface.

It was shown that il-TMP is immiscible in the PBAT, but organizes itself into dissipative nodules that form, as shown by profile analysis in AFM, a smooth interphase with the matrix, consisting in softer dangling polymer chains. Being continuous, the PBAT matrix keeps most of its properties while the nodules just hinders the defaults propagation under stress, increasing the strain at break. To confirm this effect macroscopically using a tearing strength test on films with and without il-TMP could be an interesting perspective, as it is directly applicable for compostable PBAT films used in agriculture.

The other ionic liquid, il-Cl, is perfectly miscible in the amorphous phases of the PBAT matrix, as observed with AFM adhesion mappings. In the MAF, the overall effect seems to be a dramatic increase of the chain mobility, explaining a huge local modulus drop (more than -50% in average) and the 60% increase in the macroscopic strain at break, with relatively free charge carriers explaining a higher conductivity than in other blends. This is partially compensated by a stiffening effect of the ionic liquid on the RAF, as it increases the activation energy associated with the relaxation of this phase. The ionic liquid has thus a double effect, allowing to optimize the mechanical properties (the macroscopic Young's modulus in only reduced by 20%) and to keep unchanged the crystalline structure and the glass transition temperature.

Through the example of PBAT, this study highlights the potential of ionic liquids, whose structurating effect could be an alternative to traditional additives to tailor and tune the properties of polymers. According to the desired modification of the properties, at least three possibilities can be identified with ionic liquids:

- A traditional plasticization effect, as reported for instance by Sankri *et al.* with an imidazolium ionic liquid on a starch matrix [2]. This would mean an increase of the strain at break, and a decrease of the Young's modulus and of the glass transition temperature.

- An increase of the strain at break with a moderate decrease of the Young's modulus, but without affecting the thermal properties, as reported for the blend with il-Cl.

- An increase of the strain at break without affecting much the modulus, as reported for the blend contaiing il-TMP.

The combination of AFM nanomechanical mappings with other advanced characterization techniques such as dielectric spectroscopy allowed to access complex structurating mechanisms that link mechanical, thermal and electric properties together, allowing to explain the influences of ionic liquids on the properties of a polymer matrix.

Acknowledgements

The authors acknowledge the French *Ministère de l'Enseignement Supérieur et de la Recherche (MESR)* and *École Doctorale Matériaux* for supporting this project. They also thank Ruben Vera from the *Centre de Diffractometrie H. Longchambon* (UCBL) for the XRD experiments, and Pierre Alcouffe (UMR5223) for the surface preparation of AFM samples.

Bibliography

[1] Jianmei Lu, Feng Yan, and John Texter. Advanced applications of ionic liquids in polymer science. *Progress in Polymer Science*, 34(5):431–448, 2009.

[2] Abdulkader Sankri, Abdellah Arhaliass, Isabelle Dez, Annie Claude Gaumont, Yves Grohens, Denis Lourdin, Isabelle Pillin, Agnès Rolland-Sabaté, and Eric Leroy. Thermoplastic starch plasticized by an ionic liquid. *Carbohydrate Polymers*, 82(2):256–263, 2010.

[3] KI Park and M Xanthos. A study on the degradation of polylactic acid in the presence of phosphonium ionic liquids. *Polymer Degradation and Stability*, 94(5):834–844, 2009.

[4] Bor-Kuan Chen, Tzi-Yi Wu, Yu-Ming Chang, and Antonia F Chen. Ductile polylactic acid prepared with ionic liquids. *Chemical engineering journal*, 215:886–893, 2013.

[5] Richard P Swatloski, Scott K Spear, John D Holbrey, and Robin D Rogers. Dissolution of cellose with ionic liquids. *Journal of the American chemical society*, 124(18):4974–4975, 2002.

[6] Sébastien Livi, Valeria Bugatti, Luis Estevez, Jannick Duchet-Rumeau, and Emmanuel P Giannelis. Synthesis and physical properties of new layered double hydroxides based on ionic liquids: Application to a polylactide matrix. *Journal of colloid and interface science*, 388(1):123–129, 2012.

[7] Luanda C. Lins, Sebastien Livi, Jannick Duchet-Rumeau, and Jean-Francois Gerard. Phosphonium ionic liquids as new compatibilizing agents of biopolymer blends composed of poly(butylene-adipate-co-terephtalate)/poly(lactic acid) (pbat/pla). *RSC Adv.*, 5:59082–59092, 2015.

[8] Thi Khan Ly Nguyen, Sébastien Livi, Sébastien Pruvost, Bluma G Soares, and Jannick Duchet-Rumeau. Ionic liquids as reactive additives for the preparation and modification of epoxy networks. *Journal of Polymer Science Part A: Polymer Chemistry*, 52(24):3463–3471, 2014.

[9] Jing Yang, Sébastien Pruvost, Sébastien Livi, and Jannick Duchet-Rumeau. Understanding of versatile and tunable nanostructuration of ionic liquids on fluorinated copolymer. *Macromolecules*, 48(13):4581–4590, 2015.

[10] G. Binnig, C. F. Quate, and C. Gerber. Atomic force microscope. *Physical Review Letters*, 56:930–933, March 1986.

[11] Q Zhong, D Inniss, K Kjoller, and VB Elings. Fractured polymer/silica fiber surface studied by tapping mode atomic force microscopy. *Surface Science Letters*, 290(1):L688–L692, 1993.

[12] M. R. Vanlandingham, S. H. McKnight, G. R. Palmese, J. R. Elings, X. Huang, T. A. Bogetti, R. F. Eduljee, and J. W. Gillespie Jr. Nanoscale indentation of polymer systems using the atomic force microscope. *The Journal of Adhesion*, 64(1-4):31–59, 1997.

[13] Manfred Radmacher, Monika Fritz, Claudia M Kacher, Jason P Cleveland, and Paul K Hansma. Measuring the viscoelastic properties of human platelets with the atomic force microscope. *Biophysical journal*, 70(1):556–567, 1996.

[14] Bruker Corporation. *PeakForce QNM User Guide (Revision E)*, 2011.

[15] T J Young, M A Monclus, T L Burnett, W R Broughton, S L Ogin, and P A Smith. The use of the peakforce tm quantitative nanomechanical mapping afm-based method for high-resolution young's modulus measurement of polymers. *Measurement Science and Technology*, 22(12):125703, 2011.

[16] Laura Picas, Pierre-Emmanuel Milhiet, and Jordi Hernández-Borrell. Atomic force microscopy: A versatile tool to probe the physical and chemical properties of supported membranes at the nanoscale. *Chemistry and physics of lipids*, 165(8):845–860, 2012.

[17] Dong Wang, Thomas P. Russell, Toshio Nishi, and Ken Nakajima. Atomic force microscopy nanomechanics visualizes molecular diffusion and microstructure at an interface. *ACS Macro Letters*, 2(8):757–760, 2013.

[18] Shib Shankar Banerjee, Andreas Janke, Uwe Gohs, Andreas Fery, and Gert Heinrich. Some nanomechanical properties and degree of branching of electron beam modified polyamide 6. *European Polymer Journal*, 88:221–230, 2017.

[19] Grégory Mertz, Fatima Hassouna, Philippe Leclère, Abdesselam Dahoun, Valérie Toniazzo, and David Ruch. Correlation between (nano)-mechanical and chemical changes occurring during photo-oxidation of filled vulcanised styrene butadiene rubber (sbr). *Polymer degradation and stability*, 97(11):2195–2201, 2012.

[20] XQ Shi, H Ito, and T Kikutani. Characterization on mixed-crystal structure and properties of poly (butylene adipate-co-terephthalate) biodegradable fibers. *Polymer*, 46(25):11442–11450, 2005.

[21] Jessica S Pereira da Silva, Juliana M Farias da Silva, Bluma G Soares, and Sébastien Livi. Fully biodegradable composites based on poly (butylene adipate-co-terephthalate)/peach palm trees fiber. *Composites Part B: Engineering*, 129:117–123, 2017.

[22] Yogaraj Nabar, Jean Marie Raquez, Philippe Dubois, and Ramani Narayan. Production of starch foams by twin-screw extrusion: Effect of maleated poly (butylene adipate-co-terephthalate) as a compatibilizer. *Biomacromolecules*, 6(2):807–817, 2005.

[23] Mukesh Kumar, S. Mohanty, S.K. Nayak, and M. Rahail Parvaiz. Effect of glycidyl methacrylate (gma) on the thermal, mechanical and morphological property of biodegradable pla/pbat blend and its nanocomposites. *Bioresource Technology*, 101(21):8406 – 8415, 2010.

[24] S Mohanty and SK Nayak. Biodegradable nanocomposites of poly (butylene adipate-co-terephthalate)(pbat) and organically modified layered silicates. *Journal of Polymers and the Environment*, 20(1):195–207, 2012.

[25] Sebastien Livi, Gabriela Sar, Valeria Bugatti, Eliane Espuche, and Jannick Duchet-Rumeau. Synthesis and physical properties of new layered silicates based on ionic liquids: improvement of thermal stability, mechanical behaviour and water permeability of pbat nanocomposites. *RSC Adv.*, 4:26452–26461, 2014.

[26] Sébastien Livi, Luanda C. Lins, Gabriela Sar, Jean-François Gérard, and Jannick Duchet-Rumeau. Supercritical co2–ionic liquids: A successful wedding to prepare biopolymer foams. *ACS Sustainable Chemistry & Engineering*, 4(2):461–470, 2015.

[27] Sebastien Livi, Valeria Bugatti, Manuel Marechal, Bluma G. Soares, Guilherme M. O. Barra, Jannick Duchet-Rumeau, and Jean-Francois Gerard. Ionic liquids-lignin combination: an innovative way to improve mechanical behaviour and water vapour permeability of eco-designed biodegradable polymer blends. *RSC Adv.*, 5:1989–1998, 2015.

[28] Benjamin Megevand, Sébastien Pruvost, Luanda C Lins, Sébastien Livi, Jean-François Gérard, and Jannick Duchet-Rumeau. Probing nanomechanical properties with afm to understand the structure and behavior of polymer blends compatibilized with ionic liquids. *RSC Advances*, 6(98):96421–96430, 2016.

[29] Sébastien Livi, Valeria Bugatti, Bluma Guenther Soares, and Jannick Duchet-Rumeau. Structuration of ionic liquids in a poly (butylene-adipate-co-terephthalate) matrix: its influence on the water vapour permeability and mechanical properties. *Green Chemistry*, 16(8):3758–3762, 2014.

[30] Jérémy Odent, Philippe Leclère, Jean-Marie Raquez, and Philippe Dubois. Toughening of polylactide by tailoring phase-morphology with p [cl-co-la] random copolyesters as biodegradable impact modifiers. *European Polymer Journal*, 49(4):914–922, 2013.

[31] Jérémy Odent, Jean-Marie Raquez, Philippe Leclère, Franck Lauro, and Philippe Dubois. Crystallization-induced toughness of rubber-modified polylactide: combined effects of biodegradable impact modifier and effective nucleating agent. *Polymers for Advanced Technologies*, 26(7):814–822, 2015.

[32] Denis Mihaela Panaitescu, Adriana Nicoleta Frone, and Cristian Nicolae. Micro- and nano-mechanical characterization of polyamide 11 and its composites containing cellulose nanofibers. *European Polymer Journal*, 49(12):3857 – 3866, 2013.

[33] Winny Fam, Jaleh Mansouri, Hongyu Li, and Vicki Chen. Improving co 2 separation performance of thin film composite hollow fiber with pebax® 1657/ionic liquid gel membranes. *Journal of Membrane Science*, 537:54–68, 2017.

[34] Priti Xavier and Suryasarathi Bose. Nanomechanical mapping, hierarchical polymer dynamics, and miscibility in the presence of chain-end grafted nanoparticles. *Macromolecules*, 49(3):1036–1048, 2016.

[35] B.V Derjaguin, V.M Muller, and Yu.P Toporov. Effect of contact deformations on the adhesion of particles. *Journal of Colloid and Interface Science*, 53(2):314 – 326, 1975.

[36] K. L. Johnson, K. Kendall, and A. D. Roberts. Surface energy and the contact of elastic solids. *Proceedings of the Royal Society of London A: Mathematical, Physical and Engineering Sciences*, 324(1558):301–313, 1971.

[37] Daniel Maugis. Adhesion of spheres: The JKR-DMT transition using a dugdale model. *Journal of Colloid and Interface Science*, 150(1):243 – 269, 1992.

[38] D.S. Dugdale. Yielding of steel sheets containing slits. *Journal of the Mechanics and Physics of Solids*, 8(2):100 – 104, 1960.

[39] Marcin Wojdyr. *Fityk*: a general-purpose peak fitting program. *Journal of Applied Crystallography*, 43(5 Part 1):1126–1128, Oct 2010.

[40] Defeng Wu, Liang Wu, Guangcai Yu, Bin Xu, and Ming Zhang. Crystallization and thermal behavior of multiwalled carbon nanotube/poly (butylenes terephthalate) composites. *Polymer Engineering & Science*, 48(6):1057–1067, 2008.

[41] Nur Oburoğlu, Nevra Ercan, Ali Durmus, and Ahmet Kaşgöz. Effects of filler type on the nonisothermal crystallization kinetics of poly (butylene terephthalate)(pbt) composites. *Journal of Applied Polymer Science*, 123(1):77–91, 2012.

[42] J Il Langford and AJC Wilson. Scherrer after sixty years: a survey and some new results in the determination of crystallite size. *Journal of Applied Crystallography*, 11(2):102–113, 1978.

[43] Mitsuru Yokouchi, Yoshio Sakakibara, Yozo Chatani, Hiroyuki Tadokoro, Tamotsu Tanaka, and Kentaro Yoda. Structures of two crystalline forms of poly (butylene terephthalate) and reversible transition between them by mechanical deformation. *Macromolecules*, 9(2):266–273, 1976.

[44] IH Hall and MG Pass. Chain conformation of poly (tetramethylene terephthalate) and its change with strain. *Polymer*, 17(9):807–816, 1976.

[45] S Havriliak and S Negami. A complex plane representation of dielectric and mechanical relaxation processes in some polymers. *Polymer*, 8:161–210, 1967.

[46] RM Briber and EL Thomas. Crystallization behaviour of random block copolymers of poly (butylene terephthalate) and poly (tetramethylene ether glycol). *Polymer*, 26(1):8–16, 1985.

[47] Ricard Herrera, Lourdes Franco, Alfonso Rodríguez-Galán, and Jordi Puiggalí. Characterization and degradation behavior of poly (butylene adipate-co-terephthalate) s. *Journal of Polymer Science Part A: Polymer Chemistry*, 40(23):4141–4157, 2002.

[48] Kazuhiro Kuwabara, Zhihua Gan, Takashi Nakamura, Hideki Abe, and Yoshiharu Doi. Crystalline/amorphous phase structure and molecular mobility of biodegradable poly (butylene adipate-c o-butylene terephthalate) and related polyesters. *Biomacromolecules*, 3(2):390–396, 2002.

[49] Angel Alegria and Juan Colmenero. Dielectric relaxation of polymers: segmental dynamics under structural constraints. *Soft matter*, 12(37):7709–7725, 2016.

[50] B Wunderlich. Reversible crystallization and the rigid–amorphous phase in semicrystalline macromolecules. *Progress in Polymer Science*, 28(3):383–450, 2003.

[51] Stephen ZD Cheng, Robert Pan, and Bernhard Wunderlich. Thermal analysis of poly (butylene terephthalate) for heat capacity, rigid-amorphous content, and transition behavior. *Macromolecular Chemistry and Physics*, 189(10):2443–2458, 1988.

[52] Hui Wang, Zengxi Li, Yanqing Liu, Xiangping Zhang, and Suojiang Zhang. Degradation of poly (ethylene terephthalate) using ionic liquids. *Green Chemistry*, 11(10):1568–1575, 2009.

[53] Ana Filipa M. Claudio, Lorna Swift, Jason P. Hallett, Tom Welton, Joao A. P. Coutinho, and Mara G. Freire. Extended scale for the hydrogen-bond basicity of ionic liquids. *Phys. Chem. Chem. Phys.*, 16:6593–6601, 2014.

[54] Stefan Spange, Ralf Lungwitz, and Alexander Schade. Correlation of molecular structure and polarity of ionic liquids. *Journal of Molecular Liquids*, 192:137 – 143, 2014. Fundamental Aspects of Ionic Liquid Science.

[55] Xiao-Yang Li, Qian Zhou, Ke-Ke Yang, and Yu-Zhong Wang. Degradation of polylactide using basic ionic liquid imidazolium acetates. *Chemical Papers*, 68(10):1375–1380, 2014.

[56] Q.F. Yue, C.X. Wang, L.N. Zhang, Y. Ni, and Y.X. Jin. Glycolysis of poly(ethylene terephthalate) (pet) using basic ionic liquids as catalysts. *Polymer Degradation and Stability*, 96(4):399 – 403, 2011.

General conclusions and perspectives

This work gives a functional methodology for AFM nanomechanical mappings in order to understand structuration phenomena in polymers. The theoretical basis and considerations were reviewed and two main studies were presented to illustrate the possibilities given by this technique. Various ways of using nanomechanical mappings, at different steps of the studies, were covered to show their versatility.

After reviewing the models from contact mechanics that are necessary to perform mechanical measurements with an AFM tip, some practical considerations and calibration methods were presented. Common imaging artifacts were identified and good practices were deduced and summarized, either from literature and from personal observations.

In the context of the development of biopolymers and the growing need to create such materials with properties that can be easily tailored, the two main studies presented in this work were centered on the understanding of the structurating behavior and properties modification of ionic liquids in biopolymers, from the macroscopic scale down to the nanoscopic one.

The role of two phosphonium-based ionic liquids, il-Cl and il-TMP, as compatibilizing agents in a PBAT/PLA biopolymer blend was first investigated. From an obvious improvement of macroscopic mechanical properties with the incorporation of 1wt% of a ionic liquid in the blend, AFM nanomechanical mappings helped to evidence the mechanisms underlying the compatibilization. First, the microstructures were evidenced using local modulus contrast, and then quantitative mappings of the adhesion force and/or the local modulus helped to localize a crystalline phase and the ionic liquids (*i.e.* at the PBAT/PLA interface). The study of the evolution of the local modulus across PBAT/PLA interfaces using the AFM mappings allowed to understand that ionic liquids tend to turn them into thicker and more cohesive interphases, by interacting with both polymers. This must be the key mechanism that help stress transfer between the soft and tough PBAT and the stiff PLA, improving the overall macroscopic mechanical properties of the blends.

In a second study, the nanoscale structuration induced by small amounts (2wt%) of the same ionic liquids in the semicrystalline PBAT matrix was investigated. Also starting from the induced modification of tensile mechanical properties (*i.e.* overall increase of the strain at break, and moderate drop of the Young's modulus in the case of il-Cl), an in-deep investigation of the phenomena underlying such modifications was proposed. AFM nanomechanical mappings of the local modulus, adhesion, dissipation energy and topography were used along other advanced characterization techniques such as dielectric spectroscopy and X-ray diffraction to identify such phenomena. It was proven that while the crystalline structure of the PBAT remains relatively unchanged by the addition of ionic liquids, the il-TMP, immiscible into the matrix, forms dissipative nodules of few hundreds nanometers in diameter that still form a cohesive interphase with the matrix, probably hindering the crack propagation, thus increasing the macroscopic strain at break, while leaving the other properties of the cocontinuous matrix relatively unchanged. The other ionic liquid, miscible into the amorphous phase of PBAT, was shown to have a double effect: while increasing dramatically the chain mobility in the bulky, mobile parts of the amorphous phase, it tends to act more like a stiffening agent in the more confined parts that are closer to the crystalline portions. AFM tip-sample adhesion force mappings showed their efficiency to identify zones in which the ionic liquid is more concentrated.

AFM nanomechanical mappings showed thus their efficiency as a powerful characterization technique, combining an outstanding resolution with the ability to map simultaneously different properties giving complementary informations about the nanoscale structure and behavior of polymer systems. The sample preparation is moreover relatively simple: cryomicrotome is

generally used, but sometimes a simple cryofracture in liquid nitrogen is the best solution tu observe bulky materials. The preparation of films, if relevant, can also be used.

This technique has still a great potential to reveal, beginning with the extension of the methods to other materials such as nanocomposites. The ability to explore the interfaces can be of great help in this field: properties gradients, for instance, in such zones can give many useful informations about the interactions between two materials. From a wider point of view, such AFM characterizations could help to establish and validate interfacial modellings in composites and blends, using for instance finite elements, in order to predict interfacial properties and optimize their strength. This could be a good step forward in fields using many composite materials, such as aircraft construction, where preventing events like delamination or fiber pull-out is critical.

Since other complementary AFM modes were developped, their integration into the methods presented in this work is extremely promising. The acquisition of electrical properties mappings are now possible simultaneously with the nanomechanical mappings, allowing for instance to map additionally the current density induced by a voltage applied between a conductive AFM tip and the sample basis or substrate. Such characterizations can give additional informations which can be extremely relevant in materials containing ionic liquids, for example.

In summary, this work proposed a complete and practical understanding of AFM nanomechanical mappings and how they can help to understand the structure-properties relationships in polymer-based materials. It would complete its objectives if it could now serve as a basis to push deeper the AFM characterizations of local properties, as they have still a great potential.

Appendix A

Elements of methodology: Average value of a property of a material

Some results displayed in this work are mean values obtained from measurements made with a calibrated AFM setup. In order to have consistent data, especially for nanomechanical properties that have potentially no equivalent for comparison, a careful statistical approach is necessary.

The following conditions were respected when displaying the average value of a property (for instance the moduli in Figure 3.11):

- A minimum of 6 images (generally between 8 and 12) are used to calculate the average.
- Those images are obtained in at least 3 different sessions (thus with a different tip, different external conditions...).
- For each image, the average deformation is equivalent to the deformation obtained on the calibration sample when calculating the tip radius.
- No evidence of tip damage or contamination is reported during the session.

Concerning the interphase thickness in Chapter 3, the measurement is made by drawing profiles across the PBAT/PLA interphases in zones presenting low topographic variations (Figure 3.8). To obtain the averages, the modulus slopes and the standard deviations for each blend (table 3.5), a minimum of 3 profiles per image were used (*i.e.* a minimum of 18 profiles in total, applying the conditions mentioned above).

In chapter 4, such a method is also used to choose the representative distribution curves of Figure 4.8. Those curves (and their interpretations) are consistent with the mean values of the DMT modulus of PBAT, shown in Figure A.1.

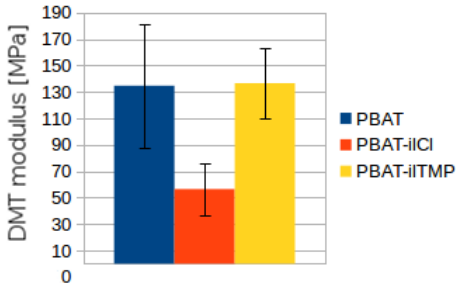

Figure A.1 – Average values of DMT modulus of PBAT/ionic liquids blends

Appendix B

List of figures and tables

List of Figures

List of Tables

FOLIO ADMINISTRATIF

THESE DE L'UNIVERSITE DE LYON OPEREE AU SEIN DE L'INSA LYON

NOM : MEGEVAND **DATE de SOUTENANCE :** 29/03/2018

Prénom : Benjamin

TITRE : Contribution of atomic force microscopy (AFM) to local mechanical characterization of polymer materials
(Apport de la microscopie à force atomique aux caractérisations mécaniques locales des matériaux polymères)

NATURE : Doctorat **Numéro d'ordre :**

Ecole doctorale : ED34 – Matériaux de Lyon

Spécialité : Matériaux polymères

RESUME : Ce travail de thèse a pour but de montrer comment des caractérisations nanomécaniques en AFM peuvent apporter une meilleure compréhension des relations structure-propriétés dans les polymères. Dans ce contexte, la technique elle-même et sa base théorique sont d'abord analysées pour mettre en œuvre une méthodologie robuste afin d'effectuer des mesures reproductibles.
Deux études principales sont menées sur un thème commun : la compréhension des interactions entre les biopolymères et les liquides ioniques (ILs). Tout d'abord, la compatibilisation des mélanges PBAT/PLA par deux ILs différents (à savoir il-Cl et il-TMP) est étudiée.
Les images AFM d'adhésion et de module local mettent en évidence les différentes microstructures, et soulignent que la compatibilisation résulte principalement d'une modification de l'interface PBAT/PLA, devenant une interphase cohésive. Ceci est dû à une interaction spécifique avec les cations et les anions de chaque liquide ionique, qui se situent préférentiellement au niveau de ces interphases.
La deuxième étude porte plus précisément sur la modification du PBAT semi-cristallin par de petites quantités des mêmes liquides ioniques. Alors que il-TMP forme des nodules dissipatifs dispersés dans la matrice et une interphase cohésive avec celle-ci, il-Cl, miscible dans la phase amorphe du PBAT, augmente la mobilité de la chaîne dans la MAF (i.e. fraction amorphe mobile) et l'entrave dans la RAF confinée (i.e. fraction amorphe rigide), conduisant à des modifications intéressantes des propriétés macroscopiques.
En plus de montrer certaines capacités intéressantes des ILs comme additifs dans les polymères, ces résultats dévoilent également un potentiel exceptionnel des caractérisations nanomécaniques en AFM pour la compréhension en profondeur des relations structure-propriétés dans les matériaux.

MOTS-CLÉS : AFM, microscopie à force atomique, propriétés mécaniques, PeakForce QNM, propriétés locales, polyester, mélange de polymères, liquide ionique, compatibilisation, polymère semi-cristallin, caractérisation

Laboratoire (s) de recherche : Ingénierie des Matériaux Polymères (IMP) de l'INSA-Lyon (UMR CNRS 5223)

Directeurs de thèse :
Jannick DUCHET-RUMEAU,
Sébastien PRUVOST

Président de jury :

Composition du jury :
Philippe LECLERE (Rapporteur)
Pascal CARRIERE (Rapporteur)
Nadine LAHOUD (Examinatrice)
Jean-Paul CHAPEL (Examinateur)